UNIVERSIDAD NACIONAL DE COLOMBIA

Spatio-temporal variability of the Atmospheric Boundary Layer in the Aburrá Valley: characterization, processes, multiscale interactions and impacts.

.

Laura Herrera Mejía

Universidad Nacional de Colombia
Facultad de Minas, Departamento de Geociencias y Medio Ambiente
Medellín, Colombia
2021

Spatio-temporal variability of the Atmospheric Boundary Layer in the Aburrá Valley: characterization, processes, multiscale interactions and impacts.

.

Laura Herrera Mejía

in Partial Fulfillment of the Requirements for the Degree of
Doctor of Philosophy

Advisors:
Carlos David Hoyos, Ph.D.
Univ. Prof. Dr. Mathias W. Rotach

Line of Research:
Boundary Layer Meteorology

Universidad Nacional de Colombia
Facultad de Minas, Departamento de Geociencias y Medio Ambiente
Medellín, Colombia
2021

You have no responsibility to live up to what other people think you ought to accomplish. I have no responsibility to be like they expect me to be. It's their mistake, not my failing.

— Richard P. Feynman

To my parents

.

Acknowledgements

It has been an unpredictable journey. First, I should probably thank the universe for keeping me alive and safe during these challenging circumstances. Five years seem like five minutes now, but in retrospect, life has taught me more lessons during these harsh times than in my 31 years of age. Of course, as something important comes to an end, you start thinking about what you could have done better or if you have made the right decisions during the process. Now, I have zero intentions of doing that here. Instead, I will use this page to give some recognition to the people that have supported me unconditionally and in so many ways that I can not even explain.

I have been encouraged, sustained, inspired, and tolerated by the most incredible group of people. I would like to start with my advisor Carlos Hoyos, and I will probably speak for more people than just myself while writing these words. Thank you for believing in me, in all of us, and for your unconditional support through these years, and not only from an academic perspective. Thank you for dedicating your life to teaching us how important it is to create opportunities for young people (whether appreciated or not) and make science something with high social relevance. Thank you for never giving up on me, on us, despite the most demanding challenges, for sharing your dreams and let us be part of them. I also want to thank Prof. Dr. Mathias W. Rotach. I'd never have imagined that my work could be shared with such high profile, worldwide recognized scientist, but on top of this, a remarkable human being. Thank you for opening the doors of your department and for always looking out for me during my time in Innsbruck.

Thanks to my few closest friends for being such a supportive team and accept me, even when we are two completely separate parts of the spectrum (I am definitely not an easy person). Thanks to my Air Quality team in SIATA, for your commitment and support, you saw me grow as a professional and trusted me to guide you, even when most of the time I was learning from you guys. Thanks to the ACInn members at the University of Innsbruck, for welcoming me into their lives. And finally, the biggest and most special thanks to my parents, my biggest cheerleaders, you never failed to love and support me.

This work was mainly supported by SIATA, The Aburrá Valley Early Warning System, fully funded by the Aburrá Valley Metropolitan Area (AMVA). By the seven-semester

faculty scholarship by Facultad de Minas of Universidad Nacional de Colombia. The Mach Grant program sponsored by the OeAD, Austria's Agency for Education and Internationalisation, and the University of Innsbrusk, Austria.

Contents

Chapter 1

Introduction

1.1 The Atmospheric Boundary Layer in Complex Terrains

Boundary-Layer Meteorology (BLM) refers to the theoretical, numerical, and experimental framework that focuses on studying the interactions between the earth's surface and the lower troposphere. These interactions are crucial for several applications in various temporal and spatial scales: from long-term energy balance and climate change assessment to extreme convection and air quality modulation; from agricultural applications to wind power generation; from homogeneous energy and momentum exchanges in large-scale regions over the ocean and flat rural areas to heterogeneous behavior on complex terrains and highly urbanized metropolitan areas. A better understanding of interactions between the earth's surface and the lower troposphere implies studying the structure and variability of the lower troposphere as a result of processes that are better described in the realm of a combination of fluid dynamics and thermodynamics. The structure of the lower troposphere includes the different interacting sublayers. Over homogeneous terrain, the Atmospheric Boundary-Layer (ABL) is defined "as that part of the troposphere that is directly influenced by the presence of the Earth's surface, and directly responds to surface forcings with a timescale of about an hour or less" (Stull, 1988). By definition, the ABL is turbulent, which means that the processes of mixing and exchange of energy, momentum, and scalars (i.e., water vapor, carbon dioxide, pollutants) from the Surface Layer (SL) to the rest of the atmosphere depend on turbulence, both thermal and mechanic (Stiperski and Calaf, 2018): Relatively low momentum diffusivity, highly convective be-

havior with rapid spatio-temporal changes, and high Reynolds numbers. In this sense, the small-scale physical processes depicted by the different terms in Turbulent Kinetic Energy (TKE) budget equation modulate the characteristics of large-scale phenomena, such as atmospheric stability regimes, development of deep convection, atmospheric pollutant dispersion, the formation of cold-pools, among several others. A careful analysis of the terms in the budget equation of TKE forms a sound basis for the discussion of observed velocity variances as well as future model improvements (Christen et al., 2009).

ABL processes and variability have been studied from various perspectives and approaches, ranging from theoretical studies to data analysis strategies to numerical modeling. One of the main challenges in studying the ABL dynamics is the high heterogeneity of the underlying forcing imposed by the earth's surface (Roth and Oke, 1993; Roth, 2000; Noppel and Fiedler, 2002; Ward et al., 2013). Ranging from abrupt changes in orography to a wide variety of land uses and roughness elements, complex terrain is the rule rather than the exception, especially when dealing with processes involving anthropogenic modified environments (Roth and Oke, 1993; Noppel and Fiedler, 2002). Nevertheless, most of our understanding of turbulence in the ABL is based on an idealized picture of real-life scenarios, e.g., horizontally homogeneous and flat terrains (HHF), implying that most of the exchange is vertical, and horizontal contributions are small and negligible (e.g., Monin–Obukhov Similarity Theory; Monin and Obukhov (1954)). However, in real-life situations such as complex mountainous terrains, multiple additional processes interact and contribute to the exchange variability at different spatial and temporal scales (Zardi and Whiteman, 2013; Rotach et al., 2015; De Wekker and Kossmann, 2015; Serafin et al., 2018; Barman et al., 2019). Not to mention that there is an increasing tendency of urban growth over rather complex environments, such as mountainous valleys, exponentially increasing the complexity and creating the need for reliable models capable of representing turbulent exchanges and complex flow fields (Moraes et al., 2005; Nadeau et al., 2013; Baklanov et al., 2015). The chaotic nature of the turbulent flow, as well as the short timescales and limited spatial extent of turbulent exchange processes, make them very difficult to represent within a Numerical Weather Prediction (NWP) model (Stiperski and Calaf, 2018).

The most important driver of the ABL's spatiotemporal variability and structure is the Surface Energy Balance (SEB) (Serafin et al., 2018). Over mountains (- valleys), the heterogeneous terrain leads to differential surface heating, producing thermally-driven winds (Whiteman, 2000). Those horizontal temperature/pressure differences lead to upslope,

up-valley, plain-to-mountain flows during the daytime, and to downslope, down-valley, mountain-to-plain flows through the night (Whiteman, 2000; Zardi and Whiteman, 2013). The thermal structure of the ABL within a valley is characterized by a diurnal cycle of build-up and breakdown of a temperature inversion (Whiteman, 2000). The latter is conditioned by the incoming solar radiation and the volume of the valley atmosphere, determined by its geomorphological characteristics (Leukauf et al., 2015, 2017). Sometimes, the inversion cannot be broken up, leading to a multi-layer structure of the valley atmosphere with different stratifications (Lehner and Rotach, 2018; De Wekker and Kossmann, 2015). Under these situations, pollutants will recirculate within the valley, which could lead to a gradual accumulation, and in some cases, the onset of critical air pollution episodes (Anquetin et al., 1998; Angevine et al., 2001; Henne et al., 2004; Rendón et al., 2015; Czarnecka et al., 2019).

In addition to the role of orography, the complexity increases when other surface properties feature small-scale variability (Serafin et al., 2018), e.g., elements with diverse roughness placed over steep slopes serving as a momentum sink for the atmospheric flow and leading to even higher uncertainty for determining the dominant processes that govern the turbulent exchanges (Wiernga, 1993). At the present time, the ABL structure and variability over highly-rough surfaces, including urban areas, are less understood (Roth and Oke, 1993), mainly because of the wide range of geometries (size, shape, and building arrangements) and materials (radiative, thermal, and moisture properties), showcasing a wide variety of boundary conditions to the atmosphere (Grimmond et al., 2004; Kotthaus and Grimmond, 2014; Schmutz and Vogt, 2019). In any given urban area, these properties are organized uniquely, which may imply that even with increasing experimental efforts, it could never be enough to develop a consistent theoretical or conceptual framework for turbulent exchange.

As in the case of the mountainous boundary-layer, several of the assumptions underlying the derivation of the classical ABL theories are most-likely invalid over rough surfaces (Rotach, 1993; Roth, 2000; Wood et al., 2010). Large obstacles at the lowest part of the SL induce mechanical turbulence that challenges the validity of the constant fluxes' assumption. In those cases, the SL is often treated by dividing it into two layers, the roughness, and the inertial sublayers. The *roughness sublayer* is the layer adjacent to the surface, where the three-dimensional flow adjusts to the effects of the many obstacles. The microscale flux fields within and just above the urban canopy are highly variable in space and time and are affected by direct interaction with the roughness elements

(Raupach et al., 1991; Roth and Oke, 1993; Britter and Hanna, 2003). The turbulent field within the roughness sub-layer must be considered as three-dimensional (Roth and Oke, 1993). At some height, z^*, the flow may be considered horizontally homogeneous (in the time average), and a 'constant' flux layer establishes. The roughness sublayer extends up to approximately two to five times the height of the roughness elements (Raupach et al., 1991). The *inertial sub-layer* is the region where the boundary layer has adapted to the integrated effect of the underlying surface, and it is usually treated by standard atmospheric boundary-layer formulas (Rotach, 1994; Britter and Hanna, 2003).

In an urban environment, the interaction between the airflow and aerodynamically rough and inhomogeneous surface exert control over the turbulence structure through different processes (Roth, 2000). Some of the most relevant are:

1. The formation of an intense shear layer near the top of the urban canopy, where the Mean Kinetic Energy (MKE) of the flow is converted into TKE, resulting in high turbulence intensity.

2. The presence of bluff-bodies increases the transport of momentum to the surface.

3. In the roughness sub-layer, the diffusivity of the flow is enhanced due to the superposition of turbulent wakes generated by individual roughness elements. Mixing generated by turbulent wakes behind individual roughness elements efficiently mixes and diffuses momentum, heat, moisture, or any other scalar quantity.

4. Diverse structures and materials lead to differential heating/cooling of sunlit surfaces, forming localized heat and mass plumes, which together with the dynamic structures of street canyons, comprise a complex system of energy and mass transport, adding spatial and temporal inhomogeneities to the system.

5. Enhanced mechanical mixing due to rougher surfaces in the urban environment, together with the urban heat island (UHI) effect, results in larger boundary-layer heights (Moraes et al., 2005).

6. The extreme heterogeneity of urban surfaces, usually at all length-scales, leads to permanent local advection.

7. Coherent structures* such as sweeps and ejections or ramp structures, can emerge

*Regions of concentrated vorticity, characteristic and flow-specific organization, recurrence, appreciable lifetime and scale (Fiedler, 1988)

in signals from the regularity or structure in the surface (Roth, 2000; Arnfield, 2003; Schmutz and Vogt, 2019)

8. Atmospheric stability near the surface shifts towards the near-neutral range, as a result of the permanent release of sensible heat due to the UHI and increased shear production (e.g. Wood et al., 2010; Schmutz et al., 2016).

9. A higher proportion of sealed surfaces and reduced green covers, compared to rural areas, usually leads to lower evaporation in cities (Oke et al., 1999; Grimmond et al., 2004), whilst the amount of energy stored in the thermal mass of buildings and anthropogenic materials becomes a major component of the energy balance (Grimmond and Oke, 1999; Offerle et al., 2006).

The above-described processes evidence the substantial changes in boundary-layer dynamics driven by heterogeneities in both complex topography and the urban surface.

1.2 Experimental studies of the ABL dynamics in Complex Terrains

Despite the difficulties in generalizing their results, experimental approaches, particularly field campaigns, are considered fundamental in order to fill the current knowledge gap concerning turbulent exchange processes over truly complex terrain. In that sense, over the past thirty years, driven by significant improvements in instrumentation, several research efforts have been devoted to studying the implications of non-ideal surfaces on turbulence characteristics, based on very detailed and well-planned field campaigns.

Regarding these field experiments conducted in order to investigate the characteristics of turbulent flows in mountainous terrain, one of the key programs is the Mesoscale Alpine Programme (MAP) Riviera Project (Rotach et al., 2004), which focused on the boundary-layer features in complex topography, using detailed field observations over the Alps of southern Switzerland, combined with high-resolution numerical modeling, aiming to characterize in detail the interactions between Alpine Valleys and the atmosphere. The Vertical Transport and Mixing (VTMX) experimental study was carried out in the Salt Lake Valley, Utah (Doran et al., 2002), and the program focused on the night-time stable stratification and the morning and evening transition periods, and urban areas affected

by the nearby elevated terrain. The scientific objectives of the Terrain-Induced Rotor Experiment (T-REX) (Grubišić et al., 2008), in The Sierra Nevada (United States), focused on improving the understanding and predictability of the coupled mountain-wave, rotor, and boundary layer system. The Mountain Terrain Atmospheric Modeling and Observations Program, MATERHORN (Fernando et al., 2015), followed four main pillars: modeling, experiments, technology, and parameterizations, all to improve mountain weather forecasts. Finally, the primary goal of one of the most recent (still in progress) campaigns, The Innsbruck Box (i-box), performed in the Alpine Inn-Valley (Austria), is to reach general conclusions about the dynamics of exchange processes over complex topography through a long-term (non-permanent) experimental set-up in combination with high-resolution numerical modeling (Rotach et al., 2017). In addition to these extensive projects, there have been a significant number of important single-site short-term studies addressing exchange processes in mountainous regions (e.g Al-Jiboori et al., 2002; Moraes et al., 2005; Hiller et al., 2008; Martins et al., 2009; de Franceschi et al., 2009; Pegahfar and Bidokhti, 2013; Hiller et al., 2008; Helgason and Pomeroy, 2012; Barman et al., 2019).

The rapid increase of urban areas over the last century, and the tendency of the human population to cluster in these large settlements, have brought the attention of the scientific community to urban-centered studies. However, the number of experiments and available data from cities remains small compared with those in natural ecosystems, considering that the deployment of turbulence, and in general, ABL measurements systems in densely-urbanized areas is technically and logistically demanding (Grimmond and Oke, 2002; Schmutz and Vogt, 2019). Three main approaches have been followed in order to investigate the alterations of the urban surface in the surface-layer exchange processes and turbulence characteristics (Kotthaus and Grimmond, 2014), including:

1. Role of intra-urban variations assessment through simultaneous observations at multiple sites (in some cases with diverse land-uses) within the same urban area (e.g., Two urban sites in Upsala, (Högström et al., 1982); Salt Lake City (Allwine et al., 2002); three rural, three urban and one suburban location in Basel, (Rotach et al., 2005); rural, suburban residential, dense urban and industrial areas in Łódź, (Offerle et al., 2006); four sites of increasing housing density in Melbourne, (Coutts et al., 2007); urban residential and suburban zones in Essen, (Weber and Kordowski, 2010); Helsinki, (Nordbo et al., 2013); two urban sites in the center of London (Helfter et al., 2016)).

2. Studies about the vertical flux variation within (-and above) an urban street canyon employing simultaneous measurements at different heights, in order to evaluate or improve microscale urban dispersion models (e.g. Roth and Oke, 1993; Rotach, 1995; Grimmond et al., 2004).

3. Variations of turbulent fluxes within one land use (e.g., the characteristics of *coherent structures* in the city of Basel using 12 years of data from single-site experiment (Schmutz and Vogt, 2019); the impact of site location and heterogeneity of the urban surface on flux observations on London (Kotthaus and Grimmond, 2014); multi-seasonal evaluation of energy, water, and carbon fluxes over Swindon (Ward et al., 2013))

1.3 Objectives and Goals

The main goal of this work is to identify and gain insight into the main processes between the synoptic- and micro-scale ends of the spectrum of atmospheric motions (including their cross-scale interactions) that modulate the ABL structure and dynamics over a complex and highly urbanized low-latitude valley. The Aburrá Valley is located in the Colombian Andes. The work follows an experimental approach, using multiple data sources, in order to evaluate the potential contribution of these phenomena on the boundary-layer variability in the study area. The intention is to shed some light on open questions regarding boundary-layer characteristics and some of their environmental implications over such complex terrain, among which are included the following:

1. Regarding the structure and variability of the valley's boundary-layer, are local-scale processes more important than the synoptic forcing?

2. Which are the implications of the structure and variability of the ABL on particular matter concentrations in an urbanized valley?

3. In a complex terrain and urbanized site, which feature the high heterogeneity of the urban surface or the rugged topography, exert more control over the exchange processes within the surface-layer?

4. Do the traditional boundary-layer scaling concepts hold over complex terrain and urbanized surfaces, so far from ideal terrains?

1.4 Methodology and observations

Geographical Context: The Aburrá Valley

The Aburrá Valley is 64 km in length, and it is located in Colombia, in the Central Andes mountain range between 6.0^o and 6.5^{o}N and 75.3^o and 75.6^{o}W. The orientation of the valley is predominantly south-to-north, south-to-northeast. The widest cross-section, from ridgeline to ridgeline, is 18.2 km, with a relatively flat section of approximately 8 km at the bottom of the valley. The narrowest section of the valley is around 3 km wide. The basin outlet is at 1290 m asl.

Figure 1.1: Geographical context of the Aburrá Valley, located in the tropical Andes, in Colombia, Department of Antioquia.

The area of the metropolitan region is 1152 km^2. Medellín, the largest and most populated city, is also the nucleus of the metropolitan area. Regarding the socio-economic aspects, Medellín exhibits high wealth inequality, with a Gini index of 0.47 (Restrepo et al., 2016), a statistical measure often used to gauge the income gap between the richest and the rest of the population. Urban population in the Aburrá Valley corresponds to 59% of the population of the entire state, and 95% of the population settled in the valley is concentrated in an area of about 340 km^2 (about 0.55% of the state's area, and 30% of

the valley's surface area).

From the turbulent exchange point of view, the region's complexity is due to the rugged topography together with the highly urbanized area. Additionally, the urban land cover reaches, in some cases, three-quarters of the hill-slope, exacerbating climate-related risks, especially flooding and landslides. The high population density in this geographic setting leads to several environmental concerns, including the recurrent onset of critical air quality episodes as a consequence of the high demand for fossil fuels linked to motor vehicles and industries, and the limited ventilation of the valley's atmosphere to disperse pollutant emissions.

Observational datasets

Due to its complexity regarding geomorphological configuration and demographical dynamics, not to mention the high predisposition of this particular region for several risk management related issues, the Aburrá Valley could be considered a natural lab for studying the complexity of surface-atmosphere interactions and the resulting impacts on the ABL structure and dynamics. The latter is the main reason for why the Aburrá Valley has the densest hydrometeorological and air-quality network in the region (more than 900 measurement sites) and has the most robust early warning system (SIATA, www.siata.gov.co) in the country, responsible not only for displaying and managing real-time information but also, but it is also in charge of building community resilience through education and social outreach, and warnings associated with climate-related risks. SIATA also perform research projects involving local environmental processes in the region (e.g., Herrera-Mejía and Hoyos, 2019; Roldán-Henao et al., 2020; Hoyos et al., 2019, 2020).

Also, as part of this study, a land-atmosphere energy exchange field campaign was designed and implemented in order to collect the relevant data to assess the main questions outlined before. In 2018, the COMPLEX (COmplex terrain Measurement Project for Land-atmosphere Energy eXchanges) campaign was designed and implemented, attempting to supplement the existing set of instruments providing observations of boundary-layer processes at larger-scales, with turbulence measurements. COMPLEX comprises seven measurement sites displayed in a cross-section of the Aburrá Valley and the Valley bottom. Each site is equipped with an integrated 3D sonic anemometer and CO_2/H_2O open-path gas analyzer (IRGASON - Campbell Scientific), a net radiometer (Kipp & Zonen), and a

multiparametric meteorological sensor (Thiess). The goal of the campaign is to provide long-term flux measurements in one of the region's highest urbanized and topographically complex areas for assessing the variability of boundary-layer processes. More detailed information about the set-up of the COMPLEX stations is included in Chapter 2.

1.5 Thesis outline

The structure of this document was decided considering that, once in final form, Chapters 3, 4 and 5 will be submitted to be considered for publication in peer reviewed journals (Chapter 2 is already published). For this reason, this thesis includes four main self-contained chapters (Chapters 2 to 5) with the results of the evaluation of the boundary-layer dynamics in a highly complex terrain at different spatio-temporal scales and some of the interactions between them.

Chapter 2 *"Characterization of the Atmospheric Boundary Layer in a Narrow Tropical Valley Using Remote Sensing and Radiosonde Observations, and the WRF Model: The Aburrá Valley Case Study"* (Herrera-Mejía and Hoyos, 2019) compares different techniques for the determination of the boundary-layer height in the Valley using several sources of information, in order to characterize its spatio-temporal variability associated with other meteorological parameters.

Chapter 3 *"An assessment of the role of surface sensible heat flux and the atmosphere inversion on the Break-Up time in a highly complex terrain"* explores the trade-off between observed proxies of the energy provided to the valley atmosphere, and of the energy required to erode the nighttime inversion, and the associated consequences of the breakup time in pollutant dispersion in the Valley.

Chapter 4 *"COMPLEX Experiment: Boundary-Layer interactions in a heavily-urbanized complex terrain"* gives an overview of the COMPLEX experiment, including a detailed description of the sites and all the complementary instrumentation and data available in the Aburrá Valley. Some preliminary findings are also included in order to highlight the research potentialities of this experiment.

Chapter 5 *"Observed turbulence characteristics in a highly urbanized Andean valley. The Aburrá Valley Case Study"* examines the applicability of *local scaling* to flux-variance relationships in order to characterize turbulence properties over a non-ideal surface.

In addition to these four chapters, a final conclusions and recommendations chapter is included, trying to bring together the overall findings and still open questions of this work.

Chapter 2

Characterization of the Atmospheric Boundary Layer in a Narrow Tropical Valley Using Remote Sensing and Radiosonde Observations, and the WRF Model: The Aburrá Valley Case Study

---

Laura Herrera-Mejía[1], **Carlos D. Hoyos**[1]

[1] *Universidad Nacional de Colombia, Sede Medellín, Facultad de Minas, Departamento de Geociencias y Medio Ambiente*

2.1 Abstract

The spatiotemporal evolution of the atmospheric boundary layer (ABL), in a narrow, highly complex terrain located in the Colombian Andes, is studied using radiosondes and remote sensing equipment. Different techniques are implemented to automatically estimate the ABL height using ceilometer backscattering profiles and a combination of a radar wind profiler and microwave radiometer retrievals. The large aerosol load from anthropogenic emissions within the valley allows the use of ceilometer-based ABL height detection methods, especially under stable atmospheric conditions. Convective atmospheres, however, favor aerosol dispersion, increasing the uncertainty associated with the estimation of the convective boundary layer using ceilometers. In contrast, the multisensor technique is more robust, performing better in stable and unstable conditions.

All ceilometer-based methods and the multisensor scheme capture the observed ABL height diurnal cycle. The main difference among ABL height retrievals occurs in the afternoon and during the night when Richardson number estimates tend to detect the top-down contraction of the residual layer, while ceilometer-based estimates detect the sudden bottom-up onset of the nocturnal stable layer. The results also show that intra-annual and annual variations of cloudiness strongly condition the ABL expansion, leading to a modulation of the ABL height diurnal cycle. The amount of aerosol particles near the surface is influenced by the evolution of the ABL, modifying the available control volume for the pollutants to interact and disperse. The evolution of ABL over the slopes and at the valley floor differs as a result of the local thickening associated with upslope winds. Weather Research and Forecasting model simulations, from a climatological point of view, skillfully simulate the observed ABL height concerning both the diurnal and annual cycles; the model skill is higher over the valley floor than over the slopes.

2.2 Introduction

A better knowledge of the atmospheric boundary layer (ABL) structure and dynamics is fundamental to understand the mechanisms associated with the behavior of meteorological variables in urban areas (Baklanov and Mahura, 2009), the evolution of air pollutant dispersion and disposal in the atmosphere (Nieuwstadt and van Dop, 1982; Kastner-Klein and Rotach, 2004), and the development of deep convection on different spatial scales (Mapes, 2000; Nesbitt and Zipser, 2003; Rochetin et al., 2014). The triggering of local convection strongly depends on the spatiotemporal variability of near-surface processes, determining the diurnal cycle of rain showers and thunderstorms as daytime solar radiation heats the surface, triggering thermal instability (Betts et al., 2002; Nesbitt and Zipser, 2003; Liu and Liang, 2010; May et al., 2012). The convective boundary layer (CBL) plays a fundamental role by acting as an interface for exchanging momentum, water vapor, gases, and pollutants from the surface into the free atmosphere (Betts, 1973). Fair weather cumuli are, for example, a result of the near-surface exchanges; hence, their life cycle is strongly coupled to the variability of surface fluxes in the ABL (Chandra et al., 2013; Brown et al., 2002; Betts and Viterbo, 2005). The diurnal cycle of lower troposphere processes, which are governed by the incidence of solar radiation, also controls the state of atmospheric stability and evolution of the ABL, modulating the concentration of pollutants from mobile and fixed sources (Yu et al., 2001; Whiteman

et al., 2014). The ABL height determines the control volume for pollutants to disperse (De Wekker and Kossmann, 2015; Lotteraner and Piringer, 2016): when the meteorological conditions are not favorable for the growth of the CBL, anthropic emissions build up and lead to critical air pollution episodes. In this sense, the ABL height implicitly determines the pollutant concentration (Dabberdt et al., 2004; Eresmaa et al., 2012; Wiegner et al., 2014). Consequently, in recent years, urban meteorology has become a priority for city planning and human health studies (Di Sabatino et al., 2013; Shrivastava et al., 2014).

Despite the importance of the ABL dynamics, there is not a single, reliable and widely accepted technique to retrieve mixing heights (Seibert et al., 2000). The lack of a robust tool is particularly critical for complex terrains where the challenge not only is restricted to the development of an ABL height retrieval algorithm but also extends to the definition of the ABL itself. De Wekker and Kossmann (2015) and Lehner and Rotach (2018) highlight current challenges in our understanding of the ABL over mountainous terrain, noting that it exhibits a multilayered structure and that the existing detection methods might be inefficient or represent different components of an intertwined dynamic. Numerous definitions and methods result in a wide range of estimates from in situ and remotely sensed measurements (Eresmaa et al., 2012; Lotteraner and Piringer, 2016). Indeed, evidence from previous studies suggests that using more than one method and different data sets is highly recommended to overcome the deficiencies of individual techniques (Emeis et al., 2008; Quan et al., 2013; Uzan et al., 2016; Wang et al., 2016; Su et al., 2017) and, in complex terrains, to capture the footprint of different processes, resulting in a multilayered structure. Among the most widely used methods are the gradient method using radiosondes (Seidel et al., 2010; Lee et al., 2014), the minimum gradient method, maximum variance using ceilometer profiles (Hayden et al., 1997; Stachlewska et al., 2012), and the bulk Richardson number method (Stull, 1988; Chandra et al., 2014; Zhang et al., 2014a).

Radiosondes are still widely regarded as the most accurate method for mixing layer height retrievals, especially for enabling direct measurements of temperature, humidity, and pressure (Lokoshchenko, 2002; Hennemuth and Lammert, 2006; Seidel et al., 2010; Emeis et al., 2012; Sawyer and Li, 2013; Zhang et al., 2014b; Lee et al., 2014). However, their limited temporal resolution does not allow the detailed evaluation of ABL evolution throughout the entire diurnal cycle. A significant improvement in remote sensing techniques over the past sixty years, in particular over the past two decades, has allowed researchers to use vertical profiles from active remote sensing instruments, such as

ceilometers, lidars, and radar wind profilers (RWPs), as well as passive sensors such as microwave radiometers (MWRs), for long-term ABL height retrievals (Hennemuth and Lammert, 2006; Nisperuza, 2015; Sundström et al., 2009; Bianco et al., 2011; Stachlewska et al., 2012; Hannesdóttir, 2013; Lotteraner and Piringer, 2016; Uzan et al., 2016), facilitating the study of the ABL temporal evolution.

The Aburrá Valley, a low-latitude highly complex mountainous terrain located between the Colombian west and central mountain ranges, is home to approximately four million people living in an area of 1152 km^2 and has endured the onset of critical air quality episodes during recent years (Figure 2.1a). The evidence suggests a substantial modulation of the local air pollutant concentration associated with ABL variability. In March 2016, a critical air quality episode highlighted the relationship between local meteorological conditions, ABL variability, and pollutant concentrations (Figure 2.1b). Pérez Arango (2008), Correa et al. (2009), and Pérez Arango et al. (2011) used wind and virtual potential temperature vertical profiles from a short field experiment (3 days in 2006 and one day in 2017) using pilot and tethered balloons to study boundary layer winds and their interaction with the free atmosphere. Their results suggest a change in the atmospheric stability, from stable to neutral conditions, at approximately 10:00 am LT. Nisperuza (2015), using a 532 nm lidar, presented evidence of a marked mid-morning transition between the stable and convective layers. The results of these studies represent the first observational steps towards a better understanding of ABL evolution within the Aburrá Valley. Despite the advances, there is a need for a long-term continuous ABL height dataset to identify and study the meteorological and climatological conditions that modulate the ABL dynamics and lead to critical air quality episodes.

The central aim of this study is to examine the ABL height variability over the Aburrá Valley, on different time scales, associating it with the evolving regional climate and the meteorological conditions within the valley that are important in modulating the ABL behavior on the local scale using observational evidence and limited-area numerical simulations using the Weather Research and Forecasting (WRF) model. In this work, ABL height refers to the distance from the surface (ground level) to the top of the boundary layer. There is a growing need for skillful ABL numerical simulations and forecasts associated with evaluating air quality projections and urban planning scenarios (Baklanov and Mahura, 2009; Wagner et al., 2014; Shrivastava et al., 2014). Moreover, correct simulation of the ABL using climate and weather models is vital for pollutant dispersion modeling, and it also conditions the overall skill of numerical weather prediction models (van der

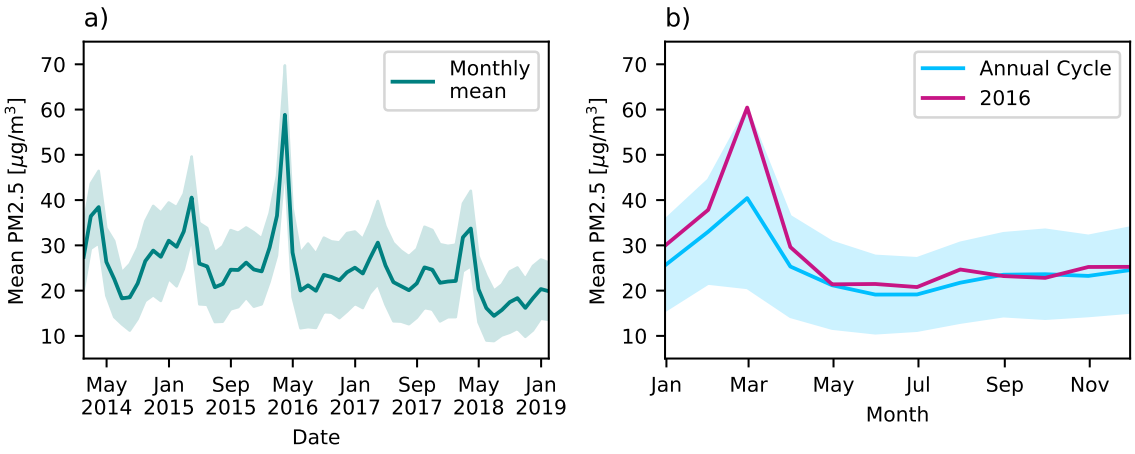

Figure 2.1: a) Monthly evolution of the average PM2.5 concentration in the Aburrá Valley (teal line). The spatial average is computed using eight PM2.5 stations (BAM1020). The period of the PM2.5 records is from January 2014 to March 2019, with an hourly temporal resolution. b) Annual cycle of the average PM2.5 concentration in the Aburrá Valley (cyan line). The magenta line corresponds to the 2016 PM2.5 monthly concentrations. In both cases, the teal/cyan shadow corresponds to the mean value +/- one standard deviation representing the variability.

Kamp and McKendry, 2010; Di Giuseppe et al., 2012; Zhang et al., 2014a). This work includes the development and implementation of both conventional and new methods to retrieve ABL heights based on information from radiosonde campaigns, ceilometers, a RWP, and a MWR. The remote sensors operate continuously as part of the Sistema de Alerta Temprana de Medellín y el Valle de Aburrá (SIATA, www.siata.gov.co). In section 2, we present a description of the data used for the ABL assessment and the different techniques implemented to estimate ABL heights from single-sensor measurements and by combining the retrievals from multiple instruments. Section 2 also includes a description of the numerical model configuration and the experimental set-up. Section 3 presents the results of the ABL height spatiotemporal analysis, identifying the climate and meteorological conditions favoring the pollutant dispersion in the Aburrá Valley. An evaluation of the ABL height simulation and forecast skill for the Aburrá Valley is also included in section 3. Finally, section 4 presents the most important conclusions of the study.

2.3 Data and Methodology

Observational and theoretical evidence suggests there are significant gradients of different meteorological variables in the lower troposphere due to the transition between the ABL and the free atmosphere, allowing the use of vertical profiles of atmospheric variables to infer the ABL height (Chandra et al., 2014). The vertical structure of the aerosol concentration, virtual potential temperature (θv), wind speed and relative humidity are some of the most commonly used profiles for indirect ABL height estimates. The ABL retrieval methods proposed in this work use data from various ceilometers, a microwave radiometer, and a boundary layer radar wind profiler. ABL height retrievals are compared to estimates using radiosonde data during intensive observation periods (IOPs).

Geographical context

Figure 2.2 shows the geographical context of the Aburrá Valley and the location of the remote sensing equipment used for ABL estimates. The valley is 64 km long, and it is located in the Central Andes mountain range between 6°N and 6.5°N and 75.3°W and 75.6°W. The widest section of the valley, from divide to divide, is approximately 18.2 km wide, and the width of the narrowest section is approximately 3 km. Most sensors are installed on the base of the valley except for the southernmost ceilometer, installed at the western hill, allowing the evaluation of ABL structure dependence on topography inside the valley.

Data

Ceilometer data

Ceilometers provide information about the laser-pulse energy that is backscattered by clouds and other atmospheric components, including particulate matter, which is expressed as the backscattering attenuated coefficient (β) (Emeis et al., 2009; Münkel and Roininen, 2010; Kambezidis et al., 2012). Measured profiles from three Vaisala CL51 ceilometers, installed at different locations inside the valley (see Figure 2.2), are used to estimate ABL heights. Vaisala CL51 ceilometers work at the 910 nm wavelength and

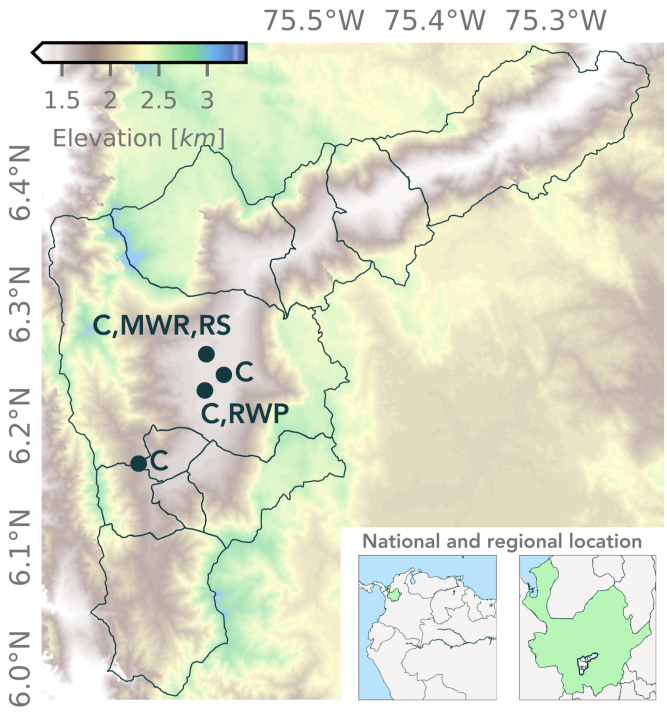

Figure 2.2: Geographical context of the Aburrá Valley, located in Colombia, Department of Antioquia. The map shows, in white to blue colors, the main topographic features of the region and the location of the remote sensing equipment used in this study, according to the following convention: C → Ceilometer, MWR → Microwave Radiometer, RS → Radiosonde, RWP → Radar Wind Profiler. Most sensors are located at the base of the valley, except for the southernmost ceilometer (Itagüí ceilometer), which is installed at a considerably higher altitude than the valley floor and at the western hill. The MWR is located at SIATA's main operations center (*Torre SIATA*).

emit a laser signal every 67 *ns*, providing backscattering attenuated coefficient measurements with a vertical resolution of 10 *m* and temporal resolution of 16 *s*. Ceilometer profiles are available continuously (with some missing data periods) since October 2014 and November 2015, at the *Torre Siata* and Itagüí sites, respectively

MWR data

MWRs measure the radiation emitted by atmospheric gases at submillimeter-to-centimeter wavelengths and are useful for retrieving the thermodynamic state of the atmosphere at different levels, allowing the assessment of atmospheric stability in real time. The Aburrá Valley MWR (Figure 2.2) is a Radiometrics MP-3000A profiler and provides continuous

retrievals of temperature, relative humidity and liquid water up to a height of 10 km above the surface under nearly all weather conditions. The MWR is located at the top of the SIATA main operations center on the valley floor, approximately 60 m from the surface, and it provides vertical profiles with variable spatial resolution: 50 m from the surface to 500 m, 100 m up to 2 km, and 250 m up to 10 km. Thermodynamic profiles are available with a 2-minute time resolution, and the data record spans from January 2013 to the date.

RWP data

Doppler radars used for vertical wind profiling rely on refractive index variations caused by changes in humidity, temperature, and pressure. The Aburrá Valley wind profiler (see Figure 2.2), a RAPTOR VAD-BL by DeTect Inc., works at a nominal frequency of 915 MHz, reaching up to 8 km above the surface under high humidity conditions (Lau et al., 2013). The RWP is designed to measure the wind profile in different modes that differ in their vertical resolution and in the atmospheric domain. In our case, we use two overlapping modes: in the higher resolution mode (60 m), the RWP measures the wind profile from 77 to 3500 m, and in the lower resolution mode (72 m) from 2500 to 8000 m. In this study, we only use the higher resolution mode since the ABL was never higher than 3500 m. The temporal resolution is five minutes. The radar was installed in January 2015.

Radiosonde data

Three five-day radiosonde IOPs were conducted from January 28 to February 2 (IOP 1), from March 24 to March 28 (IOP 2) and from May 4 to May 8 (IOP 3), in 2015. During each IOP, there were eight radiosonde flights per day launched at the base of the valley from the Torre SIATA site, resulting in a total of 120 atmospheric profiles. The design of the IOPs responds to the aim of sensing the atmosphere during the three main seasons in the Andean Region of Colombia: dry, dry-to-wet transition and wet seasons; however, anomalous meteorological conditions resulted in atmospheric behavior different from the typical climatological patterns expected over the region. During the three IOPs, the surface air temperature, surface wind speed, and surface relative humidity were remarkably homogeneous, and they were characterized by persistent cloudiness, particularly during

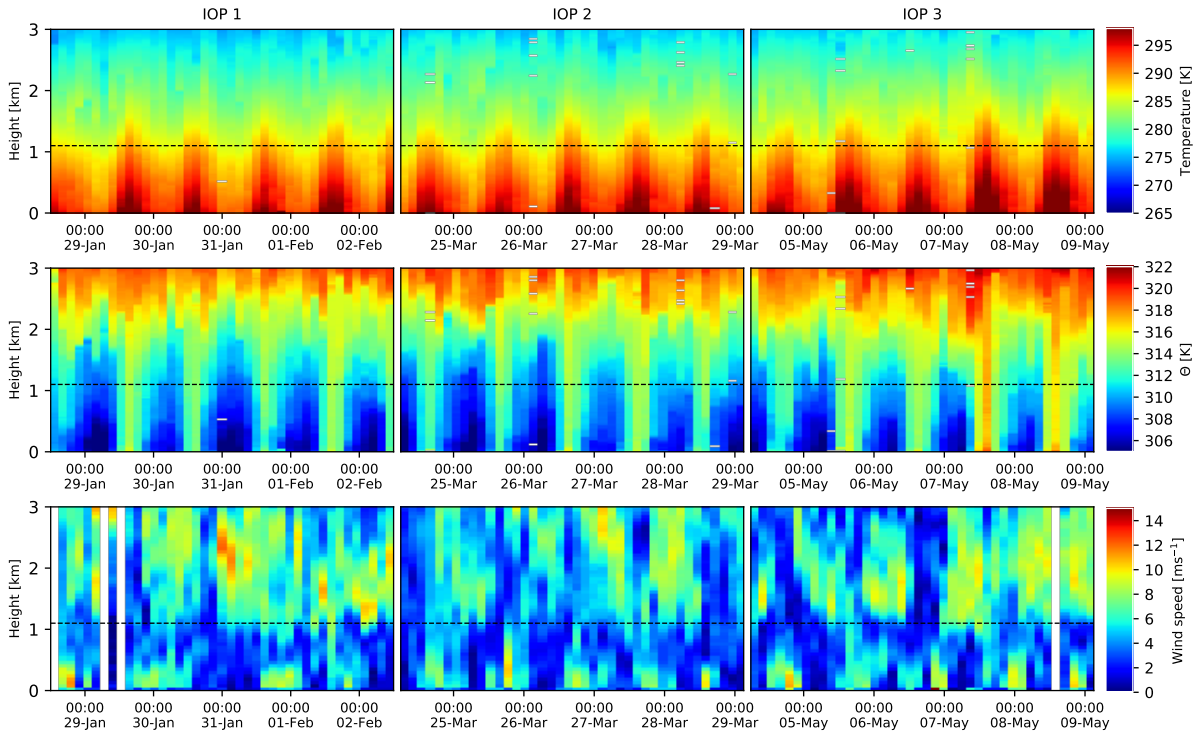

Figure 2.3: Vertical profiles of lower troposphere air temperature, potential temperature and wind speed during the three Radiosonde IOPs. The left, center and right columns represent Radiosonde IOP 1, 2 and 3, respectively. The horizontal dashed line corresponds to the average depth of the valley.

early morning hours, and isolated precipitation events. The average surface air temperature for the entire 5-day period was 21.8, 21.7 and 23.2 ^{o}C, respectively. The average surface wind speed was 3.1, 2.9, and 3.2 ms^{-1} for IOPs 1, 2 and 3, respectively, and the average relative humidity was 61.4, 61.8 and 55.5 %. The most salient difference among the three IOPs is the cumulative rainfall: 2.2, 16.4, and 6.8 mm, respectively. These differences, however, do not considerably condition the behavior of the atmospheric stability during the IOPs. Figure 2.3 presents the measured vertical profiles of the lower troposphere air temperature, virtual potential temperature, and wind speed for the three IOPs for the first 3 km showing a marked diurnal cycle. The amplitude of the diurnal cycle is particularly high up to approximately 2-2.5 km, where the direct influence of the surface seems to decay considerably. Despite the apparent regularity, the maximum height of the thermal expansion varies from day to day, unequivocally leading to ABL variability. Regarding the wind speed, it can be seen that the magnitude is considerably higher above the valley, as expected, with values inside the valley typically less than 3 ms^{-1} and approximately 8 ms^{-1} at 2 km.

In-situ, satellite, and reanalysis data

In addition to the atmospheric profiles obtained using ceilometers, MWR, RWP, and radiosondes, we use in-situ records of fine particulate matter (PM2.5) concentration from eight BAM1020 (MetOne equipment) monitoring stations installed in the valley, 5-minute precipitation records from two tipping-bucket gauges installed at Torre SIATA, 1-minute radiation from a Kipp & Zonen pyranometer also at Torre SIATA, and 1-minute wind speed and direction from two Vaisala all-in-one WXT520 weather stations installed at the Torre SIATA and Itagüí sites. In addition to the in-situ data, we also use the 3-hourly Tropical Rainfall Measuring Mission (TRMM) 3B42 v7 product, which is in good agreement with in-situ stations globally and regionally (TRMM, 2011; Kummerow et al., 1998; Huffman et al., 2007; Ceccherini et al., 2015), and low-, medium-, and high-level cloud data from the ERA-Interim global reanalysis project (Dee et al., 2011). The TRMM-3B42 v7 product has a 0.25° by 0.25° spatial resolution, and a coverage spanning the entire zonal band from 50°S to 50°N. The spatial resolution of the ERA-Interim data set is approximately 80 km.

Determination of ABL heights using ceilometers

ABL height detection methods using ceilometer backscatter intensity (BI) profiles are based on the assumption that a significant aerosol concentration reduction takes place at the top of the ABL, in the transition between the well-mixed near-surface troposphere and the "free" troposphere. During fair-weather days, BI profiles often provide an excellent depiction of the ABL evolution within the valley and throughout the day. Figure 2.4a shows an example of the ceilometer BI for May 9, 2015. A 300-400 m high stable layer is clearly observed between 03:00 and 09:00 LT. A secondary layer transition, with a smaller BI amplitude, is positioned between 1000 and 1500 m between 00:00 and 04:00 LT. The latter corresponds to the residual layer. At approximately 09:30 LT, the stable layer tends to disappear due to the transition to a CBL. The onset of the CBL generates a reduction in BI, and consequently, the ABL is significantly more difficult to detect using aerosols as a proxy. Initiation of the CBL leads to the formation of fair-weather cumuli with a height of 2-3.5 km between 10:00 and 18:00 LT. This behavior is observed until 16:00-18:00 LT when the mixing processes cease, and the onset of the stable layer starts to occur.

The ceilometer-based methods allow the identification of internal layers within the

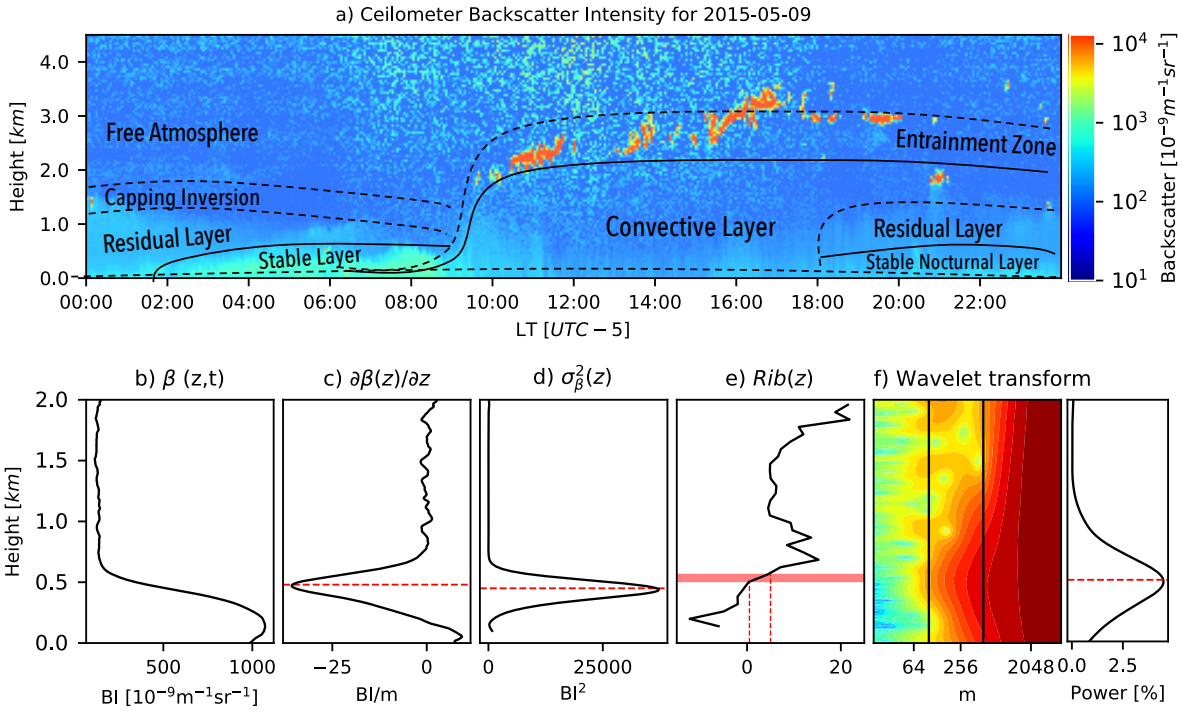

Figure 2.4: a) Evolution of the ceilometer BI vertical profiles (blue to red colors) for May 9, 2015. Colors represent BI measured by the SIATA Vaisala CL51 ceilometer located at the center-bottom of the valley. The lines correspond to the vertical cross-section of the ABL structure over land (modified from Garratt (1992)). The Figure shows a remarkable correspondence between aerosol and fair-weather cumuli dynamics during the day and the prototypical evolution of the ABL. b) Average ceilometer BI for May 9, 2015, between 09:30 and 10:00 local time. c), d), e) and f) ABL height detection for May 9, 2015 using the minimum gradient method, maximum variance scheme, Richardson number-based multisensor methodology, and a wavelet transform-based method, respectively. The horizontal red area in e) marks the estimated ABL height using R_ibc from 1 to 5, and the vertical red dashed lines correspond to R_ibc =1 and 5.

ABL caused by weak mixing and stratification (Emeis et al., 2008; Young, 2013; Young and Whiteman, 2015). Most profiles are complex and show multiple breakpoints due to aerosol accumulation on weakly mixed layers, the presence of clouds, high humidity conditions, and the inherent multilayer nature of ABL in complex terrains (Martucci et al., 2010; Lehner and Rotach, 2018; Serafin et al., 2018). The ceilometer-based ABL height detection methods used herein correspond to the minimum gradient method, maximum variance scheme, and a continuous wavelet transform-based technique. Considering the ABL definition by Stull (1988), we use 30-minute average BI profiles for ABL detection to maximize the signal-to-noise ratio, concomitantly providing sufficient information about the ABL structure and temporal variability.

Minimum gradient and maximum variance methods

One of the most common tools for determining the ABL height using BI profiles is the vertical gradient method proposed by Hayden et al. (1997), which has been used by several authors (Steyn et al., 1999; Muenkel et al., 2004; Emeis et al., 2012; Stachlewska et al., 2012). The minimum of the vertical gradient profile is considered to be the ABL height. Figure 2.4b shows the average ceilometer BI for May 9, 2015 (Figure 2.4a), between 09:30 and 10:00 LT, and as an example, Figure 2.4c shows the results for the ABL height detection using the minimum gradient method. On the other hand, the maximum variance method locates the sharpest changes in the BI profiles due to the layer transition by finding the maximum variance in the vertical profile. The variance profile is calculated using a 200 m sliding window. Figure 2.4d shows the detection using the maximum variance method.

One of the main advantages of ceilometers is the ability to operate continuously under any atmospheric conditions. However, in the presence of rain, cloud droplets, and hail, light is scattered more efficiently in comparison to aerosol-only scattering (Young, 2013). As a result, the profiles do not represent the typical behavior in the atmosphere, and the transition between layers becomes almost impossible to detect. Therefore, clouds and precipitation have to be filtered out before determining the ABL height using ceilometers. To overcome this issue, we developed a simple algorithm to detect cloud layers in the profiles and subsequently filter them out using linear interpolation of BI between the cloud-free edges to complete the missing data where the cloud is located.

Continuous wavelet transform-based method

The vertical distribution of aerosols in the troposphere is the result of complex nonlinear interactions among several physical processes occurring on a broad set of temporal and spatial scales. This interaction and multilayer structure of the ABL in mountainous terrains (Lehner and Rotach, 2018; Serafin et al., 2018) imposes difficulty in the automatic determination of the ABL height. A spectral analysis tool such as the wavelet transform is ideal for detecting changes in the BI profile associated with the height of the ABL by isolating the appropriate spatial scales and identifying the maximum variance close to the surface. Various authors have successfully used wavelet-based strategies for automatic ABL detection (Morille et al., 2007; Baars et al., 2008; Cohn and Angevine, 2000;

Granados-Munoz et al., 2012). However, most studies have used the Haar function as the mother wavelet and a fixed dilation parameter. In this paper, we use the full discretization of the continuous wavelet transform (CWT) technique following the formulation described by Torrence and Compo (1997) using Morlet and Paul wavelets.

The methodology proposed herein for ABL detection using CWT is performed by (i) constructing the wavelength-height wavelet spectrum; (ii) integrating the wavelet spectrum on selected spatial scales corresponding to the vertical extent of the physical processes involved in the ABL structure, in this paper on scales ranging from 50 to 500 m; (iii) detecting, bottom-to-top, the maxima in the band-passed spectrum, where the ABL height typically corresponds to the first maximum; and (v) nevertheless, checking the relative magnitude of the subsequent spectral peaks to guarantee the presence of a considerable BI reduction. If the reduction is not significant, the algorithm selects the following spectral peak, and step (v) is repeated. Figure 2.4f shows the ABL detection for the profile in Figure 2.4b using the CWT-based scheme. The Figure shows the wavelength-height spectrum, the band-passed spectrum, and the selection of the maximum corresponding to the estimated ABL height.

Richardson number method: ABL height determination using RWP and MWR profiles

We propose and implement a novel multisensor scheme for continuous ABL detection combining information from the RWP and the MWR. The profiles obtained from these two sensors allow the estimation of the bulk Richardson number (Rib), a dimensionless parameter that is typically implemented using radiosonde data. The method integrates dynamic and thermodynamic variables to establish a critical threshold Rib_c where the turbulent flow becomes laminar in the free atmosphere (Stull, 1988; Eresmaa et al., 2006; Granados-Munoz et al., 2012; Zhang et al., 2014a; Schween et al., 2014; Chandra et al., 2014). The Rib, for a specific z level, is computed as follows

$$Rib(z) = \frac{g}{\theta_s} \frac{(\theta(z) - \theta_s)}{(u(z)^2 + v(z)^2)} z \tag{2-1}$$

where θ_s is the potential temperature for a reference level near the surface, $\theta(z)$ is the potential temperature, and $u(z)$ and $v(z)$ are the zonal and meridional wind components. The RWP and the MWR are located inside a radius of approximately 3 km and have different vertical resolutions. Thus, to estimate Rib, preprocessing of the data is

required. Figure 2.4e shows an example of ABL height detection using the multisensor *Rib*-based method for different Rib_c, showing good agreement with the previously described ceilometer-based methods.

The selection of a Rib_c is not straightforward as it potentially influenced not only by the vertical resolution of the profiles but also by the measurement strategy used for obtaining the wind speed and potential temperature (Seibert et al., 2000). Figure 2.5a shows an example of the diurnal evolution of the Richardson number profile for February 2, 2015. The profiles show a marked transition from stable conditions in the morning (from 00:00 to approximately 10:30 LT) to a thermally unstable regime (10:30 to 15:30 LT), to stable again during the night. Vertical gradients of *Rib* under stable conditions are very high, with all the isolines closely grouped. The Figure also shows an expansion of the low *Rib* area between 10:00 and 18:00, and a clear separation of the isolines during the convective stage. Under stable conditions, the differences in isoline height as a function of Rib_c are not substantial, being less than 100 m; however, during the convective phase, these differences could exceed 1000 m in a single day. It is interesting to note that isolines corresponding to $Rib_c = 1, 2, 3$, which are closer to the surface, are more variable than those for Rib_c =4,5, underlining two aspects: (i) the irregularity of convective activity near the surface, and (ii) the maximum height of thermal convection as suggested by the relatively smooth upper isolines. Figure 2.5b shows the diurnal cycle of the mixed layer height estimated using the multisensor method with different Rib_c for the period from January 2015 to June 2018. Similar to Figure 2.5a, while the general behavior according to different Rib_c is the same, there are considerable differences in the ABL height. These differences have practical implications since the maximum ABL height for deep valleys might determine whether or not aerosols are able to disperse away from the surface and outside of the valley.

Determination of ABL height using Radiosondes

We use two methods to estimate the ABL height using radiosonde data. The first approach corresponds to the Holzworth method, commonly referred to as the parcel method (Holzworth, 1964). This method establishes that the ABL height is determined by the first interception between the virtual potential temperature profile ($\theta_v(z)$) and the dry-adiabat ascending from the surface, corresponding to the height where the parcel is in equilibrium with its surroundings (Holzworth, 1964; Lokoshchenko, 2002; Münkel et al., 2006; Seidel

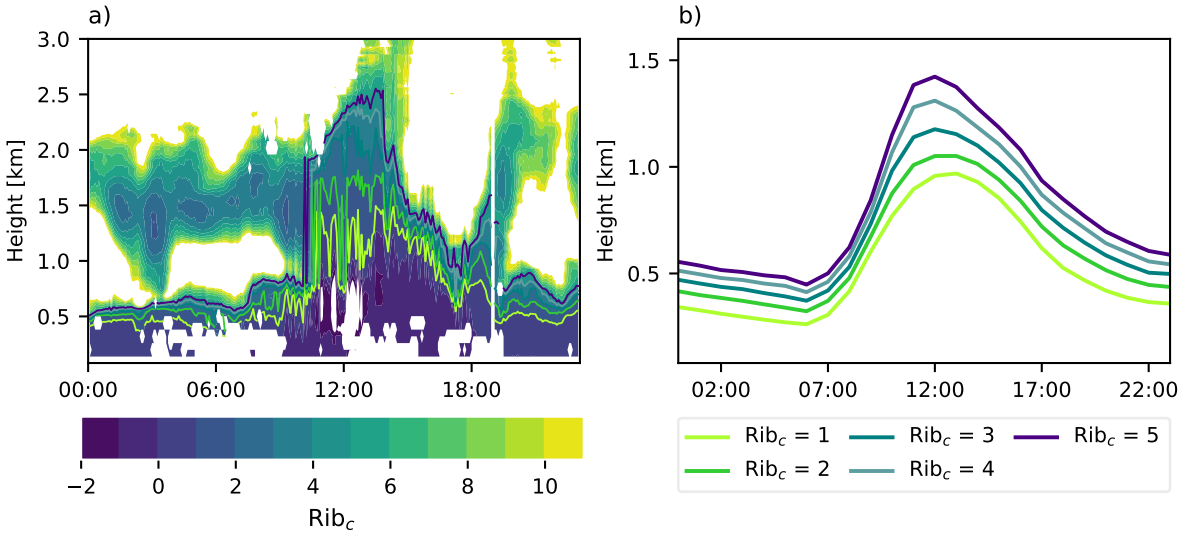

Figure 2.5: a) Evolution of the Richardson number (*Rib*) profile for February 2, 2015. The lime-to-purple lines correspond to contours of different $Rib_c = 1, 2, 3, 4, 5$. b) diurnal cycle of the mixed layer height retrieved using the multisensor method with different Rib_c. The period used for the estimation of the diurnal cycle corresponds to January 2015 to June 2018.

et al., 2010). The second approach corresponds to the *Rib* method described previously. In this case, potential temperature, wind speed and direction are obtained directly from the radiosondes. Zhang and Li (2019) recently presented a long-term assessment (30-year, 1988–2017) of the climatological characteristics of the ABL over Japan, showing that the bulk Richardson number method performed the best among all the methods tested. Other authors, such as Rampanelli and Zardi (2004), have proposed algorithms based on the potential temperature profiles from soundings to find the CBL using best-fit concepts. We explored Rampanelli and Zardi (2004) methodology but the results were not robust during all cases.

WRF ABL forecast assessment

The WRF model, version 3.7.1 (Skamarock et al., 2008), is the basis for the operational numerical weather forecasts issued by SIATA on a daily basis. We used the output of the daily 00Z WRF 24-hour forecasts for three years, focusing on the evaluation of the representativeness of the ABL diurnal cycle and the skill assessment of the 24-hour average ABL height numerical forecasts (0-24 hour forecast horizon). The model configuration includes three nested domains with 18 (191 x 191), 6 (82 x 118) and 2 (136 x 136)

Table S1: WRF model schemes and parameterizations (see Skamarock et al. (2008) for details).

Process	Scheme
Microphysics	Eta (Ferrier)
Radiation	Rapid Radiative Transfer Model (RRTMG)
PBL	Mellor-Yamada-Janjić
Land surface	Unified Noah land-surface model
Surface	Monin-Obukhov (Janjić Eta)

km grid spacing, and 40 vertical levels up to 50 hPa. The first domain (18 km), from 10°S to 20°N and from 60°W to 90°W, covers the entire geography of Colombia, the Caribbean Sea, the Colombian sector of the Pacific Ocean, and Amazonia, to include the main external forcing factors of the regional atmospheric circulation and precipitation over the territory. The second domain (6 km) includes the Andean region of Colombia (1° to 10°N, and 72° to 78°W). The third and last domain (2 km) is centered around the Aburrá Valley and extends from 5° to 7.5°N and from 74.5° to 76.8°W. The model runs use the output from the 12UTC Global Forecast System (GFS) output as initial and boundary conditions. The integration time step is 90, 60, and 10 s in the 18, 6, and 2 km domains, respectively. SIATA operational forecasts include different ensemble members with different microphysics parameterizations. Table S1 summarizes the schemes and parameterizations selected for the ABL analysis in this study. We focus on the assessment of the ABL height corresponding to the highest grid spacing domain.

2.4 Results

This section presents the results of the different schemes used for estimating the ABL height, highlighting the capabilities of the various instruments and the robustness of these estimations under different atmospheric conditions, assessing the temporal and spatial variability of the ABL height, and studying first-order aspects of the role of regional climate in modulating boundary layer processes.

Assessment of the ABL Detection

Figure 2.6 shows examples of ABL height estimations for 2015-03-04, 2016-03-13, 2018-01-25, and 2018-02-26, presented together with the evolution of BI profiles using the Torre SIATA ceilometer. In general, all ABL height estimations satisfactorily reproduce the diurnal evolution associated with radiation forcing and thermally forced convection. All ceilometer-based ABL heights show a relatively good correspondence among them and, as expected, with the observed BI profiles. Initiation of the atmospheric instability is the main driver of the ABL structure; this process is characterized by the triggering of thermal convection near the surface and is modulated by the increasing temperature gradient between the lower atmosphere and the surface. As the surface temperature increases, air parcels start to ascend, which is usually evident after 09:00-10:00 LT. Figure 2.6 shows that the ABL reaches the maximum height at approximately 13:00 LT; at this moment, the temperature gradient between the surface and the atmosphere starts to reverse, and a cooling mechanism initiates, forcing a shrinkage of the layer. Once the surface is no longer receiving the energy from solar radiation, the convective layer becomes the residual layer, as the nocturnal stable layer concurrently develops.

One of the most salient features that differentiates the ABL height estimates takes place after 16:00 LT when the Richardson number method tends to detect the relatively slow top-down contraction of the residual layer, while ceilometer-based estimates appear to detect the sudden bottom-up onset of the nocturnal stable layer. The CWT-based method is the only ceilometer-based technique that shows a preference for selecting the residual layer as the height of the ABL. Detection of the nocturnal stable layer by the maximum variance and minimum gradient methods is likely caused by the combination of high anthropic aerosol emissions associated with the afternoon commute and the sudden stabilization of the near-surface atmosphere as a result of the solar radiation reduction. In other words, sufficient aerosols are emitted to quickly replenish the control volume confined by the surface and the first atmospheric capping inversion, causing a noticeable discontinuity in the BI. The CWT method, in contrast, tends to isolate the residual layer as a result of the BI reduction. Detection of the residual layer by Richardson number estimates is a direct consequence of the processes contrasted in the adimensional number, indicating that turbulence does not shut down in the entire column immediately with the onset of near-surface stability (the atmosphere is turbulent between the top of the nocturnal boundary layer and the top of the residual layer), but rather decays with the

slow weakening of sensible heat flux.

While all dates in Figure 2.6 correspond to dry days (no precipitation), the dates in the top panels were predominantly cloudy as shown in the ceilometer profiles with a cloud ceiling of approximately 1.2 to 2.5 km. The average specific humidity in the first 2 km in the dates of both top panels, from radiometer retrievals, was approximately 20% higher than usual, ranging between 11 and 12 gkg^{-1}. Similarly, the average cloud radiative forcing in the 06:00-18:00 LT for these two days was approximately -150 Wm^{-2} compared to a clear day. Given the reduction in solar radiation reaching the surface, it is likely that sensible heat flux was also anomalously low. Potential temperature profiles from the MWR (not shown) suggest that both days were predominately stable, leading to pollutant accumulation near the surface. The average daily PM2.5 concentration for both days was, in fact, 61 and 81 μgm^{-3}, which is considerably higher than the long-term average (see Figure 2.1). Under these conditions, aerosols become excellent tracers of ABL behavior. In addition, atmospheric humidity accentuates the size of hygroscopic aerosol particles, enhancing the near surface ceilometer BI signal (Emeis et al., 2012; Young and Whiteman, 2015).

In contrast, the last two dates in Figure 2.6 correspond to fair weather days, with clear skies, and some isolated cumuli over the valley. The cloud radiation forcing is relatively weak (less than 20 Wm^{-2} in magnitude), and the specific humidity is lower compared with the first two dates (approximately 9 gkg^{-1}). Under the mentioned circumstances, the sensible heat exchange tends to be sufficient to break the lower-troposphere stability, establishing a convective regime after 10:00 LT. After the atmosphere becomes unstable, and the vertical dispersion takes place, aerosol concentrations near the surface and within the convective layer considerably lessen: once aerosols surpass the depth of the valley, trade winds generally advect pollutants away to the east of the Aburrá Valley. The 24-h average PM2.5 concentration was considerably lower than for that the first two dates (31.6 and 38.8 μgm^{-3}, respectively). During dates with similar weather conditions, ceilometer-based techniques tend to represent well the nocturnal boundary layer, but the reduction of tracers results in a less skillful ABL detection. In contrast, the Richardson number methodology is robust in all four cases, allowing a direct ABL height estimation with no dependence on the existence of tracers. However, the main drawback of the Richardson number technique is its dependence on the proper selection of a critical threshold.

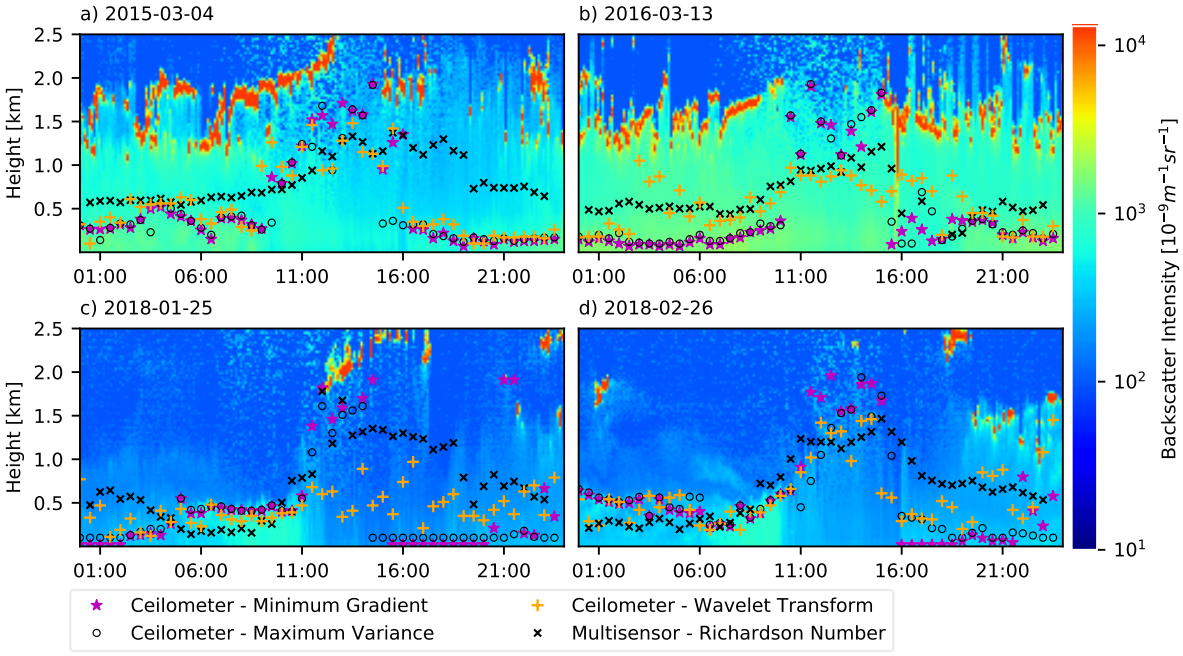

Figure 2.6: The panels show ABL height estimations for different dates (2015-03-04, 2016-03-13, 2018-01-25, and 2018-02-26) using techniques based on remote sensing retrievals. The ABL height estimations are presented over the evolution of ceilometer backscatter profiles (Torre SIATA site). Purple stars show ABL height using the minimum gradient algorithm, black circles using the maximum variance method and orange plus-signs using the CWT-based scheme. Black Xs show the ABL height estimations using the multisensor Richardson number technique.

ABL height estimates comparison using radiosondes

The first step in the ABL height intercomparison is to evaluate the pertinence of the Holzworth and Richardson number methods using radiosonde data as reference values. ABL height estimates are intercompared considering different Rib_c to find an optimal threshold. The scatterplots in the first row in Figure 2.7 show the level of agreement between the Holzworth method and three different Rib_c (0.25, 1, 3). Pearson correlation and root mean square (RMS) deviations are shown in each of the panels, and the colors of the full circles correspond to the hour (local time) of the radiosonde flights. The distribution of colors in a time-ABL height clustered fashion suggest that both methods, in all three cases, represent well the existence of a marked ABL diurnal cycle during IOPs. The correlations among both the Holzworth and Richardson number estimates are very high, with a maximum of 0.75 for $Rib_c = 0.25$. The least RMS deviation is also obtained for $Rib_c = 0.25$. The dispersion level among the Holzworth-Richardson

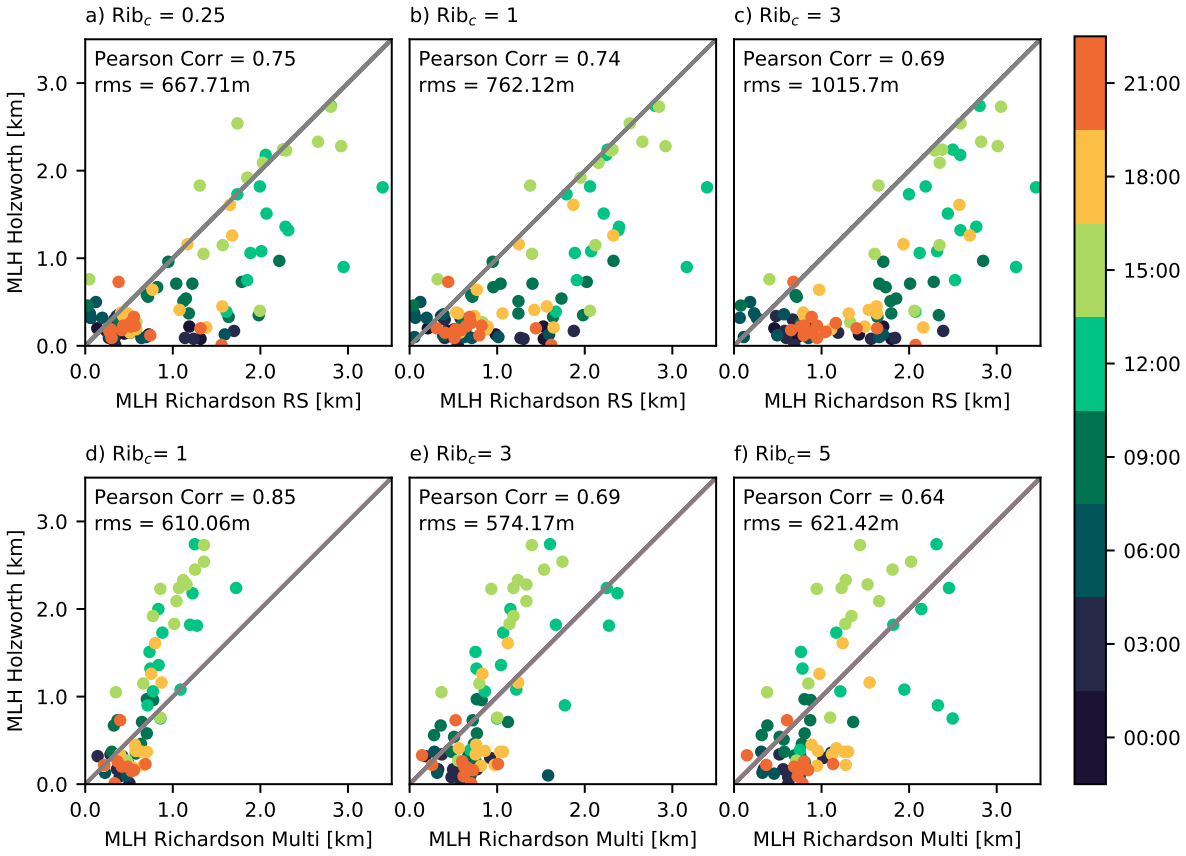

Figure 2.7: First row: Scatterplots showing the level of agreement between the Holzworth method and three different $Rib_c = 0.25, 1, 3$. Second row: Scatterplots showing the comparison between the Holzworth method ABL height estimates and the multisensor Richardson-number estimates for three different $Rib_c = 1, 3, 5$. The panels show, in each case, the Pearson correlation and root mean square (RMS) deviations. The color of the full circles corresponds to the hour (local time) of the radiosonde flights.

ABL estimates, expressed as the RMS deviation, is significant; however, it is important to consider the fact that on some occasions, both methods represent different sublayers within the ABL, as discussed in the previous section: Richardson ABL height estimates correspond to a top-down approach, while Holzworth estimates correspond to a bottom-up approach. This phenomenon is also evident in the figure since Richardson number ABL height estimates tend to be higher than those using the parcel method, and the dispersion is higher during the convective stage and contraction of the residual layer. Considering the overall evidence, we select both Holzworth and $Rib_c = 0.25$ radiosonde-based methods as references for comparing remote sensing ABL height estimates.

The scatterplots in the second row in Figure 2.7 show the comparison between the

Holzworth estimates and the multisensor Richardson number ABL height estimates for three different Rib_c (1, 3, 5). The figures show the same general features regarding the ABL diurnal cycle. In this case, the optimal Rib_c selected for the multisensor method is different from the one used for radiosonde-based estimates, confirming its dependence on the measurement strategy. Additionally, the highest correlation does not coincide with the lowest RMS deviation. For this reason, and to summarize the intercomparison results, we use a Taylor diagram to contrast all the ceilometer and multisensor estimates with the two radiosonde reference estimates during the IOPs (see Figure 2.8). Taylor diagrams allow the evaluation of the degree of correspondence between two patterns in terms of their correlation, their centered RMS deviations, and the amplitude of their variations represented by the individual standard deviations (Taylor, 2001). The diagram uses normalization of the dimensional quantities considering that we use two different radiosonde references. In other words, ABL height estimates are scaled relative to the standard deviation of the corresponding reference, either Holzworth or $Rib_c = 0.25$, in each case.

The intercomparisons in Figure 2.8 include, in different groups organized by shape and color palette, five sets of estimates comparing Holzworth, the reference, with radiosonde Richardson number estimates (blue circles), five sets of estimates comparing Holzworth with multisensor Richardson number estimates (pink-to-violet squares), three sets comparing Holzworth with ceilometer-based estimates (green triangles), five sets comparing radiosonde $Rib_c = 0.25$ with multisensor Richardson number estimates (purple crosses), and three sets comparing radiosonde $Rib_c = 0.25$ with ceilometer-based estimates (orange-to-brown rhombs). In general, twelve out of sixteen radiosonde vs. remote sensing estimates show a correlation greater than 0.5; however, all estimates underrepresent the variability observed in ABL heights from radiosondes. The latter result is in part explained by the finding that the vertical resolution of the radiosonde is higher than that of the ceilometer, MWR, and RWP. Overall, the methodology showing the highest correspondence with the Holzworth technique during IOPs, considering correlation and a balance between RMS deviation and variability representation, is the Richardson number multisensor method with $Rib_c = 4$. If the radiosonde $Rib_c = 0.25$ is used as a reference, the highest agreement is achieved with the multisensor $Rib_c = 4$ and ceilometer maximum variance method. Considering this result, the analysis in the following subsection will focus on the multisensor $Rib_c = 4$ and ceilometer maximum variance method.

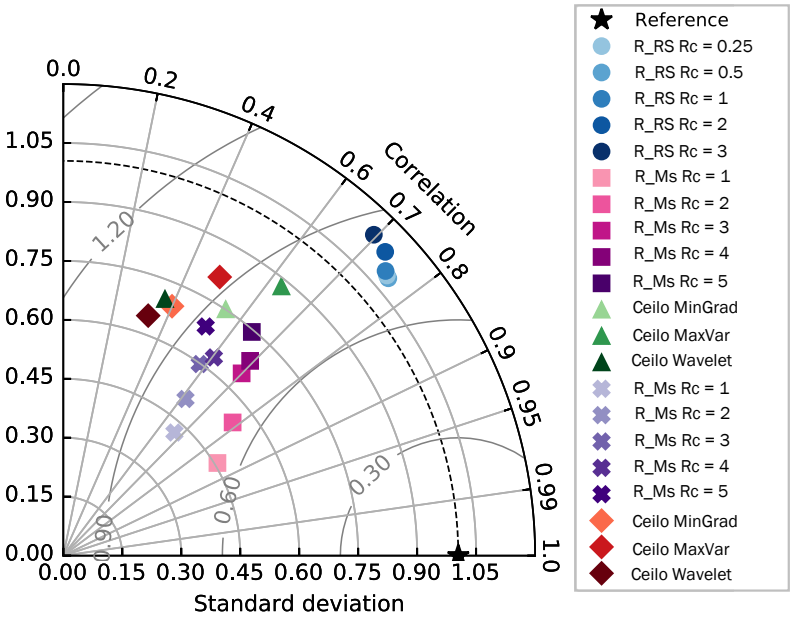

Figure 2.8: Normalized Taylor diagram for ABL height estimates using as reference sets radiosonde estimations with the Holzworth and Richardson number with $Rib_c = 0.25$. The intercomparisons include, in groups organized by shape and color palette, five sets of estimates comparing Holzworth with radiosonde Richardson number estimates with $Rib_c = 0.25, 0.5, 1, 2, 3$ (blue circles), five sets comparing Holzworth with multisensor Richardson number estimates with $Rib_c = 1, 2, 3, 4, 5$ (pink-to-violet squares), three sets comparing Holzworth with ceilometer-based estimates, including the minimum gradient, maximum variance and wavelet transform methods (green triangles), five sets comparing radiosonde $Rib_c = 0.25$ with multisensor Richardson number estimates with $Rib_c = 1, 2, 3, 4, 5$ (purple crosses), and three sets comparing radiosonde $Rib_c = 0.25$ with all three ceilometer-based estimates (orange-to-brown rhombs).

ABL height long-term comparison

Radiosonde ABL height estimates are based on direct measurements of atmospheric profiles and, hence, constitute an important reference for the estimates in this study. However, the radiosonde-based estimates are also prone to artifacts associated with the Lagrangian nature of the platform: radiosonde profiles do not correspond to the same atmospheric column, and in a narrow valley, the differences between the profiles at the base and at the hills could potentially be large, introducing uncertainty in the ABL estimates. In our case (Figure not shown here), most of the radiosonde flights below 4500 m are within the area sensed by the MWR and RWP in the same altitude range, however, there is a westward biased towards the hills in the radiosonde that could potentially affect the intercompari-

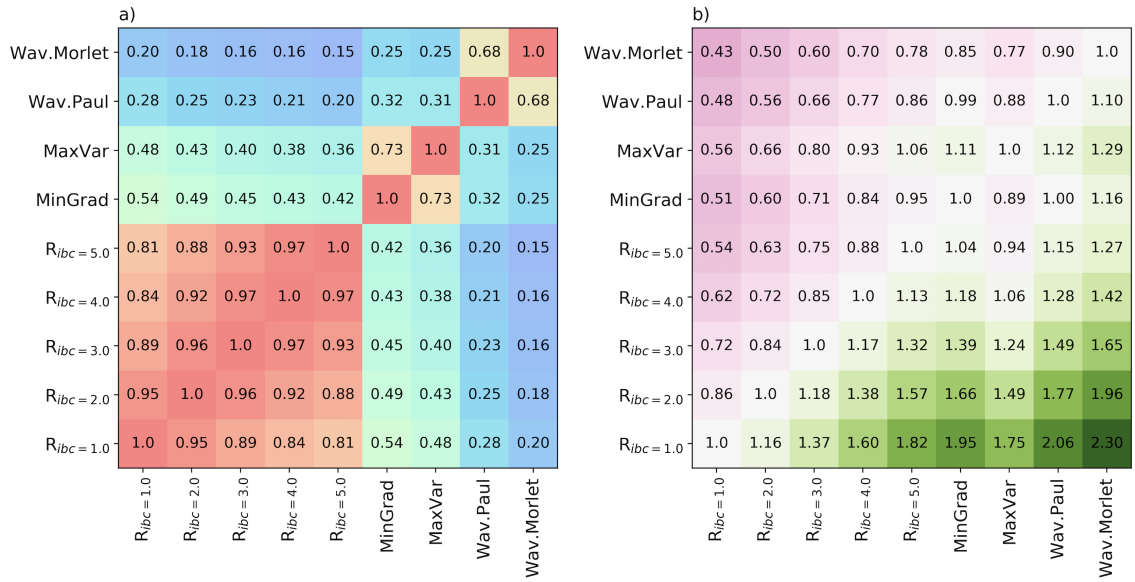

Figure 2.9: a) ABL height cross-correlation array; each pixel corresponds to the zero-lag correlation between all the 30-minute resolution ABL height time series for all the methods. b) The amplitude of each ABL height time series obtained with the method denoted in each row relative to the method in each column. Values larger than 1 (green colors) indicate that the method listed in the corresponding row suggests higher ABL variability than the method in the column. Conversely, purple colors are associated with underestimation of variability.

son. Figure 2.9 summarizes a detailed long-term assessment of the ABL height estimates obtained with the different schemes. Since none of the methods could be selected a priori as a reference standard, Figure 2.9a shows the cross-correlation array in which each pixel corresponds to the zero-lag correlation between all 30-minute resolution ABL height time series for all the methods, and Figure 2.9b presents the amplitude of each time series obtained with the method denoted in each row relative to the method in each column.

The first evident feature is that, in terms of variability, the ABL height estimates obtained with mutations of the same base method such as ceilometer-variance (minimum gradient and maximum variance) methods, ceilometer CWT-based methods, and Richardson number methods are very similar among the approaches, with correlations larger than 0.68 despite the high temporal resolution used in the analysis. The CWT-based methods show the lowest correlations with the other methods, and the correlation between the minimum gradient and maximum variance methods with the Richardson number method is larger for lower values of the critical Richardson number. The latter characteristic is due to the sensitivity of the ceilometer-variance methods and the low critical Richardson number ($Rib_c = 1$) estimates to the highly variable near-surface atmospheric changes in

time; hence, the variability of the estimates is higher than those obtained using $Rib_c = 4$. This phenomenon is also clear in Figure 2.9b, where the overall variability (amplitude of the diurnal cycle and intraday variability) of the ABL height series is largest for estimates using the Richardson number method with $Rib_c = 1$ and lowest for CWT-based estimates.

An assessment of ABL height estimates with the different schemes suggests that, in the presence of stable atmospheres, the ABL height estimates using the three backscatter-based methods exhibit high correspondence with each other. If the BI profiles present well-defined vertical structures with noticeable transitions, the retrievals are usually very robust. By the time the convective layer starts to develop due to the onset of atmospheric instability, the concentration of aerosols near the surface and within the valley decreases. In this case, backscatter-based estimates diverge from one method to the other, and it is not possible to distinguish which of the methods is more accurate in determining the ABL height. In the latter cases, the Richardson number method becomes a more robust tool for estimating the ABL height.

ABL height temporal variability

The long-term ABL height identification allows the assessment of the influence of local-scale phenomena versus regional forcing on ABL variability. In this section, we examine the most salient time scales present in the ABL height time series, identifying the processes that lead to the existence of such variability. Spectral analysis of the long-term ABL height time series allows identifying the main temporal scales of ABL variability. The average ABL height spectrum was estimated using the fast Fourier transform (FFT), and the variability of the spectrum itself was evaluated by computing a sliding FFT with a fixed temporal window, to asses the regularity (stationarity) of the spectral peaks in terms of their amplitude, as a response to regional forcing. Figure 2.10a shows the average FFT spectrum and the variability of the spectra (+/- one standard deviation) for all block-moving 21.333-day (1024 30-minute data points) ABL height series, estimated using the maximum variance method. We use the mentioned ABL height series considering a length of the ceilometer record longer than that of the RWP. Each 21.333-day spectrum is also computed after tapering the signal using a Hann window. The relative variance is estimated by integrating the FFT spectrum between 20 and 24 hours and dividing the result by the series variance. The most salient ABL time scale with a period shorter than 21.333 days, in terms of variance, corresponds to the diurnal cycle, caused by the

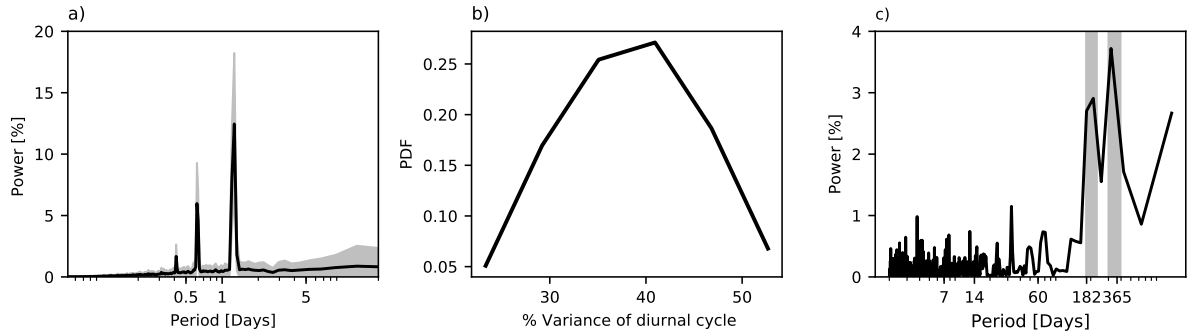

Figure 2.10: Fast Fourier transform (FFT) spectrum for ABL height series estimated using the maximum variance method. The FFT is computed after tapering the signal using a Hann window. The spectrum in a) corresponds to the average FFT spectrum and spectra variability (+/- one standard deviation in gray) for all block-moving 21.333-day (1024 30-min data points) ABL height series. b) Histogram of the relative variance (in percentage) of the diurnal cycle obtained from all 21.333-day spectra. The relative variance is estimated by integrating the FFT spectrum between 20 and 24 hours and dividing the result by the series variance. c) FFT spectrum of the daily ABL height series. The gray vertical bars mark the semiannual and annual spectral peaks.

modulation controlled by solar radiation and the onset of convective activity. The other noticeable spectral peaks in Figure 2.10a correspond to the harmonics of the diurnal cycle (8 and 12-hour peaks).

Figure 2.10a suggests the presence of substantial temporal variability of the relative amplitude of the diurnal cycle. Considering the latter, Figure 2.10b presents the histogram of the relative variance of the diurnal cycle, as a percentage, obtained from all the 21.333-day spectra, showing that the diurnal cycle represents, in some cases, just approximately 25% of the total variance, as compared with more than 50% in other cases. In other words, the amplitude of the diurnal cycle changes on the annual and semiannual time scales. The practical implications of this variability of the amplitude of the diurnal cycle are linked to the knowledge that a low-amplitude ABL diurnal cycle could lead to pollutant accumulation. The spectrum of 100 m BI (not shown), a proxy for the aerosol concentration, also shows a marked diurnal cycle and a 7-day peak (and 14 and 21-day subharmonics), implying important variability due to the weekly pollutant emission cycle within the valley. After filtering out the diurnal cycle, the ABL height spectrum (Figure 2.10c) shows significant annual and semiannual peaks that are potentially associated with the cloud radiative forcing resulting from the progression of the Intertropical Convergence Zone (ITCZ) over Colombia. In addition to these spectral peaks, there are

other low-variance intraseasonal spectral peaks that are not explored in this work. It is important to note that the length of the ABL height series is approximately 3.5 years, precluding the exploration of interannual timescales.

Figures 2.11a and d present the diurnal cycles for the multisensor Richardson number $Rib_c = 4$ and maximum variance ABL height estimates, respectively. The shaded band represents the plus and minus half standard deviation. Both time series show the remarkable diurnal cycle, with similar variability around the mean values. In the long term, the most evident difference appears to be the same as that described in section 3.1 regarding the multisensor method preference for detecting the residual layer and BI methods for selecting the nocturnal stable layer. The consequence, in the case of the maximum variance method, is an almost symmetric diurnal cycle, while the multisensor method cycle is clearly asymmetric following the typical evolution of the near-surface radiative energy balance. On the valley floor, the thermal turbulence triggered by the incoming solar radiation triggers sensible heat flux and, as a consequence, the mixing process, causing the near-surface layer to grow. Figures 2.11b and e show the average monthly ABL height in the 11:00-15:00 LT interval (convective period). We focus on this time period given its importance for the vertical dispersion of pollutants outside the valley. The correlation among both monthly series is high (0.6), but the amplitude of the multisensor series is higher because ceilometer-based convective layer estimates tend to be shallower when aerosol concentrations are low. Both series show a large variability around the mean value, and in some cases, the monthly mean ABL height in the convective period is lower than the average depth of the valley (1100 m). Figures 2.11c and f show the monthly percentage of the days when the ABL height surpasses the top of the valley during the 11:00-15:00 LT interval, using estimates from the Richardson and maximum variance method. On average, considering both methods, the convective boundary layer in the 11:00-15:00 LT interval in the Aburrá Valley surpasses the top of the mountains 45% of the days. Months with low percentages of above-valley ABL and scarce effective below-cloud scavenging are prone to trigger critical air quality episodes.

In addition to the diurnal and annual cycles, there is important ABL variability over longer timescales. Figures 2.12a and b show the evolution of the monthly diurnal cycle of the ABL height at the base of the valley using the multisensor Richardson number estimates with $Rib_c = 4$ and the maximum variance method, respectively. The black contour corresponds to the depth of the Aburrá Valley. If the ABL does not reach this critical threshold, once the convective phase ceases, the aerosols will recirculate within the

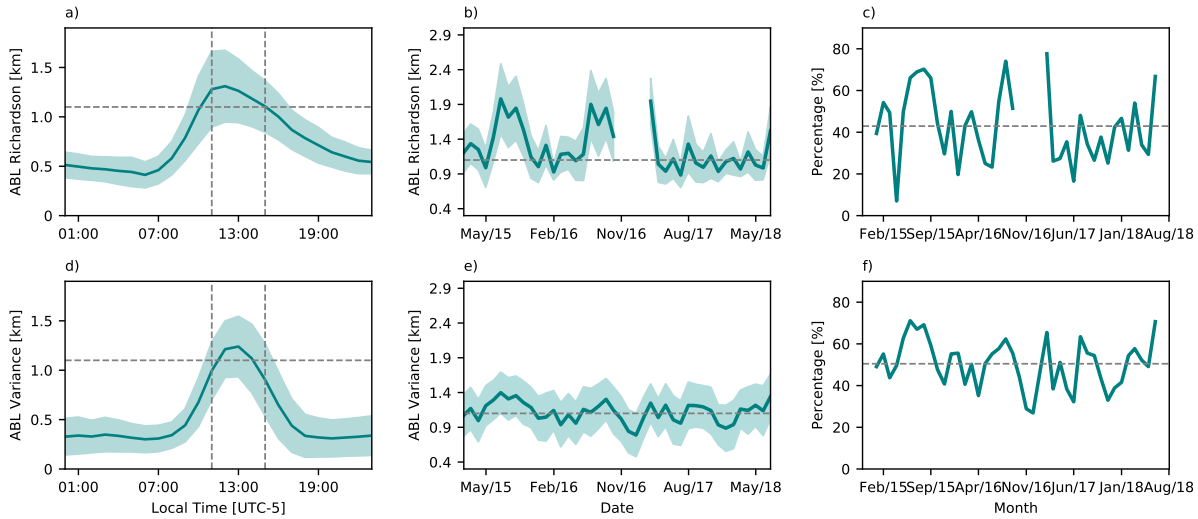

Figure 2.11: a) Diurnal cycle of the ABL height estimates using the multisensor Richardson number method. The horizontal dashed line corresponds to the average depth of the valley. The vertical dashed lines correspond to 11:00 and 15:00 LT. b) Monthly time series of average ABL height in the period between 11:00 and 15:00 LT for the multisensor Richardson number method. c) Monthly percentage of days when the ABL height surpasses the top of the valley during the 11:00-15:00 LT interval, using the estimates from the Richardson method. d), e) and f) Same as a), b), and c) using the maximum variance method. In all panels, the shaded band corresponds to plus and minus half standard deviation.

valley, prompting an increase in aerosol concentration during the night as the residual layer shrinks. The monthly evolution of the ABL height diurnal variability presents evidence of significant differences among the different months, suggesting a strong variability most likely as a result of external forcing associated with the migration of the ITCZ over Colombia. Figure 2.12c presents the evolution of the monthly diurnal cycle precipitation at the Torre SIATA site, showing an important evolution of daytime versus nighttime rainfall events, with wet seasons characterized by important nighttime stratiform rainfall and daytime convective precipitation events. The importance of the ABL height, together with nighttime rainfall, is evident: Figure 2.12d shows that months with a shallow ABL height and limited nighttime rainfall result in BI peaks 100 m from the surface, a proxy for the pollutant concentration. It can be observed how, in general, during March (dashed horizontal lines), the ABL height barely reaches the critical threshold and the nighttime is scarce, leading to the highest annual concentrations. Conversely, months such as July or August, when the ABL tends to be the deepest of the year, present the lowest aerosol concentration. Since 2017, strong regulations were implemented by the environmental authority to reduce emissions during the critical air pollution episodes in March, effectively

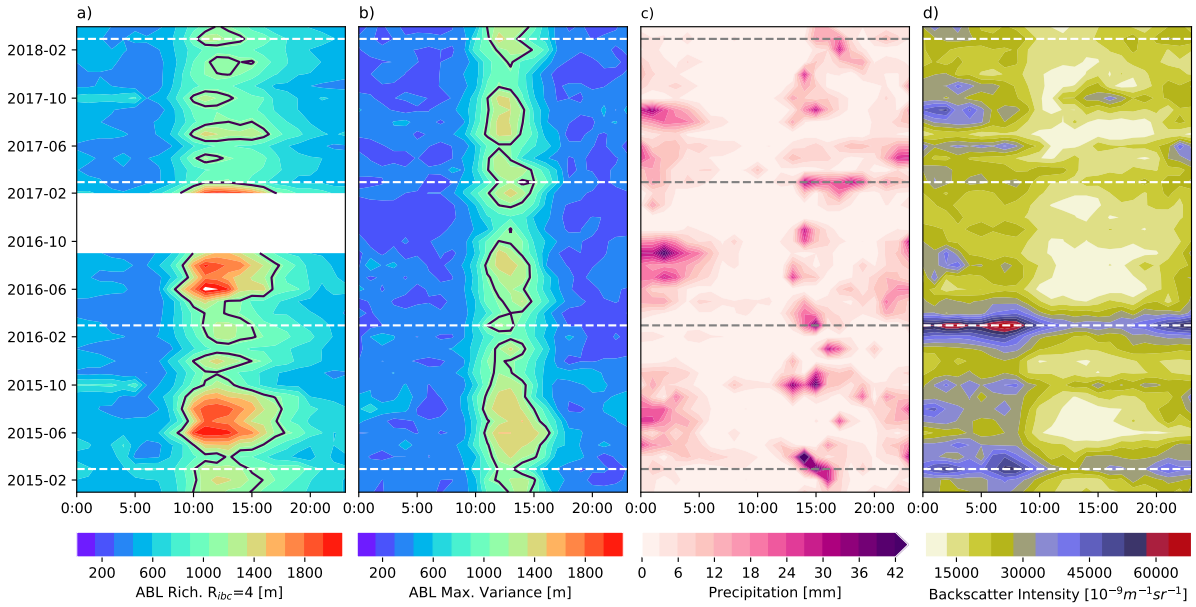

Figure 2.12: a) and b) Evolution of the monthly diurnal cycle of the ABL height at the base of the valley using the multisensor Richardson number estimates with $Rib_c = 4$ and the maximum variance method, respectively. The black contour corresponds to the depth of the Aburrá Valley. c) and d) Evolution of the monthly diurnal cycle precipitation, and BI, respectively, at the Torre SIATA site. Dashed horizontal lines correspond to the months of March of 2015 to 2018.

reducing the pollutant concentration in comparison to other years.

Figures 2.13 and 2.14 show the clear influence of the regional climate in the efficient expansion of the ABL during the day in the Aburrá Valley. Figure 2.13 shows the spatial pattern of the correlation between the anomaly of the daily mean ABL height relative to the long-term mean and the daily cumulative precipitation from the TRMM 3B42 product. The pattern shows a negative correlation between the ABL height in the Aburrá Valley and precipitation in the Andean region of Colombia. Precipitation in the mountainous region modulates the daily ABL height; large values of daily cumulative precipitation, associated with cloudiness in the region lead to negative anomalies of ABL height. Figure 2.14 confirms the impact of the radiation forcing by clouds on the ABL growth, showing a negative correlation between the low-level and mid-level cloud fraction and ABL height.

Figure 2.15a presents the relationship between the mean radiation in the 06:00 to 18:00 LT period and the anomaly of the daily mean ABL height relative to the long-term mean, showing a marked and direct relationship between radiation and the ABL height, as suggested before, with low radiation associated with ineffective growth of the ABL.

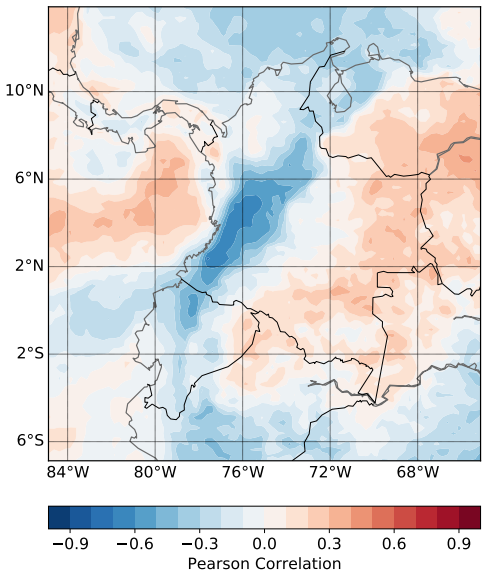

Figure 2.13: Spatial pattern of the correlation between the anomaly of the daily mean ABL height relative to the long-term mean and the daily cumulative precipitation from the TRMM 3B42 product.

Precipitation (and cloudiness) is also an important modulator of the radiation and hence the ABL height, with rainy days corresponding to below-the-mean daily ABL height. Additionally, Figure 2.15b presents the scatter plot between the anomaly of the daily mean ABL height and the average daily PM2.5 concentration in the valley, showing a marked conditional association between these two variables. Days with extreme PM2.5 concentrations only occur when the daily mean ABL height is below the long-term average. Complementarily, days with a below average ABL height and low PM2.5 concentrations correspond to rainy days, most likely favoring below-cloud scavenging.

Other studies have also shown a link between negative anomalies of ABL height and pollutant accumulation (Mamtimin and Meixner, 2011; Liu et al., 2013; Tang et al., 2016; Pal et al., 2014, 2015). Pal et al. (2014) specifically studied the effect of ABL height on the diurnal variability of aerosol concentration at a valley site, finding an inverse relationship between a decreasing trend in ABL height and an increasing tendency in near-surface pollutant concentrations, in particular, the fine fraction (0.3–0.7 μm). However, Pal et al. (2014) evidence is from a short field campaign compared to the long-term analysis included here.

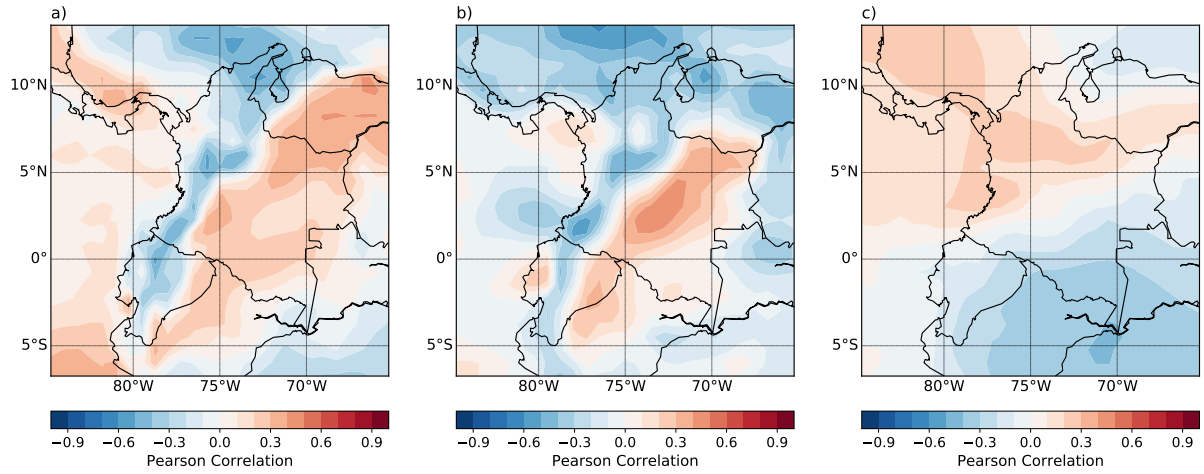

Figure 2.14: a), b) and c) Correlation between low-level, mid-level, and high-level cloud fraction and ABL height in the Aburrá Valley, respectively.

ABL height spatial variability

The divergence of winds in a synoptic scale, the structure of the mesoscale circulation, and the development of valley winds driven by topography and temperature gradients, considerably influence the thermal and mechanical turbulent fluxes, which in turn modulate the evolution of the ABL in complex terrains (Bianco et al., 2011; De Wekker and Kossmann, 2015). Within the valley, the height of the ABL changes considerably from one location to another, and more so if these locations correspond, for example, to the valley floor and to a slope location. Figure 2.16a shows the long-term ABL height diurnal cycle at a valley floor (Torre SIATA) and western hill (Itagüí) sites using the maximum variance method. While the month-to-month evolution is similar, with the same months with a low (March, October, and November) and a high ABL (January, June, and July), the maximum ABL height in the early afternoon is considerably less at the western hill site (65-70% of the ABL at the base of the valley) and, more importantly, the time of the maximum tends to be delayed by an hour. Throughout most of the day, the absolute ABL height at the western hill location is lower than the ABL at the base of the valley; however, after 16:00 LT, the opposite occurs. Considering that the maximum variance method in the afternoon tends to favor the selection of the nocturnal stable layer, in relative terms, the onset of the nocturnal stable layer in the western hill occurs later than at the base of the valley. The diurnal cycle of radiation in both sites (not shown) is similar; hence the observed differences are not due to insolation but rather an indirect response due to the differences in surface wind behavior among both sites. Figures 2.16b and c

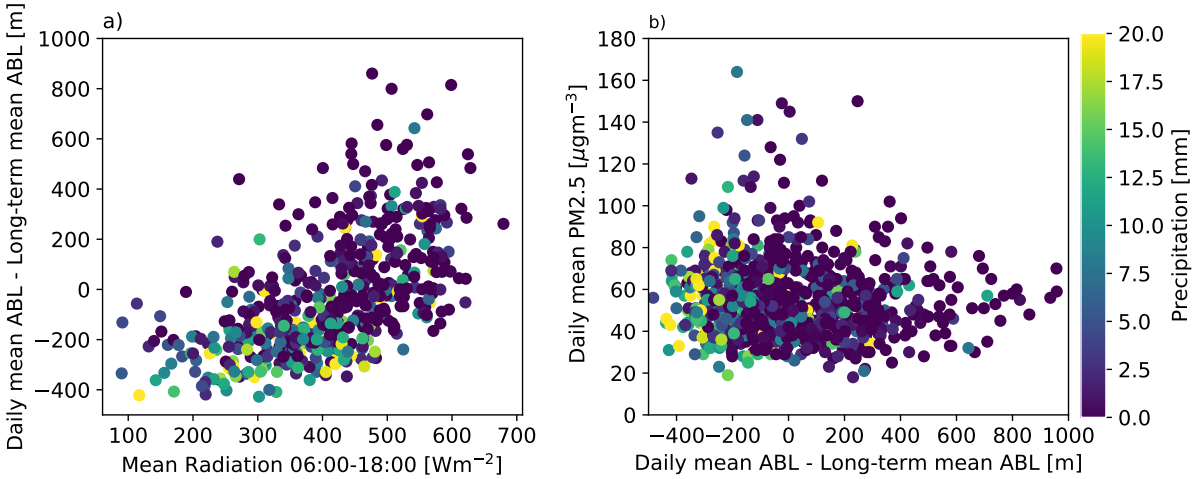

Figure 2.15: a) Relationship between the mean radiation in the 06:00 to 18:00 LT period and the anomaly of the daily mean ABL height relative to the long-term mean. b) Scatter plot between the anomaly of the daily mean ABL height and the average daily PM2.5 concentration in the valley.

show the diurnal cycle of wind direction at the base of the valley and at the western hill site, respectively. At the valley floor, winds are from the north (upvalley) all day; at the western hill, winds are downslope from the west (SW, W, NW) before 06:00 LT, upslope from the east from 06:00 LT to 16:00 LT, and downslope again after 16:00 LT. Upslope winds in the 06:00-16:00 LT period thicken the boundary layer height locally, effectively delaying the onset of the nocturnal stable layer (De Wekker and Kossmann, 2015; Serafin et al., 2018).

WRF simulations

Figures 2.17a to c show the spatial distribution of the diurnal cycle of the ABL height relative to the surface, computed for the 2-km domain, using all the WRF 24-hour forecasts runs described in Section 2. The black lines in the center of each panel correspond to the political division of the Aburrá Valley (as shown in Figure 2.2). Each panel corresponds to an 8-hour period. Figure 2.17a corresponds to the average ABL height in the 00:00 to 08:00 LT interval, and Figures 2.17b a and c to the 08:00-16:00 LT, and the 16:00-23:59 LT, respectively. The evolution of the diurnal cycle, as represented by WRF, shows the signature of topography and solar radiation forcing, with the development of the convective layer in the 08:00-16:00 LT. The dashed line in the Figure corresponds to

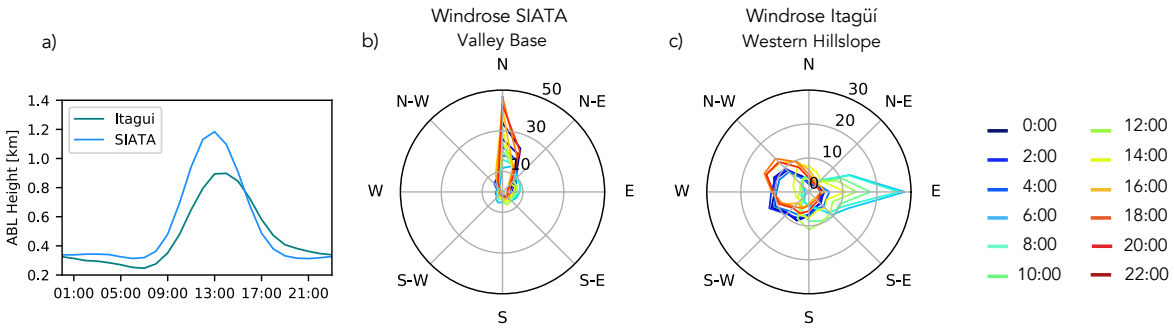

Figure 2.16: a) Annual cycle of ABL height at the base of the valley (Torre SIATA site) and at the western hill (Itagüí site) using the ceilometer-based maximum variance method. Diurnal cycle of wind direction at b) the base of the valley site and c) the western hill site. The frequency of the wind direction is plotted as a wind rose in two-hourly fashion. Note that the times listed on the right correspond to the beginning of the two-hour interval.

the cross-section of the Aburrá Valley shown in Figure 2.17d, and it is remarkably clear that the deepest convective layer occurs over the Aburrá Valley, in the densely populated and urbanized area. Figure 2.17d shows the average diurnal evolution of ABL height over the Aburrá Valley, following the terrain as represented in the model. Each colored line corresponds to one hour of the diurnal cycle. The model simulations skillfully represent the general features of the observed ABL height diurnal cycle within the valley. The top of the ABL is below the height of the surrounding mountains before 10:00 LT and after 17:00 LT. In the 10:00-17:00 LT period, the radiation-driven thermal expansion of the lower troposphere leads to an ABL deeper than the valley, favoring moisture and pollutant exchange with the free troposphere.

Figure 2.17 hints at an interesting aspect regarding the simulated thickness of the ABL in the middle of the valley compared with over the slopes and over the relatively flat terrain at the east of the valley. During both stable stratification and unstable conditions, the maximum ABL height occurs in the middle of the valley, which highlights, among other factors related to the magnitude of the turbulent heat fluxes, the thicker valley-inversion heights compared with the slope-flow-layer heights (Lehner and Rotach, 2018; Serafin et al., 2018). Figure 2.18 shows the average ABL in the 2-km WRF domain categorized by land use category. As suggested before, the deepest ABL corresponds to the urbanized area, where the integrated sensible heat flux is larger than for other areas. In contrast, the forested areas exhibit the smallest ABL heights, as a result of the small Bowen Ratio typical of tropical forests.

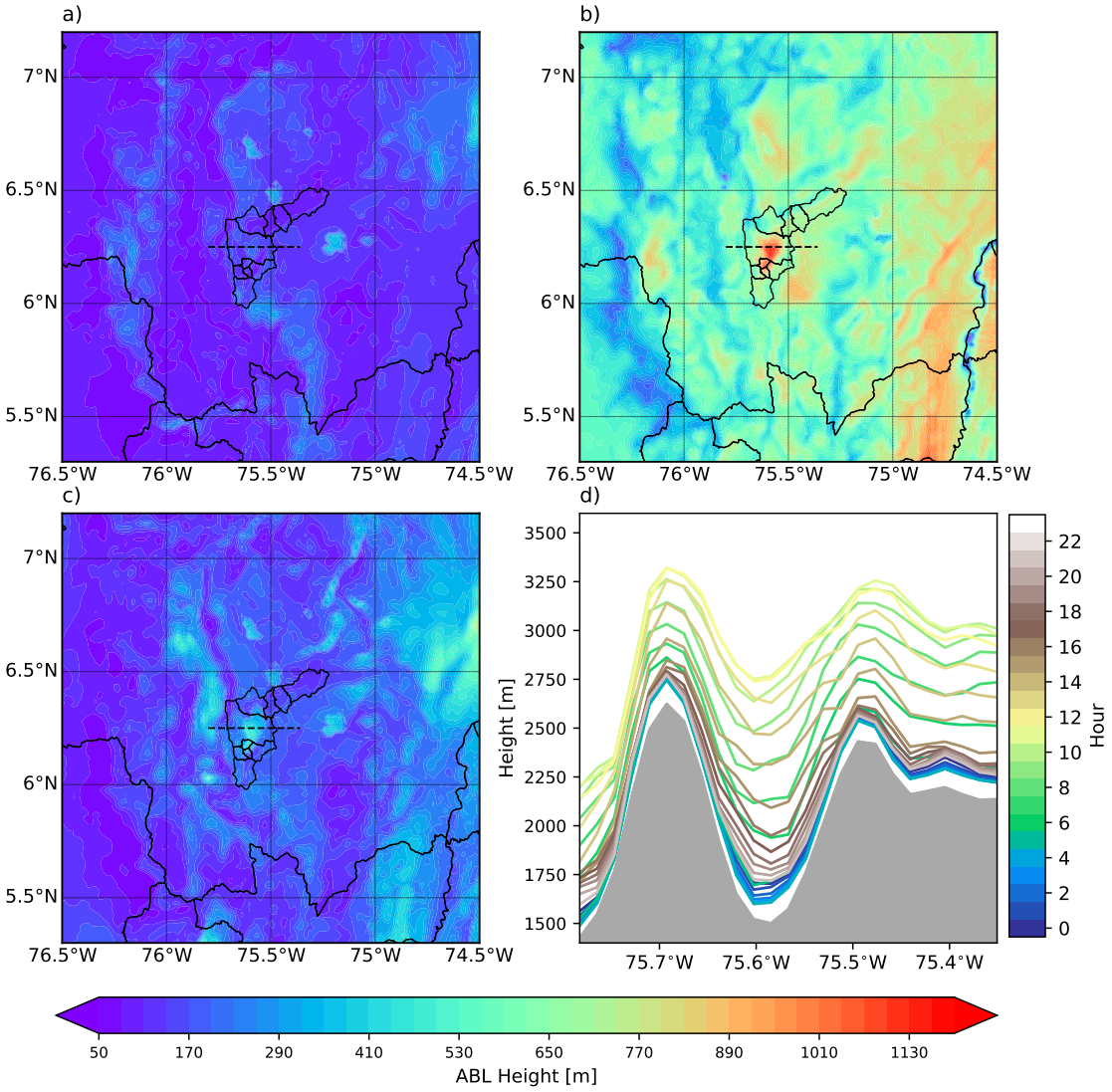

Figure 2.17: a) to c) Spatial distribution of the diurnal cycle of the ABL height relative to the surface, computed for the 2-km domain, using all the WRF 24-hour forecasts runs described in Section 2. The black lines in the center of each panel correspond to the political division of the Aburrá Valley (as shown in Figure 2.2). Each panel corresponds to an 8-hour period; a) average ABL height in the 00:00 to 08:00 LT interval, b) the 08:00-16:00 LT and c) the 16:00-23:59 LT. d) Average diurnal evolution of ABL height following the terrain for all the 24-hour WRF forecasts runs available. Each color line corresponds to one hour of the diurnal cycle.

Figures 2.19a and b show, similar to Figure 2.12a, the evolution of the monthly diurnal cycle of the ABL height at the base of the valley and at the western hill, respectively, as simulated using WRF. The continuous (dashed) black contour corresponds to the 1100 m ABL height isoline in WRF (observations-Richardson method). From a climatological point of view, the correspondence between the observed and simulated ABL height is

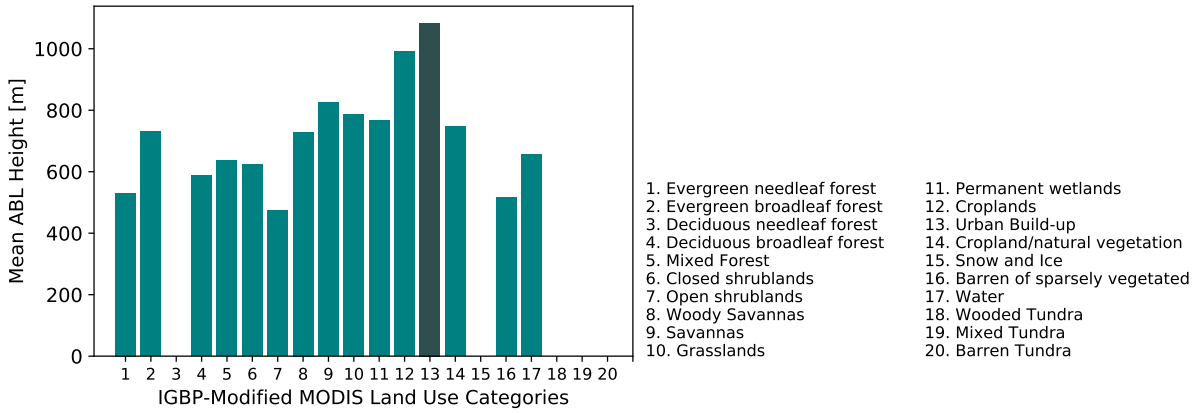

Figure 2.18: Average ABL in the 2-km WRF domain by IGBP land use category. Category 13 corresponds to urban and built-up areas, and category 12 to croplands. Categories 1 to 7, with the smallest ABL, correspond to different types of forests (1-5) and shrublands (6-7), and categories 8 to 10 to savannas and grasslands.

good concerning both the diurnal and annual cycles (see Figure 2.12), suggesting that the evolution of the ABL in WRF responds well to the slow-evolving regional forcing. However, it is possible to observe that the ABL expansion rate during morning hours in the model is higher than in the observations, which is a crucial feature with practical implications for air quality. This is easier to see in Figures 2.19c and d, showing the comparison between the long-term average ABL height diurnal cycle from WRF forecast simulations for the grid model colocated with the Torre SIATA site (valley floor) and the Itagüí site (western hill), and the Richardson number and maximum variance method estimations. Figures 2.19c and d also suggest that the skill of the model simulating the ABL height evolution is considerably higher for the valley floor than for the western hill site. The latter results are different from the studies in predominantly flat terrains. The work by Hu et al. (2010) explored the performance of different planetary boundary layer schemes in the WRF Model in the south-central United States region, given their importance simulating the ABL height. Despite the relevance of the results, the terrain featured are very different from those present in the Colombian Andes and more so in the urbanized Aburrá Valley. In order to improve the ABL simulations at the hill site, it would be desirable in a subsequent study to evaluate the performance of urban canopy parameterizations as in Salamanca et al. (2011) but in complex terrains.

The skill of the model representing the diurnal and annual cycle of the ABL height appears to be the result of the proper simulation of the cloud radiative forcing. Figure 2.20a shows evidence of the conditional relationship between daily low-level cloudiness,

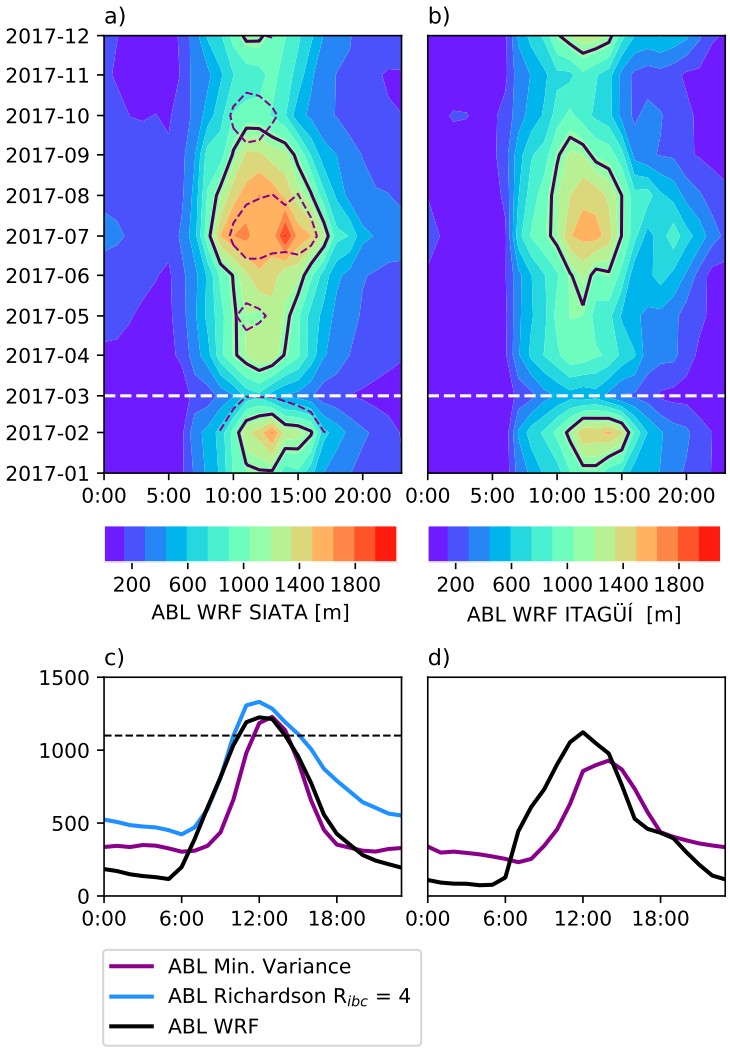

Figure 2.19: a) and b) Evolution of the monthly diurnal cycle of the ABL height at the base of the valley and at the western hill, respectively, as simulated using WRF. The continuous (dashed) black contour corresponds to the 1100 m ABL height isoline in WRF (observations-Richardson method). c) and d) Comparison between the long-term average ABL height diurnal cycle from WRF forecast simulations (black line) for the grid model colocated with Torre SIATA site (valley floor) and the Itagüí site (western hill), and the Richardson number (blue line) and maximum variance method (purple line) estimations.

represented as the 600 hPa cloud fraction, the 24-hour average shortwave radiation reaching the surface, and the ABL height. In the model, high values of low-level cloud fraction are associated with negative radiative forcing and low values of ABL heigh, similar to the observations. In contrast, low values of low-level cloud fraction allow, in general, the efficient expansion of the ABL during the daytime. However, the low-level cloud fraction is not the only variable controling the shortwave radiation reaching the surface, thus

low values of low-level cloud fraction is a necessary but not sufficient condition for high radiative forcing and ABL expansion, as suggested in Figure 2.20a.

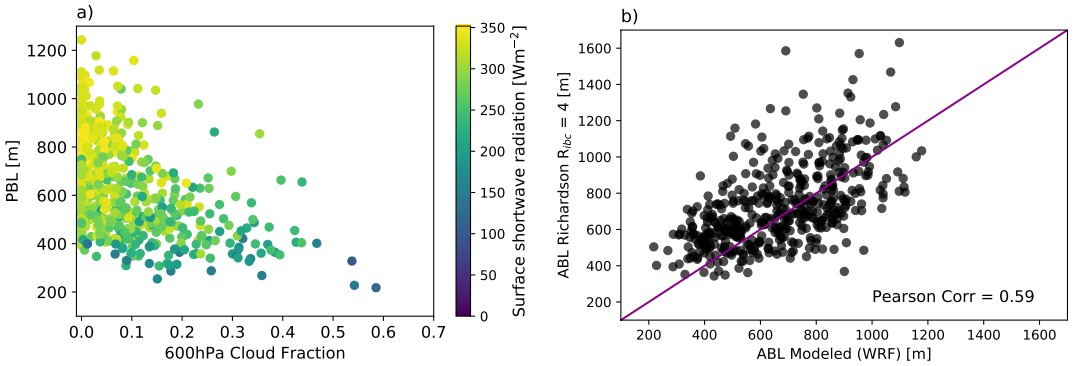

Figure 2.20: a) Scatter plot of the daily low-level cloudiness, represented as the 600 hPa cloud fraction, and the 24-hour average ABL height, categorized by shortwave radiation reaching the surface (in colors). b) Scatter plot of the 24-hour ABL forecasts and the estimated one using the Richardson number method. The Pearson correlation between both variables is 0.59.

An assessment of the ABL height forecast skill at the base of the Aburrá Valley is presented in Figure 2.20b. The Figure shows the scatter plot and the correlation between the 24-hour ABL forecasts and the estimated ABL using the Richardson number method. The linear relationship is clear from the Figure and the correlation is high (0.59), suggesting a good agreement between the observed values of ABL height and the forecasts. The only evident issue is that, in some cases, the expansion of the ABL is underestimated by the model. In general, the results of the assessment skill of the model are encouraging from the applications point of view, considering the fact that the processes involved in the advanced simulation of the ABL are complex, and depend on different coupled parameterizations.

2.5 Conclusions and Discussion

The primary goal of this work is the study of the variability of ABL in time and space in a narrow tropical urban valley in order to explore the interaction between the complex terrain and the tropospheric processes in local and regional spatial scales. One of the current research challenges in our understanding of the ABL over mountainous terrain is related to its multilayered structure. The development of a deep CBL in the Aburrá Valley is vital for the local development of extreme precipitation events and for reducing

the likelihood of critical air quality episode occurrences. The implemented schemes use atmospheric profiles from remote sensing retrievals and measurements, from ceilometers, a radar wind profiler, and a microwave radiometer. Four ABL height detection methods are implemented, three using ceilometer backscatter intensity observations and one using the obtained adimensional bulk Richardson number.

In all cases, the ABL height estimates capture the diurnal cycle associated with the radiation forcing and the thermally forced convection. The temperature gradient between the surface and the lower troposphere is one of the primary modulators of the ABL structure. All ABL height estimates show a high correspondence among the methods, especially under stable conditions, which favors the appearance of marked transitions in the lower atmosphere. Under stable conditions, ABL detection using ceilometer-based methods is very reliable since aerosols become excellent tracers of ABL evolution. After the atmosphere becomes unstable and vertical dispersion takes place, the aerosol concentration near the surface and within the convective layer considerably decreases, reducing the reliability of ceilometer-based methods. In contrast, the Richardson number methodology does not depend on the existence of tracers and is, in general, more reliable than ceilometer-based methods. The principal challenge using the Richardson number technique is the selection of an optimal critical threshold for its value.

Despite the dependence on the selection of an optimal threshold, a detailed intercomparison of ABL height retrievals suggests that the Richardson number multisensor method and the ceilometer-based maximum variance technique show the highest correspondence with the Holzworth technique during the radiosonde IOPs. The main difference between the ABL height retrievals occurs after 16:00 LT when the Richardson number ABL height estimations tend to detect the slow top-down contraction of the residual layer, while ceilometer-based estimations appear to detect the sudden bottom-up onset of the nocturnal stable layer. After 16:00 LT, sufficient anthropic aerosols quickly replenish the control volume confined between the surface and the first atmospheric capping inversion, causing a noticeable discontinuity in the backscattering intensity, consequently swaying the backscatter intensity methods to detect the nocturnal stable layer. The Richardson number ABL height method identifies the residual layer as a direct consequence of the turbulence not shutting down immediately with the onset of near-surface stability.

In addition to the diurnal cycle, the results suggest the existence of intra-annual and annual spectral peaks triggered by ITZC modulation of cloudiness, precipitation, and surface incident radiation. The lowest average ABL heights occur during October, November,

December, and March, where the ABL height does not exceed, on average, the depth of the Aburrá Valley. In contrast, July and August are the months with the thickest ABL, exceeding the critical threshold. When the climate conditions are not favorable for ABL expansion, the anthropic emissions build up and lead to critical air pollution episodes. In this sense, the ABL height implicitly determines the pollutant concentration over time and space. In other words, the amount of aerosol particles at the lower troposphere is influenced both by anthropogenic emissions and by the vertical dispersion conditioned by topography and the ABL dynamics, namely, the evolution of the ABL height. The meteorological conditions during March are, as a result of regional scale forcing, the most adverse for the vertical dispersion of pollutants, thus becoming the most sensitive period of the year for reaching unhealthy pollutant concentrations within the valley. During this month, ABL is relatively shallow, and the effect of scavenging processes is limited given the reduced nocturnal rainfall.

These results for the transition season (March), in contrast to the dry and wet seasons, hints at an essential question in air quality studies regarding the estimation of the relative portion of particulate matter that is removed from the local atmosphere by convectively triggered vertical dispersion and by scavenging processes. In March 2016, for example, the average monthly ABL did not reach the critical threshold limiting vertical aerosol dispersion. The unfavorable conditions were exacerbated by a prolonged absence of recurrent precipitation as a result of El Niño conditions limiting the scavenging processes, thus leading to a "perfect storm" type condition favoring pollutant accumulation and leading to the occurrence of the most critical air quality episode in the region.

Regarding the spatial variability, the absolute ABL maximum height above the surface at the western hill is considerably less than at the valley floor, and the peak time of the maximum height tends to be delayed by approximately one hour. Additionally, the onset of the nocturnal stable layer in the western hill occurs later than at the base of the valley. These disparities appear to be linked to the differences in surface wind direction, with upslope winds at the western hill acting to thicken the boundary layer height locally. In contrast, WRF model simulations skillfully represent the general features of the observed ABL height diurnal cycle within the valley, indicating that the thickness of the ABL in the middle of the valley is higher compared with the slopes and higher-altitude flat terrain, representing the thicker valley-inversion heights relative to the slope-flow-layer heights. The model simulations also capture the ABL annual cycle resulting from the slow evolving regional forcing associated with the migration of the ITCZ. However, the

skill of the model simulating the ABL height evolution is considerably higher for the valley floor than for the western hill site, emphasizing the need to improve our current understanding and modeling capabilities for boundary layers over complex terrain. The assessment of the 24-hour forecasts of the ABL height at the base of the valley is quite promising, showing a high correlation between the simulated and estimated values. These results are remarkable considering the fact that the processes involved in the simulation of the ABL depend on different parameterizations.

Chapter 3

An assessment of the role of surface sensible heat flux and the atmosphere inversion on the Break-Up time in a highly complex terrain

---

Laura Herrera-Mejía[1], **Carlos D. Hoyos**[1], **Mathias W. Rotach**[2]

[1] *Universidad Nacional de Colombia, Sede Medellín, Facultad de Minas, Departamento de Geociencias y Medio Ambiente*

[2] *Department of Atmospheric and Cryospheric Sciences, University of Innsbruck, Austria*

3.1 Introduction

The formation of nocturnal Stable Boundary Layers (SBLs) and temperature inversions has important implications for urban areas, particularly those situated in complex terrain valleys. These range from physical processes, including the modulation of momentum, heat, and moisture exchange, to practical ones associated with pollutant accumulation near the surface, as well as the formation of Urban Heat Islands (UHI). Most pollutants emitted during the evening and throughout the night, together with those that return to the surface due to the top-down contraction of the residual layer, remain trapped in the valley at least until the static destabilization of the lower atmosphere (e.g. Doran et al., 2003; Schnitzhofer et al., 2009; Fernando et al., 2010; Saide et al., 2011; **?**; **?**; Rendón et al., 2014; Herrera-Mejía and Hoyos, 2019). Depending on valley geomorphological characteristics and the meteorological conditions surrounding the morning transition, pollutants

may exit the valley atmosphere or recirculate. The latter could lead to a gradual deterioration of the air quality, and in some cases, to the onset of critical air pollution episodes (Anquetin et al., 1998; Angevine et al., 2001; Henne et al., 2004; Rendón et al., 2015; Czarnecka et al., 2019).

From the point of view of the local static stability assessment, the destabilization of the lower atmosphere is tied to the complete neutralization of the temperature inversion. This neutralization is also referred to as the *inversion breakup* (e.g., Whiteman, 1982; Rendón et al., 2014, 2015; Leukauf et al., 2017). The inversion destruction is linked to the occurrence of the necessary and sufficient conditions for the development of the Convective Boundary Layer (CBL). In general, the onset of the CBL leads to efficient energy, moisture, and pollutant exchange between the surface and the free atmosphere (Leukauf et al., 2015). On the other hand, from a non-local point of view, and considering the vertical structure of the lower atmosphere in a valley (e.g. Lehner and Rotach, 2018), air parcels can move through stable sections in between well-mixed layers (Stable Valley Atmosphere, SVA) due to the buoyancy of the parcel with respect to the environment, creating turbulence in these regions that would have been considered stable from local considerations (Stull, 1991). The generation of thermals in the non-local static instability context is associated with the growth of the mixed layer. In cases where the depth of the mixed layer exceeds the valley crest height, there is also an important exchange of energy, moisture, and pollutants between the surface and the atmosphere above the valley, allowing its ventilation even without a complete profile neutralization.

Establishing under which conditions the nighttime inversion is eroded, allowing the valley ventilation (non-local instability), is not a trivial issue, especially for urbanized valleys where the complexity of the terrain and the urban landscape directly influence the evolution of the SBL (Rendón et al., 2014). Factors such as valley geometry, which induces topographic shading, soil water holding capacity and moisture, urban area fraction and roughness, and the overall valley circulation, are key in governing the inversion erosion in complex-urban environments. Some authors have explored the influence of these factors in the morning transition through both modeling (Whiteman and McKee, 1982; Bader and McKee, 1985; Colette et al., 2003; Whiteman et al., 2004; Zoumakis and Efstathiou, 2006; Beare, 2008; Rendón et al., 2014; Leukauf et al., 2015), and field experiments (Whiteman, 1982; Angevine et al., 2001; Nadeau et al., 2020), highlighting the need for a better understanding and representation of the physical processes controlling the timing of the transition for improving numerical weather prediction and air pollution models (Angevine

et al., 2001; Colette et al., 2003; Beare, 2008; Rendón et al., 2014).

Whiteman (1982) and Whiteman and McKee (1982) categorized the neutralization processes over mountainous valleys, predominantly rural, as a function of the interaction of two mechanisms. The first mechanism is considered local, and corresponds to the CBL growth from the bottom of the inversion resulting from radiative heating of the surface (Nadeau et al., 2020). The second mechanism depends on the valley circulation, in which the replacement of air masses at the valley bottom with air from the upper atmosphere through slope winds, causes the top of the inversion layer to collapse. Depending on the relative role of each of the described mechanisms, the neutralization of the lower atmosphere falls into three possible patterns, the first two resulting from the mechanisms previously mentioned, acting independently, and the third and last pattern to the simultaneous action of both mechanisms (Whiteman, 1982). The idealized modeling experiments by Bader and McKee (1985) also suggest an essential role of both mechanisms in thermal inversion destruction.

Whiteman et al. (2004) reached different conclusions for high-latitude sinkholes, for which the evidence suggests that inversion erosion occurs mainly through subsidence warming, indirectly forced by the upslope flows. Valley geometry has a strong effect both on forcing the prevailing neutralization pattern and its timing, with inversions persisting longer in deeper valleys (Colette et al., 2003). The presence of extensive urban development over complex topography leads to alterations in the surface-atmosphere exchanges, enhancing valley floor heating through the formation of UHI. The induced heat due to the UHI may intensify the thermal turbulence production, accelerating the onset and growth of the CBL (Rendón et al., 2015). Furthermore, slope winds tend to increase in magnitude as a consequence of strong temperature gradients appearing across the urbanized hills. The latter favors the inversion erosion through the second and third neutralization patterns. In addition to the processes mentioned above, the evidence hints that wind shear plays a vital role in driving the Turbulent Kinetic Energy (TKE), and in the morning transition (Beare, 2008).

From a broader perspective, regardless of terrain characteristics and in terms of energy balance, the neutralization of the inversion occurs when the total energy provided to the valley atmosphere (Q_{prov}, following the notation used in Leukauf et al. (2015)) via surface sensible heat flux (H) is equal to the energy required to erode the nocturnal SBL (Q_{req}) (Whiteman and McKee, 1982; Angevine et al., 2001; Leukauf et al., 2016). Following the neutralization, the additional energy injected into the valley atmosphere is used, in part,

to expand the CBL until the exchanges between the surface and the free atmosphere peak, resulting in a more efficient pollutant vertical transport. Leukauf et al. (2016) proposed a non-dimensional *breakup parameter* (B) defined as the ratio between Q_{req} and Q_{prov}, combining the effect of the atmospheric stability and the surface heating to assess the energy exchange processes. Leukauf et al. (2017) performed simulations, using the Weather Research and Forecasting (WRF) model (Skamarock et al., 2008), in different energy exchange scenarios characterized by different surface heating, initial atmospheric stability, and terrain geometry, to test the dependence of the exported heating on B. They found that the amount of heat exported from the valley decreases exponentially as B increases and that there is a critical condition over which the complete SBL neutralization never occurs.

Despite the importance of the relationship between Q_{req} and Q_{prov} to understand the timing of the lower atmosphere neutralization or that of the ML expansion above the valley's crest and its potential to modulate pollutant concentration, particularly for urbanized valleys, there is insufficient observational evidence of this effect. Recently Halios and Barlow (2018) studied the morning transition using ground-based remote sensing and in situ instrumentation in central London, finding that buoyant production of TKE at the surface and shear production in the upper half of the atmospheric boundary layer (ABL) erode the stable layer. They highlighted the importance of regional flows, such as low-level jets, in determining the urban boundary layer structure and growth.

The goal of this research is to gain insight into the processes mentioned above, based on the study of the trade-off between observed proxies of the energy provided to the valley atmosphere such as H, and of the energy required to erode the nighttime inversion, both key in the growth of the mixed layer depth in a low-latitude, highly urbanized complex-terrain valley. We also investigate the practical implications of the relative variability of these two proxies regarding the air quality and explore the efficiency of the energy injected into the atmosphere. Previous results suggest a substantial modulation of the local air pollutant concentration associated with ABL variability (Herrera-Mejía and Hoyos, 2019). We analyze nine months of ground-based remotely sensed thermodynamic profiles and in situ observations, including data from a microwave radiometer, a radar wind profiler, a 3D sonic anemometer, automatic weather stations, and air quality monitoring sensors. Furthermore, we evaluate the role of the valley circulation, primarily the vertical wind shear, and the regional meteorological conditions at different levels in the atmosphere, on the SBL erosion efficiency.

Section 3.2 presents a detailed description of the study area and the observational dataset. Section 3.3 the different thermodynamic proxies used in this study for the assessment of Q_{req} and Q_{prov}. Section 3.4 includes the results of the relationship between the selected Q_{req} and the Q_{prov}. The section explores the SBL erosion efficiency, its dependence on local and regional meteorological conditions, the implications on air quality, and the intra-annual variability associated with the meteorological conditions in the valley. Finally, section 3.5 presents the most important conclusions of the study.

3.2 Geographical context and datasets

We use in situ and ground-based remote sensing observations, as well as satellite and reanalysis information from February 1 to November 21, 2018. Ground-based instrumentation is located along and across the region of interest, a heavily urbanized low-latitude narrow valley located in Colombia. In the analysis, all days with available data are considered, regardless of the meteorological conditions; in other words, we do not pre-select fair-weather days for the analysis. In a low-latitude environment, such days correspond to less than 1% of the data, which would restrict the study to very few cases, focusing on the exceptional circumstances and not the expected scenarios. The datasets comprise wet, transition, and dry seasons.

Geographical Context

The study uses information from the Aburrá Valley monitoring network. The Aburrá Valley is located in Colombia, in the Andes Cordillera, between 6°N and 6.5°N and 75.3°W and 75.6°W (see Figure 5.1), and it is characterized through a major bend between a south-to-north and a southwest-to-northeast section. The widest cross-section of the valley, from ridgeline to ridgeline, is 18.2 km, with a relatively flat section of approximately 8 km at the bottom. The narrowest valley floor section is around 3 km wide. The mean depth of the valley is 1100 m. The highest peak, approximately at 3110 m.a.s.l, is in the western crest. The basin outlet is at 1290 m.a.s.l.

From the point of view of turbulent exchanges, the complexity of the region is due to the rugged topography and the highly urbanized area. More than four million people are settled in an area of 1152 km^2. Additionally, the urban area reaches, in some locations,

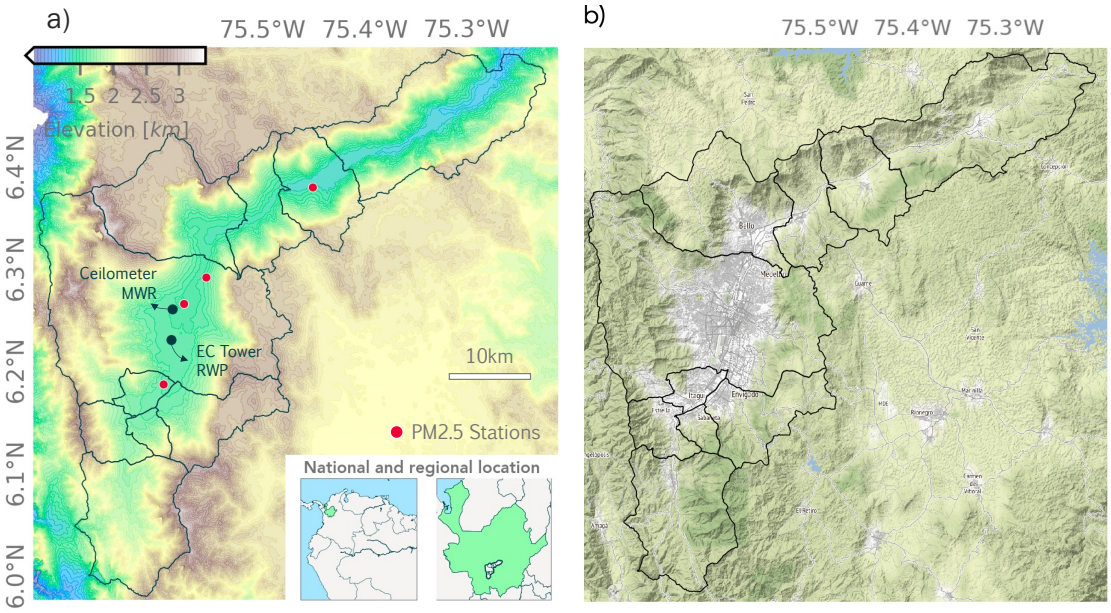

Figure 3.1: a) Geographical context of the Aburrá Valley, located in northern South America, Colombia, Department of Antioquia, north of the equator. The map shows, in brown to blue colors, the height above sea level, the main topographic features in the region, and the location of the sensors used in the study, including a microwave radiometer (MWR), a ceilometer, air quality monitoring stations, and a sonic anemometer. b) Hillshade relief map of the study area, displaying the urbanized areas of the valley, in gray.

three-quarters of the hill-slope extension. The high population density in this geographic setting leads to several environmental challenges. These include the recurrent onset of critical air quality episodes due to the high demand for fossil fuels linked to motor vehicles and industries and the limited ventilation of the valley's atmosphere for pollutant dispersion.

Sensors and datasets

The Aburrá Valley observations used in this study were obtained from the real-time meteorological and air-quality monitoring network of the Medellín and the Aburrá Valley Early Warning System (SIATA, www.siata.gov.co).

Microwave Radiometer (MWR). An MP-3000A MWR, manufactured by Radiometrics, provides continuous information of the vertical temperature and relative humidity profiles in the Aburrá Valley up to 10 km from the top of SIATA's main operation cen-

ter, approximately 60 m above the surface (see Figure 5.1a). The site is inside a sports complex, surrounded by different types of urban land uses. The MWR is a passive remote sensor that measures the radiation emitted by atmospheric gases using 31 different submillimeter-to-centimeter wavelengths. The MWR is useful for the retrieval of the thermodynamic state of the atmosphere at different levels, thus allowing the assessment of atmospheric stability. The temperature and relative humidity retrieval algorithm used in this case includes a modification from the one provided by Radiometrics. The modification uses a regression-based algorithm using sounding data, similar to the methodology in Massaro et al. (2015), yet using neural networks. The MWR provides vertical profiles with a 2-minute temporal resolution and variable spatial resolution: 50 m from the surface to 500 m, 100 m up to 2 km, and 250 m up to 10 km. The lower-troposphere retrievals (below 4 km above the surface) are used to calculate the proxies for Q_{req}. Roldán-Henao et al. (2020) show that the skill of the temperature and moisture retrievals using the MWR is high. The correlations of the potential temperature and virtual potential temperature profiles obtained using MWR and radiosondes, from the surface up to 1100 m, is >0.85.

Radar Wind Profiler (RWP). The RWP uses refractive index variations caused by changes in humidity, temperature, and pressure, to retrieve vertical profiles of winds (Lau et al., 2013). The Aburrá Valley wind profiler, a RAPTOR VAD-BL by DeTect Inc., works at a nominal frequency of 1290 MHz, reaching up to approximately 8 km above the surface under high humidity conditions. The RWP is designed to measure the wind profile in various operation modes that differ in their vertical resolution, as well as in the atmospheric domain sensed. The operation of the RWP includes two overlapping modes: in the higher resolution mode (60 m), the RWP retrieves the wind profile from 77 to 3500 m, and in the lower resolution mode (72 m), from 2500 to 8000 m. In the present study, only data from the higher resolution mode is used. The temporal resolution is five minutes.

Eddy-Covariance flux tower. An Eddy-Covariance tower equipped with a CSAT3 ultrasonic anemometer (Campbell Scientific) is used to obtain the three wind components (u', v', and w') and sonic temperature (T_s') with a sampling rate of 20Hz. The instrument is installed 10 m above the surface, on a mast located next to the local airport (see Figure 5.1a). The absence of tall buildings in the surrounding area prevents the data from being strongly affected by the local circulation. Raw data are stored at full resolution in 24-hour files, and the statistical first- and second-order moments are calculated using 30-min block periods. After applying standard data quality controls (periods flagged by

the instrument, checks for large data gaps and consistency limits, and data despiking), a coordinate double-rotation was applied to each 30-min interval to obtain the along-wind u and cross-wind v components. The latter ensures that the magnitude of the mean lateral and vertical components of the velocity vanishes for each of the averaging interval (e.g. McMillen, 1988; Finnigan et al., 2003; Stiperski and Rotach, 2016). Additional post-processing procedures include flux corrections (Webb et al., 1980; Moore, 1986; Schotanus et al., 1983), and assessing of non-stationarity (following Foken and Wichura (1996)). A detailed description of the post-processing steps will be included in a separate publication (Herrera-Mejía et al. in preparation).

Air-quality monitoring stations and ceilometers. All of the criteria air pollutants defined by the United States Environmental Protection Agency (U.S. EPA), except for lead, are routinely monitored in the region, in a 37-station comprehensive and accredited monitoring network. For this study, data from four in-situ PM2.5 stations equipped with a U.S. EPA Federal Equivalent Method (FEM) Met One Instruments BAM-1020 monitor is used. These stations are located along the base of the valley, some of them intentionally selected far from the location of the MWR and the CSAT3 (see Figure 5.1a), so as to indirectly test the representativeness of the proxies for Q_{req} and Q_{prov} for the entire valley. Retrievals from three Vaisala CL51 ceilometers (910 nm wavelength) are used to illustrate the structure of the vertical profile of aerosols in different Q_{req} scenarios. The ceilometer used is installed at the same site as the MWR (see Figure 5.1a). Ceilometers provide information regarding the laser-pulse energy backscattered by clouds and other atmospheric components, including aerosols, expressed as the backscattering attenuated coefficient (Emeis et al., 2009; Kambezidis et al., 2012; Wiegner et al., 2014).

Reanalysis and satellite data. ERA5 reanalysis data (Hersbach et al., 2020) is used to calculate the velocity potential corresponding to the reanalyzed wind fields. For the estimation of both variables, the wind field is separated into two components, the rotational ($\overrightarrow{V}_{rot}$) and the divergent component ($\overrightarrow{V}_{div}$) of the flow. The divergent winds are used to calculate a velocity potential (χ), satisfying that the winds flow out low potentials and $\overrightarrow{V}_{div} = \nabla\chi$. In other words, χ is obtained as the solution to the equation $\nabla^2\chi = \nabla\cdot\overrightarrow{V}$ (Krishnamurti et al., 2013; Laing and Evans, 2015). We also use the Outgoing Longwave Radiation (OLR) from the NOAA daily interpolated dataset (Liebmann and Smith, 1996).

WRF. We used the output of the operational daily 00Z WRF (version 3.7.1) 24-hour forecasts for three years. The model configuration includes three nested domains with 18

(191 x 191), 6 (82 x 118) , and 2 (136 x 136) km grid spacing, and 40 vertical levels up to 50 hPa. The description of the domains and the model setup are described in detail in Herrera-Mejía and Hoyos (2019).

3.3 Methodology

The observational assessment of turbulent fluxes, vertical structure of virtual potential temperature (θ_v) and wind components, regional meteorology, and air quality allows studying the variability of the inversion breakup as a function of proxies representing Q_{req} and Q_{prov}, the SBL erosion, and the impacts on local particulate matter (PM) concentration in a narrow, low-latitude valley. We use the Aburrá Valley datasets as a case of study. Considering the observational approach described in the following paragraphs, in the context of the present study, and different from the previously cited works, the term *inversion breakup* refers to the injection of enough energy Q_{prov} in the ABL, in the form of sensible heat flux H, to offset the Q_{req} in order to generate, at least, non-local instability. The latter ensuring that the depth of the mixed layer exceeds the valley crest height at some point after the non-local instability is achieved. Herrera-Mejía and Hoyos (2019) studied the diurnal evolution and variability of the depth of the mixed layer using different techniques, including a multi-sensor Richardson number approach (MWR+RWP). The maximum average mixed layer height, 1310 m agl, is reached between 12:00 and 13:00 LT, exceeding the average valley crest height. Considering the day-to-day variability, the maximum mixed layer thickness exceeded the average depth of the valley in 75% of the days in their assessment. The minimum average mixed layer height is 413 m agl, at 06:00 LT.

The methodology includes (i) the assessment of the magnitude and the intra-diurnal evolution of the proxies for Q_{req}, (ii) the evaluation of the surface H as a proxy for Q_{prov}, (iii) the study of the breakup time variability and the SBL erosion, (iv) the assessment of the role of local and regional meteorology on the SBL erosion efficiency, and (v) the estimation of the breakup time impact on the fine PM (PM2.5) concentration near the surface. We also examine the Q_{req}-Q_{prov} relationship from operational weather forecasts to explore whether the WRF model reproduces the observed relationship under realistic simulation conditions.

To better understand when and under which conditions the inversion breakup occurs,

we start by assessing and comparing the characteristics of the valley atmosphere before sunrise, using thermodynamic profiles obtained from a MWR, and the energy provided to the valley's atmosphere in the form of H. The thermodynamic profiles allow establishing a proxy for the amount of energy required to erode the stably stratified boundary layer, until the breakup occurs (Q_{req}). H is estimated using the eddy-covariance (EC) technique based on the turbulent fluctuations of the wind speed and sonic temperature measured using a 3D sonic anemometer. The overall approach combines high-frequency measurements near the surface with macroscopic observations of the atmosphere in the vertical profile.

The inversion breakup assessment using a data analysis approach involves challenges associated with the spatial representativeness of each of the variables considered in the study. The latter is arguably the main reason why similar studies in the literature follow a modeling-based approach rather than an observational one. Turbulent fluxes estimated from in-situ observations generally represent the local-scale variability conditioned to the intrinsic heterogeneities of the terrain. In contrast, the thermodynamic profiles represent the macroscopic features of the atmosphere. Therefore, it is necessary to evaluate whether the observational datasets used in this study are suitable for the primary purpose and whether they reproduce the overall dynamics around the morning transition. Notwithstanding the potential limitations, the analysis using data sets of independent and different nature constitutes a robust assessment of the inversion breakup process. The covariability among the datasets used in the study would imply a coherent response or connection among different atmospheric scales considered.

Proxies for Q_{req}

An accurate determination of Q_{req} depends, first, on a precise definition of the breakup time in the context of the present study. The breakup time is defined as the moment when the convective inhibition energy in the lower troposphere is compensated by the injection of H, triggering non-local instability within the valley's atmosphere and establishing the initial conditions for the boundary layer growth phase. Following the work by Angevine et al. (2001), for flat terrain, numerous authors (e.g. Beare, 2008; Nadeau et al., 2020) have defined the inversion breakup as the onset of the CBL, the time at which the nocturnal inversion in the surface layer has been fully eroded and turbulent eddies from the surface reach a certain depth (e.g., Angevine et al. (2001) used 200m above ground level). To some extent, the size of the eddies may be assessed observationally.

The appropriate selection of a proxy for Q_{req} is not straightforward, mainly because such an index should adequately represent the entire volume of the valley's atmosphere. We consider thermodynamic indices such as the Convective Inhibition Energy ($CINE$) and the vertical gradient of θ_v at the lower troposphere ($d\theta_v/dz$) computed using thermodynamic profiles obtained using a MWR. $CINE$ indicates the amount of energy inhibiting the updraft of air parcels and is also an indirect measurement of the lower troposphere stability: as the stability of the atmosphere increases, $CINE$ becomes more negative. Conversely, unstable atmospheres correspond to $CINE$ nearing zero. $CINE$ is estimated as

$$CINE = \int_{SFC}^{LFC} g\frac{T'_v - T_v}{T_v}dz,$$

where LFC is the level of free convection, SFC is the surface level, T_v is the virtual temperature of the environment, and T'_v is the virtual temperature of the parcel (Peppler, 1988). On occasions, the LFC largely exceeds the depth of the valley, where the trade winds advect eastward the H and the pollutants emitted at the surface. As a result, the amount of energy required for $CINE$ to become zero is larger than the amount of energy required to erode the stability within the valley. Also, the mechanisms that lead to changes in the thermodynamic profile above the valley may not be fully linked to the turbulent exchanges near the surface, but the forcing could be associated with the synoptic scale. To address this potential issue, and to have more control over the $CINE$ integration height, the LFC is forced to a maximum of 1200 m, just above the average depth of the valley (see Figure 5.1). The modified index is referred to as $CINE_{1200}$.

In order to explicitly state that the vertical gradient of θ_v, $d\theta_v/dz$, is obtained from discrete profiles, we change the notation to $\Delta_z\theta_v$, where $\Delta_z\theta_v$ is computed as the difference between θ_v at height z and θ_v at height $z - \Delta z$, $\theta_v(z) - \theta_v(z - \Delta z)$. z correspondes to the height above ground level (agl). We consider $\Delta z = 200$m, with an exception for $\Delta_{200}\theta_v$, computed as $\theta_v(200magl) - \theta_v(50magl)$ to avoid the potential effects of the roughness sublayer.$\Delta_z\theta_v$ has been extensively used as a proxy for the inversion strength (e.g. Whiteman, 1982), considering that $d\theta_v/dz > 0$ corresponds to stable stratification, $d\theta_v/dz = 0$ to neutral conditions, and $d\theta_v/dz < 0$ to an unstable atmosphere (Peppler, 1988; Curry and Webster, 1999). We consider $\Delta_z\theta_v$ for different atmospheric layers within the valley's atmosphere.

We use different proxies for Q_{req} in order to test the sensitivity of the results to different stability estimations. The proxies considered for Q_{req} on a daily time scale include the minimum values of $CINE$ and $CINE_{1200}$ after sunrise considering the topographic

shading, and to the maximum value of $\Delta_z\theta_v$ at different atmospheric layers within the valley's atmosphere.

Inversion breakup time

Based on the different proxies for Q_{req}, the breakup time is assumed to have occurred when $CINE = 0$ (or relatively close to zero -we use $|CINE| < 20$ J kg^{-1} as a threshold-), and when $\Delta_z\theta_v$ becomes zero after having been positive.

Figures 3.2a and b depict the steps used to assess the strength of the stability (Q_{req}) and the determination of breakup time for a particular day. The figure shows the methodology using $\Delta_{200}\theta_v$ as an example; however, a similar approach is followed with the other layers considered and when using $CINE$ and $CINE_{1200}$. In the example, the proxy for the strength of the stability is determined as the maximum positive $\Delta_{200}\theta_v$ after sunrise. According to Figure 3.2a, the value representing the strength of the instability for that particular date is 1.26 K. Figure 3.2b marks the breakup time, after 11:00 LT, corresponding to the moment when $\Delta_{200}\theta_v = 0$.

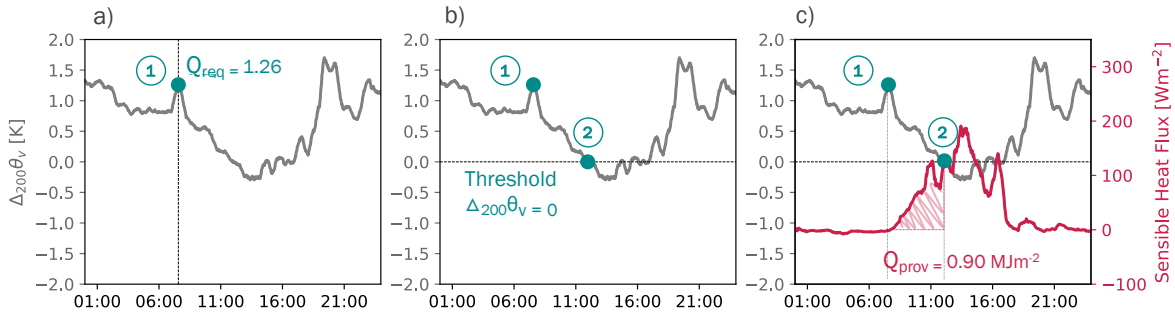

Figure 3.2: Graphical representation of the steps used to assess the strength of the stability (Q_{req}) and the breakup time for a particular day. This example uses $\Delta_{200}\theta_v$ as a proxy for Q_{req}, but a similar methodology is followed for other proxies. a) The proxy for the strength of the stability is recorded as the maximum positive $\Delta_{200}\theta_v$ after sunrise. b) Detection of the breakup time. c) Estimation of Q_{prov} as the time integral of H from the moment used to record the strength the stability (maximum Q_{req} after sunrise) until the inversion breakup.

Proxy for Q_{prov}

The proxy used for the daily Q_{prov} (see Figures 3.2c) is the time-integrated surface H from the moment used to record the strength of the stability (maximum Q_{req} after sunrise) until the inversion breakup (see Figures 3.2a and b, respectively). The proxy is based on a modified version of the methodology presented in Angevine et al. (2001), which is based on the boundary layer growth equation in Garratt (1992). The difference with their approach is that since we used different proxies for Q_{req}, we also obtain different estimations for Q_{prov}.

The methodology assumes that the temperature profile is mainly modified from the bottom as a function of sensible heating. This encroachment approach may introduce biases, given that it does not account for the θ_v profile modification in the lower troposphere, hence the stability modulation due to horizontal thermal advection. However, the observational evidence from MWR retrievals (not shown) suggests that θ_v in the valley's atmosphere mainly varies as a result of vertical processes, with potential temperature changes lagging those in layers closer to the ground. The H is estimated using the EC technique with a block-averaging period of 30 minutes.

Role of breakup time in air quality

As per the definition, the breakup time is closely related to thermodynamically driven vertical dispersion processes. Consequently, the erosion of the SBL may play a vital role in pollutant concentration. The hypothesis is that the earlier the SBL erosion, the faster the vertical dispersion of pollutants occurs, lowering the average daily values of different pollutants. In the Aburrá Valley, PM2.5 is the most critical air pollutant.

The analysis of the impact of the inversion breakup time on the air pollution near the surface of the valley is accomplished by assessing the changes in probability density functions of PM2.5 concentration when constructed as a function of different breakup time thresholds.

Role of local and regional meteorology on the breakup time

One of the challenges in better understanding the ABL in complex terrain, and in particular, the morning transition, relates to the multiscale nature of the processes that modulate the phenomena. The overall behavior of the atmosphere at different levels exhibits signs of multiscale interaction, both in time and space. The latter is particularly true for the ABL over complex terrains, where the diurnal cycle, including the transition from the SBL to the CBL, is modulated by processes evolving on different temporal and spatial scales (e.g. Serafin et al., 2018; De Wekker and Kossmann, 2015).

The large-scale modulation of the ABL could occur directly through kinetic energy transfer between different scales of motion or indirectly via regional and large-scale changes in the conditions that favor or inhibit cloud formation, leading to surface radiative forcing. Thus, there are at least two competing hypotheses to assess. The first hypothesis is that positive anomalies of large-scale convection could enhance the growth of the ABL through kinetic energy transfer and large vertical pressure gradients in the entire atmospheric column forcing mass exchanges between the valley's atmosphere and the free atmosphere. On the other hand, the second hypothesis is that enhanced convection leads to cloud formation that reduced the radiation reaching the surface, slowing down the growth of the ABL. For this reason, it is essential to explore not only the turbulent exchanges but also the potential role of the valley flow (in particular, the magnitude of the vertical wind shear within the valley's atmosphere) and the synoptic atmospheric circulation on the breakup time.

In the tropical environment, pressure patterns persist for very long periods, and the pressure and geopotential height gradients are typically weak, even during the passage of storm systems or perturbed weather in general. For this reason, the wind field is more useful than the pressure or geopotential height fields in describing the synoptic conditions in the tropics. In this regard, the velocity potential anomalies summarize the effect of synoptic-scale convection, allowing the tracking of upper-level divergence or convergence.

In the overall assessment, three different atmospheric scenarios are considered to estimate the potential differences in the magnitude of the vertical wind shear within the valley's atmosphere and differences in the synoptic atmospheric circulation as a function of the breakup time. In this case, in all scenarios considered $Q_{req} > \overline{Q_{req}}$. These scenarios correspond to cases when the nighttime inversion is strong (high Q_{req}) and i) the magni-

tude of the energy forcing provided to reach the morning transition via sensible heating is lower than the 33th percentile among all days considered in the study, ii) times when the energy provided to reach the transition is between the 33th and the 66th percentile, iii) and days for which the energy provided to the system, before reaching the transition, is larger than the 66th percentile.

3.4 Results

One of the main challenges in assessing the inversion breakup from an observational perspective is to ensure that measurements from in-situ sensors and ground-based remote sensing equipment represent the overall ABL variability in the valley. The latter is not only a challenge but a source of uncertainty in all ABL observational studies. While this challenge is difficult to overcome, it is possible to evaluate the holistic coherence and consistency among all variables in the dataset, and their capability to represent the ABL dynamics. Considering that most variables used in this study are obtained using different measurement techniques, high co-variability and interdependence in the dataset would indicate a skillful representation of the zeroth- and first-order valley dynamics, including the major spatial and temporal scales of variability.

Figure 3.3a depicts the interrelationship between the hourly H, $\Delta_{200}\theta_v$, and $CINE_{1200}$. Evidently, negative values of $\Delta_{200}\theta_v$ correspond to near-zero values of $CINE_{1200}$, and conversely, positive values of $\Delta_{200}\theta_v$ are associated with negative values of $CINE_{1200}$. The Pearson correlation between $\Delta_{200}\theta_v$ and $CINE_{1200}$ is -0.80. Figure 3.3b shows the correlations among all the Q_{req} proxies considered, including $\Delta_{200}\theta_v$, $\Delta_{800}\theta_v$, $\Delta_{Total}\theta_v$ ($\theta_v(1200\,m\,agl) - \theta_v(50\,m\,agl)$), $\Delta_{Sup}\theta_v$ ($\theta_v(800\,m\,agl) - \theta_v(50\,m\,agl)$)), $CINE$, $CINE_{1200}$, and $CINE_{1500}$. The magnitude of the linear correlations among all Q_{req} proxies, except between $CINE$ and $\Delta_{Sup}\theta_v$, is over 0.6, emphasizing the high covariance between the virtual temperature at different heights in the lower troposphere, below LFC. This result serves as evidence of the strong dependence of the temperature profile on the surface heating, rather than on thermal advection. It is important to note that in 47 out of the total 291 days with data available, the inversion breakup, as defined in the present study, was not reached.

Figure 3.3a shows that, for strong surface forcing to the ABL (high values of H), the likelihood of positive values of $\Delta_{200}\theta_v$ is very low. In other words, it is unlikely to have

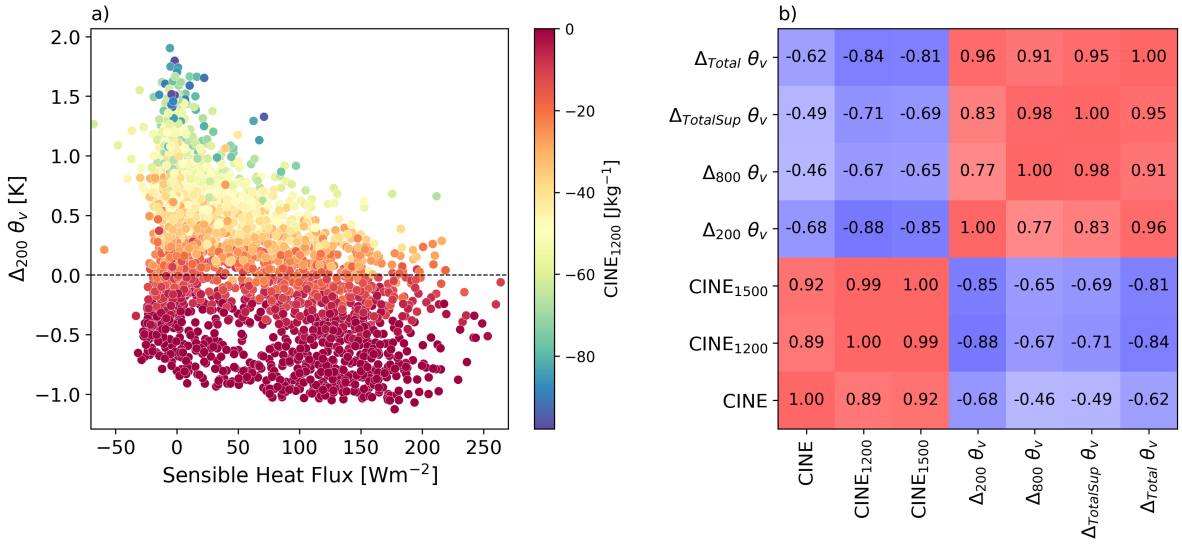

Figure 3.3: a) Observed covariability between H, $\Delta_{200}\theta$, and $CINE_{1200}$. Colors indicate the magnitudes of $CINE_{1200}$. The figure shows $CINE_{1200}$ increases (less negative) as the slope of the potential temperature profile $\Delta_{200}\theta_v$ changes from positive to negative, reaching its highest negative values when the forcing is low and $\Delta_{200}\theta$ is close to zero. b) Correlation matrix among all the Q_{req} proxies considered, including $\Delta_{200}\theta_v$, $\Delta_{800}\theta_v$, $\Delta_{Total}\theta_v$ $(\theta_v(1200magl) - \theta_v(50magl))$, $\Delta_{Sup}\theta_v$ $(\theta_v(800magl) - \theta_v(50magl)))$, $CINE$, $CINE_{1200}$, and $CINE_{1500}$. Colors in the correlation matrix indicate positive (red) or negative (blue) values for the Pearson coefficient; the darker the color, the higher the magnitude of the correlation.

stable stratification when the heating is strong. Correspondingly, when H is larger than 150 Wm^{-2}, the average of $CINE_{1200}$ is -7.5 Jkg^{-1}. The large spread of the data at the bottom portion of the H-$\Delta_{200}\theta$ scatterplot is a consequence of the fact that the transition from a stable to an unstable atmosphere is a cumulative process, which does not depend exclusively on the magnitude of the surface forcing at a given time, but also on multiple additional factors (essentially on H during the hours before the breakup). Furthermore, the observed relationship between H and the incoming radiation (not shown) is very high, with a correlation of 0.89. Despite the different nature of the physical principles used to measure the different variables, the high covariability corresponds well with the expected behavior of the ABL, suggesting a clear link between the radiative forcing and H with the evolution of the nocturnal inversion within the valley. Based on these results, it is possible to follow the described observational approach. Additionally, considering the high correlations in 3.3b, the subsequent results are obtained using two proxies of Q_{req}: a near-surface stability proxy ($\Delta_{200}\theta_v$), and a lower-troposphere column integrated proxy ($CINE_{1200}$). Results using other proxies are similar and do not alter the main conclusions

of this study.

Q_{req} vs. Q_{prov}

Figures 3.4a and b show the relationship between Q_{req}, using $CINE_{1200}$ and $\Delta_{200}\theta_v$ as proxies, respectively, and Q_{prov} prior to the temperature profile neutralization, as defined. Each point on the scatterplot corresponds to a specific day between February and November 2018. Both diagrams show a remarkable correspondence between the two selected proxies for Q_{req}, providing evidence that Q_{prov} indeed is required to be higher when the magnitude of Q_{req} is large, regardless of the proxy used. The Q_{req}-Q_{prov} relationship is not linear. There appears to be a threshold in the strength of the inversion (Q_{req}), over which there is a considerable spread in the Q_{prov} before neutralization, implying that, in some cases, for the same Q_{req} the magnitude of Q_{prov} could be four to six times larger than usual before achieving SBL neutralization. The latter suggests the existence of a heating efficiency similar to the findings of Leukauf et al. (2017). This is explored further in subsection 3.4.

The relationship observed in both diagrams in Figure 3.4 suggests a different state of the atmosphere for cases corresponding to the lower and upper parts of the scatter plots. To further explore this behavior, Figure 3.5 shows the comparison of the state of the atmosphere on two contrasting days, corresponding to the larger circles in Figure 3.4. The first case, with a high Q_{req}, corresponds to February 22, 2018 (see Figures 3.5a, b, c and, d), and the second case, with a low Q_{req}, corresponds to October 12, 2018 (lower panels) (see Figures 3.5e, f, g, and, h). The Figure includes the evolution of the θ_v profile, from 05:00 UTC-5 to 14:00 LT, the vertical profile of wind speed and wind direction, the ceilometer backscattering intensity profile from the surface up to 2.5 km, and finally, the hourly evolution of PM2.5 concentration.

The θ_v profiles reveal a strong nighttime inversion on February 22, 2018 (Figure 3.5a), resulting in a considerable amount of energy required to erode the SBL, a notably shallow ABL, and a late breakup time (14:45 UTC-5). The shallow ABL persisted after 14:00 as a direct consequence of the presence of high cloudiness (see Figure 3.5c) diminishing the incoming short-wave radiation to the surface. The RWP shows relatively strong north-easterly winds ($> 6ms^{-1}$) near the surface and up to approximately 400 m throughout the morning. The wind profile shows a reduction of the wind speed during the morning,

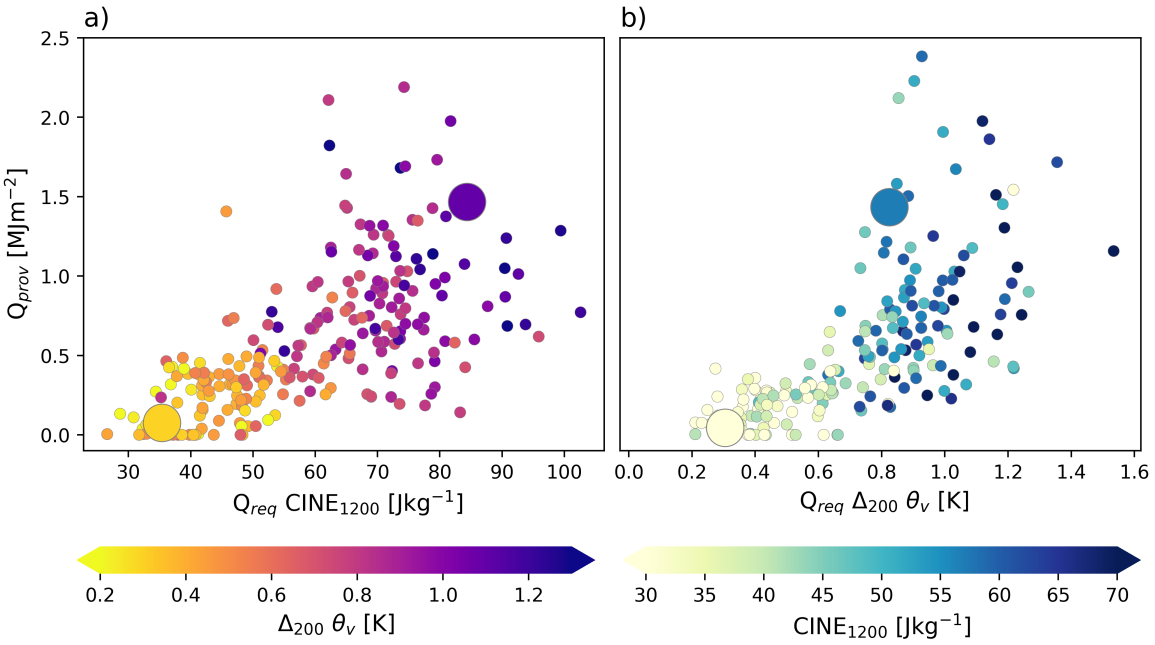

Figure 3.4: Scatter plots of the selected proxies for Q_{req}, a) $CINE_{1200}$ and b) $\Delta_{200}\theta_v$, and Q_{prov} as retrieved following the methodology in Figure 3.2. It is important to note that panel a) uses $-CINE_{1200}$. Each point in the scatter plots corresponds to a specific day between February and November 2018. The larger circles correspond to two contrasting days, February 22, 2018, and October 12, 2018 as described in the text.

above 400 m and up to the average depth of the valley (1200 m agl) where the speed is higher due to the trade winds. In this case, the vertical exchanges within the valley atmosphere are restricted by the fact that no large eddies are being formed. In consequence, under these conditions, pollutants do not mix efficiently, as can be observed both in the relatively high ceilometer backscattering intensity and in the PM2.5 hourly concentration record (Figures 3.5c and d). On October 12, 2018, the atmospheric environment was diametrically opposite. Clear skies allowed for a swift transition from stable to unstable conditions, an early breakup time (08:00 UTC-5) with an efficient ABL growth, and low backscattering intensities and PM2.5 concentration. An important feature is that winds within the ABL are considerably weaker in the morning time on October 12 than during the same period on February 22. A similar finding is reported in Halios and Barlow (2018), with a negative relationship between the growth rate of the mixing layer and the wind speed. More important than the magnitude of the wind speed, wind shear at the top of the ABL is higher on October 12 than on February 22. The latter could imply a larger ABL growth rate due to increased mechanical turbulence by shear production, leading to entrainment.

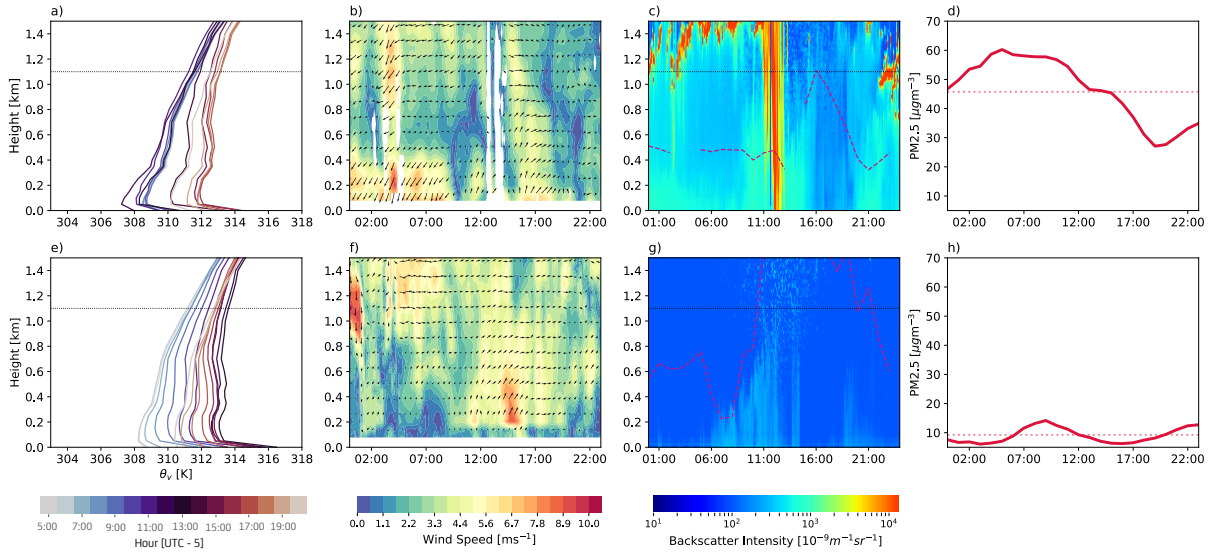

Figure 3.5: The panels show different atmospheric variables for two contrasting days. The upper panels correspond to February 22, 2018, and the lower panels to October 12, 2018. Panels a) and e) show the hourly evolution of the θ_v profile, from 05:00 UTC-5 to 14:00 LT. Panels b) and f) the time-height cross-sections of wind speed and direction. Panels c) and g) the ceilometer backscattering intensity profiles from the surface up to 2.5 km. Panels d) and h) the hourly evolution of PM2.5 concentration. The red dotted line corresponds to the PM2.5 average value for the entire day.

The absence of a marked top-of-the-atmosphere radiation and surface air temperature seasonality in low-latitudes does not imply an insignificant valley-scale response to the annual climatology. In fact, the annual cycle in the tropics does impose variable large scale forcing, modulating the ABL variability. In the tropics, the seasonality of the Intertropical Convergence Zone (ITCZ) modulates local cloudiness, precipitation, and surface incident radiation, altering the characteristics of the nocturnal inversion and the erosion of the SBL.

Figure 3.6a shows a time-dependent clustering in the Q_{req} vs. Q_{prov} scatterplot around two different seasons (Feb-Jun and Jul-Nov). The clustering suggests that the strength of the nighttime inversion, hence the energy required to erode the SBL, changes significantly throughout the year. Consequently, the inversion-breaking time also varies (see Figure 3.6b). From February to mid-June, the proxy for Q_{req} is, on average, twice as large as that for the July-November period, and the inversion breakup occurs later in the day, in some cases even after 14:00 UTC-5.

Figure 3.7, similar to 3.4b but calculated using information from the WRF forecast runs.

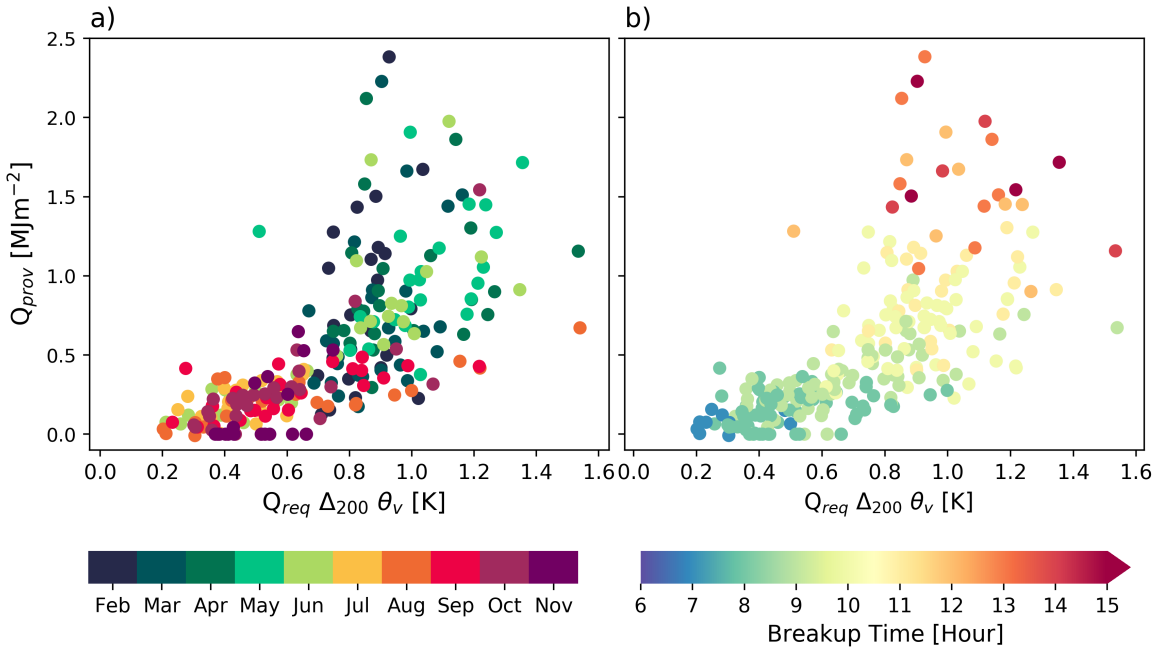

Figure 3.6: a) Evidence of seasonal dependence of the Q_{req} and heating efficiency. b) Evidence of breakup time variability as a function of Q_{req} and heating efficiency.

The diagrams for the WRF runs show, in general, a similar behavior to the observations, but with a larger spread Q_{prov} for large Q_{req}, suggesting a larger variability in the heating efficiency in the model. The time of the inversion breakup also varies similar as in Figure 3.6b.

Heating efficiency

The previous results show a non-linear relationship between Q_{req} and Q_{prov}, and reflect an increase in Q_{prov} spread with the magnitude of Q_{req}, with implications for the breakup time. In a closed system, sensible heating would be used to raise the lower troposphere temperature, expanding the ABL, and none of the energy would be exported to the free atmosphere. Under these idealized conditions, the relationship between Q_{req} and Q_{prov} would be bijective (one-to-one correspondence). If there are, however, atmospheric conditions that lead to heat being exported out of the valley's atmosphere, the heating efficiency would be diminished and most likely variable (e.g. Leukauf et al., 2017). Figure 3.8a shows, for different Q_{req} intervals, the 10th, 50th, and 90th Q_{prov} percentiles, with their corresponding regression functions. For the 10th and 50th percentiles, and up to approximately the 70th (not shown), Q_{req} and Q_{prov} follow a linear relationship. This

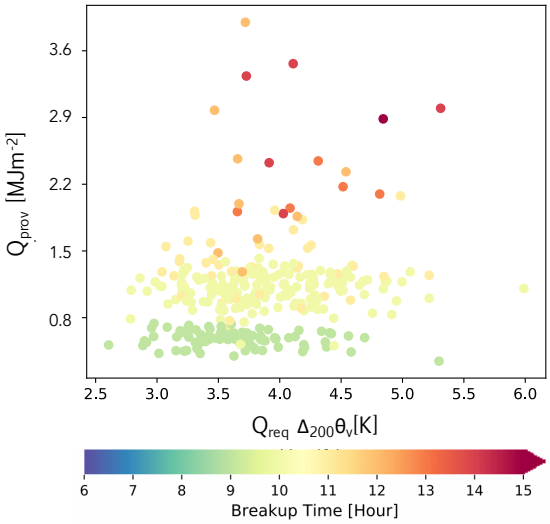

Figure 3.7: Scatter plots of $\Delta_{200}\theta_v$ and Q_{prov} following the methodology in Figure 3.2 using information from the WRF forecast runs. The colors correspond to the breakup time in each case.

suggests that, in 70% of the cases, the energy provided is mostly used to warm up the atmosphere within the valley: There is a linear relationship between Q_{req} and Q_{prov} for all the percentiles explored up to the 70th, and the changes in the slopes among different percentiles are not considerable. In contrast, from the 75th percentile onwards, Q_{prov} increases exponentially with Q_{req}.

Consequently, there appears to be a variable heating efficiency rate that is more evident for larger values of Q_{req}, with direct effects on the breakup time: the present observations suggest that, for all days with very low heating efficiency (large values of Q_{req} and Q_{prov} above the 66th percentile), the breakup occurs later than 13:00 LT. Therefore, it is essential to evaluate which mechanisms or atmospheric patterns are associated with low heating efficiency. Previous work link this possible leakage of energy with the valley circulation and the wind speed (Angevine et al., 2001; Leukauf et al., 2016; Nadeau et al., 2020). This is explored in the following section. The breaking times vary from 07:00 to approximately 16:00 UTC-5, depending on the heat efficiency rate. When the heat efficiency is low (i.e., in the upper part of Figure 3.8b), the nighttime inversion breaks late in the afternoon (after 14:00 LT), being unfavorable for pollutant dispersion as shown in the previous subsection.

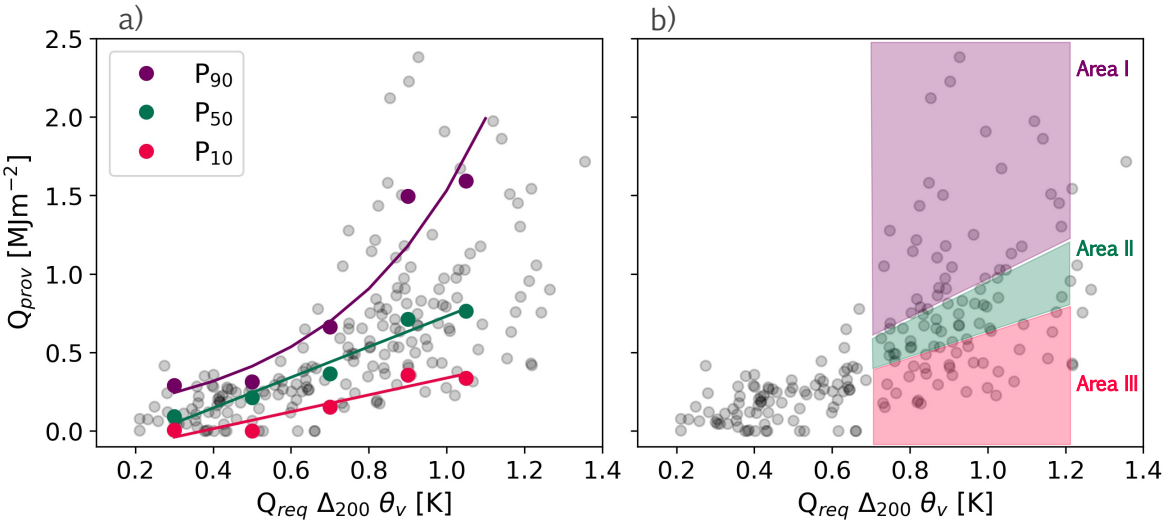

Figure 3.8: a) Regression functions for the 10th, 50th, and 90th Q_{prov} percentiles and Q_{req}. The regression functions are obtained for each percentile after binning the Q_{req} in intervals, and obtaining the corresponding 10th, 50th, and 90th Q_{prov} percentile for each of the intervals. b) Selection of three graphical areas in the Q_{req}- Q_{prov} diagram for composite analyses. The areas correspond to cases above the mean Q_{req}, and below the 33th Q_{prov} percentile (Area III), between the 33th and the 66th percentile (Area II) and above the 66th percentile (Area I).

Role of local wind shear

To evaluate the potential influence of wind speed and vertical shear on the heating efficiency during the morning transition, we conducted a composite analysis of these variables during three different subsets of dates. The three subsets of dates with contrasting heating efficiency correspond, in all cases, to values above the mean Q_{req}, and (i) Q_{prov} values below the 33th percentile, (ii) between the 33 and the 66th percentile, and (iii) above the 66th percentile (see Figure 3.8b). Figure 3.9a to c, and d to f, show the wind speed and the vertical wind shear, respectively, for the three subsets of dates. Area I corresponds to the lowest heating efficiency among the three subsets. Conversely, Area III corresponds to the highest heating efficiency (less energy provided to reach neutralization for a similar amount of Q_{req}). The evidence in the Figure indicates that for lower wind speeds near the surface between 06:00 and 10:00 UTC-5, and more notably, for higher vertical wind shear, the inversion breakup occurs earlier and with less energy provided to the atmosphere in the form of surface H.

The observed enhanced shear corresponding to dates in the Area III set compared to the other sets is elevated, being maximum across the top of the SBL at the entrainment zone,

rather than near the surface. Even under low wind speeds and with shear differences less than 1 ms^{-1}, the observational evidence suggests that shear production of TKE cannot be neglected. From the observations, the elevated shear appears to play an important role in enhancing the erosion of the SBL, likely by generating TKE.

Different authors have studied the role of elevated shear in the evolution of the CBL, most using a modeling approach and some using observations in flat terrains (e.g. Angevine, 1999; Fedorovich et al., 2001; Conzemius and Fedorovich, 2006; Fedorovich and Conzemius, 2008; Halios and Barlow, 2018). However, there is no consensus on whether a mean elevated shear enhances or suppresses entrainment. Conzemius and Fedorovich (2006) state that the boundary layer begins to grow due to increasing surface H and entrainment, with air from the free atmosphere being engulfed by convective thermals and becoming part of the boundary layer, a process that is modified by the presence of an elevated shear (Fedorovich et al., 2001). Compared to the effect of surface shear, the influence of elevated shear across the inversion on turbulence in the SBL and CBL is much less studied. It is clear that in addition to the often dominant buoyancy forcing, the CBL development is modulated by wind shear, which modifies considerably the internal structure of the lower troposphere. Therefore from this point of view, the timing of the breakup is modulated by the evolution of the surface H and the amount of mechanical turbulence due to wind shear.

Very few studies have explored the role of the elevated shear in a setting characterized by complex terrain and urbanization. The observational evidence presented here is not in agreement with the results presented in the theoretical work by Hunt and Durbin (1999). They found that the elevated shear prevented the entrainment process and the generation of TKE by deforming thermals so that they do not penetrate as effectively into the inversion, interfering with the entrainment, a process referred to as shear sheltering. However, in their work, they did not consider the potential effects of density stratification and the complex terrain setting. In their results, thermals do not overshoot their equilibrium level, and the CBL growth is slower. Fedorovich et al. (2001) and Conzemius and Fedorovich (2006) explore the directional effect of the elevated wind shear on the turbulent exchange across the capping inversion in Large Eddy Simulation (LES) experiments. In the numerical experiments, when the mixed-layer air has a higher momentum than the air above the inversion (negative elevated shear), CBL growth is enhanced contrary to the sheltering process described by Hunt and Durbin (1999). In contrast, in cases of positive shear, CBL growth is diminished. In contradiction to the mentioned modeling results, the

evidence in Figure 3.9c and d shows a case where higher positive elevated shear (mixed-layer air has less momentum than the air above the inversion) leads to faster erosion of the SBL compared to when the positive elevated shear is weaker. The evidence suggests that the elevated shear does result in thermal damping at the inversion layer inhibiting the entrainment; conversely, it likely favors TKE generation and intensification of vertical transport of air from the mixed layer into the above-inversion region. The coincidence in the modeling studies and the results in Figure 3.9 lies in that the elevated shear appears to be much more important than the surface shear in the erosion of the SBL.

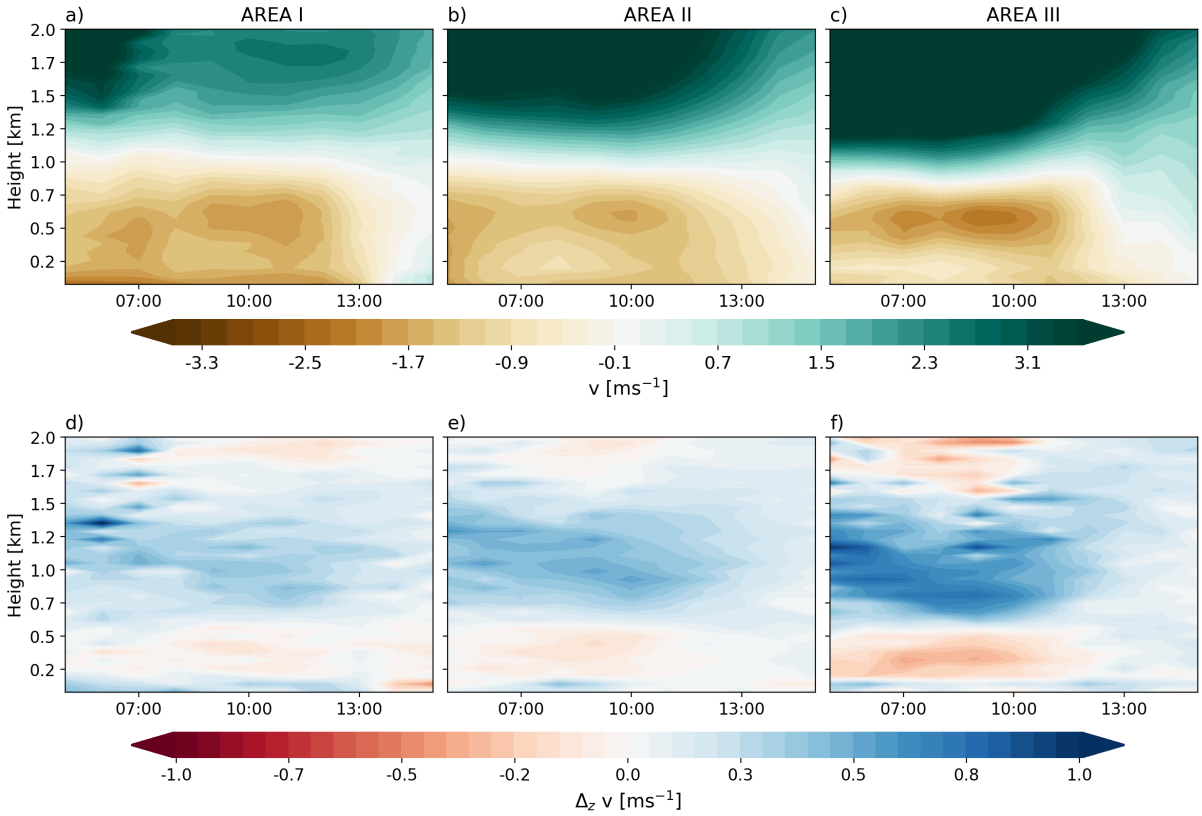

Figure 3.9: Temporal evolution of the profiles of the meridional winds (a,b,c) and vertical wind shear (d,e,f) from 05:00 UTC-5 to 14:00 LT, for each set (Areas I, II, and III) defined in Figure 3.8.

In addition to the vertical wind speed and wind shear, the magnitude of the upslope-downslope winds for the sets of days in Areas I, II, and III was also contrasted. The results do not show considerable and consistent differences among the three sets of dates.

Role of synoptic conditions

The role of synoptic conditions on the ABL evolution over the Aburrá Valley is assessed considering the velocity potential, and OLR anomalies. The anomalies are computed as the difference between the daily average of the variable of intestest and the monthly average of the same variable. The velocity potential, and OLR average anomalies for the set of days corresponding to Areas I, II, and III in Figure 3.8b are shown in Figures 3.10, and 3.11, respectively. Together, these variables represent the overall regional-scale convective activity.

The results suggest that, overall, for a similar Q_{req} values, the erosion of the SBL occurs not only faster but also with lower values of Q_{prov} (higher heating efficiency) for cases when the deep convection is inhibited regionally. Conversely, the SBL erosion is delayed, often until the afternoon, in scenarios when the regional deep convective activity is enhanced. In the latter case, the Q_{prov} values are three-four times larger than in the former conditions.

Figure 3.10a, b and c show, for Area I, positive velocity potential anomalies at 700 hPa over northern South America, weak anomalies at 500 hPa, and negative anomalies at 200 hPa, respectively. Since positive (negative) velocity potential anomalies indicate convergence (divergence), the previous configuration indicates an enhancement of the deep convective activity in the region. In tropical South America, an enhanced deep convective activity often leads to cloud formation. Figure 3.11a shows negative OLR anomalies associated with Area I, which agrees with the observed velocity potential configuration in Figure 3.10a, b and c. The velocity potential and OLR anomalies for Area II are the weaker of the three cases (see Figures 3.10d, e, f, and 3.11b). Conversely, Figures 3.10g, h, and i show, for Area III, negative velocity potential anomalies at 700 hPa over northern South America, weak anomalies at 500 hPa, and positive anomalies at 200 hPa, respectively. Such configuration, in stark contrast to the configuration shown for Area I, suggests a suppression of the deep convective activity in the region. OLR anomalies for Area III are positive (see Figure 3.11c), corroborating the regional deep convective inhibition. The stream function anomalies at 700 and 500 hPa suggest an anomalously higher easterly flow for Area I compared to westerly anomalies for Area III, which are also in agreement with the convective contrast described before (not shown).

The deep convective activity and OLR contrast for the dominant regional conditions

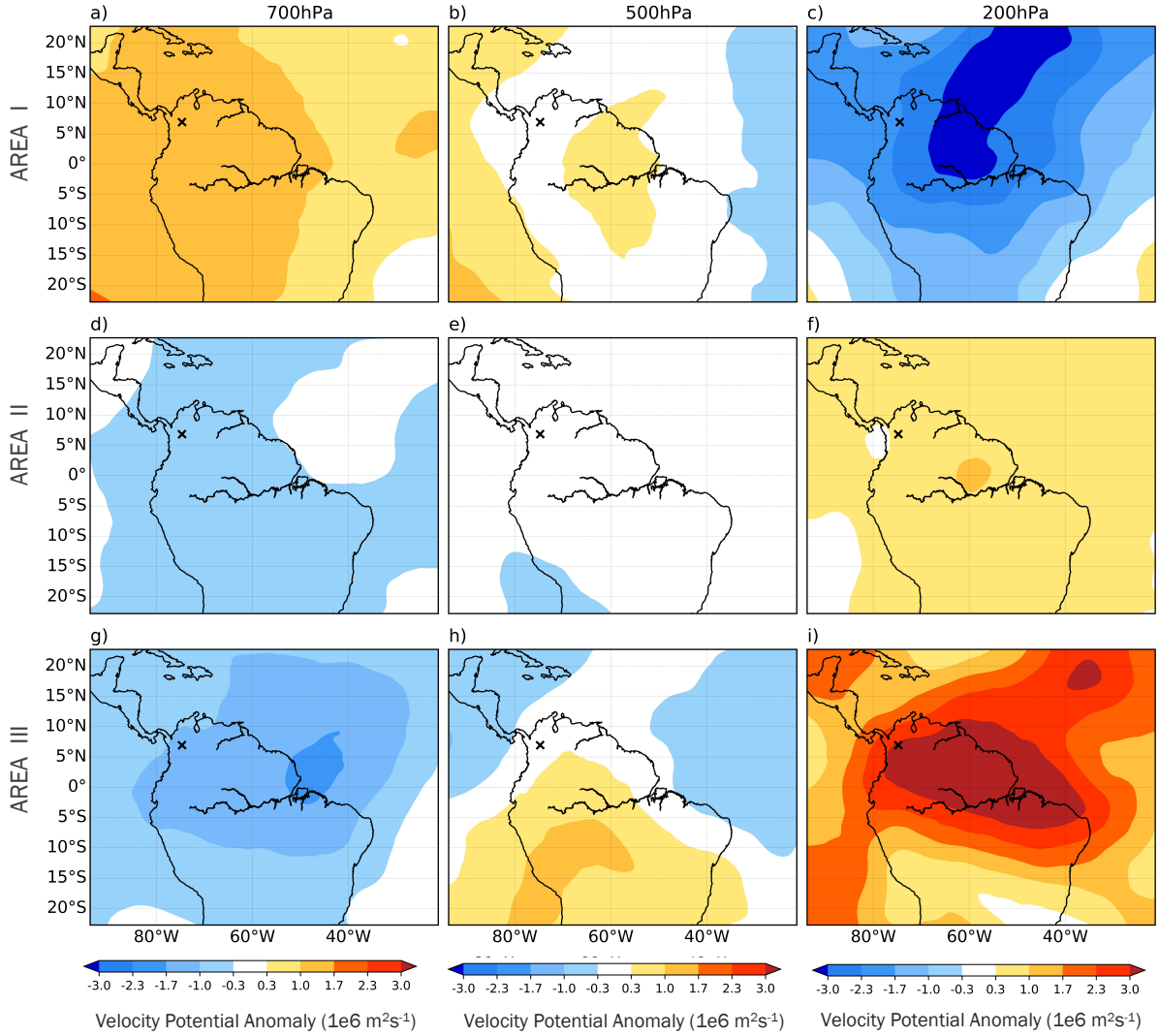

Figure 3.10: Average velocity potential anomalies for different atmospheric leves and for each of the set of dates (Areas I, II, and III) selected in Figure 3.8b. The top row corresponds to Area I, the middle row to Area II, and the bottom row to Area III. Panels a), d), and g) correspond to anomalies at 700 hPa. Panels b), e), and h) to anomalies at 500 hPa. Panels c), f), and i) to anomalies at 200 hPa. The x mark corresponds to the location of the Aburrá Valley.

in Area I vs. Area III suggests that the radiative forcing associated with deep convective clouds plays a more dominant role in modulating the SBL erosion than the dynamical effect of the regional-scale convection. The average radiation reaching the surface between 06:00 and 12:00 UTC-5 for Area I is 401 Wm^{-2} and for Area III is 472 Wm^{-2}. It is expected that this 71 Wm^{-2} difference in radiation leads to a belated erosion of the SBL. However, the radiation difference in itself does not directly explain the larger Q_{prov} required in these cases, considering that Q_{req} at 06:00 UTC-5 is similar. Nevertheless,

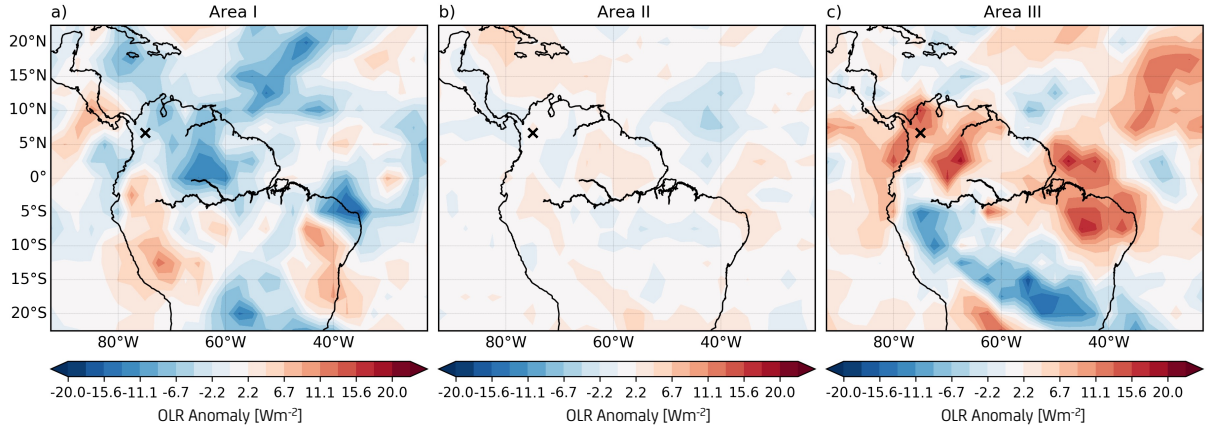

Figure 3.11: Similar to Figure 3.10 but for average OLR anomalies.

it does suggest that the extended SBL erosion period leads to inefficient heating of the ABL. It is likely that with longer erosion times, different processes such as heat export outside of the valley linked to upslope flow (e.g. Noppel and Fiedler, 2002) lead to lower heating efficiency.

Daily PM2.5 concentrations as a function of breakup time

The timing of the inversion breakup plays an important role in modulating air pollutant concentration. The PDFs for the daily average PM2.5 concentration, conditioned on breaking times occurring within four different hours during the day (Figure 3.12), suggest that, as the inversion breakup time occurs later in the day, the likelihood of higher PM2.5 concentrations increases. The concentration of aerosols in the valley's atmosphere is mainly influenced by the anthropogenic emissions at surface level and by the vertical dispersion of pollutants after the inversion breakup (e.g. Herrera-Mejía and Hoyos, 2019). In cases of a late breakup, emissions accumulate within the SBL until thermal turbulence is activated, after which pollutants are lifted out of the valley if the mixed layer height exceeds the valley crest height. For the specific case of the Aburrá Valley, where atmospheric pollutant dispersion out of the valley is almost entirely thermodynamically driven, the magnitude of the turbulent exchange must be large enough for the ABL to reach the mountain peaks, where the pollutants are advected away far from the valley by the trade winds.

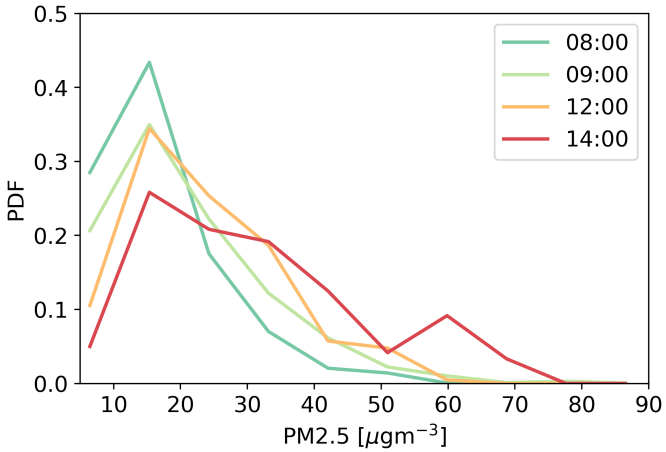

Figure 3.12: Probability density functions of daily PM2.5 concentrations in the atmosphere near the surface as a function of breakup time.

3.5 Conclusions

The variability and implications of the timing of the stable boundary layer breakup have been examined for a narrow valley located in the tropical Andes Cordillera using a combination of in-situ turbulent scale observations and remotely sensed macroscopic features of the local atmosphere. Given the topographic features of the region, it is imperative to understanding when and under which conditions the nocturnal inversion breaks up because it corresponds to the time when the exchanges between the surface and the free atmosphere intensify and reach their maximum, resulting in a more efficient pollutant vertical transport.

The assessment is based on an observational diagnostic framework developed to study the breakup time using proxies for the energy required to erode the atmospheric inversion (Q_{req}) and the amount of energy provided to the atmosphere via sensible heating (Q_{prov}), combining high frequency measurements near the surface with macroscopic observations of the atmosphere in the vertical profile. In this framework, the inversion breakup occurs when Q_{prov} via surface sensible heat flux (H) is equal to Q_{req}. Different thermodynamic indices were considered as proxies for Q_{req}, including changes of virtual potential temperature in the vertical at the lower-troposphere ($\Delta_z\theta_v$) and $CINE$. The inversion breakup assessment using the proposed framework involves challenges associated with the spatial representativeness of each of the variables considered in the study. However, the high covariability between the hourly H, $\Delta_{200}\theta_v$, $\Delta_{800}\theta_v$, $\Delta_{Total}\theta_v$ ($\theta_v(1200) - \theta_v(50)$),

$\Delta_{Sup}\theta_v$ $(\theta_v(800) - \theta_v(50)))$, $CINE$, $CINE_{1200}$, and $CINE_{1500}$ indicates a coherent response among different atmospheric scales considered, hence serving as validation of the proposed methodology, regardless the limitations.

The relationship between Q_{req} and Q_{prov} allows concluding that Q_{prov} indeed is higher when the magnitude of Q_{req} is large, regardless of the proxy used. However, the observations indicate that the Q_{req}-Q_{prov} relationship is by no means simple. The evidence suggests the existence of non-constant heating efficiency for large values of Q_{req}, similar to the findings of Leukauf et al. (2017). In approximately 70% of the cases, the energy provided is mostly used to warm up the valley's atmosphere. In contrast, for approximately 25% of the cases, Q_{prov} increases exponentially with Q_{req}.

The vertical wind shear appears to be an important factor modulating the breakup time, hence the apparent heating efficiency. Higher vertical wind shear is linked to the earlier erosion of the SBL, with less energy provided to the atmosphere in the form of surface H. Moreover, the higher vertical wind shear does not occur near the surface. Instead, it is elevated, and it is maximum across the top of the SBL at the entrainment zone, suggesting that shear production of TKE cannot be neglected. The elevated shear, regardless of directional considerations, appears to play an essential role in enhancing the erosion of the SBL, likely by generating TKE. The evidence suggests that the timing of the breakup depends not only on the surface H but also on the amount of mechanical turbulence due to the elevated wind shear. The observational evidence presented here is important since there is no consensus on whether a mean elevated shear enhances or suppresses entrainment.

The synoptic conditions also play a role in the ABL evolution over the Aburrá Valley and breakup time. Velocity potential and OLR anomalies indicate that the erosion of the SBL occurs faster and with lower values of Q_{prov} (higher heating efficiency) when the deep convection is inhibited regionally. Conversely, the SBL erosion is delayed in scenarios when the regional deep convective activity is enhanced. The contrast in deep convective activity and OLR linked to variable heating efficiency suggests that the radiative forcing associated with deep convective clouds plays a dominant role in modulating the SBL erosion than the dynamical effect of the regional-scale convection. The difference in average radiation between 06:00 and 12:00 UTC-5 between cases with high and low heating efficiency was found to be approximately 70 Wm^{-2}. This difference is considerable and translates into considerably different breakup time, and with longer erosion times, various processes such as heat export outside of the valley through upslope flow reduce the heating efficiency.

The results suggest a large breakup time variability as a function of heating efficiency. In addition, the breakup time variability has been shown to have a profound impact on local air quality within the valley. The evidence indicates that, for later breakup times, the likelihood of higher PM2.5 concentrations increases considerably. In cases of a late breakup in complex terrains, anthropogenic emissions accumulate within the SBL until thermal turbulence is activated.

Chapter 4

COMPLEX Experiment: Boundary-Layer interactions in a heavily-urbanized complex terrain

Laura Herrera-Mejía[1], Carlos D. Hoyos[1], Mathias W. Rotach[2], Julián D. Urán[3]

[1] *Universidad Nacional de Colombia, Sede Medellín, Facultad de Minas, Departamento de Geociencias y Medio Ambiente*

[2] *Department of Atmospheric and Cryospheric Sciences, University of Innsbruck, Austria*

[3] *Sistema de Alerta Temprana de Medellín y el Valle de Aburrá (SIATA), Área Metropolitana del Valle de Aburrá (AMVA)*

4.1 Introduction

The rapid worldwide increase of urban areas during the last century and the continued tendency of the population to cluster in these large settlements have brought the attention of the scientific community, highlighting the need to carry out urban-centered studies (e.g., Roth, 2000; Arnfield, 2003; Grimmond, 2006; Souch and Grimmond, 2006; Castán-Broto and Bulkeley, 2013; Wood et al., 2010). These studies have focused not only on the small-scale physical processes on which weather forecasts rely (Baklanov et al., 2018) but also on the impact of the local changes and variability on the global climate and vice versa (e.g., Rosenzweig et al., 2018). Cities are environments characterized for the high surface roughness, with a mixture of multiple land surface covers, materials, and obstacle geometries, modulating the surface energy (-mass) balance, creating their distinct climate

and micro-climates (Oke et al., 1999; Grimmond et al., 2004). The growth of urban areas is also linked with the increase in the likelihood of climate- and weather-related risks, including heat stress hazards, flash flooding, and critical air quality episodes (Ward et al., 2013; Bohnenstengel et al., 2015). One of the most salient features of urban areas is the alteration of the average temperature and its variability throughout the diurnal cycle compared to rural areas. The tradeoff between evapotranspiration, restricted by the absence of vegetation, and sensible heat flux, enhanced by the built environment, leads to elevated urban temperatures establishing urban heat islands (UHI) (Barlow et al., 2015). The less energy used for evaporation, the more energy is available for heating the lower troposphere, raising the urban air temperatures, and increasing the likelihood of thermal stress (Ward and Grimmond, 2017). On the other hand, emissions of pollutants and greenhouse gases have become the leading environmental concerns associated with expanding metropolitan areas worldwide (Santosa et al., 2008; Cleugh and Grimmond, 2012; Bohnenstengel et al., 2015; Kumar et al., 2018). The growth of population, energy consumption, and the expansion of the current transportation models have led to the growth of pollutant injection into the atmosphere, worsening air quality conditions in urban areas, and altering the anthropogenic radiative forcing (Mayer, 1999; Li et al., 2015). The link between pollution and greenhouse gases is part of the urban ecology, where the emissions are outpacing our capacity to implement control measures (Grimm et al., 2008).

Accurate climate and weather forecasts in urban areas and the surrounding region are vital for the stability and growth of the economy, for the sustainable development of the region, for promoting strategic planning, and for optimal water and risk management policies, including early warning plans associated with the occurrence of extreme hydrometeorological events and critical air pollution episodes (Ward and Grimmond, 2017). The accuracy of the forecasts is intricately tied to the level of knowledge of the urban surface-atmosphere exchanges (Grimmond et al., 2004), highlighting the significance of, and the need for, research on the atmospheric boundary layer (ABL) variability, transcending the scientific curiosity and becoming an issue of high social relevance (van der Kamp and McKendry, 2010; Di Giuseppe et al., 2012; Chandra et al., 2014; Zhang et al., 2014a).

Highly populated urban centers (e.g., those with more than four million inhabitants) are often located in developing countries. Among the top 20 world's largest metropolitan areas in 2020, 14 are located in developing countries. In these cities, the economic growth is characterized by immense economic inequality, increasing the vulnerability of a signifi-

cant portion of the population to extreme weather/air quality/climate variations, inducing and magnifying adverse health impacts on the population (Baklanov et al., 2015). The complexity of the urban infrastructure (high surface heterogeneity, and multiple energy and pollutants sources and sinks), together with the heightened vulnerability, makes big cities highly complex environments that constitute one of the biggest challenges in terms of understanding the interactions and exchanges within the surface layer (Kotthaus and Grimmond, 2014). Adding an extra layer of complexity, a considerable number of cities located in the world's mountainous areas are currently facing significant urban growth (e.g., the European Alps, the Andes) (Perlik et al., 2001; Di Sabatino, 2016), leading to a nonlinear increase in their vulnerability. Under this scenario, multiple additional surface-atmosphere interactions and processes could contribute to the momentum, mass, and energy exchange at different spatial and temporal scales (Zardi and Whiteman, 2013; Rotach et al., 2015; De Wekker and Kossmann, 2015; Serafin et al., 2018), further magnifying the uncertainties to determine the processes that govern the turbulent exchanges (Wiernga, 1993), preventing the scientific community from accurately reproducing those interactions in the local scale in the context of numerical models. Thus, complexity is not exclusively associated with terrain characteristics but also with the actual spatio-temporal structure of the resultant turbulent exchanges (Stiperski et al., 2019).

Despite the difficulties for generalizing their results, experimental approaches, particularly field campaigns, are considered fundamental in order to fill the current knowledge gap concerning turbulent exchange processes over truly complex terrain. In that sense, over the last thirty years, driven by significant improvements in instrumentation, several research efforts have been dedicated to studying the implications of non-ideal surfaces on turbulence characteristics, based on very detailed and well-planned field campaigns. These field projects could be classified into two main approaches: i) campaigns addressing the implications of the urban characteristics on the surface-atmosphere interactions and the urban boundary layer, highlighting the modulation of air quality and dispersion processes (Rotach, 1993; Roth, 2000; Allwine et al., 2002; Kastner-Klein and Rotach, 2004; Rotach et al., 2005; Choi et al., 2016; Zou et al., 2018, and references therein), and ii) studies focused on understanding flow dynamics and turbulent exchange processes in mountainous terrains (Doran et al., 2002; Fernando et al., 2015; Rotach et al., 2017). In addition to these comprehensive projects, there have been a significant number of single-site short-term studies addressing exchange processes in mountainous regions (e.g., Moraes et al., 2005; Hiller et al., 2008; Martins et al., 2009; de Franceschi et al., 2009; Pegahfar and Bidokhti, 2013; Pegahfar and Zawar-Reza, 2017; Hiller et al., 2008; Helgason

and Pomeroy, 2012; Nadeau et al., 2013; Barman et al., 2019). These campaigns have produced a large amount of data describing turbulent exchanges in different terrain and meteorological scenarios. This data is extremely valuable for studying specific features of turbulence in complex terrains. However, most of these field campaigns and single-site studies do not address the *joint* complexity of high-density urban features over mountainous topography; moreover, all the field campaigns have been carried out in extra-tropical latitudes. In fact, the number of atmospheric boundary layer (ABL) studies focused on tropical atmospheres both from theoretical and experimental approaches remain significantly limited (e.g. Pérez Arango, 2008; Pérez Arango et al., 2011; Correa et al., 2009; Moraes et al., 2005; Martins et al., 2009; Pegahfar and Bidokhti, 2013; Nisperuza, 2015; Pegahfar and Zawar-Reza, 2017; Herrera-Mejía and Hoyos, 2019; Barman et al., 2019; Henao et al., 2020; Rendón et al., 2020), compared to the mid-latitude counterpart. Consequently, operational weather forecasts over tropical-mountainous-highly urbanized areas have multiple sources of uncertainties, higher than over high-latitude regions.

Due to its complexity regarding geomorphological configuration and demographical dynamics, not to mention the high predisposition of this particular region for several risk management related issues, the Aburrá Valley is considered a natural lab for studying the complexity of surface-atmosphere interactions and the resulting impacts on the ABL structure and dynamics. Over the Aburrá Valley, a significant proportion of extreme precipitation events originate from in-situ local convection, and there is also substantial evidence that air pollutant concentration is considerably modulated by the ABL variability (Herrera-Mejía and Hoyos, 2019; Roldán-Henao et al., 2020). Results from a field campaing study in the Aburrá Valley are not only relevant for this region but they are also expected to provide general insights on the ABL variability for urbanized complex-terrain regions. A long-term field campaign on land-atmosphere turbulent exchanges has been designed and implemented to collect relevant data to assess the variability of turbulent exchanges in a highly-urbanized, complex-terrain, low-latitude region. The main goal of the campaign is to generate long-term information on turbulent exchanges useful for addressing questions regarding the spatio-temporal variability of boundary-layer processes and the ABL in these scenarios, the implications for pollutant concentrations, the influence on local convection, the interaction of the ABL with the regional and synoptic atmospheric conditions, and also for numerical model evaluations and testing theoretical findings obtained for flat and homogeneous terrains. A better knowledge of the ABL structure and dynamics is fundamental for understanding the air pollutant dispersion in the atmosphere (Nieuwstadt and van Dop, 1982; Kastner-Klein and Rotach, 2004), the

urban meteorology (Baklanov and Mahura, 2009), and the development and evolution of deep convection.

The COmplex terrain Measurement Project for Land-atmosphere Energy eXchanges (COMPLEX) campaign started in 2018, attempting to supplement the existing set of instruments providing observations of boundary-layer processes with turbulence measurements. COMPLEX is a long-term experimental setup placed in a highly urbanized Andean valley that offers high-quality turbulence datasets to gain insights into the micrometeorological phenomena and fill in the current knowledge gap regarding exchange processes in urban-mountainous terrains. Along with other instrumentation, including in-situ meteorological gauges and ground-based remote sensors, COMPLEX aims to serve as a platform to investigate the relative contribution of the urban area and the complex topography in the resulting ABL dynamics and turbulence characteristics in the Valley. COMPLEX data also aims to serve as a framework for evaluating the applicability of the current surface-layer theories (i.e., MOST scaling), which are mostly based on the assumption of horizontally homogeneous and flat (HHF) terrain, which are still the foundation for most of the operational numerical weather prediction (NWP) models, even in complex environments.

Section 4.2 presents a detailed description of the study area, the description of the COMPLEX measurement sites, including the stations footprints, as well as the other sensors already existing in the valley. Section 4.3 presents an introductory description of meteorological features of the valley, and a preliminary assessment of the wind valley circulation, the surface energy balance in the valley, and the locally-scaled turbulence statistics.

4.2 Experimental Layout

Geographical context

The COMPLEX campaign takes place in the Aburrá Valley, a low-latitude, highly-complex mountainous terrain located in the Colombian Andean region, in the central mountain range, with an extension of 1152 km^2, being home to about four million people. Medellín, the second-largest city in Colombia, together with nine other municipalities, is

located in the Aburrá Valley. These ten municipalities, the Aburrá Valley Metropolitan Area (AVMA), represent the second-largest metropolitan area in the country in terms of population and economy. AVMA is the sixteenth Latin America's metropolitan area in terms of the total population*, but the first in terms of population density, followed by Mexico City. In fact, AVMA is the most densely populated metropolitan area among all of those located in OECD (Organisation for Economic Co-operation and Development) countries.

At the same time, the Aburrá Valley is by far the terrain with the highest topographical complexity among the largest metropolitan areas in Latin America listed before. The Aburrá Valley is characterized by a major bend between a south-to-north and a southwest-to-northeast section. The widest cross-section from ridgeline-to-ridgeline is 18.2 km, with a relatively flat section of approximately 8 km. The narrowest cross-section is around 3 km wide. The highest peak is on the western hill (at 3110 m.a.s.l), and the basin outlet is at 1290 m.a.s.l. From the turbulent exchanges point of view, the region's complexity is due to the rugged topography and the heavily urbanized area. The built-up surface expands over 340 km^2 (about 30% of the Valley's total area, and 0.55% of the state's area), with all kinds of construction types, sectorized according to per capita income levels. Fifteen or more story buildings are concentrated downtown and in the wealthiest communes †. The high population density in this geographic setting leads to several environmental concerns, including the recurrent onset of critical air quality episodes due to the high demand for fossil fuels linked to motor vehicles and industries and the limited ventilation of the valley's atmosphere to disperse pollutant emissions, and it also exacerbates climate-related risks, especially flooding and landslides.

COMPLEX sites

During the last ten years, the Aburrá Valley hydrometeorological and air-quality monitoring network has been consolidating into one of the densest and more robust in the region, with more than 900 measurement sites of several different variables. This densification responds to the climate- and environmental-related risks in the region, which are a function of the intensity and frequency of the natural hazards, and the high physical susceptibility

*After the metropolitan areas of Sao Paulo, Mexico City, Buenos Aires, Rio de Janeiro, Lima, Bogotá, Santiago, Belo Horizonte, Caracas, Guadalajara, Monterrey, Porto Alegre, Brasília, Montreal, Fortaleza, Salvador, and Recife

†Medellín's urban area is administratively subdivided into communes formed by neighborhoods

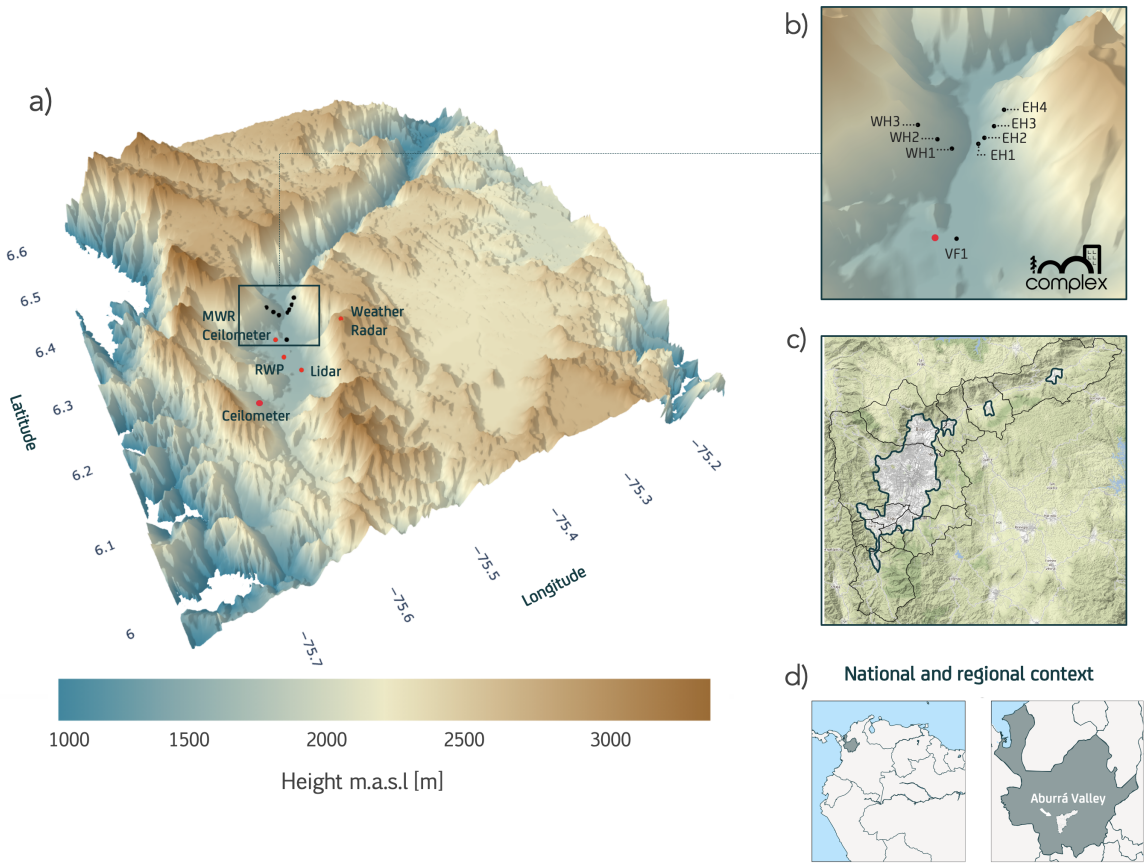

Figure 4.1: Geographical context of the Aburrá Valley. a) and b) Digital elevation model of the study area. The color scale describe, in blue to brown colors the main topographic features in the region. Black dots show the location of COMPLEX flux towers, and red dots the remote sensing equipment part of SIATA's hydrometeorological network, considered support instrumentation for COMPLEX experiment. Map c) shows the $340m^2$ extension of the urban cover in the Valley. The urban area reaches, in some locations, three-quarters of the hill-slope extension. d) Regional context of the Aburrá Valley, located in northern South America, Colombia, Department of Antioquia, north of the equator.

and social vulnerability to these hazards. The monitoring network is operated as part of the region's early warning systems SIATA (Sistema de Alerta Tempranas del Valle de Aburrá, www.siata.gov.co). SIATA is an applied science project of the region's environmental authority. SIATA is in charge of the management, analysis, and dissemination of the real-time information as well as building community resilience through education, social outreach, and emission of warnings associated with climate- and weather-related risks based on real-time hazard assessment and numerical meteorological and hydrological forecasts.

The COMPLEX campaign was designed and implemented, attempting to complement the already existing set of instruments in the Aburrá Valley for observing the boundary-layer processes at larger scales with turbulence measurements (i.e., eddy-covariance sensors). COMPLEX includes eight measurement sites deployed in a fully urbanized cross-section of the Valley (see Figure 5.1), where buildings are mainly two-to-four story residential buildings forming a relatively well-defined roof level (see Figure 4.2). The eddy-covariance sensors are placed in one of the narrowest cross-sections in the Valley, where the topography is more complex. One additional measurement site is located downtown, right in the center of the Valley's broadest sections where multiple surface types are involved, including vegetated surfaces, the river, roads, and buildings of variable heights. This particular site also allows evaluating the implications of the different topographic features inside of the Valley on the turbulent exchanges.

Figure 4.2: Images of two COMPLEX sites, (left) EH1 and (right) VF1. These photographs were taken with a camera on board an unmanned aerial vehicle during the land cover characterization process.

The eddy-covariance systems are mounted on 1.2 m cross-arms attached to triangular-section (equilateral) reinforced towers. The side of the triangular section is 40cm. The towers are installed on the rooftops of buildings that are identified as the tallest ones in the surrounding area (see Figure 4.2 for examples). The height of the towers is variable and depends on the construction and geometry of each roof (see Table S6). Each tower is equipped with an integrated 3D sonic anemometer and a CO_2/H_2O open-path gas analyzer (IRGASON) connected to a CR6 or CR1000X datalogger (both from Campbell Scientific, USA). Each site also includes lower temporal-resolution measurements from a net radiometer NR-LITE2 (Kipp & Zonen), and a multiparametric meteorological sensor

(Thiess). In the EH1 site, a CNR4 Radiometer and a SI-111-SS Infrared Radiometer Sensor (Kipp & Zonen) are also installed to allow energy balance assessments. Data transfer is accomplished via a wireless network connection (LiteBEAM 5GHZ antennas, Ubiquiti networks), enabling daily remote data-collection and real-time instrumentation monitoring. The eddy-covariance systems sample at 20 Hz rate and the raw data is stored at full resolution in 24-hour files. The data post-processing using the EddyPro® 7.0.6 (LICOR Inc.) software allows the generation of files containing 30-min turbulence statistics information.

Table S1: Basic characteristics of the measurement sites within COMPLEX campaign, as well as the main morphological parameters in the source areas (80% of the footprint). Each station name indicates the valley hillslope where it is located (East or West), and the Valley Floor (VF), and a cardinal number associated with the position on the hill starting at the Valley floor.

		Local Slope	Aspect	Altitude	Surface Characteristics			
ID	Name	(°)	(°)	(mASL)	z_S(m)	z_H(m)	d(m)	z_o(m)
EH_1	**Villa Niza**	13.49	196	1491	27	6.76	4.73	0.68
EH_2	**Villa Socorro**	14.16	183	1551	19	6.71	4.70	0.67
EH_3	**Popular**	17.70	192	1641	31	7.27	5.09	0.73
EH_4	**Candelaria**	15.80	205	1843	20	8.10	5.67	0.81
VF_1	**SENA**	4.21	152	1469	42	8.90	6.23	0.89
WH_1	**ITM**	7.43	139	1523	20	6.10	4.27	0.61
WH_2	**CASD**	5.98	132	1627	20	7.12	4.98	0.71
WH_3	**Castilla**	15.95	123	1760	22	6.83	4.78	0.68

The process of calculating the aerodynamic characteristics for each COMPLEX station follows a morphometric height-based approach. In this case, we consider that, to a first-order, the zero-plane displacement length (z_d) and the roughness length (z_o) are related to the height of the roughness elements (Grimmond and Oke, 1999) as follows,

$$\begin{aligned} z_d &= f_d * z_H \\ z_0 &= f_0 * z_H, \end{aligned} \tag{4-1}$$

where z_H is the average obstacle height in the influence zone of each station (i.e., station footprint), and f_d and f_0 are empirical coefficients derived from observations. For this study, we use $f_d = 0.7$ and $f_0 = 0.1$ following Grimmond and Oke (1999) suggestion for urban surfaces. Retrievals of z_H for each station footprint were obtained by subtracting the Digital Elevation Model (DEM) to the Digital Surface Model (DSM) at a 5.3 cm/px

resolution, obtained through photogrammetry (4056x3040 pixel resolution) using an RGB - 12 Megapixel camera aboard an unmanned aerial vehicle (DJI - Innovations Inc.). Climatological footprints were estimated following a parameterization for Flux Footprint Prediction (FFP) presented by Kljun et al. (2015) (see http://footprint.kljun.net/). The source area used for calculating z_H is the 80% of the impact area. The employed footprints correspond to the aggregation of all unstable, stable, and near-neutral cases, for the 7-month period (Jan-Jul 2020).

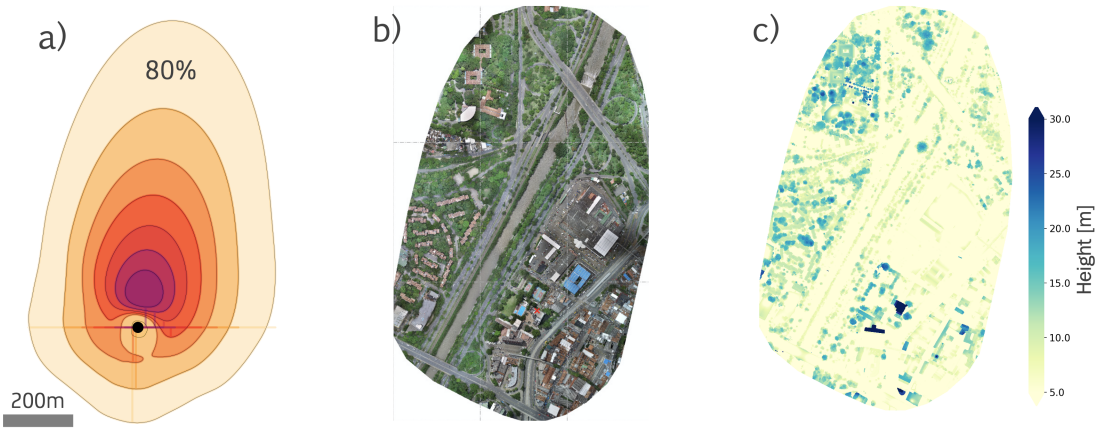

Figure 4.3: Example of the followed steps for the estimation of z_H for the Valley floor site (VF1). a) 6-month climatological footprint estimated using the Flux Footprint Prediction model of Kljun et al. (2015). Each contour of the turbulent flux footprint indicates 10, 20, ..., 80% flux of the contributing source area. b) RGB image of the source area. c) Map of elevated structures in the flux tower source area, obtained through photogrammetry using a camera aboard an unmanned aerial vehicle. The resulting average obstacle height for VF1 footprint $z_H = 8.9$ m

Considering that the depth of the roughness sublayer is typically assumed to be 2–5 times the mean obstacle height (Raupach et al., 1991), it is reasonable to conclude that the measurements in the COMPLEX stations are made in the inertial sublayer (see Table S6). Measurements of turbulence properties should be conducted within the inertial sublayer to obtain results that are fully representative of turbulent fluxes over the underlying urban surface(Zou et al., 2018).

Long-term in-situ and remote sensing observations

As mentioned before, COMPLEX was designed and implemented to complement the already existing robust hydrometeorological monitoring network operated by SIATA (see Table S2), useful for supporting risk and environmental management operations. All

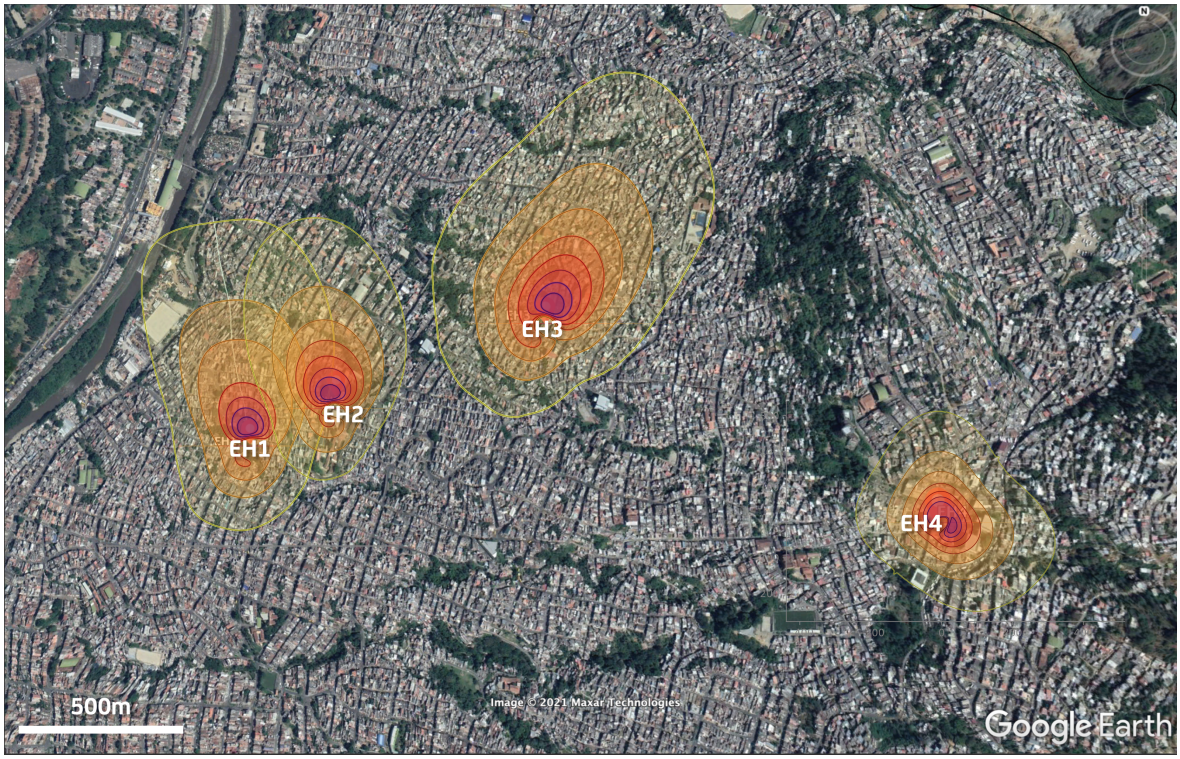

Figure 4.4: Google Maps image (Image©2021 Maxar Tecnologies) of the area surrounding the COMPLEX campaign (Eastern hillslope). The contours indicate the climatological footprint for each flux tower, respectively, estimated using the Flux Footprint Prediction model of Kljun et al. (2015), based on seven months of data from January - July 2020

the data generated by SIATA is also used for applied research processes. Precipitation in the Valley is measured (and transmitted in real-time) via multiple types of sensors. The primary source of precipitation information is a 350-kW C-band polarimetric and doppler weather radar. In-situ precipitation measurements include a dense tipping-bucket network, several multiparametric automatic weather stations, which also measure other meteorological parameters such as temperature, humidity, pressure, and winds, and a network of in situ disdrometers (Table S2).

The ABL structure and variability in the Valley are closely linked to the development of extreme precipitation events and to the pollutant concentration in the surface layer, thus representing a major concern for local risk management and environmental authorities. Vertical profiles from diverse ground-based remote sensing instruments, including a Microwave Radiometer (MWR), a Radar Wind Profiler (RWP), three lidar Ceilometers, and a scanning Lidar, are used operationally for monitoring the ABL dynamics.

Ceilometers. SIATA routinely operates three Vaisala CL51 ceilometers to obtain

Figure 4.5: Same as 4.4 but for West Slope stations

high-resolution vertical profiles of the lower-troposphere structure based on the backscatter intensity from aerosols. CL51 ceilometers work at the 910 nm wavelength and emit a laser signal every 67 ns, providing backscattering attenuated coefficient measurements with a vertical resolution of 10m and temporal resolution of 16 s. ABL height estimates are available operationally with a 30 min resolution (see Chapter 2 for details).

Microwave radiometer. MWRs measure the radiation emitted by atmospheric gases at submillimeter-to-centimeter wavelengths and are useful for retrieving the thermodynamic state of the atmosphere at different levels, allowing the assessment of atmospheric stability in real time. The Aburrá Valley MWR provides continuous retrievals of temperature, relative humidity, and liquid water up to a height of 10 km above the surface under nearly all weather conditions. The MWR is located at the top of the SIATA main operations center on the valley floor, approximately 60m from the surface, and it provides vertical profiles with variable spatial resolution: 50 m from the surface to 500 m, 100 m up to 2 km, and 250 m up to 10 km.

Wind Profiler. Doppler radars used for vertical wind profiling rely on refractive index variations caused by changes in humidity, temperature, and pressure. The Aburrá Valley wind profiler (see Figure 5.1) works at a nominal frequency of 1290 MHz, reaching

Table S2: List of complementary in-situ and remote sensing instruments of the COMPLEX experiment.

	Number	Reference	Manufacturer	Res.	First Record *
Multiparametric	30	4.920x.00.00x	Thiess	5min	2010-01-01
	12	WXT 520	Vaisala	5min	2013-08-01
Tipping-buckets	139	6464	Davis	1min	2011-03-12
Air Quality	31	BAM1020/22	MetOne	1h	2007-08-01
	7	200E	Teledyne	1min	2012-04-01
	9	400E	Teledyne-Thermo	1min	2012-06-04
	2	T300/48C	Teledyne-Thermo	1min	2008-03-01
	1	100E	Teledyne	1min	2014-02-01
Lidar Ceilometers	3	CL-51	Vaisala	10sec	2014-10-01
Scanning Lidar	1	LR101-ESS-D200	Raymetrics	5min	2018-06-08
MWR	1	MP-3000A	Radiometrics	2min	2013-01-01
RWP	1	Raptor VAD-BL	DeTect Inc.	5min	2015-01-01
Weather Radar	1	-	EEC	5min	2012-01-02

* The date corresponds to the earliest record

up to 8 km above the surface under high humidity conditions (Lau et al., 2013). The RWP is designed to measure the wind profile in different operation modes that differ in their vertical resolution and in the atmospheric height range. In our case, we use two overlapping modes: in the higher resolution mode (60 m), the RWP measures the wind profile from 77 to 3500 m, and in the lower resolution mode (72 m) from 2500 to 8000 m.

Scanning aerosol Lidar. SIATA operates a Raymetrics elastic lidar, an active remote sensing instrument using a 1064 nm Nd:YAG laser with a 20 Hz pulse repetition rate, with a 30 mJ energy per pulse. The laser frequency is tripled to generate pulses at 355 nm wavelength. The pulse duration in the order of 6 to 9ns, obtaining a spatial resolution up to 3.5 m, sensing up to 10-15 km. The system is equipped with a receiving telescope and a wavelength separation unit which enables incoming beam separation into parallel and orthogonal polarization. This polarization separation allows the particle identification according to the orthogonal to parallel ratio.

Finally, the criteria pollutants defined by the United States Environmental Protection Agency (EPA), except for lead, are routinely monitored by SIATA. The air quality monitoring is conducted using reference and equivalent measurement methods. The SIATA

monitoring network also includes a hydrological component not described here.

4.3 Valley meteorology and preliminary findings

Evolution of key meteorological parameters in a Tropical urbanized valley

The absence of a marked top-of-the-atmosphere radiation and surface air temperature seasonality in low-latitudes does not imply an irrelevant influence of the seasonal cycle on the evolution of the ABL. In the tropics, the latitudinal migration of the Intertropical Convergence Zone (ITCZ) (e.g., Schneider et al., 2014) imposes a large scale forcing on the local cloudiness, precipitation, and surface incident radiation, thus modulating the atmospheric stability and the exchange processes between the valley boundary layer and the free troposphere.

The daily mean temperature in the Aburrá Valley typically ranges from 18°C to 26°C throughout the year. Figure 4.6 presents evidence of the seasonally-induced local variability associated with the ITCZ seasonal cloud forcing. Figure 4.6a shows the monthly diurnal cycle of the vertical gradient of virtual potential temperature, θ_v, at the lower troposphere ($d\theta_v/dz$) computed using the thermodynamic profiles retrieved by the MWR. In particular, the Figure shows $\Delta_{200}\theta_v$ ($\theta_v(1200\,m\,agl) - \theta_v(50\,m\,agl)$), as a proxy for near-surface atmospheric stability. Positive values of $\Delta_{200}\theta_v$ are associated with near-surface stability, while negative values indicate instability. The most salient features in the Figure are the predominant stability conditions around March, which lead to the onset of critical air-quality episodes (Herrera-Mejía and Hoyos, 2019), and the marked close-to-symmetric diurnal cycle, with a maximum around noon.

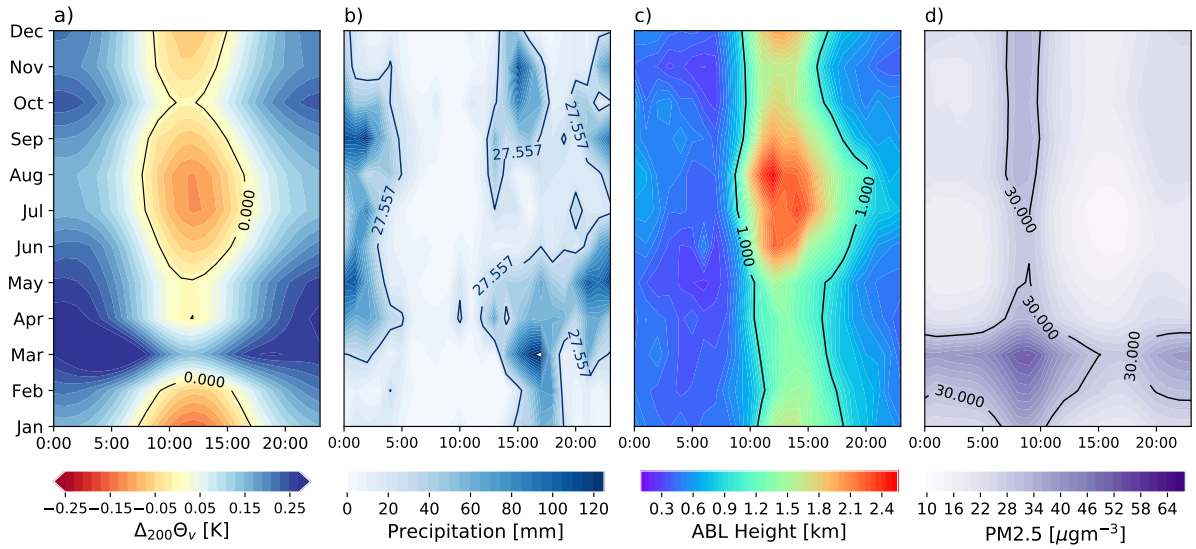

Figure 4.6: Monthly daily cycles of a) $\Delta_{200}\theta_v$ a near-surface stability proxy, b) Precipitation measured at the valley floor, c) ABL height at the base of the valley estimated using the multisensor Richardson number and d) PM2.5 concentration measured also at the valley floor.

Overall, precipitation in the region exhibits a bimodal pattern (Figure 4.6b), with peaks in the periods between April-May and October-November also modulated, from a climate perspective, by the migration of the ITCZ (Poveda, 2004; Poveda et al., 2006). On the other hand, throughout the year, the daily cycle exhibits a marked cycle of occurrence of daytime vs. nighttime rainfall events, with wet seasons characterized by substantial nighttime (20:00-5:00 UTC-5) stratiform precipitation and daytime (13:00-18:00 UTC-5) convective precipitation events. The convective events are intense and short-lived (30-50 minute), and stratiform events are low-intensity and long-lived. However, and unlike the near-surface stability proxy, the shape of the diurnal cycle changes from month to month. From January to March, precipitation occurs predominantly during the daytime; from April to September, the peak in precipitation occurs during nighttime, and from October to December, the precipitation is truly bimodal.

The monthly diurnal cycles of the valley's boundary layer height (at the valley floor) are shown in Figure 4.6c. The boundary layer height was estimated using a multisensor technique based on the bulk Richardson number (see Chapter 2 for detailed information). During the entire year, the maximum average mixed layer height, ∼1310 m agl, is reached between 12:00 and 13:00 LT, exceeding the average valley crest height. Considering the day-to-day variability, the maximum mixed layer thickness exceeds the average depth of the valley in 75% of the days (Herrera-Mejía and Hoyos, 2019). The evolution of the

ABL height presents evidence of significant differences in magnitude among the different months but a similar diurnal cycle. The highest depth of the ABL occurs 12:00 to 13:00 UTC-5 and the lowest around 05:00-06:00 UTC-5. The deepest ABL occurs between July and October, and the thinnest around March.

In general, atmospheric stability and a thin ABL restrict the rise of pollutants from the surface and over the valley's crest (where they can be advected away by the trade winds), leading to pollutant accumulation within the valley's atmosphere in association with anthropogenic emissions. As a result of the contrasting effects of nighttime and daytime precipitation on the aerosol concentration due to net effect of pollutant scavenging and atmospheric stabilization, the month-to-month variability of the diurnal cycle of precipitation also modulates the air quality in the region, partly determining the likelihood of occurrence of critical air quality episodes (Roldán-Henao et al., 2020). The daytime precipitation leads to atmospheric stabilization, hence decreasing the occurrence of vertical updrafts. Figure 4.6d presents evidence of a strong link between the valley boundary-layer height, the location of a precipitation event in the daily cycle, and the resulting pollutant concentration close to the valley surface (Roldán-Henao et al., 2020). Figure 4.6d presents the monthly diurnal cycle of PM2.5, showing higher concentrations during March, and around 07:00 to 08:00 UTC-5. Months with a shallow ABL height and limited nighttime rainfall (i.e., March) result in PM2.5 concentration peaks, reaching in some cases unhealthy Air Quality Indexes (AQI) according to EPA regulations (PM2.5 concentrations exceeding $55\mu gm^{-3}$). However, months with similar (low) boundary layer heights but enhanced nighttime precipitation events (i.e., October), are favored by the bellow cloud scavenging, resulting in a positive precipitation net effect, with low aerosol load in the valley atmosphere.

Assessment of the valley-wind system in an Andean urbanized valley

A better understanding of the diurnal evolution of mountain winds systems in general, and that for specific urbanized valleys, is crucial for several important social applications, including urban planning in mountainous regions. The spatio-temporal variability of air pollutant concentration is strongly tied to the valley circulation. The operations of cable-propelled transit systems that are being integrated more often in the last two decades as a form of urban mass transit in mountainous metropolitan areas demand a

detailed understanding of the diurnal evolution of mountain winds. The trend of using cable-propelled systems as urban mass transportation started in the Aburrá Valley and has now been implemented in several cities in countries like Venezuela, Algeria, Brazil, Austria, and others (Heinrichs and Bernet, 2014; Tischler and Mailer, 2019). An accurate representation and simulation of the diurnal evolution of mountain winds is also crucial for skillful weather forecasting in mountain areas. In metropolitan areas, these forecasts are needed, among others, for risk management purposes.

The general structure of the winds in mountainous areas under fair weather includes upslope, up-valley, and plain-to-mountain flows during the daytime, and down-valley and mountain-to-plain flows during nighttime (e.g. Whiteman, 2000; Zardi and Whiteman, 2013). The evolution of mountain winds is modulated by the differential heating of the atmosphere that lead to pressure differences, generating thermally-driven winds (Whiteman, 2000). The diurnal reversal of the slope, valley, and mountain-plain wind systems is a very robust and prevalent feature in most valleys in different latitudes. However, the combination of densely urbanized cities settled in complex-terrain valleys, diverse terrain configurations, and valley alignment, constitutes a challenge when attempting to generalize the main features of wind valley circulations.

The Aburrá Valley appears to be an exception to the rule regarding a marked reversal of slope and valley winds. Figure 4.7 presents wind roses for each of the complex stations showing the diurnal cycle of wind direction. The wind direction at the eastern slope stations shows a predominantly northerly wind during the entire day at stations EH1 and EH2. These two stations are the closest to the axis of the valley. Station EH3 shows evidence of an incipient slope wind reversal combined with the northerly flow seen at EH1 and EH2. At station EH3, during daytime (nighttime), the wind blows predominantly from the northwest (northeast). Station EH4, the highest and farthest from the valley axis, shows a marked diurnal wind reversal. At station EH4, during daytime (nighttime), the wind blows predominantly from the northwest (southeast). At the western slope, the wind direction at stations WH1, and WH3, do not show a marked wind reversal; rather, they exhibit a predominantly northeasterly flow. Similarly, the COMPLEX station at the valley floor VF1, shows predominant winds from the north during the entire diurnal cycle.

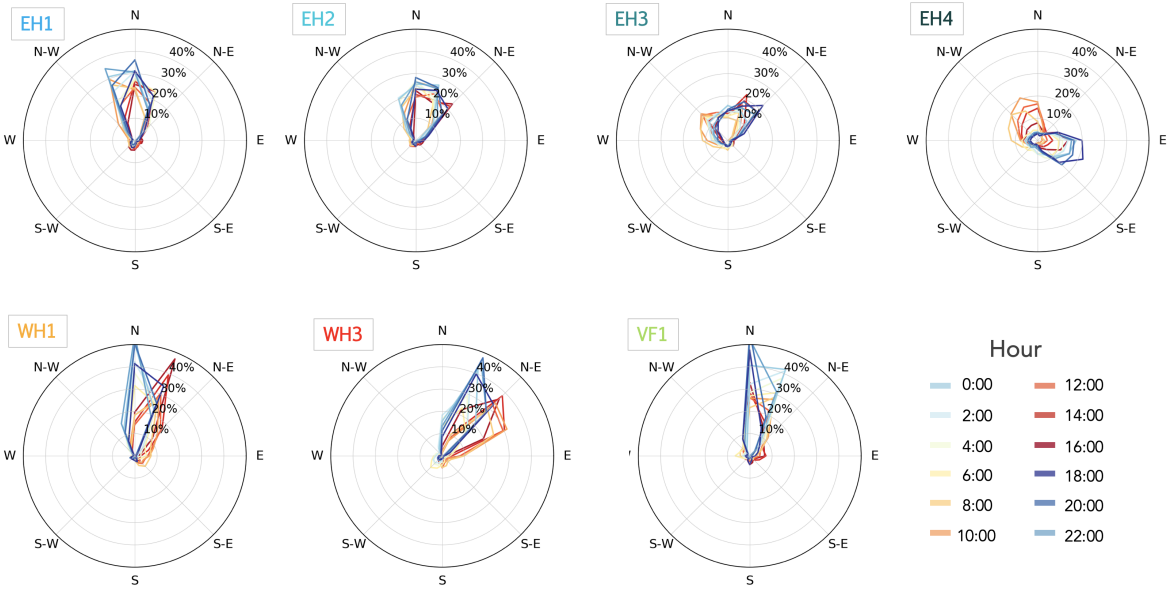

Figure 4.7: Wind roses for each of the COMPLEX stations showing the diurnal cycle of wind direction. Each color corresponds to a different hour of the day.

Evidence from other weather stations in the valley also point to an intricate structure of the wind circulation. Figure 4.8 shows the spatial distribution of all the automatic weather stations available in the Aburrá Valley, and the diurnal cycle of the wind direction in selected stations. The stations are selected to illustrate some of the interesting features in the thermally-driven flows. Only one of the stations on the valley floor, the southernmost station, shows a marked day-night reversal of the wind aligned with the valley axis. The northernmost valley floor station in the Figure shows an evident influence of an isolated 82 m high hill (*El Volador hill*) located to the northwest of the station and near the valley's axis. The hill alters the thermally-driven flow observed at the station, which features northerly and downhill winds during the night and uphill winds during the day. The evidence suggests that the presence of the 82 m hill completely offsets the valley circulation at the station.

The wind roses of the stations at the western and eastern hills of the valley also suggest a more dominant role of the sub-basins in controlling the thermal features that modulate the predominant wind direction over those thermal effects of the larger Aburrá Valley. The westernmost station in the Figure, installed in the southern hill of the Santa Elena creek basin, shows a clear daytime-nighttime uphill-downhill southward-northward wind reversal, suggesting a very limited role of the Aburrá Valley in driving the wind direction. Different from the station on the Santa Elena sub-basin, one of the largest within the

Aburrá Valley, the stations on the western hill are installed on smaller sub-basins; however, the evidence still shows a dominant role of the sub-basins in determining the thermal structure around the stations.

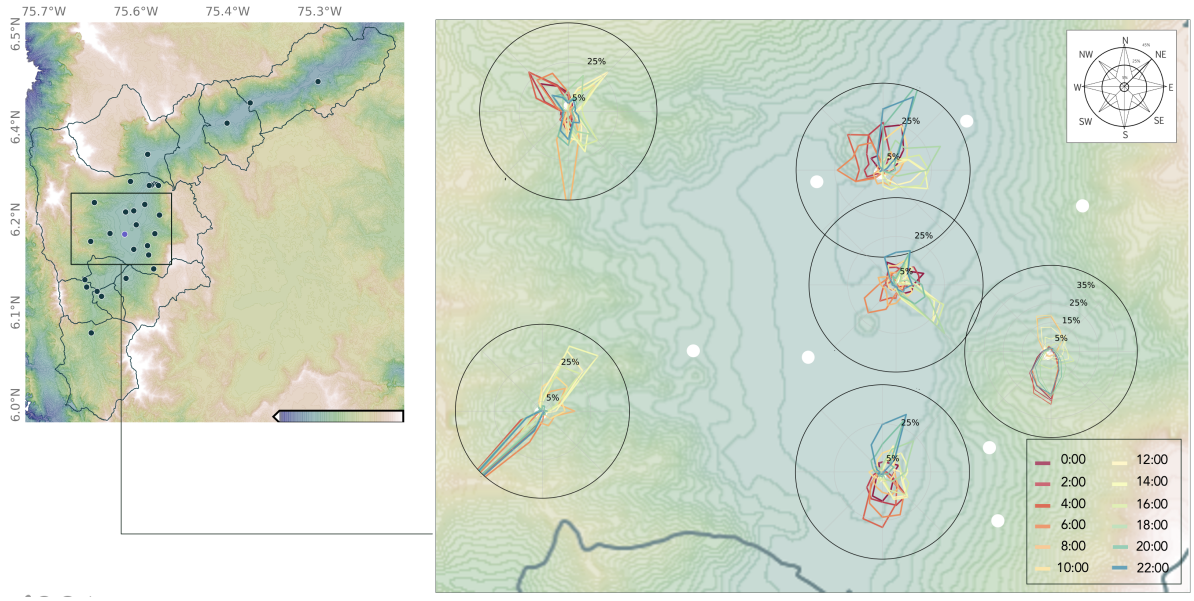

Figure 4.8: The left panel shows the spatial distribution of all the automatic weather stations available in the Aburrá Valley. The right panel shows wind roses in selected slope and valley floor weather stations, showing the diurnal cycle of wind direction. Each color corresponds to a different hour of the day.

The wind direction observations from the COMPLEX stations and the weather stations network suggest that the overall geomorphology of the valley, with its changes from wide to narrow, to wide sections, modulating changes in wind speed, together with the intra-valley topographic features and the many sub-basins ("mini-valleys"), and the heterogeneity of the urban surface in terms of obstacles and thermal properties, alter the structure of the expected thermal winds. These facts represent at the same time a challenge for the complete understanding of the wind circulation in the Aburrá Valley, but also an opportunity for urban meteorology modelers to use the COMPLEX dataset for testing and improving the representation of important physical processes or mechanisms in the state-of-the-art urban models for their use in real-word scenarios.

Surface energy balance on an urbanized cross-section of a tropical Valley

Knowledge of the surface energy balance is considered fundamental for a a better understanding of the boundary layer meteorology and climatology of any site (Oke, 1988). Anthropic modifications to the environment have led to significant alterations to the energy balance; thus, surface energy fluxes (and CO_2 fluxes) of an urban environment differ significantly from those of surrounding rural areas (Roth et al., 2017), resulting in important modifications of the global energy balance. COMPLEX, a campaign not only deployed in an urban environment but in a topographically complex surface (which also has repercussions on the energy balance), represents a unique opportunity for assessing the relative contributions of both environments in the energy (and CO_2) budgets, and to contribute to the understanding of current open issues such as the energy balance closure.

Here, given the current lack of measurements (and modeling experiments) to resolve the other balance components in 6 out of 7 sites during the evaluated period, we only assess the variability of three of the components of the surface energy balance: the net radiation (Q^*), the sensible heat flux Q_H, and the latent heat flux Q_{LE} as a function of the different land cover fractions and slope location. A total of 12 months of data (2020-01-01 to 2020-12-31) are used to calculate the diurnal cycles for the aforementioned balance components for the COMPLEX sites. The results are presented in Figure 4.9, together with the land cover fraction for each station.

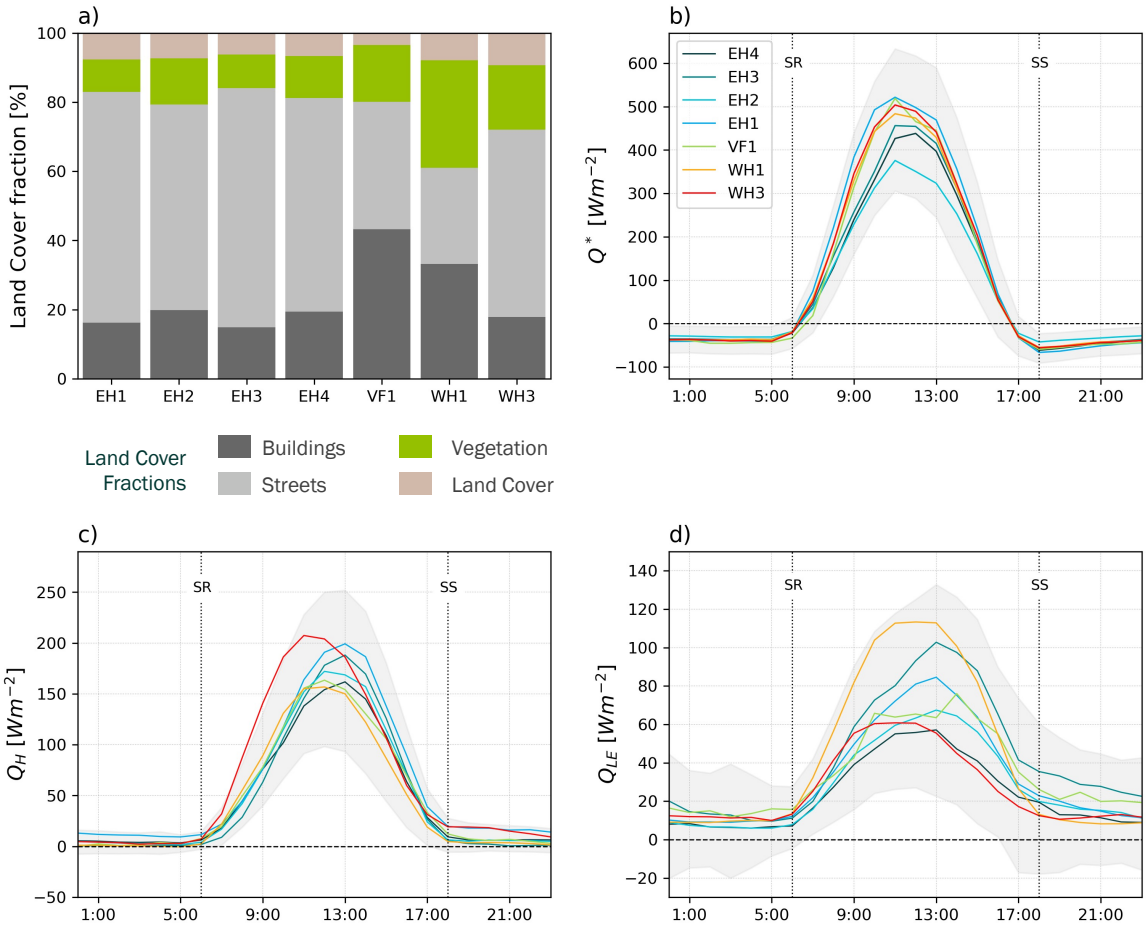

Figure 4.9: a) Land cover fractions within the 80% of the footprint for each COMPLEX site. Mean daily cycles of b) net all-wave radiation, c) sensible heat , d) latent heat, for each COMPLEX station during study period (January-December 2020). Grey shaded areas are ±1 standard deviation. SR and SS indicate Sunrise and Sunset respectively

The surface morphological properties on the source areas of each COMPLEX site exhibit a dominant presence of impervious areas ('gray surfaces'), ranging from 60% to 85% of the footprint for each tower (Figure 4.9a). This percentage remains almost constant for the stations at the east-hillslope and the Valley floor; meanwhile, for the west-hillslope towers, the proportion of vegetated area increases up to 27% and 39% in stations WH3 and WH1 respectively, which has a clear impact on the energy balance characteristics from site to site and on the overall energy structure of the valley.

Net radiation Q^* in the Aburrá Valley (Figure 4.9b) peaks around solar noon and turn positive (negative) about half an hour after (before) sunrise (sunset). The magnitude of the Q^* peak ranges between $380 Wm^{-2}$ at EH2 and $530 Wm^{-2}$ at EH1 with a long-term

average for all sites of $471 W m^{-2}$. At night Q^* varies between -200 and -10$W m^{-2}$. These values are similar to those obtained by Roth (2007) who summarized some (sub)tropical cities (12°N and 32°N) and reported values ranging from 400 to 600$W m^{-2}$ based on short-term measurements. Moreover, they agree with results from a more recent study, where Roth et al. (2017) analyzed the multi-seasonal variability of ∼7 years of data over a residential neighbourhood of Singapore.

Regarding the Q_H diurnal variation (Figure 4.9c), cycles peak around solar noon, the western hill stations and the valley floor station peak at 11:00-12:00 LT, meanwhile the eastern hill stations tend towards a peak at 13:00 LT. There exist a significant difference between WH3 and the other six flux towers cycles, with WH3 ascending faster and more than the rest. The magnitude of Q_H at night strongly depends on the characteristics of the land cover, particularly on the relative amount of impervious surface area versus the available vegetation in the footprint of the measurement point. The high urban density of COMPLEX sites prevent Q_H from becoming negative (with the exception of WH1 site with the largest fraction of green area), even after the net radiation changes direction in the evening. As a consequence, the nocturnal atmosphere in the urban environment remains unstable (although close to near-neutral) as a result of the release of the stored heat and the anthropogenic component input. This represents a characteristic feature of urban environment found in several similar studies (e.g., Roth et al., 2017).

The temporal variability of Q_{LE} is similar to that of other cities with peak values observed close to solar noon. This time, the magnitude of WH1 station peak is significantly larger than for the other sites, responding to the amount of vegetation in the source area of the station, and demonstrating the influence of available energy in driving evapotranspiration. Similar to other suburban sites Q_{LE} remains above zero during nighttime.

Locally-Scaled turbulence integral statistics

Turbulence intensity

Turbulence intensity is defined as $I_i = \sigma_i / U$, with $i = u, v, w$, and it is function of the Reynolds stresses and the mean velocity profile of the flow. It represents the intensity of wind velocity fluctuation. I_i depends on the height of observation, the surface roughness, and stability (Roth, 2000). In an urban environment, given the surface's characteristic

roughness, I_i could be up to twice as much as the corresponding rural reference value. This behavior is not necessarily a result of increasing σ_i, but due to retardation of the flow close to the urban canopy. σ_i will vary randomly due to the strongly sheared wind profile.

Figure 4.10 presents the variability of I_i for neutral conditions ($|\zeta| \leq 0.01$) for COMPLEX sites, plotted with the correspondent empirical fits found by Roth (2000) based in 9 urban high quality experiments. Although the variability of I_i with the non-dimensional height Z_s/Z_H follows the expected exponentially decreasing shape, with the highest value and increased variability closer to the canopy top (i.e., $Z_s/Z_H = 1$), I_i values are significantly larger than the reference curve. For the COMPLEX campaign, this could suggest that the mean flow U is actually lower than for a 'typical' urban area placed on a flat terrain by the action of the complex topography.

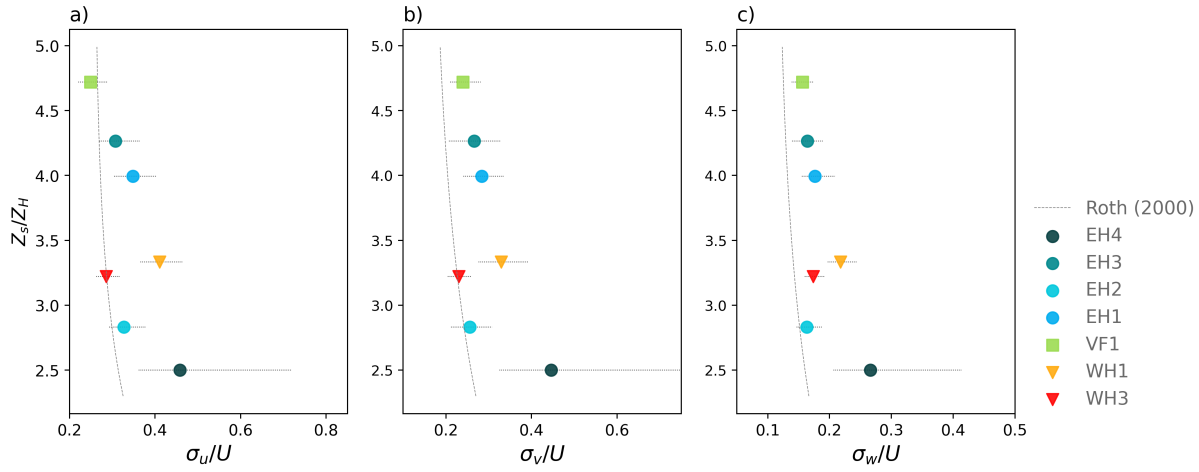

Figure 4.10: Variation of a) σ_u/U, b) σ_v/U and c) σ_w/U for neutral conditions with non-dimensional heights z_s/z_H. Horizontal black-dashed lines represent the IQR for each station (-height). Grey dashed line correspond to empirical fits found by Roth (2000) based in 9 urban high quality experiments

Wind speed close to the surface in the valley does not exceed 1-2 ms^{-1}, this reduced ventilation also has significant consequences for the horizontal dispersion of atmospheric pollutants at the valley floor. The effect of the horizontal advection in the valley could be considered negligible compared to the removal potential of the thermodynamically driven vertical dispersion processes and the wash-out effect of the nighttime precipitation events (Roldán-Henao et al., 2020).

Locally-scaled turbulence statistics

One of the current interests in boundary-layer research and thus, one of the main goals of the COMPLEX campaign, is to evaluate the performance of current theoretical frameworks, particularly the Monin Obukhov Similarity Theory (MOST, Monin and Obukhov (1954)), over complex-far from 'ideal' surfaces, being the case for urban environments and mountainous terrains. MOST was never intended to be extrapolated to highly inhomogeneous surface layers where its basic principles are largely violated (e.g., constant turbulent fluxes in the vertical). However, in the absence of any other suitable conceptual approach to be used in complex terrain, it should be determined how far we are from obtaining a set of universal functions and representing turbulence characteristics of these types of underlying surfaces based on this scaling approach. Besides, it is imperative to analyze whether or not some unrecognized processes can contribute to the small-scale variability in complex terrain, which can complement the available list of key variables (see Stull (1988)) and lead to successful scaling. As the first step towards that direction, *Local Scaling* has emerged in order to better understand turbulence characteristics in complex terrain Nieuwstadt (1984). Under this approach, the parameters in the similarity functions are assumed to be 'localized', linked to their respective measurement height z. Several previous studies have presented turbulence statistics of complex terrain under the local scaling framework, (e.g., Nadeau et al., 2013; Rotach et al., 2017; Sfyri et al., 2018; Stiperski and Calaf, 2018) and have demonstrated the successful application of it.

Figure 4.11 shows the non-dimensional standard deviations of vertical velocity as a function of local stability $\sigma_w/u_{*l} = \Phi_m(\zeta)$ for unstable stratification, for a station in the East Hill-slope, EH3, COMPLEX site with the largest terrain slope. ζ represents the local stability parameter ($\zeta = z/\Lambda$), and Λ is defined as the local Obukhov length ($\Lambda = -\frac{1}{k}\frac{u_{*l}^3}{\overline{w'\theta'_l}}\left(\frac{g}{\theta_v}\right)^{-1}$). Subscript l denotes localized mean variables, as in the case for u_{*l}, the local friction velocity. As reference, in Figure 4.11a we plot three scaling curves representing three different surface types, the classical HHF curve reference purposed by Panofsky and Dutton (1984) (solid-black line). The black dashed line represents the best-fit curve for a station in the Swiss Alps, based on data over a highly-complex mountainous terrain (30°–41°), found by Nadeau et al. (2013); finally, for the urban reference (dotted black line), we use a scaling relationship found by Zou et al. (2018) for one sensor at $z = 3.4Z_H$ level over an urban canopy in Changzhou, China.

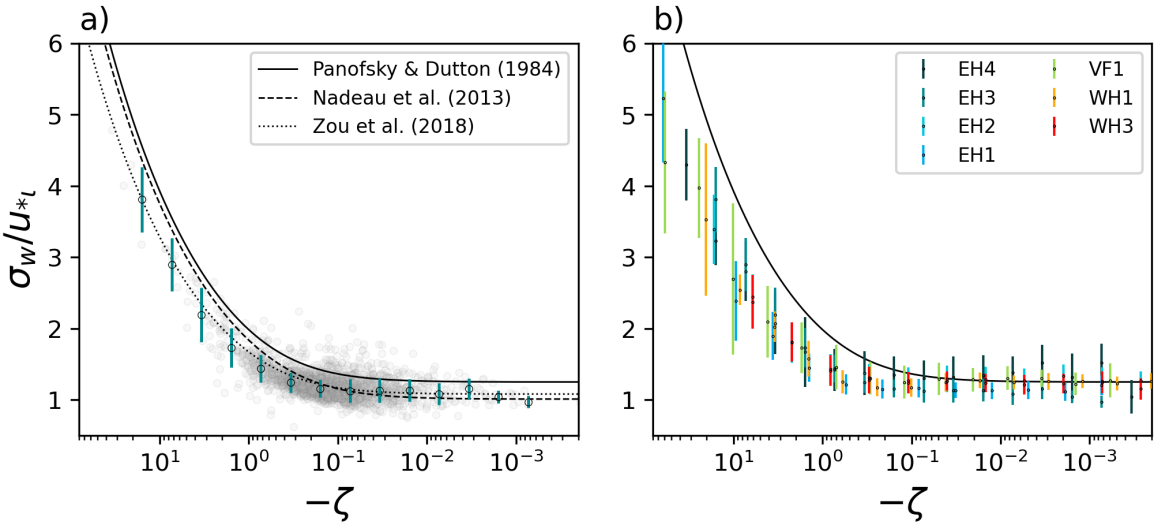

Figure 4.11: Scaled standard deviation of vertical wind velocity as a function of local stability for unstable stratification from (a) site EH3, for an 7-month period between Jan- Jul 2020 (gray circles), and (b) binned averages from all COMPLEX sites. Error bars represent the standard deviation of all data points falling into this bin. For comparison, black line represents the reference curve for HHF terrain (Panofsky and Dutton, 1984), the black-dashed line shows the best-fit curve for mountainous complex terrain (Nadeau et al., 2013), and black-dotted line the best-fit curve for an urban surface given by Zou et al. (2018)

The scatter of the individual data points of the normalized vertical velocity is considerably lower than for the horizontal components u and v (not shown), and they suggest some degree of local scaling. The 1/3 power law (predicted by theoretical considerations) function seems to reasonably describe the relationship between σ_w/u_{*l} and ζ in the free convection limit (Garratt, 1992) for all COMPLEX stations. However, the magnitude of Φ_w data points appear to be lower than the HHF reference suggested by Panofsky and Dutton (1984), particularly for strong unstable stratification, closely following the urban reference from Zou et al. (2018). This validates previous results from studies above urban surfaces (e.g., Rotach, 1993; Feigenwinter et al., 1999; Quan and Hu, 2009; Wood et al., 2010; Fortuniak et al., 2013). The data show a slight increase of σ_w/u_{*l} within the near-neutral regime, then the values decrease with increasing instability, resulting in a minimum value around $-0.5 \leq \zeta \leq -0.1$ for all the stations. This phenomenon has been reported previously in some studies over urban surfaces (e.g., Feigenwinter et al., 1999; Roth, 2000; Christen, 2005; Zou et al., 2018). Apparently, this behavior can only be found in urban environments; however, the reason remains unclear.

From bin averages in Figure 4.11b, it is not clear that any relationship exist between the dependence of Φ_w on ζ with any particular (-evident) feature or complexity induced by the terrain, such as slope or distance to the valley floor, neither of any characteristic of the surface roughness. As a first tentative conclusion we may highlight the potential of the local similarity approach for describing the standard deviation of wind velocity components.

4.4 Outlook

The COmplex terrain Measurement Project for Land-atmosphere Energy eXchanges (COMPLEX) is a unique long-term field experiment in the Aburrá Valley, a natural low-latitude laboratory to study the interaction of the influences associated with the urban landscape and the complex terrain on the valley circulation and on the energy exchanges between the surface and the atmosphere. Long-term observations of the variability of turbulent exchanges on tropical latitude are rare, and for that reason constitutes a very valuable tool for the atmospheric community not only to test the validity of similarity-based theories but also to develop new and modern parameterizations of turbulent fluxes in urban and complex-terrain settings.

Chapter 5

Observed turbulence characteristics in a highly urbanized Andean valley. The Aburrá Valley Case Study

Laura Herrera-Mejía[1], **Carlos D. Hoyos**[1], **Mathias W. Rotach**[2]

[1] *Universidad Nacional de Colombia, Sede Medellín, Facultad de Minas, Departamento de Geociencias y Medio Ambiente*

[2] *Department of Atmospheric and Cryospheric Sciences, University of Innsbruck, Austria*

5.1 Introduction

Most of our understanding of the behavior and structure of the Atmospheric Boundary Layer (ABL) relies on similarity theory, a useful theoretical tool where, based on the principle that boundary layer observations frequently show consistent and repeatable characteristics, only a few non-dimensional parameters are required to understand and estimate the main turbulence properties (Stull, 1988). The empirical relationships developed under a scaling method seek to be universal functions, and they represent a powerful tool when describing or comparing turbulence characteristics between sites. However, the similarity scaling is based on assumptions of statistically stationary turbulence over horizontally uniform surface layer (canonical surface layer), which are rarely met in the 'real world' (Nordbo et al., 2013; Schmutz and Vogt, 2019). The Monin–Obukhov similarity theory (MOST) (Monin and Obukhov, 1954) was developed under assumptions that include horizontally homogeneous and flat terrains, constant fluxes with height in the surface layer, and quasi-stationary turbulence. MOST never meant to be extrapolated

to heterogeneous and non-flat surfaces, where those basic principles are largely violated (Stiperski et al., 2019). However, the lack of any other conceptual framework has thus far led to this theory being employed in weather prediction and climate models over all types of terrains, including urban areas, to infer turbulent fluxes from mean meteorological variables. It also remains the most used and widely accepted similarity scaling theory for the atmospheric surface layer (Foken, 2006). The discussion has recently focused on whether or not MOST can be a suitable framework for surfaces characterized by being far from ideal, where similarity relationships become severely challenged (Stiperski et al., 2019).

The first experimental attempts to evaluate MOST were conducted over flat, homogeneous terrains, where its fundamental assumptions could be assumed mostly valid (e.g. Wyngaard et al., 1971; Panofsky and Dutton, 1984). Acknowledging the fundamental limitations of MOST when dealing with non-ideal surfaces, which can induce spatial and temporal perturbations to the atmospheric flow, and also the importance of an accurate numerical representation of surface-layer turbulence in numerical weather prediction and air pollution modeling (Baklanov and Grisogono, 2006), several recent studies have attempted to validate the turbulence scaling functions in complex surfaces, such as mountainous terrains (e.g., Martins et al., 2009; de Franceschi et al., 2009; Nadeau et al., 2013; Babić et al., 2016a,b; Rotach et al., 2017; Sfyri et al., 2018; Stiperski and Calaf, 2018; Stiperski et al., 2019), and urban environments (e.g., Roth and Oke, 1993; Roth, 2000; Al-Jiboori et al., 2002; Wood et al., 2010; Fortuniak et al., 2013; Pegahfar and Bidokhti, 2013; Pegahfar and Zawar-Reza, 2017; Zou et al., 2018). However, describing and modeling the behavior of winds and turbulence over a complex terrain still remains a challenging issue in the atmospheric boundary layer research. Under these conditions, the hypothesis of equilibrium between surface and the local fluxes cannot be assumed to be true apriori given the presence of large rough elements and thermal inhomogeneities. Consequently, surface fluxes cannot be considered scaling parameters within the whole domain of the surface layer.

Local similarity has then emerged as the first step towards a better understanding of turbulence characteristics in non-ideal surfaces (Nieuwstadt, 1984). Under this approach, the variables in the similarity functions are assumed to be 'localized,' and linked to their respective measurement height z, which renders the flow dynamically similar everywhere or locally invariant (Roth, 2000). As a result, the scaling relations coefficients may change, but not their original form of the scaling equations (Sfyri et al., 2018). In the local

similarity framework, z is a vital parameter (Nadeau et al., 2013).

Local scaling initially arises from the need to study turbulent properties on measurement sites above the surface layer, which is the case of the pioneering work of Nieuwstadt (1984) in the stable boundary layer. From that, some studies have successfully applied local scaling over non-ideal surfaces. Roth (2000) made a comprehensive review of turbulence observations over urban areas, including results of more than fifty different studies *, demonstrating that it was a useful approach to study the physical properties of urban boundary-layer flows. During the last couple of decades, some studies have also validated the local scaling approach over urban surfaces, which is the case of Al-Jiboori et al. (2002) with observations from a 325 m meteorological mast in Beijing, China, and Wood et al. (2010) with turbulence measurements from an eddy-covariance system at 190 m above the city of London, UK. Pegahfar and Bidokhti (2013), and Pegahfar and Zawar-Reza (2017), to our knowledge, are the only studies that have addressed the complexity of the urban surface in mountainous terrain, working with data from a three-level measurement tower in Tehran, Iran.

The applicability of MOST over what is considered a complex surface is still an open issue due to many difficulties when applying traditional scaling rules; this represents a significant step back when aiming to evaluate and improve numerical weather prediction over these types of terrain. The aim of this study is to test the applicability of the local scaling framework in the surface layer over an urban-mountainous terrain using several one-level observations from a cross-section in a Tropical Andean Valley. We investigate the applicability of flux–variance relationships for wind velocity components, scalars (temperature and humidity), and Turbulent Kinetic Energy (TKE) dissipation rate. Our results are compared with previous results in the literature.

5.2 Theoretical Background

MOST establishes that the structure and characteristics of turbulence in the surface layer can be described through scaling parameters derived from dimensionless ratios of meteorological variables (Monin and Obukhov, 1954). Furthermore, MOST states that any quantity describing the flow in this portion of the atmosphere can be normalized by one in the following scaling groups,

*The conclusions were based on fourteen high-quality experiments

$$u_{*l} = (\overline{u'w'_l}^2 + \overline{v'w'_l}^2)^{1/4}, \tag{5-1}$$

$$\theta_{*l} = -\frac{\overline{w'\theta'_l}}{u_{*l}}, \tag{5-2}$$

$$q_{*l} = -\frac{\overline{w'q'_l}}{u_{*l}}, \tag{5-3}$$

where, the subindex l denotes the *local scaling* approach, meaning that values are scaled at their corresponding measurement height, z, instead of using surface-layer values. Thus, u_{*l} represents the local friction velocity, and $\overline{u'w'_l}$ and $\overline{v'w'_l}$ are the local vertical kinematic momentum fluxes of the along-wind u and cross-wind v wind-speed components, respectively. $\overline{w'\theta'_l}$ is the local value of the vertical kinematic heat flux, $\overline{w'q'_l}$ the local vertical kinematic humidity flux, θ is potential temperature, κ (≈ 0.4) is the von Kármán constant, and g ($= 9.81ms^{-2}$) is the acceleration due to gravity. The over-bar denotes time-averaging, while the prime denotes a turbulent perturbation around the evolving mean values. The velocity variables are normalized using the u_{*l}, while the temperature and humidity variables are normalized using the characteristic temperature (θ_{*l}) and humidity scales (q_{*l}), respectively.

Local scaling predicts that each dimensionless quantity can be described, and is a universal function of the non-dimensional stability parameter, defined as the ratio $\zeta = (z-d)/\Lambda$, being z the measurement height above the ground, d the zero-plane displacement height, and Λ the local Obukhov length, which is defined as,

$$\Lambda = -\frac{1}{k}\frac{u_{*l}^3}{\overline{w'\theta'_l}}\left(\frac{g}{\overline{\theta_v}}\right)^{-1}, \tag{5-4}$$

where Λ represents the ratio of mechanical to thermal production/destruction of turbulence. ζ is, therefore, a measure of local stability (positive/negative values correspond to stable/unstable stratification at level z).

In the local scaling framework, the standard deviations of the wind velocity components σ_i, where i = (longitudinal -u, lateral -v, vertical -w), are scaled as, $\Phi_i = \sigma_i/u_{*l}$. The scaled standard deviation of temperature and humidity are defined as $\Phi_\theta = \sigma_\theta/\theta_{*l}$ and $\Phi_q = \sigma_q/q_{*l}$, respectively, and the dimensionless turbulent kinetic energy (TKE) dissipation

rate as $\Phi_\epsilon = \epsilon/u_{*l}^3$. Φ represents a set of universal similarity functions, different for each parameter. Its formulation varies with atmospheric stability.

The general form of the local similarity relationships of wind velocity fluctuations for unstable ($\zeta \leq 0$) and stable ($\zeta > 0$) stratification in the MOST framework can be written as,

$$\Phi_i = \alpha_i(1 + \beta_i |\zeta|)^{c_i} \tag{5-5}$$

The coefficients α_i, β_i, and c_i must be empirically determined. The α_i parameter represents the value of a particular normalized standard deviation in the near-neutral limit and can be interpreted as a measure of the isotropy of the flow (Panofsky and Dutton, 1984; Nadeau et al., 2013). The β_i parameter is directly related to the stability parameter ζ, and its magnitude reflects the degree of the influence of atmospheric stability on σ_i/u_{*l}. The exponent c_i is often presumed to be equal to 1/3 under unstable conditions because of the theoretical prediction of the asymptotic behavior by MOST at the free convection limit (Garratt, 1992; Roth, 2000). This assumption has been extensively validated for different studies in all kinds of terrain (e.g., Panofsky and Dutton, 1984; Quan and Hu, 2009; Nadeau et al., 2013; Babić et al., 2016b; Stiperski and Calaf, 2018; Stiperski et al., 2019). For stable conditions some observations in urban areas have support the validity of the 1/3 value for the exponent c_i (e.g., Quan and Hu, 2009; Fortuniak et al., 2013; Zou et al., 2018). Grachev et al. (2013) discussed the influence of different kinds of turbulence (the Kolmogorov turbulence for $Rf \leq Rf_{cr}$ and the non-Kolmogorov turbulence for $Rf > Rf_{cr}$, where Rf is the flux Richardson number, and the critical value Rf_{cr} is about 0.20–0.25) on the dependence of σ_w/u_{*l} on increasing stability. They found that σ_w/u_{*l} remains almost constant under stable conditions when $Rf \leq Rf_{cr}$, whereas it increases with increasing stability when $Rf > Rf_{cr}$. A comprehensive review of various formulations of Φ functions for wind components can be found in de Franceschi et al. (2009).

Regarding the universal similarity functions for temperature and humidity, the most general form can be written as,

$$\Phi_{\theta,q} = a_{\theta,q}(b_{\theta,q} + c_{\theta,q}\zeta)^{d_{\theta,q}}, \tag{5-6}$$

Again, $a_{\theta,q}$, $b_{\theta,q}$, $c_{\theta,q}$ and $d_{\theta,q}$ are the appropriate similarity coefficients, and need to be estimated from field campaigns data. Sfyri et al. (2018) and Fortuniak et al. (2013) present extensive reviews of similarity relations for the non-dimensional temperature and humidity standard deviations found in the literature. According to the literature, the accurate

functional form to relate σ_θ/θ_* with ζ seems less clear than for the wind components. The adopted functional forms selected for COMPLEX data will be further explained in Section 5.4.

5.3 Data and Methodology

The datasets used for this research were collected during the first semester of 2020 (January 1st -July 31st), using seven integrated 3D sonic anemometers and CO_2/H_2O open-path gas analyzers (IRGASON) connected to a CR6 or CR1000X datalogger (both from Campbell Scientific, Logan, Utah, USA). The instruments were placed in eddy-covariance towers installed in a fully urbanized cross-section of a Tropical Andean Valley (Aburrá Valley, Colombia). The Aburrá Valley is a densely populated valley [†] located between the Colombian west and central Andean mountain ranges, between 6°N and 6.5°N and 75.3°W and 75.6°W, it is characterized through a major bend between a south-to-north and a southwest-to-northeast section (see Figure 5.1). The broadest cross-section from ridgeline-to-ridgeline is 18.2 km, with a relatively flat section of approximately 8 km. The narrowest section of the Valley is around 3 km wide. The highest peak is on the western hill (at 3110 m.a.s.l), and the basin outlet is at 1290 m.a.s.l. This set of measurements is part of the COMPLEX (COmplex terrain Measurement Project for Land-atmosphere Energy eXchanges) campaign, a long-term experimental set-up designed and implemented to study surface-atmosphere interactions and the resulting impacts on the atmospheric boundary layer (ABL) structure and dynamics in a densely built complex terrain setting in the tropics (for more details of the campaign see Chapter 4).

The eddy-covariance systems are mounted on 1.2m cross-arms attached to triangular reinforced towers with a fixed section of 40cm. The towers are installed on buildings' rooftops, identified as the tallest ones in the surrounding area. Their heights are variable and determined by each roof's structure and geometry (see Table S6). Each station name indicates the valley hillslope where it is located (East or West) and a cardinal number associated with the position on the hill starting at the Valley floor. Thus, EH1 is a station installed in the Eastern Hillslope and is the closest to the Valley floor, compared to the other three stations at the same side of the valley (see Figure 5.1).

[†]More than four million people are settled in an area of 1152 km^2

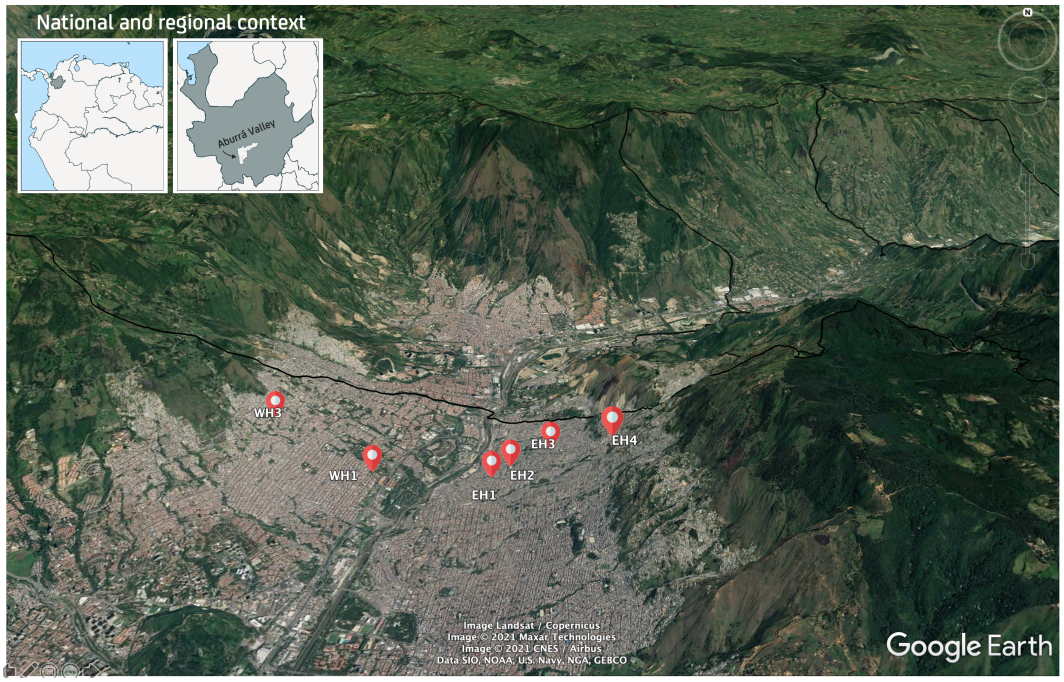

Figure 5.1: COMPLEX sites in a cross-section of the Aburrá Valley, Colombia (Google Earth)

Table S1: Characteristics of the measurement sites within COMPLEX campaign. Station ID with an **E** (-**W**) correspond to those towers placed in the eastern (-western) hillslope of the valley's cross-section, meanwhile **VF** stands for Valley Floor. The numbers correspond to the position of the towers in each hillslope, thus, stations **1** are the closest to the valley base.

		Local Slope	Aspect	Altitude	Morphological Parameters*			
ID	Name	(°)	(°)	(mASL)	z_S(m)	z_H(m)	d(m)	z_o(m)
EH_1	Villa Niza	13.49	196	1491	27	6.76	4.73	0.68
EH_2	Villa Socorro	14.16	183	1551	19	6.71	4.70	0.67
EH_3	Popular	17.70	192	1641	31	7.27	5.09	0.73
EH_4	Candelaria	15.80	205	1843	20	8.10	5.67	0.81
VF_1	SENA	4.21	152	1469	42	8.90	6.23	0.89
WH_1	ITM	7.43	139	1523	20	6.10	4.27	0.61
WH_3	Castilla	15.95	123	1760	22	6.83	4.78	0.68

* Aerodynamic roughness characteristics were calculated following a morphometric height-based approach, assuming that, to a first-order, the zero-plane displacement length (z_d) and the roughness length (z_o) are related to the height of the elements (Grimmond and Oke, 1999). Being $z_d = f_d * z_H$ and $z_0 = f_0 * z_H$. Where z_H is the average obstacle height in the influence zone of the station (footprint), f_d and f_0 are empirical coefficients derived from observations. For this study, we use $f_d = 0.7$ and $f_0 = 0.1$ following Grimmond and Oke (1999) suggestion for urban surfaces.

Each eddy-covariance system samples the atmosphere at 20Hz. The raw data is stored in 24-hour files, maintaining the 20Hz resolution. The first- and second-order statistical moments are calculated using 30-min block period, following a relatively common choice in atmospheric turbulence studies, using the EddyPro® 7.0.6 (LICOR Inc.) software. Each averaging interval is transformed into streamline coordinates using the double rotation method, by which the mean lateral and vertical velocity components are brought to zero (i.e., $\overline{w} = \overline{v} = 0$) (e.g., McMillen, 1988). This procedure also compensates for possible sensor misalignments from a reference system with vertical axis along with the local gravity (de Franceschi et al., 2009). Next, the Reynolds decomposition (Stull, 1988) is performed using block averaging. Zero-plane displacement height information is applied to the stations (see Table S6).

As in all turbulence-related studies, we attempt to obtain the highest-quality data before testing and assessing the validity of conventional theories. The data quality preliminary assessment includes removing the periods flagged by the instrument comprising all detectable electronic malfunctionings and also excluding all 30-min intervals with more than 1% of missing data. The EddyPro® algorithm also checks for each variable absolute limits, and then spikes are removed following the Vickers and Mahrt (1997) procedure (1% as a threshold value for each 30-Min period). If the number of consecutive spikes is less or equal to three, linear interpolation from neighboring values is used to replace them. The procedure also includes flux corrections such as compensation for density fluctuations, WPL correction (Webb et al., 1980), frequency response (Moore, 1986), and correction of sonic temperature for humidity (Schotanus et al., 1983). As in de Franceschi et al. (2009), and Babić et al. (2016a,b), we assume that the sonic temperature $T_s = T(1+0.51q)$, where T is the air temperature, and q is specific humidity, is a good approximation of the virtual potential temperature θ_v.

The stationarity of the time series is one of the bases of similarity theory (Babić et al., 2016a). We use the Foken and Wichura (1996) stationarity test, at a standard 30% level, considering that it most often detects the largest number of non-stationary time intervals compared to other tests in the literature (Večenaj and De Wekker, 2015). The percentage of non-stationary 30-minute periods in our dataset varied between 40 and 60%, depending on the measurement site. Finally, following Klipp and Mahrt (2004), Večenaj and De Wekker (2015),and Babić et al. (2016a), we set thresholds for specific parameters such as kinematic momentum flux (0.001 ms^1), kinematic heat flux (0.001 K ms^1), and standard deviation of each wind speed component (0.04 ms^1). Also, intervals with the

local wind speed less than 0.2 ms^{-1} are omitted.

Dimensionless TKE dissipation

The TKE is an important variable for boundary-layer flows, as it characterizes the level of turbulence (Babić and Rotach, 2018). In the normalized TKE budget equation, Φ_ε represents the dimensionless TKE dissipation rate, a term to quantify the conversion of TKE into internal energy. In order to determine Φ_ε and its dependence on stability, we follow the expression

$$\Phi_\varepsilon = \frac{kz\varepsilon}{u_{*l}^3}, \tag{5-7}$$

where ε is the turbulence dissipation rate. ε needs to be estimated experimentally. According to the literature, there are two methods to determine ε in the ABL; one is called the 'direct method' (Champagne et al., 1977), which is based on the assumption of local isotropy using Taylor's hypothesis. The second method, the one followed in this paper, is called the *indirect method* or *Inertial dissipation method*, which is based on Kolmogorov (1941) hypothesis (e.g., Christen et al., 2009; Večenaj et al., 2011; Babić and Rotach, 2018). This formulation of ε requires the existence of an *Inertial Subrange* in which local isotropy is present.

Kolmogorov (1941) introduced the *equilibrium theory* of turbulence with an idealized picture of the energy spectrum, where the *inertial subrange* (IS) corresponds to the portion of the spectrum characterized by the fact that turbulent energy is neither produced nor dissipated in this range but only transported. According to Kolmogorov's hypothesis, in the IS the turbulence can be assumed to be locally isotropic, relying on the assumption of a gradual loss of anisotropy as energy is transferred to smaller scales. Consequently, in the IS, the spectral density must not depend on the energy production. In contrast, in the IS the spectral density can only be a function of ε and κ (wavenumber), indicating that ε controls the dynamics of turbulence. Through dimensional analysis, Kolmogorov derived the shape of the TKE spectrum in the IS as

$$E(\kappa) = \alpha_K \varepsilon^{2/3} \kappa^{-5/3}, \tag{5-8}$$

where α_K is the proportionality factor known as the Kolmogorov constant. Experimental evidence suggests that $\alpha_K = 1.55$ (e.g., Stull, 1988). According to 5-8, the energy spectra must exhibit a $-5/3$ slope in the IS; however, it does not work the other way around, meaning that the $-5/3$ behavior of spectra does not necessarily imply the presence of

the IS. Under this local isotropy hypothesis, and since ε should be the same for all three coordinate directions, the spectral density of the longitudinal velocity $F_{1,1}(\kappa_1)$, the lateral $F_{2,2}(\kappa_1)$ and the vertical velocity spectral density $F_{3,3}(\kappa_1)$ are approximately equal, and can be derived from 5-8 as follows (e.g., Wyngaard, 2010)

$$F_{2,2}(\kappa_1) = F_{3,3}(\kappa_1) = \frac{4}{3}F_{1,1}(\kappa_1). \tag{5-9}$$

A further consequence of local isotropy is that $\alpha_2 = \alpha_3 = \frac{4}{3}\alpha_1$. Thus, the spectra for v and w are placed higher than the u spectrum in the IS. Equation 5-9 constitute a comprehensive test for the IS in spectral analysis of a time series; a 4/3 ratio of the spectra of transverse (v) to streamwise (u) velocity components and of the spectra of vertical (w) to streamwise (u) velocity components is anticipated in the IS, which is considered more stringent than the -5/3 slope in the log-log spectra.

By invoking Taylor's hypothesis (i.e. $\kappa_1 = 2\pi f/\overline{u}$, with $\overline{u}$ corresponding to the mean wind speed and f to the natural frequency), it is possible to transform the power spectra from wavenumber to frequency ($\kappa_1 F_{i,i}(\kappa_1) = f S_{i,i}(f)$). In that domain, only within the IS, ε could be evaluated from

$$\varepsilon = \frac{2\pi}{\overline{u}}\left[\frac{f^{5/3}S_{i,i}(f)}{\alpha_i}\right]^{2/3}, \tag{5-10}$$

assuming $\alpha_u = 0.55$ (Sreenivasan, 1995). Spectral densities $S_{i,i}(f)$ are calculated for each 30-min run computing the Fast Fourier Transform (FFT) of the 20Hz wind data using a Hamming window. To calculate spectral slopes for each velocity component, we do not fix a frequency domain as in other studies (e.g., Babić and Rotach, 2018; Večenaj et al., 2011; Grachev et al., 2015). Instead, we find the frequency domain iteratively, following a methodology that allows considering potential changes of the limits of the IS and the uncertainty associated with the methods used to fit the slopes.

The iterative methodology starts with the ad-hoc definition of a frequency domain (by defining the limits of a frequency interval) where the IS is expected to occur. For each 30-min period, in the first iteration, three different methods are used to fit the slope of the frequency spectra in the predefined frequency domain. The methods include (i) a robust least absolute deviation (LAD) power fitting technique using the Broyden–Fletcher–Goldfarb–Shanno (BFGS) optimization algorithm (i.e., the BFGS algorithm finds the optimal coefficients of a power function $y = ax^b$ by minimizing the absolute deviation), (ii) a robust least absolute deviation (LAD) linearized fitting technique using

the BFGS optimization algorithm (i.e., $y = ax^b$ is first linearized as $\ln y = \ln a + b \ln x$ before finding the optimal $\ln a$ and b), and (iii) a regular least-squares fit of the linearized function as in (ii). In each case, the methodology modifies the limits of the frequency domain iteratively to find the IS as the range where the slope found with the fitting techniques is closest to -5/3. If the closest slope using all three fitting techniques is not within a 10% deviation of -5/3, the 30-min period is discarded. Then, for each 30-min period and using the mean of the three fitted slopes, ε is estimated independently for each of the three velocity components.

Evaluation of scattering in the datasets

In order to quantify the dispersion of the different Φ_i estimated across all the eddy-covariance sites, as well as to assess their agreement with the reference scaling curves (Φ_i^R) and to investigate the possible association of the Φ_i dispersion with terrain and surface characteristics, we follow a simple methodology proposed by Stiperski et al. (2019). The dispersion from the selected reference scaling curve is quantified by first calculating the median of the absolute deviations for each eddy-covariance as follows

$$\overline{\Delta\Phi_i} = M|\Phi_i^R - \Phi_i|. \tag{5-11}$$

Note that the magnitude of the deviations is closely related to the selected reference curve. The dispersion across the different sites is represented by the interquartile range of the different $\overline{\Delta\Phi_i}$ as

$$IQR_i = P_{75}(\overline{\Delta\Phi_i}) - P_{25}(\overline{\Delta\Phi_i}). \tag{5-12}$$

The $\overline{\Delta\Phi_i}$ and the IQR_i are calculated for each scaling variable and each stability regime. We use HHF (or HIF) scaling relationships as reference curves, Panofsky and Dutton (1984) for wind velocity components, and Cabauw reference from Sfyri et al. (2018) for temperature and humidity.

5.4 Results and Discussion

The data post-processing and quality control lead to discarding a significant amount of 30-min periods, particularly over complex terrain (Stiperski and Rotach, 2016). Under

the latter scenario, the first question that arises is about the representativeness of the results obtained after applying such stringent quality criteria. Table S6 presents the final number of 30-min periods considered in the different analyses after using the quality criteria described in Section 5.3 for each COMPLEX station. On average, 30% of the intervals are discarded. There is no apparent relationship between the amount of data discarded and any morphological parameter of the COMPLEX campaign.

Table S2: Number of 30-min intervals that satisfy the minimum QC (no large data gaps, no unrealistic values, and no spikes) within the observed period of 210 days (out of a total of 10080 possible intervals). The number of stationary and also the number of time intervals which are stationary and have uncertainty $< 50\%$ (used for the analysis in this study) is given.

Criteria	EH1	EH2	EH3	EH4	VF1	WH1	WH3
Minimum QC	8628	8481	8266	8757	8120	6140	7298
Stationarity	5779	5489	2929	3759	3640	4658	4870

Dimensionless Standard Deviations of Wind Velocity Components

In this section, the standard deviations of longitudinal, lateral and vertical wind components σ_i, with $i = u, v, w$, are analyzed in terms of the non-dimensional (-localized) stability parameter ζ, in a heavily urbanized Tropical mountainous terrain. Universal functions for velocity components are evaluated based on Equation 5-5. Note that c_i is set to be 1/3, following the methodology from previous studies that have shown successful cases for local scaling (Al-Jiboori et al., 2002; Nadeau et al., 2013; Babić et al., 2016b; Stiperski and Calaf, 2018). The results are reported in Figures 5.2 to 5.6. We consider the entire stability range for each station instead of just choosing a specific one. The stability parameter ranges from free convective conditions ($\zeta = -190$ in VF1) to very stable ($\zeta = 28$ in EH4). In the near-neutral range ζ reaches very small values, with the smallest value (1.2×10^{-6}) occurring at the WH3 station.

In the near-neutral regime ($\zeta \to 0$), the non-dimensional velocity fluctuations become independent of stability and tend to a constant value, represented by α_i (Babić et al., 2016b). Table S3 shows the average α_i values (based on averages for stable and unstable conditions) and the individual values obtained for all COMPLEX sites for the entire period of analysis. The Table also includes some near-neutral values from previous studies using the local scaling hypothesis and a similar form for the flux–variance relationships applied over different surface conditions

(including Panofsky and Dutton (1984) for HHF). The comparison among the α_i values needs to be carefully made since the underlying surface, the overall nature of the flow, and data processing tools vary among all the experimental campaigns.

Table S3: Non-dimensional standard deviations for near-neutral conditions using the local similarity framework reported for several studies over different terrain conditions.

Reference	α_u	α_v	α_w	Surface Type
Panofsky and Dutton (1984)	2.39 ± 0.03	1.92 ± 0.05	1.25 ± 0.03	HHF
Roth (2000)	2.32 ± 0.16	1.81 ± 0.20	1.25 ± 0.07	Urban ($z > 2.5z_H$)
Al-Jiboori et al. (2002)	1.76	1.6	1.22	Urban ($z = 10z_H$)
Wood et al. (2010)	2.3	1.85	1.35	Urban ($z = 22z_H$)
Zou et al. (2018)	2.17	1.61	1.18	Urban ($z = 3.4z_H$)
Moraes et al. (2005)	2.4	2.2	1.20	River Valley
Nadeau et al. (2013)	2.85	2.24	0.98	Steep Alpine Slope
Pegahfar and Bidokhti (2013)	2.71	2.80	2.35	Urban-Mountainous
COMPLEX - Average	**2.20**	**1.87**	**1.22**	Urban-Mountainous
EH4	2.32	2.13	1.35	$z = 2.5z_H$
EH2	2.58	2.05	1.28	$z = 2.8z_H$
WH3	2.00	1.58	1.24	$z = 3.2z_H$
WH1	2.37	1.92	1.25	$z = 3.3z_H$
EH1	2.25	1.76	1.13	$z = 3.9z_H$
EH3	2.10	1.79	1.12	$z = 4.2z_H$
VF1	2.05	1.98	1.30	$z = 4.7z_H$

In agreement with several previous studies (including HHF and complex terrains), results for α_i from the COMPLEX datasets exhibit a large anisotropy of the flow with $\sigma_u/u_{*l} > \sigma_v/u_{*l} > \sigma_w/u_{*l}$ when $\zeta \to 0$. The α_i averages for the COMPLEX campaign are in good agreement with the coefficients obtained for fourteen urban experiments listed in an extensive review by Roth (2000). Most α_i values are consistently smaller than those obtained by Panofsky and Dutton (1984) for HHF terrain, highlighting the possible influence of the roughness sublayer; however, this is not the case for all seven sites. To analyze in detail the influence of different roughness and topography features within the Valley, Figure 5.2 shows the α_i values for each COMPLEX station.

The EH2 station is the only site in which all the α_is are consistently larger compared to the canonical values listed in Panofsky and Dutton (1984). Meanwhile, the α_is for EH1, EH3, WH1, and WH3 are always smaller than the reference values. However, it is not possible to conclude

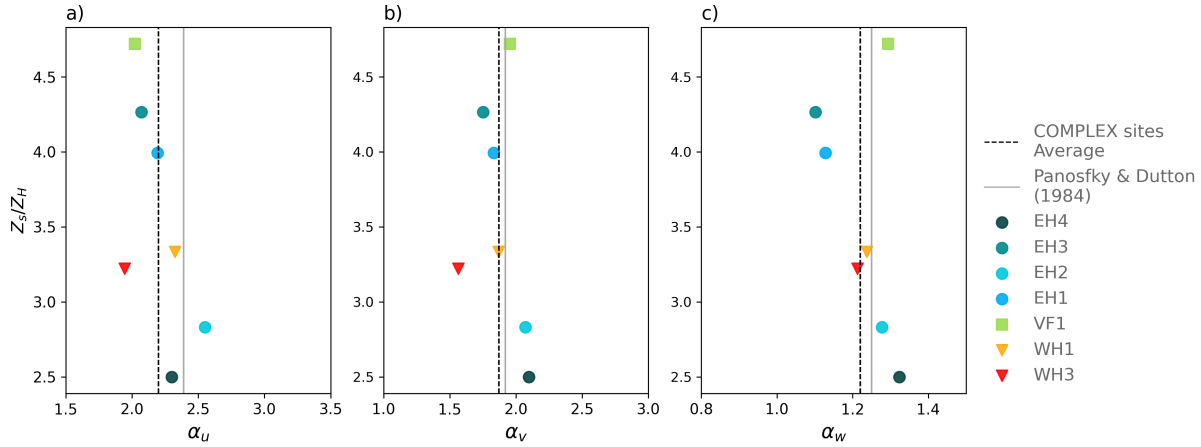

Figure 5.2: Fitting coefficients α_i as a function of z_S/z_H for all COMPLEX sites. Color and symbol associated with each station is given in the upper legend, together with the gray line, which denote the flat terrain values given in Panofsky and Dutton (1984). Average α_i values for the entire campaigns are presented in black dashed lines

whether the normalized standard deviations of the velocity components near the urban canopy top are larger or smaller than those over flat terrain (e.g., Zou et al., 2018).

Similar to the conclusions in Roth (2000), a direct association of the α_is with surface roughness is not evident from our results since values do not show a clear relationship with the Z_H/Z_S ratio. This could be due to the fact that, even though the COMPLEX sites exhibit different Z_S/Z_H ratios, some other site characteristics can not be excluded from the analysis in order to isolate the influence of surface roughness on the velocity variances. The α_w shows a decreasing trend for all the hillslope stations (excluding VF1), with a similar decreasing rate than Zou et al. (2018), who evaluated similarity relationships within the roughness sublayer, and until $z = 3.4Z_H$. Some authors have proposed that for measurements in urban areas, the wake effects of buildings enhance turbulence fluctuations near the urban canopy top (e.g., Zou et al., 2018); thus, α_i values tend to be larger than those in ideal surfaces. However, there is still no consensus about whether the normalized standard deviations of velocity components near the urban canopy top are larger or smaller than those over flat terrain, further, or if those are a function of surface roughness (Roth, 2000). In our case, the values of $\sigma_{u,v}/u_{*l}$ at the lowest measurement height (EH4, $z = 2.5Z_H$) are, in fact, larger than the typical values obtained over flat terrain (dotted line in 5.2), however that is not the case for α_u.

de Franceschi et al. (2009) highlighted the importance of valley geometry when studying complex mountainous terrain, such as narrow valleys. In particular, de Franceschi et al. (2009) notes the relevance of the effects of the sidewalls (physical boundary determined by the mountain hillslopes) on the horizontal dimension of the eddies, which causes $\sigma_{u,v}/u_{*l}$ to be smaller compared

to HHF terrain, where the maximum eddy size is only constrained by the ABL depth. The latter statement contrasts with previous conclusions by Panofsky and Dutton (1984), ensuring that $\sigma_{u,v}/u_{*l}$ tend to be larger for complex terrain. The de Franceschi et al. (2009) statement is valid only under the assumption that the valley is narrower than the ABL height. Under these conditions, the valley can physically constrain the most energetic convective eddies and influence their size, as evidenced by Babić et al. (2016a) for the flux-variance similarity analysis in Owens Valley, California. Based on our results, we could not validate the de Franceschi et al. (2009) statement since $\sigma_{u,v}/u_{*l}$ are not consistently smaller in all the COMPLEX stations, and the difference between both horizontal components for the hillslope stations is not very different from Panofsky and Dutton (1984) results for HHF terrain or others listed in Table S3.

Figures 5.3 and 5.4 presents the scaled standard deviations of the wind components as a function of ζ. Left columns in both Figures show an example for WH3 site. Gray circles represent each 30-min period that have passed the high-quality criteria. Binned averages are also presented, with error bars representing the standard deviation of all data points falling into each bin. As reference, the Figure also includes the formulations for HHF terrain from Panofsky and Dutton (1984), mountainous terrain from Nadeau et al. (2013), and urban surface by Zou et al. (2018).

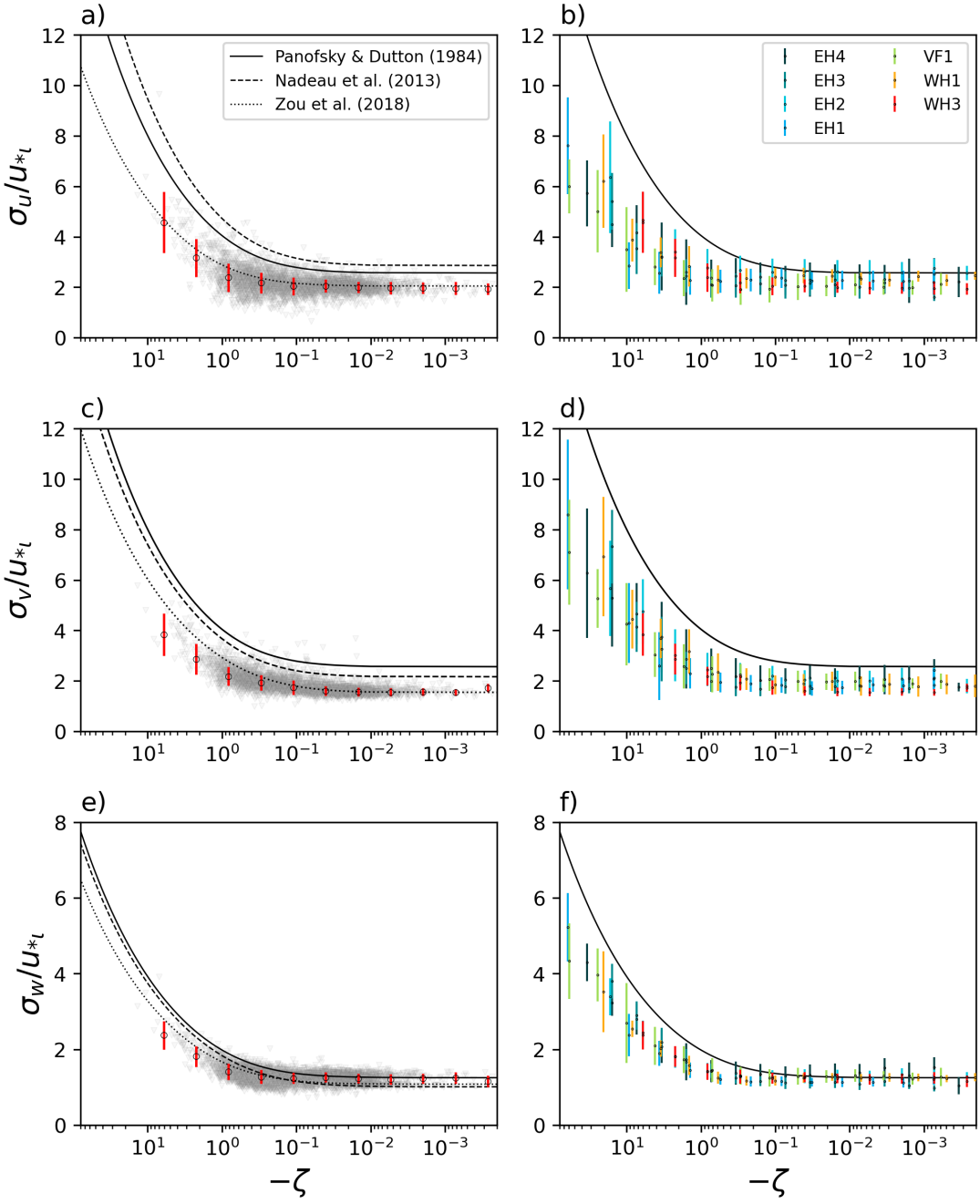

Figure 5.3: Locally-scaled, dimensionless standard deviation of a) longitudinal -u, b) lateral -v, and c) vertical -w wind components fluctuations for unstable stratification as a function of ζ for seven COMPLEX datasets that have passed the high-quality criteria, denoted by different colors and symbols (see legend). Left column shows WH3 site, for an 7-month period between Jan- Jul 2020 (gray circles), and right column the binned averages from all seven COMPLEX sites. Error bars represent the standard deviation of all data points falling into this bin. For comparison, black line represents the reference curve for HHF terrain (Panofsky and Dutton, 1984), the black-dashed line shows the best-fit curve for mountainous complex terrain (Nadeau et al., 2013), and black-dotted line the best-fit curve for an urban surface given by Zou et al. (2018)

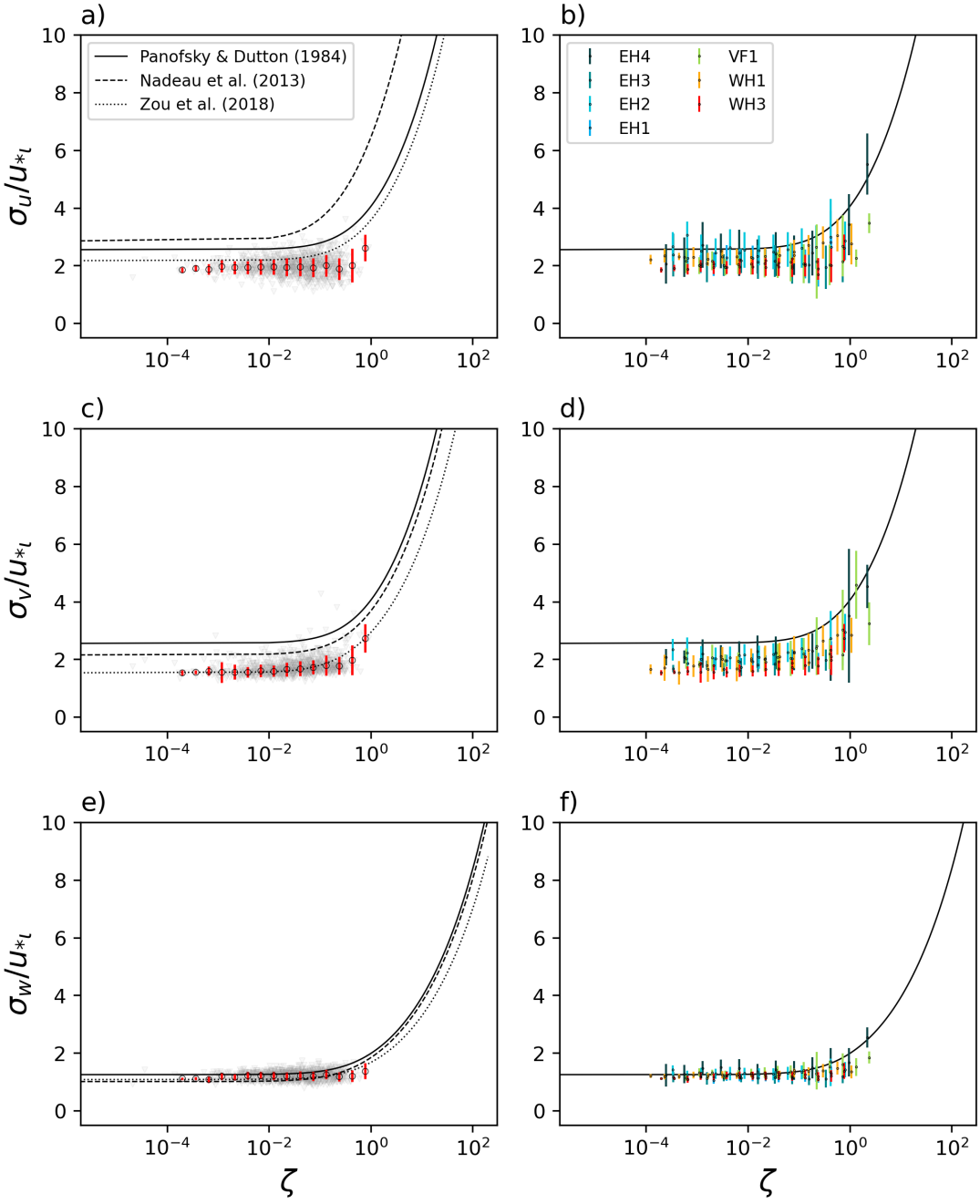

Figure 5.4: Same as 5.3 but for stable stratification

The results show a large dispersion within the data points from each COMPLEX site (see $\Delta\Phi_i$ in Figure 5.5). The dispersion is significantly higher for both horizontal wind velocity components $\Phi_{u,v}$ than for the vertical fluctuations Φ_w, especially under convective conditions, agreeing with previous results obtained over urban surfaces and complex terrains (e.g., Moraes et al., 2005; de Franceschi et al., 2009; Nadeau et al., 2013; Babić et al., 2016b; Zou et al., 2018; Stiperski et al., 2019). The data points cluster close to the reference HHF line for weakly

(un)stable conditions, although they are predominantly lower throughout the stability range. Similar behavior has been found in previous studies for urban surfaces (e.g., Al-Jiboori et al., 2002) and mountainous terrains (e.g., Nadeau et al., 2013). The results for the vertical velocity variance show a better collapse onto the scaling curve regardless of the measurement site; thus validating Panofsky and Dutton (1984) results, and suggesting that the σ_w/u_{*l} is independent of flow disturbances associated with non-uniform terrains and, in our case, also of the roughness of the urban surface. Furthermore, the results indicate that for weakly stable (-unstable) conditions ($\zeta < 0.5$), the value of σ_w/u_{*l} remains constant and independent of ζ, whereas, under very stable and free convective conditions, it increases with ζ following a 1/3 power law. This result agrees with several previous studies in non-ideal terrain, including for Al-Jiboori et al. (2002), Moraes et al. (2005), and Nadeau et al. (2013).

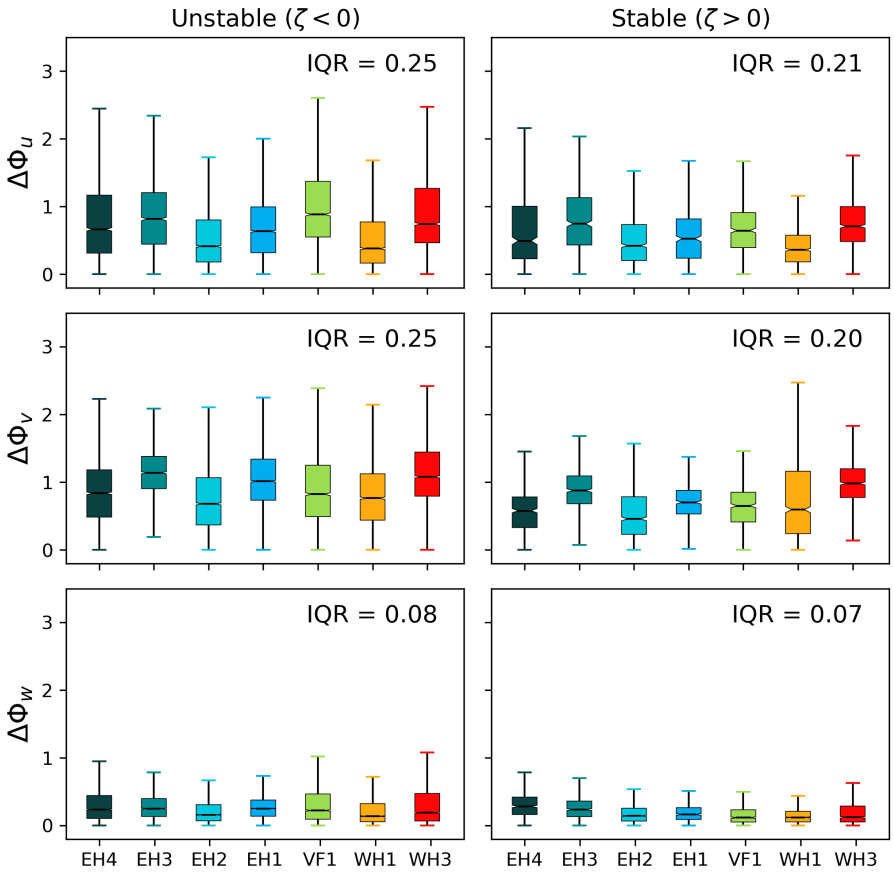

Figure 5.5: Box plots of absolute deviations (a)–(e) $\Delta\Phi_i$ where i = u, v, w, respectively, of the scaled data from the corresponding scaling relations (equations (8)–(12)): as a function of the data set (color), for unstable (left column) and stable (right column) stratification. The IQR, which represents the level discrepancy between sites, is listed on top-right corner of each panel.

The fluctuations of the horizontal wind velocity components are primarily governed by large quasi-horizontal eddies, meaning that their variance is mostly contained in the low frequencies

(Zhang et al., 2001). Meanwhile, variations in the vertical velocity can be explained by the high-frequency end of the energy spectrum, where eddies are small and comparable to the measurement height. Panofsky and Dutton (1984) argued that these small eddies are never far from equilibrium since they adapt quickly to variations in the terrain; in consequence, σ_w/u_{*l} has to be independent of topography and from all the disturbances associated with the flow over non-uniform terrain. Even under nearly-ideal terrain conditions, there exists considerable uncertainty in the literature regarding the scaling of the horizontal velocity variances (e.g. Kaimal et al., 1972; Panofsky et al., 1977) and they are commonly assumed not to obey surface layer scaling, especially for convective conditions (Al-Jiboori et al., 2002; Martins et al., 2009; Stiperski et al., 2019). There is an important debate in the science community on whether the current MOST scaling variables are appropriate for the horizontal wind components. Some authors have posed that in the convective boundary layer, the ABL depth h (which constrains the size of large eddies dominating the horizontal dynamics) and the convective velocity scale w_*, should be considered two relevant scaling variables (e.g. Panofsky et al., 1977). Recently Stiperski and Calaf (2018) (further explored in Stiperski et al. (2019)) found that clustering the data according to the anisotropy of the flow significantly improves the scaling even over highly complex terrain. The anisotropy appears as a potentially powerful tool and the next step to improve similarity scaling relations over non-ideal surfaces.

For all the COMPLEX sites, both horizontal components $\Phi_{u,v}$, exhibit a dependence on stability for $\zeta > 0.5$, showing an increasing tendency with increasing (un)stability. The latter implies that under stable stratification, wind velocity fluctuations do not follow z-less scaling (Sorbjan, 1987), as previously suggested by Stiperski et al. (2019) scaling relationships for different datasets in complex terrains. Klipp and Mahrt (2004) suggested that this could be an indication of self-correlation, which is not addressed in this chapter.

Variability between the different COMPLEX sites is represented by IQR values included in each panel in Figure 5.5. In the case of COMPLEX, for both horizontal velocity components, the dispersion among the different stations is larger, with variations of the order of 20-25%. According to Stiperski et al. (2019), the high dispersion between the stations could be an indication of the *location-dependent* nature of scaling in complex terrain. Regarding the vertical wind component, variability between sites is significantly lower than for the horizontal components (less than 10%), as was the case for the scatter within each individual dataset.

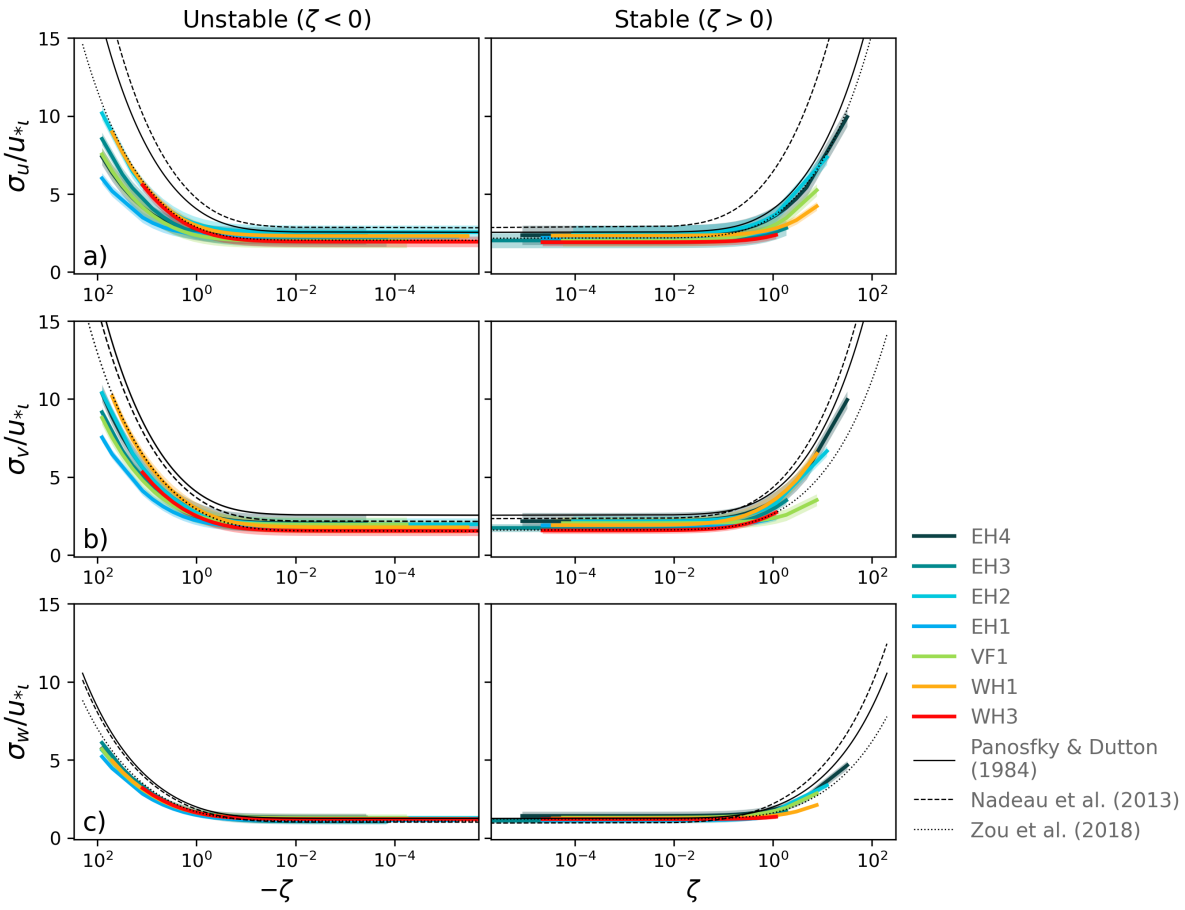

Figure 5.6: Best-fit curves of non-dimensional a) longitudinal -u, b) lateral -v, and c) vertical -w wind components fluctuations and unstable (left) and stable (right) stratification as a function of ζ standard deviations. Solid, dashed and dotted black lines denote previous scaling relationships given by Panofsky and Dutton (1984) for HHF terrain, Nadeau et al. (2013) for mountainous-complex terrain, and Zou et al. (2018) for an urban environment, respectively. The shaded areas represent the Median Absolute Deviation (MAD).

Figure 5.6 shows best-fit curves for each individual station. For all wind components and stability ranges (except for σ_w under unstable conditions), the scaling relations differ not only from the classical HHF relations but also from site to site, suggesting again, as it was already highlighted by Stiperski et al. (2019), that scaling might be inherently local and therefore negating the possibility of a universal theory of turbulence, at least for these particular set of variables. The dispersion between the different curve fits for all stations is higher for the horizontal velocity components, especially in the unstable stratification regime, corresponding with the scatter level in data points shown in Figure **??**. In general, the best-fit curves for the COMPLEX stations show a higher correspondence with previous scaling relationships over urban surfaces found by Zou et al. (2018), than with the mountainous-terrain references (i.e., Nadeau et al., 2013). The latter conclusion could be a manifestation of a dominant effect of the roughness elements on

turbulent properties even over the complex topography.

For $\sigma_{u,v}$, under unstable conditions, although the curves do not collapse onto a single scaling line, the best-fit curves cluster around the urban reference scaling. This level of agreement with the urban reference scaling is not so clear for the stable regime in any of the three velocity components. Furthermore, it is not possible to explain the level of discrepancy between the observations and the HHF reference curve and the relative magnitude of Φ_i by any particular (-evident) feature or complexity induced by the terrain, such as slope or distance to the valley floor, neither by any particular characteristic of the surface roughness.

Table S4: List of best-fit similarity relations for the non-dimensional wind components $\Phi_{u,v,w}$ standard deviations, for the COMPLEX sites, for unstable and stable stratification. The Coefficients are derived from 1/3 power law fit in Eq. 5-5 for each COMPLEX station

Site	u		v		w			
	α_u	β_u	α_v	β_v	α_w	β_w	Stability	Stability Range
EH$_1$	2.23	0.11	1.76	0.93	1.11	1.23	Unstable	$-85 < \zeta < -4 \times 10^{-6}$
	2.17	1.53	1.93	0.64	1.12	0.32	Stable	$2 \times 10^{-5} < \zeta < 1$
EH$_2$	2.53	0.79	1.98	1.42	1.27	1.03	Unstable	$-86 < \zeta < -2 \times 10^{-6}$
	2.53	0.39	2.13	1.58	1.26	0.32	Stable	$7 \times 10^{-5} < \zeta < 13$
EH$_3$	2.06	0.53	1.73	1.94	1.08	2.06	Unstable	$-80 < \zeta < -1 \times 10^{-4}$
	2.09	0.03	1.78	1.50	1.11	0.58	Stable	$1 \times 10^{-6} < \zeta < 2$
EH$_4$	2.33	0.42	2.03	1.43	1.30	0.98	Unstable	$-150 < \zeta < -4 \times 10^{-3}$
	2.34	2.84	2.17	2.05	1.41	0.90	Stable	$9 \times 10^{-6} < \zeta < 30$
VF$_1$	1.96	0.52	1.96	0.83	1.25	1.09	Unstable	$-190 < \zeta < -4 \times 10^{-5}$
	2.00	1.48	1.94	3.24	1.28	1.94	Stable	$5 \times 10^{-5} < \zeta < 7$
WH$_1$	2.34	0.80	1.75	3.42	1.23	1.17	Unstable	$-44 < \zeta < -3.8 \times 10^{-6}$
	2.28	2.73	1.89	4.98	1.24	1.66	Stable	$3.1 \times 10^{-5} < \zeta < 6.3$
WH$_3$	1.96	1.67	1.55	3.09	1.20	1.34	Unstable	$-104 < \zeta < -1 \times 10^{-6}$
	1.94	-0.0	1.57	3.02	1.22	0.28	Stable	$2 \times 10^{-5} < \zeta < 0.9$

Dimensionless Standard Deviations of scalars

Dimensionless Standard Deviations of Temperature

Normalized standard deviations of scalars such as temperature (θ), and humidity (q) as a function of stability, have been less studied than the behavior of the wind components, and even less over complex non-ideal surfaces than for near-to-ideal conditions. Recently, some studies have suggested different similarity functions for scalars over urban areas (e.g. Roth, 2000; Al-Jiboori et al., 2002; Wood et al., 2010; Fortuniak et al., 2013; Zou et al., 2018), and complex-mountainous terrain (e.g. Moraes et al., 2005; Martins et al., 2009; de Franceschi et al., 2009; Nadeau et al., 2013; Sfyri et al., 2018). Figure 5.7 shows the normalized standard deviation of temperature (panel a)) and humidity (panel b)) as a function of ζ for the seven COMPLEX sites, for unstable (left) and stable (right) stratification. As a reference for an ideal surface, we use the scaling curve obtained by Sfyri et al. (2018) using the Cabauw datasets, a weakly inhomogeneous and flat terrain (HIF) in the Netherlands.

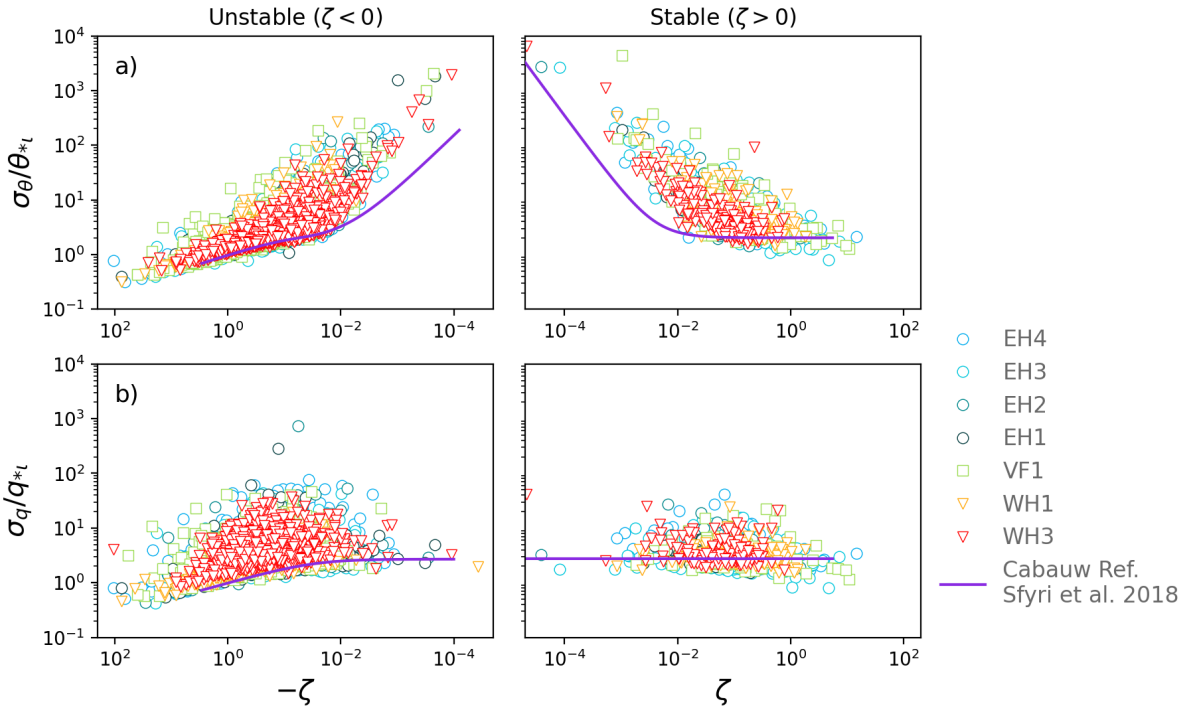

Figure 5.7: Locally-scaled, dimensionless standard deviation of a) temperature and b) humidity fluctuations and unstable (left) and stable (right) stratification as a function of ζ for seven COMPLEX datasets that have passed the high-quality criteria, denoted by different colors and symbols (see legend). Purple line denote reference line given by Sfyri et al. (2018) for weakly inhomogeneous and flat terrain (Cabauw) in the Netherlands.

A large dispersion is evident for the standard deviation of temperature in stable and unstable stratification for all COMPLEX sites. However, unlike the velocity fluctuations, the scatter is larger under stable conditions. Some studies previously reported the same behavior (e.g. Pahlow et al., 2001; Stiperski et al., 2019) that, according to Mahrt (1999) it is probably caused by the sporadic nature of nighttime turbulence. The increased temperature dispersion observed in Figure 5.7a has been previously found and studied in detail by Sfyri et al. (2018). They identified four possible reasons: i) post-processing issues, ii) erroneous determination of the zero-plane displacement height, iii) non-constant fluxes, and iv) coordinate system. However, according to their respective tests, none of these reasons seem to be conclusively responsible for this behavior. They finally concluded that the inhomogeneity of the study area and the complexity of the terrain were likely the reason for the large temperature variability in their datasets. In the case of the COMPLEX stations, the magnitude and variability of the Φ_θ values do not seem to be associated with, or explained by, the mountain slope.

The values of σ_θ/θ_* for the COMPLEX sites exhibit a dependence on stability for both unstable and stable stratification, decreasing with increasing (un)stability. In the near-neutral regime, when $\zeta \to 0$, σ_θ/θ_* increases strongly, whereas it levels off and slowly approaches a constant value in the high-end of the stable range, where weak turbulence inhibits the exchanges with the surface; thus, becoming independent of ζ. Similar to the results obtained by Rotach et al. (2017) and Sfyri et al. (2018) with the i-Box datasets, a multi-site campaign at the Inn Valley, Austria (a highly-complex mountainous rural terrain), Φ_θ values in Figure 5.7 are, on average, larger than the reference within the unstable range ($\zeta < -0.05$) for all the COMPLEX sites. Further, within the near-neutral regime ($|\zeta| \leq 0.05$), they completely separate from the HIF reference for all the evaluated datasets. Regarding the stable stratification, the depicted functions differ significantly from the HFI reference.

According to the literature, the functional form that describes the dependence of σ_θ/θ_* on ζ remains unclear, and several formulations have been suggested for different types of surfaces. For unstable stratification (outside the near-neutral regime), starting from Eq. 5-6, different studies have used one of two common functional forms. The first was proposed by Wyngaard et al. (1971) on the basis of the free convection MOST similarity theory ($\Phi_\theta = a_\theta(-\zeta)^{c_\theta}$), and the second is similar to the relationship for the wind components (Eq. 5-5). These two relations are only valid outside the near-neutral regime, in which most authors restrict their analyses, given the large variability and high uncertainty beyond this limit, partly associated with the low accuracy of the measurements for such small values. Here, in order to address the entire stability range, similar to Sfyri et al. (2018), we analyze the near-neutral (unstable) and the unstable regime separately. For the unstable regime we set $c_\theta = -1$ and $e_\theta = 0$ in Eq. 5-6, and for the near-neutral (unstable), $c_\theta = -1$ and $b_\theta = 0$. To our knowledge, there exists no

other study analyzing temperature scaling relationships in the near-neutral regime for an urban surface. For the stable regime, we use an expression that already includes the effect of weak heat flux for near-neutral conditions, previously used by other studies (e.g. Pahlow et al., 2001; Tampieri et al., 2009; Sfyri et al., 2018). The three functional forms are summarized as follows

$$\phi_\theta = \left\{ \begin{array}{ccc} a_\theta(b_\theta - \zeta)^{d_\theta} & for & \zeta \leq -0.05 \\ a_\theta(-\zeta)^{d_\theta} + e_\theta & for & -0.05 \leq \zeta \leq 0 \\ a_\theta \zeta^{d_\theta} + e_\theta & for & \zeta \geq 0 \end{array} \right\} \tag{5-13}$$

We left the exponent d_θ as a free parameter and fit it using the observational COMPLEX data. Figure 5.8a shows the best-fit curves of the standard deviations of the non-dimensional temperature for each COMPLEX station. Additionally, in Table S5, the non-linear best-fit functions between Φ_θ and ζ are shown for every COMPLEX site for unstable ($\zeta \leq -0.05$), near-neutral (unstable) ($-0.05 < \zeta \leq 0$) and stable ($\zeta \geq 0$) conditions. In Figure 5.8a, the black dashed line represents the best fit curve for a station in the Inn Valley, found in Sfyri et al. (2018). In their research, they work with five different stations. Here, we select the CS-NF27 Hochhauser site, with a 27° slope, corresponding to the steepest mountain-slope site in their campaign. For the urban reference (dotted black line), we use a scaling relationship found by Zou et al. (2018) for one sensor at $z = 3.4Z_H$ level over an urban canopy in Changzhou, China. For the latter study, only the stability ranges outside the near-neutral regime were analyzed ($|\zeta| > 0.05$).

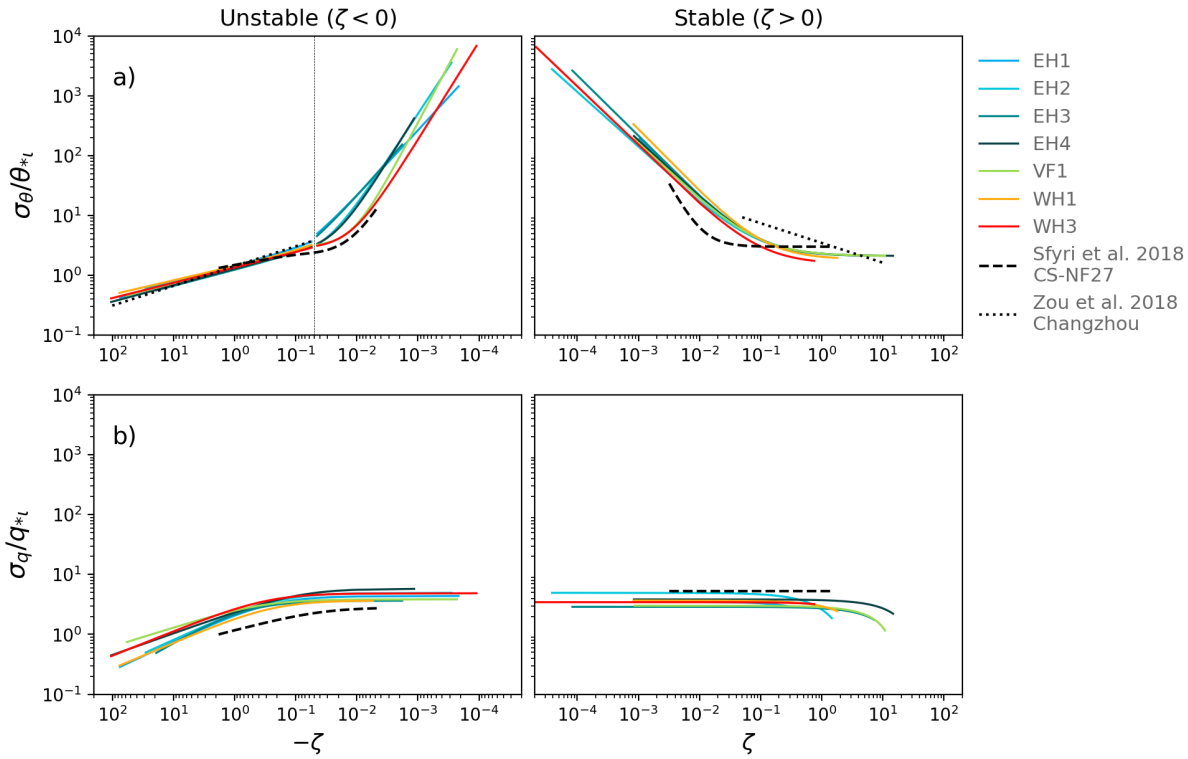

Figure 5.8: Best-fit curves of non-dimensional a) temperature , b) humidity fluctuations and unstable (left) and stable (right) stratification as a function of ζ standard deviations. Black and magenta lines denote previous scaling relationships given by Sfyri et al. (2018) for mountainous-complex terrain, Zou et al. (2018) for an urban environment, respectively. *The shaded areas represent the Median Absolute Deviation (MAD).*

In the unstable regime ($\zeta < -0.05$), the curves for all COMPLEX stations scale better than for the other stability ranges; furthermore, they closely fit the classical -1/3 power law, with the exponent d_θ varying between -0.23 and -0.27. The coefficient b_θ is close to 0 in all cases, demonstrating that Wyngaard's expression fits better the COMPLEX data (i.e. $\Phi_\theta = -a_\theta \zeta^{d_\theta}$). As for a_θ, which determines the magnitude of the curves, the average value for the COMPLEX stations is 1.34, which is larger than the HIF reference (0.99) and the average i-box sites (1.23). However, it is lower than other studies conducted in urban surfaces, which is the case of Zou et al. (2018) (1.45) and Quan and Hu (2009) (1.5).

As mentioned before, the dependence of σ_θ/θ_* on the local stability parameter under near-neutral conditions is rarely reported in the literature. As pointed out by several authors, within the MOST framework, the large scatter for $|\zeta| \to 0$ is likely caused by the presence of unsteadiness and heterogeneity in air temperature in the boundary layer (e.g. Zhang et al., 2001; Tampieri et al., 2009; Wood et al., 2010; Liu et al., 2017). σ_θ could not be equal to 0 due to these inhomogeneities, even as the heat flux goes to zero when approaching neutral conditions. Thus,

large values of $\sigma_\theta/\theta_{*l}$ can be found under neutral conditions when $\theta_{*l} \to 0$—demonstrating that θ_* is not a suitable scale when heat flux approaches zero. In the near-neutral (unstable) region, Tampieri et al. (2009) suggested an exponent $d_\theta = -1$, rather than the classical $d_\theta = -1/3$. For the COMPLEX sites, the exponent d_θ is closer, although always larger in magnitude, to -1, varying between -1.1 in station EH1 and -1.92 in VF1. This result is opposite to the results in Sfyri et al. (2018) for the i-Box datasets, where the valley floor site (CS-VF0) exhibited the lowest slope with a value of -1.1. There does not seem to exist a dependence of d_θ on any morphometric feature of the surface. The near-neutral (unstable) range presents the largest differences between the best-fit curves.

Table S5: List of best-fit similarity relations for the non-dimensional temperature Φ_θ standard deviations, for the COMPLEX sites, for unstable, near-neutral (unstable) and stable stratification.

Site	a_θ	b_θ	c_θ	d_θ	e_θ	Stability	Stability Range
EH1	1.42	-0.02	-1	-0.27	0	Unstable	$-85 < \zeta < -0.05$
	0.12	0	-1	-1.10	1.00	Near-neutral (uns)	$-0.05 < \zeta < -4 \times 10^{-6}$
	0.18	0	1	-1.00	2.09	Stable	$2 \times 10^{-5} < \zeta < 1$
EH2	1.35	-0.01	-1	-0.23	0	Unstable	$-86 < \zeta < -0.05$
	0.01	0	-1	-1.55	1.87	Near-neutral (uns)	$-0.05 < \zeta < -2 \times 10^{-6}$
	0.19	0	1	-0.93	2.09	Stable	$7 \times 10^{-5} < \zeta < 13$
EH3	1.22	-0.02	-1	-0.26	0	Unstable	$-80 < \zeta < -0.05$
	0.09	0	-1	-1.17	1.00	Near-neutral (uns)	$-0.05 < \zeta < -1 \times 10^{-4}$
	0.16	0	1	-1.02	2.09	Stable	$1 \times 10^{-6} < \zeta < 2$
EH4	1.27	-0.01	-1	-0.27	0	Unstable	$-150 < \zeta < -0.05$
	0.00	0	-1	-1.65	2.40	Near-neutral (uns)	$-0.05 < \zeta < -4 \times 10^{-3}$
	0.19	0	1	-0.98	2.09	Stable	$9 \times 10^{-6} < \zeta < 30$
VF1	1.36	-0.01	-1	-0.26	0	Unstable	$-190 < \zeta < -0.05$
	0.00	0	-1	-1.92	3.0	Near-neutral (uns)	$-0.05 < \zeta < -4 \times 10^{-5}$
	0.19	0	1	-0.96	2.09	Stable	$5 \times 10^{-5} < \zeta < 7$
WH1	1.41	-0.02	-1	-0.23	0	Unstable	$-44 < \zeta < -0.05$
	6.56	0	-1	-2.99	2.23	Near-neutral (uns)	$-0.05 < \zeta < -3.8 \times 10^{-6}$
	0.18	0	1	-1.05	1.84	Stable	$3.1 \times 10^{-5} < \zeta < 6.3$
WH3	1.34	-0.00	-1	-0.25	0	Unstable	$-104 < \zeta < -0.05$
	0.00	0	-1	-1.64	2.75	Near-neutral (uns)	$-0.05 < \zeta < -1 \times 10^{-6}$
	0.15	0	1	-0.99	1.53	Stable	$2 \times 10^{-5} < \zeta < 0.9$

For stable stratification, the dependence of Φ_θ on ζ has a larger uncertainty. There is no

consensus in the literature on whether the standard deviation of temperature within this range follows a z-less scaling. Some studies have found that a constant value over the entire range is enough to describe the independence of Φ_θ from the stability parameter (e.g. Nieuwstadt, 1984; Shao and Hacker, 1990; Andreas et al., 1998; Al-Jiboori et al., 2002) (with values of 3, $\sqrt{12}$, 3.2, 3.1, respectively). On the other hand, some authors have pointed out that the local similarity functions of temperature under stable stratification follow the form described in Eq. 5-13, (e.g. Pahlow et al., 2001; Quan and Hu, 2009; Wood et al., 2010; Nadeau et al., 2013; Liu et al., 2017; Sfyri et al., 2018; Zou et al., 2018), with the exponent d_θ varying between the typical $-1/3$ and a value of -1. For the COMPLEX sites in the stable range, the differences with the selected reference best-fit curves are quite substantial. Although the best-fit curves for some of the COMPLEX stations do level off and tend to a constant value, this happens in a much higher stability level compared with the reference ($\zeta > 1$); also, the value is lower than those previously reported in the literature ($e_\theta = 2.09$). For strong stable stratification, the best-fit curves of the COMPLEX sites scale satisfactorily, except for WH3 which places lower than the other six curves. The non-linear coefficient d_θ, which represents the exponent, is close to -1 for all the stations, varying between -0.93 and -1.05, agreeing with Pahlow et al. (2001) who recommended an exponent of 1 for near-neutral (stable) conditions in horizontally inhomogeneous and flat terrain.

Dimensionless Standard Deviations of Humidity

The similarity functions for the standard deviation of humidity (Φ_q) are presented and discussed in this section. Figure 5.7b shows the normalized standard deviation of humidity as a function of ζ for the seven COMPLEX sites, for unstable (left) and stable (right) stratification. The dispersion among the data points appears very high for both stability ranges. However, unlike the temperature fluctuations, the variability is larger for the unstable stratification regime, similar to previous results for urban areas (e.g. Fortuniak et al., 2013), but opposite to what Sfyri et al. (2018) found for the i-Box datasets for the Inn Valley. Throughout the unstable regime, the values of Φ_q are clearly larger than the reference values, although they closely follow the exponential form. Under stable stratification, several previous studies, including the HIF reference, suggest the independence of σ_q/q_* from the local stability parameter (e.g. Andreas et al., 1998; Fortuniak et al., 2013; Sfyri et al., 2018), however, regardless of the high dispersion of the data, some of the COMPLEX sites show that there actually exists a degree of dependence, with Φ_q decreasing with increasing stability. For this reason, we decided to fit an exponential expression instead of a constant value in the entire domain, as follows

$$\Phi_q = \begin{cases} a_q(bq - \zeta)^{d_q} & for \quad \zeta \leq 0 \\ a_q(b_q + \zeta)^{d_q} & for \quad \zeta \geq 0 \end{cases} \tag{5-14}$$

The best-fit curves for the normalized standard deviation of humidity for each of the COMPLEX sites are presented in Figure 5.8b. As mentioned before, absolute values of Φ_q in the unstable regime are higher than those suggested by the reference for HIF terrain. Further, the values are higher than those for mountainous-complex terrains (black dotted line in Figure 5.8b. According to Fortuniak et al. (2013), in urban areas, the non-stationarity in the water vapor emission at ground level due to variations in traffic intensity could be a reason for these high values. Furthermore, Fortuniak et al. (2013) also points out the fact that cities are, in general, relatively dry environments. Thus the enhanced humidity variability could also be a result of entrainment processes at the boundary-layer top. However, this is not necessarily the case in the COMPLEX experimental campaign: the Tropical environment imposes a relatively high relative humidity background. In this case, it is likely that the combination of high spatiotemporal rainfall variability, together with the high variability in land cover, leads to the observed dispersion in Φ_q.

Table S6: List of best-fit similarity relations for the non-dimensional humidity Φ_q standard deviations, for the COMPLEX sites, for unstable and stable stratification.

Site	a_q	b_q	c_q	d_q	e_q	Stability
EH1	2.29	0.26	-1	-0.4	0	Unstable
	0.0072	5.0	1	3.84	0	Stable
EH2	2.41	0.21	-1	-0.4	0	Unstable
	0.0003	6.73	1	4.99	0	Stable
EH3	2.97	0.71	-1	-0.6	0	Unstable
	0.0499	22.6	1	1.29	0	Stable
EH4	2.39	0.08	-1	-0.3	0	Unstable
	0.0460	39.8	1	1.19	0	Stable
VF1	2.73	0.34	-1	-0.3	0	Unstable
	0.1628	17.7	1	1.01	0	Stable
WH1	1.96	0.23	-1	-0.4	0	Unstable
	0.0316	10.0	1	1.99	0	Stable
WH3	2.91	0.28	-1	-0.4	0	Unstable
	0.1953	9.89	1	1.25	0	Stable

Turbulence dissipation rate

As we previously mentioned in Section 5.3, the 4/3 ratio of the lateral and vertical velocity spectra to the longitudinal velocity spectrum is a more robust and stringent condition for the IS than the $-5/3$ slope in the power spectra. Testing for local isotropy allows determining where the IS is located for the COMPLEX sites in order to calculate ε and test the local stability dependence of Φ_ε. Results for the latter test, for each COMPLEX site, are presented in Figure 5.9.

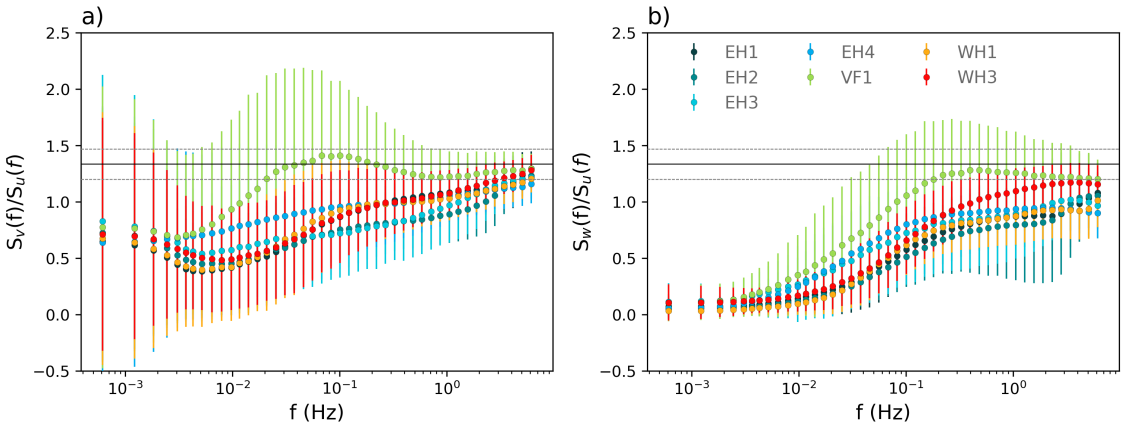

Figure 5.9: Median values of bin-averaged a) lateral -v and b) vertical -w to the longitudinal -u spectral densities ratios for the seven COMPLEX sites (denoted by different colors). Vertical lines for each interval correspond the spread around the mean value, represented by the IQR. Horizontal black solid and gray dashed lines correspond to a $\pm 10\%$ deviation from 4/3 isotropic ratio.

For each site, the spectral ratios S_v/S_u and S_w/S_u correspond to the median values, and their respective spread is represented by the IQR. Apparently, at the high-frequency end (after $f \approx 3$ Hz), all stations tend to converge towards a 4/3 value for the lateral-to-longitudinal velocity component; however, for most of the hillslope stations, this value is never reached. The valley floor station VF1 (green dots) appears to have different behavior than the other sites, with a faster and earlier increase of the S_v/S_u ratio, fully reaching the isotropic ratio around $f \approx 0.03$ Hz. Similar behavior can be observed in the vertical-to-longitudinal spectral ratio, being the VF1 station the only one reaching the 4/3 value at $f \approx 0.3$ Hz. The other six stations converge towards a value of approximately 1 ($\pm 10\%$). Smaller ratios of S_w/S_u are commonly found in the literature for experiments over non-homogeneous surfaces (forests) and complex terrains (e.g. Christen et al., 2009; Večenaj et al., 2011; Babić and Rotach, 2018). Over nearly flat and slightly inhomogeneous terrain, Chamecki and Dias (2004) found that for most of their runs (3 out of 4), values of S_w/S_u never reached the isotopic ratio, meanwhile for the horizontal components, the ratio predicted by isotropy is, in fact, reached. This result is validated by Babić and Rotach (2018) over a multi-level eddy-covariance tower placed on a heterogeneous surface. For all levels,

S_v/S_u reaches the theoretical value of 4/3; meanwhile, S_w/S_u is significantly lower than this reference and converge towards a value lower than 1. Chamecki and Dias (2004) concluded that this behavior might be due to currently available sonic anemometers, which are unable to resolve the full IS of the velocity spectra. Biltoft (2001) posed that this discrepancy between theory and measurements is due to the anisotropy induced by shear and buoyancy in the IS. According to Babić and Rotach (2018), another possible cause could be the consequence of the spectral processing methods; however, from the COMPLEX results, it is not possible to associate this discrepancy with processing methods since at least one of the sites reaches the expected value according to the theory, i.e., 4/3. The isotropic ratio is anticipated theoretically, and as pointed out by Biltoft (2001), there is no convincing experimental support for this theoretical ratio.

For the COMPLEX datasets, ε is evaluated for each velocity component separately. Results are shown in Figure 5.10.

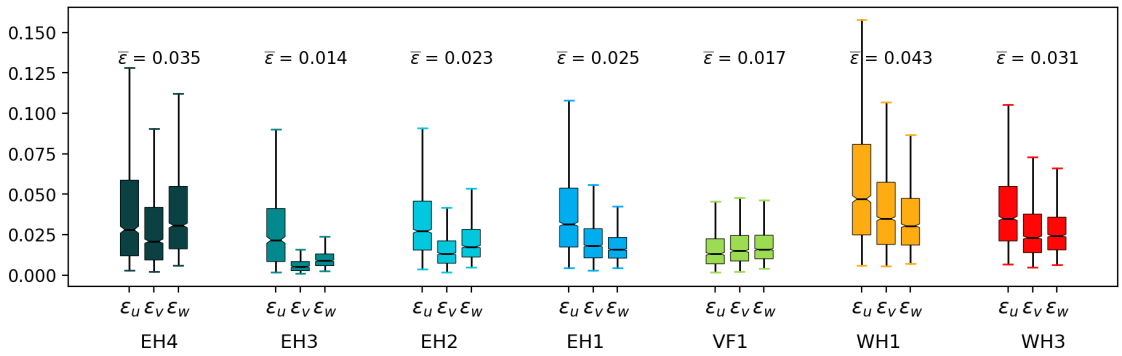

Figure 5.10: Box plots of the estimate dissipation rates for the three velocity wind components $\varepsilon_{u,v,w}$ for COMPLEX sites. The value of the mean $\bar{\varepsilon}$ for each station is listed above each set of box plots

For VF1, where the isotropic range is reached for both S_v/Su and S_w/S_u ratios, the differences between the estimated values of ε for the three velocity components are negligible. Those differences increase significantly for the hillslope stations, as well as the spread within each ε_i estimates. There is no correspondence between the dissipation rates estimated for both horizontal components (i.e., $\varepsilon_{u,v}$), which is expected from results in Figure 5.9, but different from previous results from Babić and Rotach (2018). Babić and Rotach (2018) found that ε_u and ε_v estimates were aligned along a 1:1 line. There is an apparent trend in both hillslopes, with ε_u being **always larger** and with larger dispersion than ε_i for the other two wind components. For the stations in the western hillslope (i.e., $WH_{1,3}$) $\varepsilon_u > \varepsilon_v > \varepsilon_w$, while for the opposite hillslope 3 out of 4 stations (i.e., $EH_{2,3,4}$) $\varepsilon_u > \varepsilon_w > \varepsilon_v$.

The non-dimensional dissipation rates $\Phi\varepsilon_{u,v,w}$ as a function of ζ are presented in Figure 5.11. Here we only show results for stations VF1 and EH3, two contrasting sites regarding their **'flux**

isotropic conditions' according to results in Figure 5.10. The rest of the stations (not shown) are in good agreement with the behavior seen in these two examples and the results in Figure 5.11.

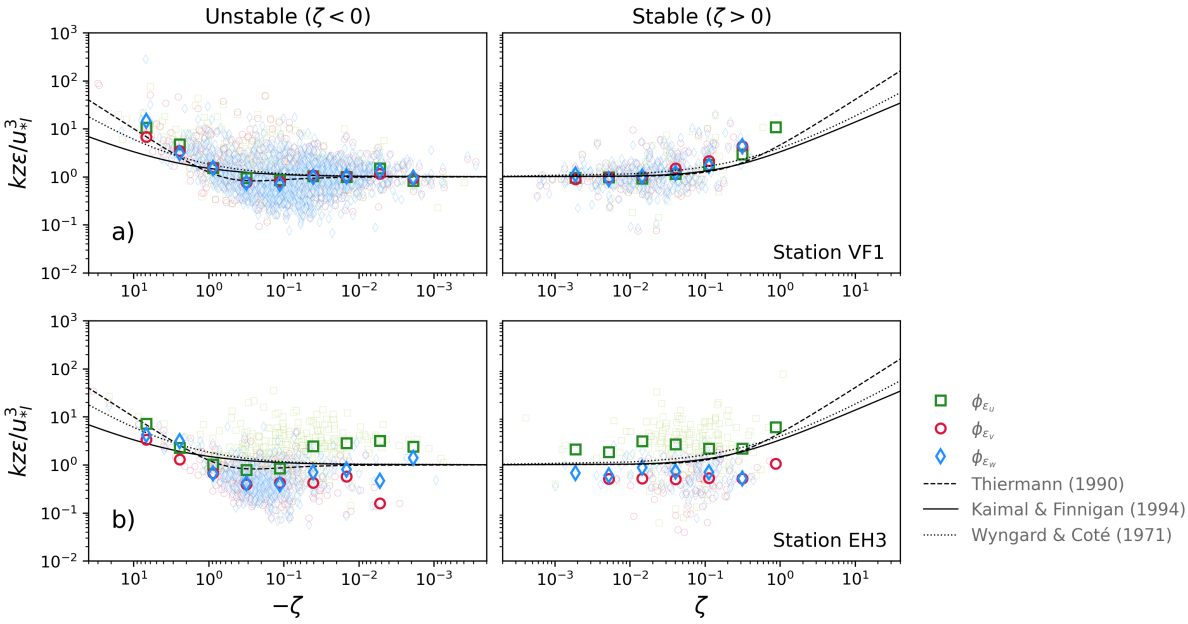

Figure 5.11: Non-dimensional dissipation rate of the TKE versus the local stability parameter ζ for a) Station VF1 and b) Station EH3, based on the three velocity components, longitudinal (green squares), lateral (pink circles), and vertical (blue rhomboids). Lighter data points corresponds to each valid run, while thicker edge-line symbols denote bin averages. Solid, dotted and dashed gray lines indicate ideal HHF terrain reference curves of Kaimal and Finnigan (1994), Wyngaard et al. (1971) and Thiermann (1990), respectively.

In agreement with the ε estimates, and validating the results of Stiperski and Calaf (2018), data with close to isotropic turbulence (see VF1) matches the reference similarity relationships better compared to cases with high anisotropy, which significantly deviates from the traditional scaling relations (see EH3). Although there is a significant dispersion for both stability regimes for $\Phi\varepsilon$ estimates in station VF1, the bin averages agree surprisingly well with the plotted reference curves, particularly with the function proposed by Thiermann (1990) for the unstable regime.

5.5 Conclusions

The main objective of this research was to examine the applicability of *local scaling* to flux-variance relationships of wind velocity fluctuations, scalars (temperature and humidity), and

TKE dissipation rate in the boundary layer of a heavily-urbanized mountainous terrain in a Tropical Andean Valley, using data from the COMPLEX campaign. The datasets consist of seven-month time series from seven EC towers placed in a cross-section of the Aburrá Valley in Colombia. Observations were conducted in the inertial sub-layer, with measurements varying from $z_S/z_H = 2.4$ to $z_S/z_H = 4.2$.

Under conditions as complex as those of the Aburrá Valley, several fundamental assumptions of the Monin–Obukhov similarity theory are largely violated, meaning that the application of local scaling is highly recommended (-necessary). In general, the obtained results demonstrated that the local similarity approach could characterize the standard deviations of velocity components, scalars (temperature and humidity), and the TKE dissipation rate satisfactorily under the whole stability range, showing the great potential of localizing the fluxes even in such complex surface. However, it is certainly not as powerful as MOST, knowing that the coefficients for each scaling function are linked to their respective measurement site. Although the scaled variables were measured in different Valley locations with diverse surface characteristics, the functional forms of the scaled relationships are similar to those obtained for ideal surfaces, indicating that MOST can be considered a special case of local similarity.

A few remarks have to be made from the results, i) in the high-stable end of the stability range, velocity wind components for some stations do not follow the z-less scaling hypothesis. The curves continue increasing as ζ increases. ii) Addressing the scalar fluctuations, an enhanced scatter can be observed in $\Phi_{\theta,q}$ for all COMPLEX stations over the whole stability range. Previous studies in complex-mountainous terrain observed the same results, except for Φ_q under unstable stratification, where this behavior could result from the presence of the urban area and/or associated to the tropical environment. iii) In the near-neutral regime, as expected, temperature fluctuations diverge and tend to high values due to heterogeneities in the boundary layer. Within this region, the slope for COMPLEX sites is (negatively) larger than the classical -1/3 and, in all cases, larger than the recently -1 suggested by Tampieri et al. (2009), agreeing with previous results from complex terrain (e.g., Sfyri et al., 2018). iv) Φ_q not independent from ζ for all COMPLEX stations.

Although COMPLEX campaign sets in a mixed mountainous-urbanized environment, some of the results suggest that the 'urban footprint' prevails over the plausible effects of the rugged topography, this based on previous results and conclusions from studies in both types of surfaces found in the literature. In the case of the Aburrá Valley, a heavily urbanized area where on average more than 75% of the EC towers surrounding areas are characterized as impervious-gray structures, it could be reasonable that modifications of the flow and coherent structures forced by the urban surface dominate dynamics in the local scale. However, under the local similarity framework, this can not be conclusive of all mountainous-urbanized environments, given its site-

dependency. Moreover, in general, results do not show any particular trend associated with the features of the surface (e.g., surface roughness or slope). The multiple degrees of freedom in such an environment make it very challenging to isolate the individual relative contribution of the different surfaces or terrain features.

Chapter 6

Overarching Conclusions and Outlook

Observational campaigns are still the most reliable tool in order to characterize and understand boundary layer processes at different scales in complex terrains, which will ultimately improve the representation of those processes in numerical weather prediction (NWP) models. However, deploying a field campaign is not an easy task. There are numerous challenges to face, especially when dealing with surfaces that are far from the definition of 'ideal.' Unfortunately, more than 80% of the earth's surface is considered topographically complex; further, with the increasing rate of urbanization of those mountainous areas, current NWP model parameterizations fall extremely short when trying to reproduce land-atmosphere interactions in such complex environments. If we also consider that NWP model physics is biased towards conditions found in mid-latitudes, reliable observational networks in (sub)tropical areas, which are currently facing aggressive growth rates, must be a top priority in order to improve numerical predictions for environmental management issues.

In this research, using observations, we worked on some relevant questions regarding the multiscale boundary-layer dynamics in an urbanized mountainous terrain, the Aburrá Valley in the Andes. We first explore the multilayered structure of the boundary layer in the Valley, and its implications on the onset of critical air quality episodes in the urban area due to the poor ventilation associated with stably stratified atmospheres. In the Valley, the temperature gradient between the surface and the lower troposphere is one of the primary modulators of the ABL structure, followed by the characteristic heat structure of the urban area. In addition to the diurnal cycle, the results suggest the existence of intra-annual and annual spectral peaks triggered by ITZC modulation of cloudiness, precipitation, and surface incident radiation. When the climate conditions are not favorable for ABL expansion, the anthropic emissions build up and lead to critical air pollution episodes. In this sense, the amount of aerosol particles at the lower troposphere is influenced both by anthropogenic emissions and by the vertical dispersion conditioned by topography and the ABL dynamics.

Regarding the spatial variability, differences in densities driven by the heterogeneous terrain result in complicated, heterogeneous ABL heights and structures. For example, observational evidence (supported by WRF simulations) in the Aburrá Valley showed significant differences between ABL structure in the valley floor vs. the slopes in terms of maximum height and maximum peak time, which appear to be linked to the differences in surface wind direction, with upslope winds at the western hill acting to thicken the boundary layer height locally.

The mechanisms responsible for driven the onset of a convective boundary layer (CBL) were also addressed. To understand and be able to predict when and under which conditions the transition from a stably stratified atmosphere to an unstable one, meaning the activation of land-atmosphere exchanges, is extremely important in heavily urbanized areas, given the clear relationship of this with the dispersion of pollutants, and the development of extreme precipitation events. To perform this analysis through the observations posed many challenges primarily involved with the representativeness of the measurements. However, the followed methodology allowed us to conclude that there certainly exists a proportional relationship between the energy provided to the atmosphere in the form of sensible heat and the nighttime inversion strength; however, this relationship is by no means simple.

Bibliography

Al-Jiboori, M. H., Xu, Y., and Qian, Y. (2002). Local similarity relationships in the urban boundary layer. *Boundary-Layer Meteorology*, 102(1):63–82.

Allwine, K. J., Shinn, J. H., Streit, G. E., Clawson, K. L., and Brown, M. (2002). Overview of URBAN 2000. *Bulletin of the American Meteorological Society*, (April):521–536.

Andreas, E. L., Hill, R. J., Gosz, J. R., Moore, D. I., Otto, W. D., and Sarma, A. D. (1998). Statistics of surface-layer turbulence over terrain with metre-scale heterogeneity. *Boundary-Layer Meteorology*, 86(3):379–408.

Angevine, W. M. (1999). Entrainment results including advection and case studies from the flatland boundary layer experiments. *Journal of Geophysical Research: Atmospheres*, 104(D24):30947–30963.

Angevine, W. M., Baltink, H. K., and Bosveld, F. C. (2001). Observations of the morning transition of the convective boundary layer. *Boundary-Layer Meteorology*, 101:209–227.

Anquetin, S., Guilbaud, C., and Chollet, J.-P. (1998). The Formation and Destruction of Inversion Layers within a Deep Valley. *Journal of Applied Meteorology*, 37(12):1547–1560.

Arnfield, A. J. (2003). Two decades of urban climate research: a review of turbulence, exchanges of energy and water, and the urban heat island. *International Journal of Climatology*, 23(1):1–26.

Baars, H., Ansmann, A., Engelmann, R., and Althausen, D. (2008). Continuous monitoring of the boundary-layer top with lidar. *Atmospheric Chemistry and Physics*, 8(23):7281–7296.

Babić, K. and Rotach, M. W. (2018). Turbulence kinetic energy budget in the stable boundary layer over a heterogeneous surface. *Quarterly Journal of the Royal Meteorological Society*, 144(713):1045–1062.

Babić, K., Rotach, M. W., and Klaić, Z. B. (2016a). Evaluation of local similarity theory in the wintertime nocturnal boundary layer over heterogeneous surface. *Agricultural and Forest Meteorology*, 228-229:164 – 179.

Babić, N., Večenaj, Ž., and De Wekker, S. F. (2016b). Flux–Variance Similarity in Complex Terrain and Its Sensitivity to Different Methods of Treating Non-stationarity. *Boundary-Layer Meteorology*, 159(1):123–145.

Bader, D. C. and McKee, T. B. (1985). Effects od shear, stability and valley Characteristics on the destruction of temperature inversions. *Journal of climate and applied meteorology*.

Baklanov, A., Grimmond, C., Carlson, D., Terblanche, D., Tang, X., Bouchet, V., Lee, B., Langendijk, G., Kolli, R., and Hovsepyan, A. (2018). From urban meteorology, climate and environment research to integrated city services. *Urban Climate*, 23:330 – 341. ICUC9: The 9th International Conference on Urban Climate.

Baklanov, A., Grimmond, C. S. B., Carlson, D., Terblanche, D., Bouchet, V., Lee, B., and Langendijk, G. (2015). From Urban Meteorology, Climate and Environment Research to Urban Integrated Services. *ICUC9 - 9th International Conference on Urban Climate jointly with 12th Symposium on the Urban Environment*, (iv).

Baklanov, A. and Grisogono, B. (2006). Atmospheric boundary layers. Nature, Theory and Applications to Environmental Modelling and Security.

Baklanov, A. and Mahura, A. (2009). *Meteorological and air quality models for urban areas*.

Barlow, J. F., Halios, C. H., Lane, S. E., and Wood, C. R. (2015). Observations of urban boundary layer structure during a strong urban heat island event. *Environmental Fluid Mechanics*, 15(2):373–398.

Barman, N., Borgohain, A., Kundu, S. S., Roy, R., Saha, B., Solanki, R., Kiran Kumar, N. V., and Raju, P. L. (2019). *Daytime Temporal Variation of Surface-Layer Parameters and Turbulence Kinetic Energy Budget in Topographically Complex Terrain Around Umiam, India*, volume 172.

Beare, R. J. (2008). The Role of Shear in the Morning Transition Boundary Layer. *Boundary-Layer Meteorology*, pages 395–410.

Betts, A. K. (1973). Non-precipitating cumulus convection and its parameterization. *Quarterly Journal of the Royal Meteorological Society*, 99(419):178–196.

Betts, A. K., Fuentes, J. D., Garstang, M., and Ball, J. H. (2002). Surface diurnal cycle and boundary layer structure over rondÃŽnia during the rainy season. *Journal of Geophysical Research: Atmospheres*, 107(D20):LBA 32–1–LBA 32–14.

Betts, A. K. and Viterbo, P. (2005). Land-surface, boundary layer, and cloud-field coupling over the southwestern amazon in era-40. *Journal of Geophysical Research: Atmospheres*, 110(D14).

Bianco, L., Djalalova, I. V., King, C. W., and Wilczak, J. M. (2011). Diurnal Evolution and Annual Variability of Boundary-Layer Height and Its Correlation to Other Meteorological Variables in California's Central Valley. *Boundary-Layer Meteorology*, 140:491–511.

Biltoft, C. A. (2001). SOME THOUGHTS ON LOCAL ISOTROPY AND THE 4/3 LATERAL TO LONGITUDINAL VELOCITY SPECTRUM RATIO. *Boundary-Layer Meteorology*, 100(December 2000):393–404.

Bohnenstengel, S. I., Belcher, S. E., Aiken, A., Allan, J. D., Allen, G., Bacak, A., Bannan, T. J., Barlow, J. F., Beddddows, D. C., Blossss, W. J., Booth, A. M., Chemel, C., Coceal, O., Di Marco, C. F., Dubey, M. K., Faloon, K. H., Flemiming, Z. L., Furger, M., Gietl, J. K., Graves, R. R., Green, D. C., Grimmond, C. S., Halios, C. H., Hamiamiamilton, J. F., Harrisison, R. M., Heal, M. R., Heard, D. E., Helfter, C., Herndon, S. C., Holmes, R. E., Hopkins, J. R., Jones, A. M., Kelly, F. J., Kotthaus, S., Langford, B., Lee, J. D., Leigh, R. J., Lewisis, A. C., Lidsidsidster, R. T., Lopez-Hilfiker, F. D., McQuaidaid, J. B., Mohr, C., Monks, P. S., Nemimitz, E., Ng, N. L., Percival, C. J., Prévôt, A. S., Ricketts, H. M., Sokhi, R., Stone, D., Thornton, J. A., Tremper, A. H., Valach, A. C., Vissisisser, S., Whalley, L. K., Williamsiamsiamsiams, L. R., Xu, L., Young, D. E., and Zotter, P. (2015). Meteorology, air quality, and health in London: The ClearfLo project. *Bulletin of the American Meteorological Society*, 96(5):779–804.

Britter, R. E. and Hanna, S. R. (2003). Flow and Dispersion in Urban Areas. *Annual Review of Fluid Mechanics*, 35(1):469–496.

Brown, A. R., Cederwall, R. T., Chlond, A., Duynkerke, P. G., Golaz, J., Khairoutdinov, M., Lewellen, D. C., Lock, A. P., MacVean, M. K., Moeng, C., Neggers, R. A. J., Siebesma, A. P., and Stevens, B. (2002). Large-eddy simulation of the diurnal cycle of shallow cumulus convection over land. *Quarterly Journal of the Royal Meteorological Society*, 128(582):1075–1093.

Castán-Broto, V. and Bulkeley, H. (2013). A survey of urban climate change experiments in 100 cities. *Global Environmental Change*, 23(1):92 – 102.

Ceccherini, G., Ameztoy, I., Hern??ndez, C. P. R., and Moreno, C. C. (2015). *High-resolution precipitation datasets in South America and West Africa based on satellite-derived rainfall, enhanced vegetation index and digital elevation model*, volume 7.

Chamecki, M. and Dias, N. L. (2004). The local isotropy hypothesis and the turbulent kinetic energy dissipation rate in the atmospheric surface layer. *Quarterly Journal of the Royal Meteorological Society*, 130(603 PART B):2733–2752.

Champagne, F. H., Friehe, C. A., and LaRue, J. C. (1977). Flux measurements, Flux Estimation Techniques, and Fine-Scale Turbulence Measurements in the Unstable Surface Layer Over Land. *Journal of the Atmospheric Sciences*, 34:1–27.

Chandra, A. S., Kollias, P., and Albrecht, B. A. (2013). Multiyear summertime observations of daytime fair-weather cumuli at the arm southern great plains facility. *Journal of Climate*, 26(24):10031–10050.

Chandra, S., Dwivedi, A. K., and Kumar, M. (2014). Characterization of the atmospheric boundary layer from radiosonde observations along eastern end of monsoon trough of India. *Journal Earth Syst. Sci*, (6):1233–1240.

Choi, W., Ranasinghe, D., Bunavage, K., DeShazo, J. R., Wu, L., Seguel, R., Winer, A. M., and Paulson, S. E. (2016). The effects of the built environment, traffic patterns, and micrometeorology on street level ultrafine particle concentrations at a block scale: Results from multiple urban sites. *Science of the Total Environment*, 553:474–485.

Christen, A. (2005). *Atmospheric turbulence and surface energy exchange in urban environments: Results from the Basel Urban Boundary Layer Experiment (BUBBLE).* PhD thesis, University of Basel, Basel.

Christen, A., Rotach, M. W., and Vogt, R. (2009). The budget of turbulent kinetic energy in the urban roughness sublayer. *Boundary-Layer Meteorology*, 131(2):193–222.

Cleugh, H. and Grimmond, S. (2012). *Urban Climates and Global Climate Change*. Elsevier B.V., second edi edition.

Cohn, S. A. and Angevine, W. A. (2000). Boundary Layer Height and Entrainment Zone Thickness Measured by Lidars and Wind-Profiling Radars. *Journal of Applied Meteorology*, 39(2000):1233–1247.

Colette, A., Chow, F. K., and Street, R. L. (2003). A Numerical Study of Inversion-Layer Breakup and the Effects of Topographic Shading in Idealized Valleys. *American Meteorological Society*, 96(19):1255–1272.

Conzemius, R. J. and Fedorovich, E. (2006). Dynamics of Sheared Convective Boundary Layer Entrainment. Part I: Methodological Background and Large-Eddy Simulations. *Journal of the Atmospheric Sciences*, 63(4):1151–1178.

Correa, M., Zuluaga, C., Palacio, C., Pérez, J., and Jímenez, J. (2009). Acoplamiento de la atmósfera libre con el campo de vientos locales en una región tropical de topografía compleja. Caso de estudio: Valle de Aburrá, Antioquia, Colombia. *Dyna*, Año 76:17–27.

Coutts, A. M., Beringer, J., and Tapper, N. J. (2007). Impact of increasing urban density on local climate: Spatial and temporal variations in the surface energy balance in Melbourne, Australia. *Journal of Applied Meteorology and Climatology*, 46(4):477–493.

Curry, J. and Webster, P. (1999). *Thermodynamics of Atmospheres and Oceans*. International Geophysics. Elsevier Science.

Czarnecka, M., Nidzgorska-lencewicz, J., and Rawicki, K. (2019). Temporal structure of thermal inversions in Ł eba (Poland). *Theoretical and Applied Climatology*, pages 1–13.

Dabberdt, W. F., Frederick, G. L., Hardesty, R. M., Lee, W. C., and Underwood, K. (2004). Advances in meteorological instrumentation for air quality and emergency response. *Meteorology and Atmospheric Physics*, 87:57–88.

de Franceschi, M., Zardi, D., Tagliazucca, M., and Tampieri, F. (2009). Analysis of second-order moments in surface layer turbulence in an Alpine valley. *Quarterly Journal of the Royal Meteorological Society*, 135(October):1750–1765.

De Wekker, S. F. J. and Kossmann, M. (2015). Convective Boundary Layer Heights Over Mountainous Terrain—A Review of Concepts. *Frontiers in Earth Science*, 3(December):1–22.

Dee, D. P., Uppala, S. M., Simmons, A. J., Berrisford, P., Poli, P., Kobayashi, S., Andrae, U., Balmaseda, M. A., Balsamo, G., Bauer, P., Bechtold, P., Beljaars, A. C. M., van de Berg, L., Bidlot, J., Bormann, N., Delsol, C., Dragani, R., Fuentes, M., Geer, A. J., Haimberger, L., Healy, S. B., Hersbach, H., HÃlm, E. V., Isaksen, L., KÃllberg, P., KÃ¶hler, M., Matricardi, M., McNally, A. P., Monge-Sanz, B. M., Morcrette, J.-J., Park, B.-K., Peubey, C., de Rosnay, P., Tavolato, C., ThÃ©paut, J.-N., and Vitart, F. (2011). The era-interim reanalysis: configuration and performance of the data assimilation system. *Quarterly Journal of the Royal Meteorological Society*, 137(656):553–597.

Di Giuseppe, F., Riccio, A., Caporaso, L., Bonafé, G., Gobbi, G. P., and Angelini, F. (2012). Automatic detection of atmospheric boundary layer height using ceilometer backscatter data assisted by a boundary layer model. *Quarterly Journal of the Royal Meteorological Society*, 138(November 2011):649–663.

Di Sabatino, S. (2016). Boundary-Layer Atmospheric Processes in Mountainous Terrain: Results from MATERHORN-X. *Boundary-Layer Meteorology*, 159(3):465–467.

Di Sabatino, S., Buccolieri, R., and Salizzoni, P. (2013). Recent advancements in numerical modelling of flow and dispersion in urban areas: A short review. *International Journal of Environment and Pollution*, 52(3/4):172–191.

Doran, J., Berkowitz, C., Coulter, R., Shaw, W., and Spicer, C. (2003). The 2001 phoenix sunrise experiment: vertical mixing and chemistry during the morning transition in phoenix. *Atmospheric Environment*, 37(17):2365 – 2377.

Doran, J. C., Fast, J. D., and Horel, J. (2002). THE VTMX 2000 CAMPAIGN. *Bulletin of the American Meteorological Society*, (APRIL):537–551.

Emeis, S., Schäfer, K., and Münkel, C. (2008). Long-term observations of the urban mixing-layer height with ceilometers. *IOP Conference Series: Earth and Environmental Science*, 1:012027.

Emeis, S., Schäfer, K., and Münkel, C. (2009). Observation of the structure of the urban boundary layer with different ceilometers and validation by RASS data. *Meteorologische Zeitschrift*, 18(2):149–154.

Emeis, S., Schäfer, K., Münkel, C., Friedl, R., and Suppan, P. (2012). Evaluation of the Interpretation of Ceilometer Data with RASS and Radiosonde Data. *Boundary-Layer Meteorology*, 143:25–35.

Eresmaa, N., Härkoönen, J., and Joffre, S. (2012). A Three-Step Method for Estimating the Mixing Height Using Ceilometer Data from the Helsinki Testbed. pages 2172–2187.

Eresmaa, N., Karppinen, A., and Joffre, S. M. (2006). Mixing height determination by ceilometer. *Atmospheric Chemistry and Physics*, 6:1485–1493.

Fedorovich, E. and Conzemius, R. (2008). Effects of wind shear on the atmospheric convective boundary layer structure and evolution. *Acta Geophysica*, 56(1):114–141.

Fedorovich, E., Nieuwstadt, F. T. M., and Kaiser, R. (2001). Numerical and Laboratory Study of Horizontally Evolving Convective Boundary Layer. Part II: Effects of Elevated Wind Shear and Surface Roughness. *Journal of the Atmospheric Sciences*, 58(6):546–560.

Feigenwinter, C., Vogt, R., and Parlow, E. (1999). Vertical structure of selected turbulence characteristics above an urban canopy. *Theoretical and Applied Climatology*, 62(1-2):51–63.

Fernando, H., Pardyjak, E., Di Sabatino, S., Chow, F. K., De Wekker, S., Hoch, S. W., Hacker, J., Pace, J., Pratt, T., Pu, Z., Steenburgh, W., Whiteman, C. D., Wang, Y., Zajic, D., Balsley, B., Dimitrova, R., and Emmitt, G. (2015). The Materhorn - Unraveling the Intricacies of Mountain Weather. *Bulletin of the American Meteorological Society*.

Fernando, H. J. S., Zajic, D., Di Sabatino, S., Dimitrova, R., Hedquist, B., and Dallman, A. (2010). Flow, turbulence, and pollutant dispersion in urban atmospheres. *Physics of Fluids*, 22(5):051301.

Fiedler, H. E. (1988). Coherent structures in turbulent flows. *Progress in Aerospace Sciences*, 25(3):231–269.

Finnigan, J. J., Clement, R., Malhi, Y., Leuning, R., and Cleugh, H. A. (2003). A RE-EVALUATIONOF LONG-TERM FLUX MEASUREMENT TECHNIQUES Part I : Averaging and Coordinate Rotation. *Boundary-Layer Meteorology*, 107(1):1–48.

Foken, T. (2006). 50 years of the Monin-Obukhov similarity theory. *Boundary-Layer Meteorology*, 119(3):431–447.

Foken, T. and Wichura, B. (1996). Tools for quality assessment of surface-based flux measurements. *Agricultural and Forest Meteorology*, 78(1-2):83–105.

Fortuniak, K., Pawlak, W., and Siedlecki, M. (2013). Integral Turbulence Statistics Over a Central European City Centre. *Boundary-Layer Meteorology*, 146(2):257–276.

Garratt, J. R. (1992). *The Atmospheric Boundary Layer*. CAMBRIDGE University Press.

Grachev, A. A., Andreas, E. L., Fairall, C. W., Guest, P. S., and Persson, P. O. G. (2013). The Critical Richardson Number and Limits of Applicability of Local Similarity Theory in the Stable Boundary Layer. *Boundary-Layer Meteorology*, 147(1):51–82.

Grachev, A. A., Andreas, E. L., Fairall, C. W., Guest, P. S., and Persson, P. O. G. (2015). Similarity theory based on the Dougherty-Ozmidov length scale. *Quarterly Journal of the Royal Meteorological Society*, 141(690):1845–1856.

Granados-Munoz, M. J., Navas-Guzmán, F., Bravo-Aranda, J. a., Guerrero-Rascado, J. L., Lyamani, H., Fernández-Gálvez, J., and Alados-Arboledas, L. (2012). Automatic determination of the planetary boundary layer height using lidar: One-year analysis over southeastern Spain. *Journal of Geophysical Research: Atmospheres*, 117:1–10.

Grimm, N. B., Faeth, S. H., Golubiewski, N. E., Redman, C. L., Wu, J., Bai, X., and Briggs, J. M. (2008). Global change and the ecology of cities. *Science*, 319(5864):756–760.

Grimmond, C. S. and Oke, T. R. (1999). Aerodynamic properties of urban areas derived from analysis of surface form. *Journal of Applied Meteorology*, 38(9):1262–1292.

Grimmond, C. S. and Oke, T. R. (2002). Turbulent heat fluxes in urban areas: Observations and a local-scale urban meteorological parameterization scheme (LUMPS). *Journal of Applied Meteorology*, 41(7):792–810.

Grimmond, C. S., Salmond, J. A., Oke, T. R., Offerle, B., and Lemonsu, A. (2004). Flux and turbulence measurements at a densely built-up site in Marseille: Heat, mass (water and carbon dioxide), and momentum. *Journal of Geophysical Research D: Atmospheres*, 109(24):1–19.

Grimmond, C. S. B. (2006). Progress in measuring and observing the urban atmosphere. *Theoretical and Applied Climatology*, 84(1):3–22.

Grubišić, V., Doyle, J. D., Kuettner, J., Mobbs, S., Smith, R. B., Whiteman, C. D., Dirks, R., Czyzyk, S., Cohn, S. A., Vosper, S., Weissmann, M., Haimov, S., De Wekker, S. F., Pan, L. L., and Chow, F. K. (2008). The terrain-induced rotor experiment. *Bulletin of the American Meteorological Society*, 89(10):1513–1533.

Halios, C. H. and Barlow, J. F. (2018). Observations of the Morning Development of the Urban Boundary Layer Over London , UK , Taken During the ACTUAL Project. *Boundary-Layer Meteorology*, 166(3):395–422.

Hannesdóttir, A. (2013). *Boundary-layer height detection with a ceilometer at a coastal site in western Denmark*. PhD thesis, Technical University of Denmark, Roskilde, Denmark.

Hayden, K. L., Anlauf, K. G., Hoff, R. M., Strapp, J. W., Bottenheim, J. W., Wiebe, H. a., Froude, F. a., Martin, J. B., Steyn, D. G., and McKendry, I. G. (1997). The vertical chemical and meteorological structure of the boundary layer in the Lower Fraser Valley during Pacific '93. *Atmospheric Environment*, 31(14):2089–2105.

Heinrichs, D. and Bernet, J. S. (2014). Public transport and accessibility in informal settlements: Aerial cable cars in medellín, colombia. *Transportation Research Procedia*, 4:55–67. Sustainable Mobility in Metropolitan Regions. mobil.TUM 2014. International Scientific Conference on Mobility and Transport. Conference Proceedings.

Helfter, C., Tremper, A. H., Halios, C. H., Kotthaus, S., Bjorkegren, A., Grimmond, C. S. B., Barlow, J. F., and Nemitz, E. (2016). Spatial and temporal variability of urban fluxes of methane, carbon monoxide and carbon dioxide above London, UK. *Atmospheric Chemistry and Physics*, 16(16):10543–10557.

Helgason, W. and Pomeroy, J. W. (2012). Characteristics of the near-surface boundary layer within a mountain valley during winter. *Journal of Applied Meteorology and Climatology*, 51(3):583–597.

Henao, J. J., Mejía, J. F., Rendón, A. M., and Salazar, J. F. (2020). Sub-kilometer dispersion simulation of a CO tracer for an inter-Andean urban valley. *Atmospheric Pollution Research*, 11(5):928–945.

Henne, S., Furger, M., Nyeki, S., Steinbacher, M., Neininger, B., de Wekker, S. F. J., Dommen, J., Spichtinger, N., Stohl, A., and Prévôt, A. S. H. (2004). Quantification of topographic venting of boundary layer air to the free troposphere. *Atmospheric Chemistry and Physics*, 4(2):497–509.

Hennemuth, B. and Lammert, A. (2006). Determination of the Atmospheric Boundary Layer Height from Radiosonde and Lidar Backscatter. *Boundary-Layer Meteorology*, 120(1):181–200.

Herrera-Mejía, L. and Hoyos, C. D. (2019). Characterization of the atmospheric boundary layer in a narrow tropical valley using remote-sensing and radiosonde observations and the WRF model: the Aburrá Valley case-study. *Quarterly Journal of the Royal Meteorological Society*, 145(723):2641–2665.

Herrera-Mejía, L. and Hoyos, C. D. (2019). Characterization of the Atmospheric Boundary Layer in a Narrow Tropical Valley Using Remote Sensing and Radiosonde Observations, and the WRF Model: The Aburrá Valley Case Study. *Quarterly Journal of the Royal Meteorological Society*, page 35.

Hersbach, H., Bell, B., Berrisford, P., Hirahara, S., Horányi, A., Muñoz-Sabater, J., Nicolas, J., Peubey, C., Radu, R., Schepers, D., Simmons, A., Soci, C., Abdalla, S., Abellan, X., Balsamo, G., Bechtold, P., Biavati, G., Bidlot, J., Bonavita, M., De Chiara, G., Dahlgren, P., Dee, D., Diamantakis, M., Dragani, R., Flemming, J., Forbes, R., Fuentes, M., Geer, A., Haimberger, L., Healy, S., Hogan, R. J., HÃlm, E., JaniskovÃ¡, M., Keeley, S., Laloyaux, P., Lopez, P., Lupu, C., Radnoti, G., de Rosnay, P., Rozum, I., Vamborg, F., Villaume, S., and ThÃ©paut, J.-N. (2020). The era5 global reanalysis. *Quarterly Journal of the Royal Meteorological Society*, 146(730):1999–2049.

Hiller, R., Zeeman, M. J., and Eugster, W. (2008). Eddy-covariance flux measurements in the complex terrain of an Alpine Valley in Switzerland. *Boundary-Layer Meteorology*, 127(3):449–467.

Högström, U., Bergström, H., and Alexandersson, H. (1982). Turbulence characteristics in a near neutrally stratified urban atmosphere. *Boundary-Layer Meteorology*, 23:449–472.

Holzworth, G. C. (1964). Estimates of Mean Maximum Mixing Depths in the Contiguous United States. *Monthly Weather Review*, 92:235–242.

Hoyos, C. D., Ceballos, L. I., Pérez-Carrasquilla, J. S., Sepulveda, J., López-Zapata, S. M., Zuluaga, M. D., Velasquez, N., Herrera-Mejía, L., Hernández, O., Guzmán-Echavarría, G., and Zapata, M. (2019). Meteorological conditions leading to the 2015 Salgar flash flood:

Lessons for vulnerable regions in tropical complex terrain. *Natural Hazards and Earth System Sciences*, 19(11):2635–2665.

Hoyos, C. D., Herrera-Mejía, L., Roldán-Henao, N., and Isaza, A. (2020). Effects of fireworks on particulate matter concentration in a narrow valley: the case of the Medellín metropolitan area. *Environmental Fluid Mechanics*, 192(6):1–31.

Hu, X.-M., Nielsen-Gammon, J. W., and Zhang, F. (2010). Evaluation of three planetary boundary layer schemes in the WRF model. *Journal of Applied Meteorology and Climatology*, 49(9):1831–1844.

Huffman, G. J., Bolvin, D. T., Nelkin, E. J., Wolff, D. B., Adler, R. F., Gu, G., Hong, Y., Bowman, K. P., and Stocker, E. F. (2007). The TRMM Multisatellite Precipitation Analysis (TMPA): Quasi-Global, Multiyear, Combined-Sensor Precipitation Estimates at Fine Scales. *Journal of Hydrometeorology*, 8(1):38–55.

Hunt, J. and Durbin, P. (1999). Perturbed vortical layers and shear sheltering. *Fluid Dynamics Research*, 24(6):375 – 404.

Kaimal, J. C. and Finnigan, J. J. (1994). *Atmospheric boundary layer flows*, volume 41.

Kaimal, J. C., Wyngaard, J. C., Izumi, Y., and Cote, O. R. (1972). Spectral characteristics of surface-layer turbulence. *Quarterly Journal of the Royal Meteorological Society*, 098(417):563–589.

Kambezidis, H. D., Paliatsos, A. G., Kappos, N., and Kasselouri, B. (2012). A Case of African Dust Transport over Athens Captured by a Ceilometer. *Advances in Meteorology, Climatology and Atmospheric Physics*, pages 1245–1250.

Kastner-Klein, P. and Rotach, M. W. (2004). Mean Flow and Turbulence Characteristics in an Urban Roughness Sublayer. *Boundary-Layer Meteorology*, 111:55–84.

Klipp, C. L. and Mahrt, L. (2004). Flux-gradient relationship, self-correlation and intermittency in the stable boundary layer. *Quarterly Journal of the Royal Meteorological Society*, 130(601 PART B):2087–2103.

Kljun, N., Calanca, P., Rotach, M. W., and Schmid, H. P. (2015). A simple two-dimensional parameterisation for Flux Footprint Prediction (FFP). *Geoscientific Model Development*, 8(11):3695–3713.

Kolmogorov, A. N. (1941). The local structure of turbulence in incompressible viscous fluid for very large Reynolds numbers. *Dokl. Akad. Nauk. SSSR*, (30):299–303.

Kotthaus, S. and Grimmond, C. S. (2014). Energy exchange in a dense urban environment - Part II: Impact of spatial heterogeneity of the surface. *Urban Climate*, 10(P2):281–307.

Krishnamurti, T., Stefanova, L., and Misra, V. (2013). *Tropical Meteorology: An Introduction*. Springer Atmospheric Sciences. Springer New York.

Kumar, R., Barth, M. C., Pfister, G. G., Delle Monache, L., Lamarque, J., Archer-Nicholls, S., TIlmes, S., Ghuse, S., Wiedinmyer, C., Naja, M., and Walters, S. (2018). How will air quality change in South Asia by 2050? *American Geophysical Union*.

Kummerow, C., Barnes, W., Kozu, T., Shiue, J., and Simpson, J. (1998). The tropical rainfall measuring mission(TRMM) sensor package. *Journal of Atmospheric and Oceanic Technology*, 15(3):809–817.

Laing, A. and Evans, J. L. (2015). *Introduction to tropical meteorology, 2nd Edition*. The COMET Program.

Lau, E., McLaughlin, S., Pratte, F., Weber, B., Merritt, D., Wise, M., Zimmerman, G., James, M., and Sloan, M. (2013). The DeTect Inc. RAPTOR VAD-BL Radar Wind Profiler. *Journal of Atmospheric and Oceanic Technology*, 30:1978–1984.

Lee, S.-J., Kim, J., and Cho, C.-H. (2014). An automated monitoring of atmospheric mixing height from routine radiosonde profiles over South Korea using a web-based data transfer method. *Environmental Monitoring and Assessment*, 186:3253–3263.

Lehner, M. and Rotach, M. W. (2018). Current Challenges in Understanding and Predicting Transport and Exchange in the Atmosphere over Mountainous Terrain. *Atmosphere*, 9(7).

Leukauf, D., Gohm, A., and Rotach, M. W. (2016). Quantifying horizontal and vertical tracer mass fluxes in an idealized valley during daytime. *Atmospheric Chemistry and Physics*, pages 13049–13066.

Leukauf, D., Gohm, A., and Rotach, M. W. (2017). Toward generalizing the impact of surface heating, stratification, and terrain geometry on the daytime heat export from an idealized valley. *Journal of Applied Meteorology and Climatology*, 56(10):2711–2727.

Leukauf, D., Gohm, A., Rotach, M. W., and Wagner, J. S. (2015). The impact of the temperature inversion breakup on the exchange of heat and mass in an idealized valley: Sensitivity to the radiative forcing. *Journal of Applied Meteorology and Climatology*, 54(11):2199–2216.

Li, H., Guo, B., Han, M., Tian, M., and Zhang, J. (2015). Particulate matters pollution characteristic and the correlation between pm (pm2. 5, pm10) and meteorological factors during the summer in shijiazhuang. *Journal of Environmental Protection*, 6(05):457.

Liebmann, B. and Smith, C. A. (1996). Description of a complete (interpolated) outgoing longwave radiation dataset. *Bulletin of the American Meteorological Society*, 77(6):1275–1277.

Liu, H., Yuan, R., Mei, J., Sun, J., Liu, Q., and Wang, Y. (2017). Scale Properties of Anisotropic and Isotropic Turbulence in the Urban Surface Layer. *Boundary-Layer Meteorology*, 165(2):277–294.

Liu, S. and Liang, X. Z. (2010). Observed diurnal cycle climatology of planetary boundary layer height. *Journal of Climate*, 23(21):5790–5809.

Liu, X. G., Li, J., Qu, Y., Han, T., Hou, L., Gu, J., Chen, C., Yang, Y., Liu, X., Yang, T., Zhang, Y., Tian, H., and Hu, M. (2013). Formation and evolution mechanism of regional haze: a case study in the megacity beijing, china. *Atmospheric Chemistry and Physics*, 13(9):4501–4514.

Lokoshchenko, M. a. (2002). Long-Term Sodar Observations in Moscow and a New Approach to Potential Mixing Determination by Radiosonde Data. *Journal of Atmospheric and Oceanic Technology*, 19(8):1151–1162.

Lotteraner, C. and Piringer, M. (2016). Mixing-Height Time Series from Operational Ceilometer Aerosol-Layer Heights. *Boundary-Layer Meteorology*, 161(2):265–287.

Mahrt, L. (1999). Stratified atmospheric boundary layers. *Boundary-Layer Meteorology*, 90(3):375–396.

Mamtimin, B. and Meixner, F. X. (2011). Air pollution and meteorological processes in the growing dryland city of urumqi (xinjiang, china). *Science of The Total Environment*, 409(7):1277 – 1290.

Mapes, B. E. (2000). Convective inhibition, subgrid-scale triggering energy, and stratiform instability in a toy tropical wave model. *Journal of the Atmospheric Sciences*, 57(10):1515–1535.

Martins, C. A., Moraes, O. L., Acevedo, O. C., and Degrazia, G. A. (2009). Turbulence intensity parameters over a very complex terrain. *Boundary-Layer Meteorology*, 133(1):35–45.

Martucci, G., Matthey, R., Mitev, V., and Richner, H. (2010). Frequency of boundary-layer-top fluctuations in convective and stable conditions using laser remote sensing. *Boundary-Layer Meteorology*, 135:313–331.

Massaro, G., Stiperski, I., Pospichal, B., and Rotach, M. W. (2015). Accuracy of retrieving temperature and humidity profiles by ground-based microwave radiometry in truly complex terrain. *Atmospheric Measurement Techniques*, 8(8):3355–3367.

May, P. T., Long, C. N., and Protat, A. (2012). The diurnal cycle of the boundary layer, convection, clouds, and surface radiation in a coastal monsoon environment (darwin, australia). *Journal of Climate*, 25(15):5309–5326.

Mayer, H. (1999). Air pollution in cities. *Atmospheric environment*, 33(24-25):4029–4037.

McMillen, R. T. (1988). An eddy correlation technique with extended applicability to non-simple terrain. *Boundary-Layer Meteorology*, 43(3):231–245.

Monin, A. S. and Obukhov, A. M. (1954). Basic laws of turbulent mixing in the surface layer of the atmosphere. *Tr. Akad. Nauk SSSR Geophiz*, 24(151):163–187.

Moore, C. J. (1986). Frequency response corrections for eddy correlation systemns. *Boundary-Layer Meteorology*, 37:17–35.

Moraes, O. L., Acevedo, O. C., Degrazia, G. A., Anfossi, D., Da Silva, R., and Anabor, V. (2005). Surface layer turbulence parameters over a complex terrain. *Atmospheric Environment*, 39(17):3103–3112.

Morille, Y., Haeffelin, M., Drobinski, P., and Pelon, J. (2007). STRAT: An Automated Algorithm to Retrieve the Vertical Structure of the Atmosphere from Single-Channel Lidar Data. *Journal of Atmospheric and Oceanic Technology*, 24(5):761–775.

Muenkel, C., Emeis, S., Mueller, W. J., and Schaefer, K. P. (2004). Aerosol concentration measurements with a lidar ceilometer: results of a one year measuring campaign. *Proceedings of SPIE–the international society for optical engineering*, 5235:486–496.

Münkel, C., Eresmaa, N., Räsänen, J., and Karppinen, A. (2006). Retrieval of mixing height and dust concentration with lidar ceilometer. *Boundary-Layer Meteorology*, 124(1):117–128.

Münkel, C. and Roininen, R. (2010). Automatic monitoring of boundary layer structures with ceilometer. Technical report, Vaisala.

Nadeau, D. F., Oldroyd, H. J., Pardyjak, E. R., Sommer, N., Hoch, S. W., and Parlange, M. B. (2020). Field observations of the morning transition over a steep slope in a narrow alpine valley. *Environmental Fluid Mechanics*, 20(5):1199–1220.

Nadeau, D. F., Pardyjak, E. R., Higgins, C. W., and Parlange, M. B. (2013). Similarity Scaling Over a Steep Alpine Slope. *Boundary-Layer Meteorology*, 147(3):401–419.

Nesbitt, S. W. and Zipser, E. J. (2003). The diurnal cycle of rainfall and convective intensity according to three years of trmm measurements. *Journal of Climate*, 16(10):1456–1475.

Nieuwstadt, F. T. (1984). The turbulent structure of the stable, nocturnal boundary layer.

Nieuwstadt, F. T. M. and van Dop, H. (1982). *Atmospheric Turbulence and Air Pollution Modelling*.

Nisperuza, D. J. (2015). *Propiedades Ópticas de los Aerosoles Atmosféricos en la Región Andina Colombiana Mediante Análisis de Mediciones Remotas : LIDAR , Fotométricas y Satelitales Presentada por Daniel José Nisperuza Toledo*. PhD thesis, Universidad Nacional de Colombia.

Noppel, H. and Fiedler, F. (2002). Mesoscale heat transport over complex terrain by slope winds - A conceptual model and numerical simulations. *Boundary-Layer Meteorology*, 104(1):73–97.

Nordbo, A., Järvi, L., Haapanala, S., Moilanen, J., and Vesala, T. (2013). Intra-City Variation in Urban Morphology and Turbulence Structure in Helsinki, Finland. *Boundary-Layer Meteorology*, 146(3):469–496.

Offerle, B., Grimmond, C. S., Fortuniak, K., and Pawlak, W. (2006). Intraurban differences of surface energy fluxes in a central European City. *Journal of Applied Meteorology and Climatology*, 45(1):125–136.

Oke, T. R. (1988). The urban energy balance. *Progress in Physical Geography*, 12(4):471–508.

Oke, T. R., Spronken-Smith, R. A., Jáuregui, E., and Grimmond, C. S. (1999). The energy balance of central Mexico City during the dry season. *Atmospheric Environment*, 33(24-25):3919–3930.

Pahlow, M., Parlange, M. B., and Porté-Agel, F. (2001). On Monin-Obukhov similarity in the stable atmospheric boundary layer. *Boundary-Layer Meteorology*, 99(2):225–248.

Pal, S., Lee, T., Phelps, S., and Wekker, S. D. (2014). Impact of atmospheric boundary layer depth variability and wind reversal on the diurnal variability of aerosol concentration at a valley site. *Science of The Total Environment*, 496:424 – 434.

Pal, S., Lopez, M., Schmidt, M., Ramonet, M., Gibert, F., Xueref-Remy, I., and Ciais, P. (2015). Investigation of the atmospheric boundary layer depth variability and its impact on the 222rn concentration at a rural site in france. *Journal of Geophysical Research: Atmospheres*, 120(2):623–643.

Panofsky, H. and Dutton, J. (1984). *Atmospheric turbulence: models and methods for engineering applications*. cited By 827.

Panofsky, H. A., Tennekes, H., Lenschow, D. H., and Wyngaard, J. C. (1977). THE CHARACTERISTICS OF TURBULENT VELOCITY COMPONENTS IN THE SURFACE LAYER UNDER CONVECTIVE CONDITIONS. *Boundary-Layer Meteorology*, 11:355–361.

Pegahfar, N. and Bidokhti, A. A. (2013). Similarity relations in a stable and relatively neutral surface layer in an urban area with complex topography (Tehran). *Environmental Fluid Mechanics*, 13(1):1–31.

Pegahfar, N. and Zawar-Reza, P. (2017). Observed turbulence characteristics in unstable conditions over the city of Tehran based on similarity theory. *Meteorology and Atmospheric Physics*, 129(5):479–494.

Peppler, R. A. (1988). A review of static stability indices and related thermodynamic parameters. Technical report, Illinois State Water Survey.

Pérez Arango, J. D. (2008). *Caracterización preliminar de la circulación en la capa límite atmosférica. Caso de estudio: Valle de Aburrá.* PhD thesis, Universidad Nacional de Colombia Sede Medellín.

Pérez Arango, J. D., Palacio Tobón, C. A., and Jiménez Mejía, J. F. (2011). Aspectos descriptivos de la circulación en la capa límite atmosférica en el Valle de Aburrá. *DESCRIPTIVE ASPECTS ON ATMOSPHERIC BOUNDARY LAYER CIRCULATION OVER THE VALLE DE ABURRA. (English)*, 7:31–41.

Perlik, M., Messerli, P., and Bätzing, W. (2001). Towns in the Alps. Urbanization Processes, Economic Structure, and Demarcation of European Functional Urban Areas (EFUAs) in the Alps. *Mountain Research and Development*, 21(3):243–252.

Poveda, G. (2004). La Hidroclimatología de Colombia: Una síntesis desde la escala interdecadal hasta la escala diurna. *Revista Academia Colombiana de Ciencias*, 28(10):201–222.

Poveda, G., Waylen, P. R., and Pulwarty, R. S. (2006). Annual and inter-annual variability of the present climate in northern South America and southern Mesoamerica. *Palaeogeography, Palaeoclimatology, Palaeoecology*, 234(1):3–27.

Quan, J., Gao, Y., Zhang, Q., Tie, X., Cao, J., Han, S., Meng, J., Chen, P., and Zhao, D. (2013). Evolution of planetary boundary layer under different weather conditions, and its impact on aerosol concentrations. *Particuology*, 11(1):34–40.

Quan, L. and Hu, F. (2009). Relationship between turbulent flux and variance in the urban canopy. *Meteorology and Atmospheric Physics*, 104(1-2):29–36.

Rampanelli, G. and Zardi, D. (2004). A method to determine the capping inversion of the convective boundary layer. *Journal of Applied Meteorology*, 43(6):925–933.

Raupach, M. R., Antonia, R. A., and Rajagopalan, S. (1991). Rough-wall turbulent boundary layers. *Applied Mechanics Reviews*, 44:1–25.

Rendón, A. M., Salazar, J. F., Palacio, C. A., and Wirth, V. (2015). Temperature inversion breakup with impacts on air quality in urban valleys influenced by topographic shading. *Journal of Applied Meteorology and Climatology*, 54(2):302–321.

Rendón, A. M., Salazar, J. F., Palacio, C. A., Wirth, V., and Brötz, B. (2014). Effects of urbanization on the temperature inversion breakup in a mountain valley with implications for air quality. *Journal of Applied Meteorology and Climatology*, 53(4):840–858.

Rendón, A. M., Salazar, J. F., and Wirth, V. (2020). Daytime air pollution transport mechanisms in stable atmospheres of narrow versus wide urban valleys. *Environmental Fluid Mechanics*, 20(4):1101–1118.

Restrepo, P. P., Hernandez, P. A., and Roldan, L. M. (2016). Informe de calidad de vida de medellin, 2016. Technical report, Medellin Como Vamos.

Rochetin, N., Couvreux, F., Grandpeix, J.-Y., and Rio, C. (2014). Deep convection triggering by boundary layer thermals. part i: Les analysis and stochastic triggering formulation. *Journal of the Atmospheric Sciences*, 71(2):496–514.

Roldán-Henao, N., Hoyos, C. D., Herrera-Mejía, L., and Isaza, A. (2020). An investigation of the precipitation net effect on the particulate matter concentration in a narrow valley: Role of lower-troposphere stability. *Journal of Applied Meteorology and Climatology*, 59(3):401–426.

Roldán-Henao, N., Hoyos, C. D., Herrera-Mejía, L., and Isaza, A. (2020). An investigation of the precipitation net effect on the particulate matter concentration in a narrow valley: Role of lower-troposphere stability. *Journal of Applied Meteorology and Climatology*, 59(3):401–426.

Rosenzweig, C., Solecki, W., Romero-Lankao, P., Mehrotra, S., Dhakal, S., and Ibrahim, S. (2018). *Climate Change and Cities: Second Assessment Report of the Urban Climate Change Research Network*. Climate Change and Cities: Second Assessment Report of the Urban Climate Change Research Network. Cambridge University Press.

Rotach, M. W. (1993). Turbulence close to a rough urban surface part II: Variances and gradients. *Boundary-Layer Meteorology*, 66(1-2):75–92.

Rotach, M. W. (1994). Determination of the zero plane displacement in an urban environment. *Boundary-Layer Meteorology*, 67(1-2):187–193.

Rotach, M. W. (1995). Profiles of turbulence statistics in and above an urban street canyon. *Atmospheric Environment*, 29(13):1473–1486.

Rotach, M. W., Calanca, P., Graziani, G., Gurtz, J., Steyn, D. G., Vogt, R., Andretta, M., Christen, A., Cieslik, S., Connolly, R., De Wekker, S., Galmarini, S., Kadygrov, N., Kadygrov,

V., Miller, E., Neininger, B., Rucker, M., Van Grosel, E., Weber, H., Weiss, A., and Zappa, M. (2004). TURBULENCE STRUCTURE AND EXCHANGE PROCESSES IN AN ALPINE VALLEY. *Bulletin of the American Meteorological Society*, (January):1367–1386.

Rotach, M. W., Gohm, A., Lang, M. N., Leukauf, D., Stiperski, I., and Wagner, J. S. (2015). On the vertical exchange of heat, mass, and momentum over complex, mountainous terrain. *Frontiers in Earth Sciences*, 3(December):1–14.

Rotach, M. W., Stiperski, I., Fuhrer, O., Goger, B., Gohm, A., Obleitner, F., Rau, G., Sfyri, E., and Vergrgeiner, J. (2017). Investigating exchange processes over complex topography: The Innsbruck box (i-Box). *Bulletin of the American Meteorological Society*, 98(4):787–805.

Rotach, M. W., Vogt, R., Bernhofer, C., Batchvarova, E., Christen, A., Clappier, A., Feddersen, B., Gryning, S. E., Martucci, G., Mayer, H., Mitev, V., Oke, T. R., Parlow, E., Richner, H., Roth, M., Roulet, Y. A., Ruffieux, D., Salmond, J. A., Schatzmann, M., and Voogt, J. A. (2005). BUBBLE - An urban boundary layer meteorology project. *Theoretical and Applied Climatology*, 81(3-4):231–261.

Roth, M. (2000). Review of atmospheric turbulence over cities. *Quarterly Journal of the Royal Meteorological Society*, 126(564):941–990.

Roth, M. (2007). Review of urban climate research in (sub)tropical regions. *International Journal of Climatology*, 27(27):1859–1873.

Roth, M., Jansson, C., and Velasco, E. (2017). Multi-year energy balance and carbon dioxide fluxes over a residential neighbourhood in a tropical city. *International Journal of Climatology*, 37(5):2679–2698.

Roth, M. and Oke, T. R. (1993). Turbulent transfer relationships over an urban surface. I : Spectral Characteristics. *Quarterly Journal of the Royal Meteorological Society*, 119(513):1071–1104.

Saide, P. E., Carmichael, G. R., Spak, S. N., Gallardo, L., Osses, A. E., Mena-Carrasco, M. A., and Pagowski, M. (2011). Forecasting urban pm10 and pm2.5 pollution episodes in very stable nocturnal conditions and complex terrain using wrf–chem co tracer model. *Atmospheric Environment*, 45(16):2769 – 2780.

Salamanca, F., Martilli, A., Tewari, M., and Chen, F. (2011). A study of the urban boundary layer using different urban parameterizations and high-resolution urban canopy parameters with WRF. *Journal of Applied Meteorology and Climatology*, 50(5):1107–1128.

Santosa, S. J., Okuda, T., Tanaka, S., Sciences, N., Sciences, N., and Utara, S. (2008). Air Pollution and Urban Air Quality Management in Indonesia. *Clean Journal*, 36:466–475.

Sawyer, V. and Li, Z. (2013). Detection, variations and intercomparison of the planetary boundary layer depth from radiosonde, lidar and infrared spectrometer. *Atmospheric Environment*, 79:518–528.

Schmutz, M. and Vogt, R. (2019). Flux similarity and turbulent transport of momentum, heat and carbon dioxide in the urban boundary layer. *Boundary-Layer Meteorology*, 172(1):45–65.

Schmutz, M., Vogt, R., Feigenwinter, C., and Parlow, E. (2016). Ten years of eddy covariance measurements in Basel, Switzerland: Seasonal and interannual variabilities of urban CO2 mole fraction and flux. *Journal of Geophysical Research*, 121(14):8649–8667.

Schneider, T., Bischoff, T., and Haug, G. H. (2014). Migrations and dynamics of the intertropical convergence zone. *Nature*, 513(7516):45–53.

Schnitzhofer, R., Norman, M., Wisthaler, A., Vergeiner, J., Harnisch, F., Gohm, A., Obleitner, F., Fix, A., Neininger, B., and Hansel, A. (2009). A multimethodological approach to study the spatial distribution of air pollution in an alpine valley during wintertime. *Atmospheric Chemistry and Physics*, 9(10):3385–3396.

Schotanus, P., Nieuwstadt, F. T., and De Bruin, H. A. (1983). Temperature measurement with a sonic anemometer and its application to heat and moisture fluxes. *Boundary-Layer Meteorology*, 26(1):81–93.

Schween, J. H., Hirsikko, a., Löhnert, U., and Crewell, S. (2014). Mixing layer height retrieval with ceilometer and Doppler lidar: from case studies to long-term assessment. *Atmospheric Measurement Techniques Discussions*, 7:4275–4319.

Seibert, P., Beyrich, F., Gryning, S.-e., Jo, S., Rasmussen, A., and Tercier, P. (2000). Review and intercomparison of operational methods for the determination of the mixing height. *Atmospheric Environment*, 34:1001–1027.

Seidel, D. J., Ao, C. O., and Li, K. (2010). Estimating climatological planetary boundary layer heights from radiosonde observations: Comparison of methods and uncertainty analysis. *Journal of Geophysical Research: Atmospheres*, 115:1–15.

Serafin, S., Adler, B., Cuxart, J., De Wekker, S. F., Gohm, A., Grisogono, B., Kalthoff, N., Kirshbaum, D. J., Rotach, M. W., Schmidli, J., Stiperski, I., Večenaj, Ž., and Zardi, D. (2018). Exchange processes in the atmospheric boundary layer over mountainous terrain. *Atmosphere*, 9(3):1–32.

Sfyri, E., Rotach, M. W., Stiperski, I., Bosveld, F. C., Lehner, M., and Obleitner, F. (2018). Scalar-Flux Similarity in the Layer Near the Surface Over Mountainous Terrain. *Boundary-Layer Meteorology*, 169(1):11–46.

Shao, Y. and Hacker, J. M. (1990). Local similarity relationships in a horizontally inhomogeneous boundary layer. *Boundary-Layer Meteorology*, 52(1-2):17–40.

Shrivastava, R., Dash, S. K., Oza, R. B., and Sharma, D. N. (2014). Evaluation of Parameterization Schemes in the WRF Model for Estimation of Mixing Height. *International Journal of Atmospheric Sciences*, 2014(February):Article ID: 451578.

Skamarock, W. C., Klemp, J. B., Dudhia, J., Gill, D. O., Barker, D. M., Wang, W., and Powers, J. G. (2008). A description of the advanced research wrf version 3. ncar technical note -475+str.

Sorbjan, Z. (1987). An examination of local similarity theory in the stably stratified boundary layer. *Boundary-Layer Meteorology*, 38(1-2):63–71.

Souch, C. and Grimmond, S. (2006). Applied climatology: urban climate. *Progress in Physical Geography: Earth and Environment*, 30(2):270–279.

Sreenivasan, K. R. (1995). On the universality of the Kolmogorov constant. *Physics of Fluids*, 7(11):2778–2784.

Stachlewska, I. S., Piadłowski, M., Migacz, S., Szkop, A., Zielińska, A. J., and Swaczyna, P. L. (2012). Ceilometer observations of the boundary layer over Warsaw, Poland. *Acta Geophysica*, 60(5):1386–1412.

Steyn, D. G., Baldi, M., and Hoff, R. M. (1999). The detection of mixed layer depth and entrainment zone thickness from lidar backscatter profiles. *Journal of Atmospheric and Oceanic Technology*, 16(1979):953–959.

Stiperski, I. and Calaf, M. (2018). Dependence of near-surface similarity scaling on the anisotropy of atmospheric turbulence. *Quarterly Journal of the Royal Meteorological Society*, 144(712):641–657.

Stiperski, I., Calaf, M., and Rotach, M. W. (2019). Scaling, Anisotropy, and Complexity in Near-Surface Atmospheric Turbulence. *Journal of Geophysical Research: Atmospheres*, pages 1428–1448.

Stiperski, I. and Rotach, M. W. (2016). On the measurement of turbulence over complex mountainous terrain. *Boundary-Layer Meteorology*, 159(1):97–121.

Stull, R. B. (1988). *An introduction to boundary layer meteorology.*

Stull, R. B. (1991). Static Stability-An Update. *Bulletin of the American Meteorological Society*, 72(10):1521–1530.

Su, T., Li, J., Li, C., Xiang, P., Lau, A. K. H., Guo, J., Yang, D., and Miao, Y. (2017). An intercomparison of long-term planetary boundary layer heights retrieved from CALIPSO, ground-based lidar, and radiosonde measurements over Hong Kong. *Journal of Geophysical Research: Atmospheres*, 122(7):3929–3943.

Sundström, A. M., Nousiainen, T., and Petäjä, T. (2009). On the quantitative low-level aerosol measurements using ceilometer-type lidar. *Journal of Atmospheric and Oceanic Technology*, 26(2005):2340–2352.

Tampieri, F., Maurizi, A., and Viola, A. (2009). An investigation on temperature variance scaling in the atmospheric surface layer. *Boundary-Layer Meteorology*, 132(1):31–42.

Tang, G., Zhang, J., Zhu, X., Song, T., Münkel, C., Hu, B., Schäfer, K., Liu, Z., Zhang, J., Wang, L., Xin, J., Suppan, P., and Wang, Y. (2016). Mixing layer height and its implications for air pollution over beijing, china. *Atmospheric Chemistry and Physics*, 16(4):2459–2475.

Taylor, K. E. (2001). Study of some factors maintaining the 'atrophie gonadique' character in experimental populations of Drosophila melanogaster. *Journal of Geophysical Research*, 106(D7):7183–7192.

Thiermann, V. (1990). *Optische Messung turbulenter Flüsse und Vorhersage der optischen Turbulenz aus einfachen Grenzschichtparametern*. na.

Tischler, S. and Mailer, M. (2019). Cable propelled transit systems in urban areas. *Transportation Research Procedia*, 41:169–173. Urban Mobility – Shaping the Future Together mobil.TUM 2018 – International Scientific Conference on Mobility and Transport Conference Proceedings.

Torrence, C. and Compo, G. P. (1997). A practical guide to wavelet analysis. *Bulletin of the American Meteorological Society*, 79(1):61–78.

TRMM (2011). Trmm (tmpa) rainfall estimate l3 3 hour 0.25 degree x 0.25 degree v7. https://doi.org/10.5067/TRMM/TMPA/3H/7.

Uzan, L., Egert, S., and Alpert, P. (2016). Ceilometer evaluation of the eastern Mediterranean summer boundary layer height-first study of two Israeli sites. *Atmospheric Measurement Techniques*, 9(9):4387–4398.

van der Kamp, D. and McKendry, I. (2010). Diurnal and Seasonal Trends in Convective Mixed-Layer Heights Estimated from Two Years of Continuous Ceilometer Observations in Vancouver, BC. *Boundary-Layer Meteorology*, 137(3):459–475.

Večenaj, Z. and De Wekker, S. F. (2015). Determination of non-stationarity in the surface layer during the T-REX experiment. *Quarterly Journal of the Royal Meteorological Society*, 141(690):1560–1571.

Večenaj, Z., de Wekker, S. F., and Grubišić, V. (2011). Near-surface characteristics of the turbulence structure during a mountain-wave event. *Journal of Applied Meteorology and Climatology*, 50(5):1088–1106.

Vickers, D. and Mahrt, L. (1997). Quality Control and Flux Sampling Problems for Tower and Aircraft Data. *Journal of Atmospheric and Oceanic Technology*, pages 512–526.

Wagner, J. S., Gohm, A., and Rotach, M. W. (2014). The impact of valley geometry on daytime thermally driven flows and vertical transport processes. *Quarterly Journal of the Royal Meteorological Society*, i(July):1780–1794.

Wang, W., Shen, X., and Huang, W. (2016). A Comparison of Boundary-Layer Characteristics Simulated Using Different Parametrization Schemes. *Boundary-Layer Meteorology*, 161(2):375–403.

Ward, H. C., Evans, J. G., and Grimmond, C. S. (2013). Multi-season eddy covariance observations of energy, water and carbon fluxes over a suburban area in Swindon, UK. *Atmospheric Chemistry and Physics*, 13(9):4645–4666.

Ward, H. C. and Grimmond, C. S. (2017). Assessing the impact of changes in surface cover, human behaviour and climate on energy partitioning across Greater London. *Landscape and Urban Planning*, 165(March):142–161.

Webb, E. K., Pearman, G. I., and Leuning, R. (1980). Correction of flux measurements for density effects due to heat and water vapour transfer. *Quarterly Journal of the Royal Meteorological Society*, 106(447):85–100.

Weber, S. and Kordowski, K. (2010). Comparison of atmospheric turbulence characteristics and turbulent fluxes from two urban sites in Essen, Germany. *Theoretical and Applied Climatology*, 102(1):61–74.

Whiteman, C. D. (1982). Breakup of temperature inversions in deep mountain valleys: Part I. Observations. *Journal of Applied Meteorology*, 21(3):270–290.

Whiteman, C. D. (2000). *Mountain Meteorology: Fundamentals and Applications*, volume 21. Oxford University Press.

Whiteman, C. D., Hoch, S. W., Horel, J. D., and Charland, A. (2014). Relationship between particulate air pollution and meteorological variables in Utah's Salt Lake Valley. *Atmospheric Environment*.

Whiteman, C. D. and McKee, T. B. (1982). Breakup of temperature inversions in deep mountain valleys: Part II. Thermodynamic Model. *Journal of Applied Meteorology*, pages 290 – 302.

Whiteman, C. D., Pospichal, B., Eisenbach, S., Weihs, P., Clements, C. B., Steinacker, R., Mursch-Radlgruber, E., and Dorninger, M. (2004). Inversion Breakup in Small Rocky Mountain and Alpine Basins. *Journal of Applied Meteorology*, 43(8):1069–1082.

Wiegner, M., Madonna, F., Binietoglou, I., Forkel, R., Gasteiger, J., Geiß, a., Pappalardo, G., Schäfer, K., and Thomas, W. (2014). What is the benefit of ceilometers for aerosol remote sensing? An answer from EARLINET. *Atmospheric Measurement Techniques*, 7:1979–1997.

Wiernga, J. (1993). Representative roughness parameters for homogeneous terrain. *Boundary-Layer Meteorology*, 63(4):323–363.

Wood, C. R., Lacser, A., Barlow, J. F., Padhra, A., Belcher, S. E., Nemitz, E., Helfter, C., Famulari, D., and Grimmond, C. S. (2010). Turbulent Flow at 190 m Height Above London During 2006-2008: A Climatology and the Applicability of Similarity Theory. *Boundary-Layer Meteorology*, 137(1):77–96.

Wyngaard, J. C. (2010). *Turbulence in the Atmosphere*. Cambridge University Press.

Wyngaard, J. C., Coté, O. R., and Izumi, Y. (1971). Local Free Convection, Similarity, and the Budgets of Shear Stress and Heat Flux. *Journal of the Atmospheric Sciences*, 28:1171–1182.

Young, J. S. (2013). *Investigation of winter time cold-air pools and aerosol layers in the salt lake valle y using a lidar ceilometer*. PhD thesis, University of Utah.

Young, J. S. and Whiteman, C. D. (2015). Laser ceilometer investigation of persistent wintertime cold-air pools in Utah's Salt Lake Valley. *Journal of Applied Meteorology and Climatology*, page 150203142804008.

Yu, H., Liu, S. C., and Dickinson, R. E. (2001). Radiative effects of aerosols on the evolution of the atmospheric boundary layer. *Journal of Geophysical Research: Atmospheres*, 107(D12):AAC 3–1–AAC 3–14.

Zardi, D. and Whiteman, C. D. (2013). *Diurnal Mountain Wind Systems*, pages 35–119. Springer Netherlands, Dordrecht.

Zhang, H., Chen, J., and Park, S.-u. (2001). TURBULENCE STRUCTURE IN UNSTABLE CONDITIONS OVER VARIOUS SURFACES. *Boundary-Layer Meteorology*, 5(1):243–261.

Zhang, Y. and Li, S. (2019). Climatological characteristics of planetary boundary layer height over Japan. *International Journal of Climatology*.

Zhang, Y., Zhang, S., Huang, C., Huang, K., Gong, Y., and Gan, Q. (2014a). Diurnal variations of the planetary boundary layer height estimated from intensive radiosonde observations over Yichang, China. *Science China Technological Sciences*, 57(11):2172–2176.

Zhang, Y., Zhang, S., Huang, C., Huang, K., Gong, Y., and Gan, Q. (2014b). Diurnal variations of the planetary boundary layer height estimated from intensive radiosonde observations over Yichang, China. *Science China Technological Sciences*, 57(11):2172–2176.

Zou, J., Sun, J., Liu, G., Yuan, R., and Zhang, H. (2018). Vertical Variation of the Effects of Atmospheric Stability on Turbulence Statistics Within the Roughness Sublayer Over Real Urban Canopy. *Journal of Geophysical Research: Atmospheres*, 123(4):2017–2036.

Zoumakis, N. M. and Efstathiou, G. A. (2006). Parameterization of inversion breakup in idealized valleys. Part I: The adjustable model parameters. *Journal of Applied Meteorology and Climatology*, 45(4):600–608.